



**THE UNIVERSITY OF QUEENSLAND**  
A U S T R A L I A

**In-Vitro Toxicology of Respirable Iron-Rich Particles Relevant to  
Mining Industry: A High Throughput Framework for Interpreting  
Environmental Particulate Matter Toxicity**

Shiva Prakash

Bachelor of Biomedical Science (Hons)

*A thesis submitted for the degree of Doctor of Philosophy at*

*The University of Queensland in 2014*

School of Medicine

National Research Centre for Environmental Toxicology

## Abstract

This project investigated the cytotoxicity profiles and toxicological properties of inhalable iron-rich particles generated by mining activity. National Environment Protection Measure (NEPM) ambient air quality regulations specifically regulate sub-10  $\mu\text{m}$  ( $\text{PM}_{10}$ ) and sub-2.5  $\mu\text{m}$  ( $\text{PM}_{2.5}$ ) diameter particle fractions corresponding to thoracic and respirable lung penetration, respectively. However, atmospheric concentrations of fugitive iron-rich particulates in iron ore mining and processing associated settlements raised concerns that NEPM limits may inadequately address the specific toxicological profile of iron-rich  $\text{PM}_{10}$  and potentially adsorbed organics in these regions. To address this, comparative cytotoxicity experiments were carried out *in-vitro* using a variety of particulate standards, featuring other frequently studied metal-oxides, to help bridge *in-vivo* and epidemiological knowledge in the literature with *in-vitro* toxicological results. This also required the development of a novel framework to interpret physical and physiological characteristics of coarse, poorly soluble metal-oxide particles by conducting a critical systematic literature review. Analysis by the ChemCentre, WA was taken into account with relation to potentially absorbed organics and the influence of Polycyclic Aromatic Hydrocarbons (PAHs) investigated.

The protocols developed by this project are applicable to high-throughput assessment of particulate matter generated by mining activity, having defined methodology to rapidly acquire sufficient quantities of  $\text{PM}_{10}$  for assays which can be multiplexed and the effects of particulate interference on assays minimised. This includes the integration of non-destructive sterilisation techniques, physical characterising by particle-sizing, particle solubility analysis and observation of particle morphology by electron microscopy and elemental analysis. Epithelial (A549), fibroblast (LL24) and monocyte differentiated macrophage (U937) cell lines were tested to build a picture of particulate effects on the major lung cell types in the lung parenchyma; the alveolar epithelium, connective tissue and immune system. The effect of lung fluid surfactants on cytotoxicity was determined, and advanced tissue culture methods were trialled to improve the differentiation between particles provided by the endpoints.

The ore samples from the Mining Area C (MAC), Yandi and Newman Hub mines in the Pilbara region were found to have an effect comparable to the cytotoxicity of micron-size iron oxide standards and selected standards of titanium dioxide, silicon dioxide and carbon black, whereas copper oxide was found to have some ten-fold greater cytotoxicity across the cell lines. However cytotoxicity as a principle differentiator of toxicity was found to be insufficient in differentiating the physiological response to iron-rich PM<sub>10</sub> and insoluble metal-oxide standards. At high concentrations the dose-response relationship plateaued at a maximum value for iron-oxide standards and iron ore samples in the A549 and LL24 cell lines, while at low doses the U937 cell line showed increased proliferation as a result of increased differentiation. Under coculture conditions, U937 was found to increase the proliferation of A549 cells in response to the Yandi, Newman and silicon PM<sub>10</sub> particles, suggesting a key role for the inflammatory response in driving cellular hyperplasia. The cytotoxic effect of Benzo-a-Pyrene (B[a]P) was assessed to represent toxic components of Polycyclic Aromatic Hydrocarbon (PAH) compounds potentially adsorbed onto iron-ore dust particles as it is of known carcinogenicity, and was found to have additive toxicity. The order of toxicity by oxidative stress is determined to be: CuO 5 µm > SiO<sub>2</sub> 10 µm > TiO<sub>2</sub> 0.1 µm > Yandi 10 µm > Newman 10 µm > MAC 10 µm > Fe<sub>3</sub>O<sub>4</sub> 5 µm, with the iron-rich PM<sub>10</sub> samples producing some 60% the response of silicon dioxide PM, an important occupational air quality pollutant with internationally recognised inhalation limits established by the World Health Organisation (WHO). It was found that iron in the iron-ore samples remained constrained to the solid phase by Inductively Coupled Plasma Mass Spectrometry (ICPMS), while silicon dioxide and copper oxide were partially soluble, potentially explaining their increased cytotoxic potential.

Lung cell lines tested were found to have differential inflammatory cytokine responses to particulates, suggesting a complex immunological involvement between particles and the lung parenchyma drives health outcomes. This endpoint showed a range of differential effects between the samples and standards dependent on sample composition and cell type. Cocultures were used to determine interactions between fibroblast cells and immune cells upon exposure to particles, and were found to alter cytotoxicity and interleukin expression profiles. In all experiments, strong cytokine responses highlighted the inflammatory potential of the

copper oxide, carbon black, silicon dioxide, titanium dioxide, Yandi, and MAC samples, although the nature of which cytokines were acutely or chronically induced and inhibited likely has a complex duration-dependent signature.

A 28-day single dose animal experiment was conducted on 8-week old C57BL/6J mice, via intratracheal dry powder insufflation. Increases in collagen deposition in the lungs were found, with the order of toxicity found to be Carbon Black 150 nm > SiO<sub>2</sub> 10 µm > CuO 5 µm > Newman 10 µm > MAC 10 µm > Yandi 10 µm > Fe<sub>3</sub>O<sub>4</sub> 5 µm. Due to the short duration of the experiment, the observed differences were less than 10% the control. The strongest two fibrosing particulates, carbon black and silicon dioxide, were also observed to have strong proliferative effects on monocyte differentiated macrophage and cocultures thereof combined with epithelial cells *in-vitro*, as well as strong cytokine induction.

In conclusion, comparative determinations of poorly-soluble particulate toxicity *in-vitro* can inform the risk of fibrotic potential *in-vivo*. However, interpreting these risks requires careful consideration of both the physical characteristics as well as immunological function, including the cytotoxic, proliferative, inflammatory and redox potential of the particles. This implies inhalation of PM<sub>10</sub> incurs a baseline toxicity related to inflammation and immune clearance, upon which shape, solubility and chemistry determine secondary toxic effects. Results from *in-vitro* studies can flag those particles which pose increased or differential risk at NEPM values. The iron-rich PM<sub>10</sub> samples tested are suspected pose systemic health risk at concentrations significantly exceeding NEPM values, albeit a general risk due to its insolubility which this study and the literature suggest is shared by other insoluble metal-oxide particulates of limited reactivity. The experiments in this study do not show consistently greater toxicological activity of the iron-ore PM<sub>10</sub> above silicon dioxide PM<sub>10</sub> of similar shape amongst the endpoints tested, however more broadly, some three-quarters of the toxicological activity was observed.

## Declaration by Author

This thesis is composed of my original work, and contains no material previously published or written by another person except where due reference has been made in the text. I have clearly stated the contribution by others to jointly-authored works that I have included in my thesis.

I have clearly stated the contribution of others to my thesis as a whole, including statistical assistance, survey design, data analysis, significant technical procedures, professional editorial advice, and any other original research work used or reported in my thesis. The content of my thesis is the result of work I have carried out since the commencement of my research higher degree candidature and does not include a substantial part of work that has been submitted to qualify for the award of any other degree or diploma in any university or other tertiary institution. I have clearly stated which parts of my thesis, if any, have been submitted to qualify for another award.

I acknowledge that an electronic copy of my thesis must be lodged with the University Library and, subject to the General Award Rules of The University of Queensland, immediately made available for research and study in accordance with the *Copyright Act 1968*.

I acknowledge that copyright of all material contained in my thesis resides with the copyright holder(s) of that material. Where appropriate I have obtained copyright permission from the copyright holder to reproduce material in this thesis.

## Publications during Candidature

Prakash S (2012) Iron Ore Dust: Using 3D Cell Cultures to Establish New Toxicity Measurement Methods. Remediation Australasia 6–7.

## Publications Included in Thesis

None

## Contributions by Others to the Thesis

Jack Ng and Cheng Peng for their technical support in experimental procedures and guidance on interpretation and statistical analysis. Jack Ng for editorial support in thesis writing and paper writing.

## Statement of Parts of the Thesis Submitted to Qualify for the Award of another Degree

None

## Acknowledgements

I sincerely appreciate and am grateful for the support of my principal supervisor, Professor Jack Ng, as well as Dr Cheng Peng who both without fail always supported my endeavours and ensured the science could be completed, and without which I would not have this once in a lifetime opportunity of contribution and personal growth. I have also enjoyed their personal companionship, wisdom and good spirits, making my time at Entox one I will always remember.

Special thanks to Professor Matti Lang, Dr Barry Chiswell, Dr Barry Noller, Dr Emmanuelle Fantino, Dr A'edah Abu Bakar and Professor Jochen Mueller for their general advice and for assessing milestones. I also thank Dr Wasantha Wickramasinghe for allowing operations to continue smoothly in the lab, Dr Peta Neale for her guidance with the flow cytometry work and Professor Alan Seawright for his expertise in histological interpretation of lung tissue. I enjoy and appreciate the company and positive outlook provided by my all my close friends at Entox, including Dr Faye Liu, Dr Dionne Arthur, and Jake O'Brien.

For experimental help outside of Entox, I thank Dr Mahmood Shahin formerly at Queensland Health Forensic and Scientific Services for sharing his expertise in animal handling during the animal exposure work. I thank Dr Darryl Whitehead of the School of Biomedical Science for his supervision during the histological staining, and Dr Nigel Waterhouse at the Queensland Institute of Biomedical Research for slide scanning work. For training and help with electron microscopy, I thank Richard Webb, Robyn Webb and Graeme Auchterlonie at the Centre for Microscopy and Microanalysis. I thank Dr Gysell Mortimer for her advice and initial experiments working with the cytometric bead assay kits at TetraQ. I thank Dr Matt Sweet for his advice on and supply of immunological cell lines. Last but not least, to Professor Lidia Morawska at QUT for her general advice on fine particle extraction methods.

I acknowledge all the remarkable staff, funding and support of The University of Queensland and the Cooperative Research Centre for Contamination Assessment and Remediation of the Environment (CRC-CARE), awarding me the PhD

scholarship and helping me in innumerable ways. I also acknowledge BHP Billiton and for their support in the program and supply of samples.

I am grateful to have made so many amazing lifelong friends from all around the world thanks to the international nature of Entox. I also could not have done without the endless supply of tea and companionship provided by Jessica Kerin, and the moral support, comradery and hilarity of the 'wolf pack'; Kurt Teubler, Ian Mulvena and David Hogan.

Finally, I am blessed to have the most caring and supportive family who have dedicated time and energy to give me the security and comfort to continue studying abroad, and have always selflessly made myself and my research their priority. Thank you dad, mum and Asha.



## Key Words

Iron ore, PM<sub>10</sub>, PM<sub>2.5</sub>, Toxicology, *In-vitro*, *In-vivo*, Fibrosis, Coculture, Inflammation, Cytotoxicity, A549 cells, U937 cells, LL24 cells, Fe<sub>3</sub>O<sub>4</sub>, Fe<sub>2</sub>O<sub>3</sub>, CuO, TiO<sub>2</sub>, SiO<sub>2</sub>, Carbon Black, nanoparticle, inhalation, dust

## Australian and New Zealand Standard Research Classifications

### (ANZSRC)

ANZSRC code: 110203, Respiratory Diseases, 20%

ANZSRC code: 100204, Environmental Biotechnology Diagnostics, 40%

ANZSRC code: 050204, Environmental Impact Assessment, 20%

## Fields of Research (FoR) Classification

FoR code: 1102, Cardiovascular Medicine and Haematology 40%

FoR code: 1002, Environmental Biotechnology 40%

FoR code: 0502, Environmental Science and Management 20%

## Table of Contents

Abstract .....	i
Declaration by Author .....	iv
Publications during Candidature .....	v
Publications Included in Thesis .....	v
Contributions by Others to the Thesis .....	v
Statement of Parts of the Thesis Submitted to Qualify for the Award of another Degree .....	v
Acknowledgements .....	vi
Key Words.....	viii
Australian and New Zealand Standard Research Classifications (ANZSRC).....	viii
Fields of Research (FoR) Classification .....	viii
List of Figures & Tables.....	xiii
List of Abbreviations used in the thesis .....	xviii
1. Introduction.....	1
1.1 Fugitive Iron-Rich Dust in Western Australia.....	1
1.2 Informing Air Quality Regulations through In Vitro Toxicology .....	3
1.3 Aims .....	4
1.2 Objectives .....	5
1.4 Thesis format .....	7
2. Review: Pathways for Comparative In-Vitro Inhalation Toxicology of Poorly Soluble Mineral Ore Particulate Emissions from Mining Industry .....	9
2.1 Abstract.....	9
2.2 Introduction .....	9
2.3 Generation of Mining Dusts.....	14
2.4 Inhalation of Particulate Matter.....	16
2.5 Pulmonary Pathologies of Mining Dust Inhalation .....	17
2.6 In-Vitro Models of Pulmonary PM Exposure .....	22

2.6.1	Respiratory Structures and PM Interactions.....	22
2.6.2	Lung-Air Interface Systems .....	25
2.6.3	2D Culture Systems .....	27
2.6.4	3D Culture Systems and Explants.....	28
2.6.5	Co-Culture Systems.....	30
2.7	Major In-Vitro Endpoints for Determining and Comparing PM Toxicity .....	31
2.7.1	Particle Characteristics and Toxicity .....	31
2.7.2	Cytotoxicity .....	37
2.7.3	Immune Mediated Clearance .....	42
2.7.4	Inflammatory Signalling and Fibrosis .....	44
2.7.5	Free Radical Generation.....	50
2.7.6	Genotoxicity and Carcinogenicity .....	53
2.7.7	Relationship of Pulmonary Models with Cardiovascular Models <i>In-Vitro</i> .....	55
2.8	Discussion.....	57
3.	Improving Toxicological Assessment of Poorly-Soluble Coarse Fraction	
	Particulates Relevant to Pulmonary Health <i>In-Vitro</i> .....	61
3.1	Introduction .....	61
3.2	Materials and Methods.....	64
3.2.1	Cyclone Separation .....	64
3.2.2	Ultrasonic Sieving.....	65
3.2.3	Fractional Sterilisation .....	66
3.2.4	Chemicals and Reagents .....	67
3.2.5	Cell Culture.....	68
3.2.6	Cytotoxic Endpoint Development.....	69
3.3	Monolayer Cytotoxicity Results .....	74
3.3.1	LL24 Monolayer Toxicity .....	75
3.3.2	A549 Monolayer Toxicity .....	77
3.3.3	Lung Surfactant and Size-Dependent Effects.....	80
3.4	3D Cytotoxicity Results .....	82
3.4.1	A549 Spheroid.....	82
3.5	Cell Contact Cytotoxicity Results .....	84
3.5.1	Insert Culture .....	84
3.6	Discussion.....	85

4. In-Vitro Comparative Toxicology of Inhalable Iron-Rich Particles from Mining Industry in Western Australia .....	88
4.1 Introduction .....	88
4.2 Materials and Methods.....	90
4.2.1 Chemicals and Reagents .....	90
4.2.2 Particle Extraction and Sterilisation.....	91
4.2.3 Particle Size Distribution Analysis .....	92
4.2.4 Particle Solubility Analysis.....	92
4.2.5 Electron Microscopy .....	92
4.2.6 Electron Density Spectroscopy .....	92
4.2.7 Cell Culture.....	93
4.2.8 Cell Proliferation Assay .....	94
4.2.9 Oxidative Stress Assay.....	95
4.2.10 Flow Cytometric Cytokine Quantification.....	95
4.3 Results .....	96
4.3.1 Sample Size Distribution .....	96
4.3.2 Sample and Standard Electron Microscopy .....	96
4.3.3 Sample and Standard Solubility .....	101
4.3.4 Elemental Analysis .....	104
4.3.5 Cell Proliferation .....	105
4.3.6 Oxidative Stress.....	111
4.3.7 Inflammatory Cytokine Induction .....	113
4.4 Discussion.....	116
5. Comparative Toxicology of Inhalable Particulate Matter to Human Lung Cell and Macrophage Cocultures .....	120
5.1 Introduction .....	120
5.2 Materials and Methods.....	121
5.2.1 Chemicals and Reagents .....	121
5.2.2 Particle Extraction and Sterilisation.....	121
5.2.3 Electron Microscopy .....	121
5.2.4 Cell Culture.....	122
5.2.5 Cell Proliferation Assay .....	123
5.2.6 Flow Cytometric Cytokine Quantification.....	123

5.3	Results .....	124
5.3.1	Cell Proliferation .....	124
5.3.2	Interleukin Data .....	131
5.3.3	Macrophage Uptake .....	134
5.4	Discussion.....	138
6.	Comparative Toxicity of Acute Inhalation of Respirable Iron-Rich Particles from Mining Industry In-Vivo.....	141
6.1	Introduction .....	141
6.2	Materials and Methods.....	142
6.2.1	Particulates and Reagents.....	142
6.2.2	Animal Selection and Handling .....	142
6.2.3	Animal Dosing .....	142
6.2.4	Animal Sacrifice.....	144
6.2.5	Histological Methods .....	144
6.3	Results .....	144
6.3.1	Lung Histology.....	144
6.4	Discussion.....	148
7.	General Discussion.....	151
8.	Future Work.....	154
9.	Bibliography.....	155
10.	Appendices.....	178
10.1	Appendix A: Raw Cytokine Data .....	178
10.1.1	Chapter 4 Experiment .....	178
10.1.2	Chapter 5 Experiment .....	180

## List of Figures & Tables

Table 1: <i>EU, US and Australian AAQG for PM<sub>10</sub> and PM<sub>2.5</sub></i> <sup>10,11</sup> .....	3
Table 2: <i>Common size classifications describing inhalable PM</i> .....	11
Table 3: WHO AQG 2005 and US EPA 2013 air quality for particulate matter: annual and 24 h mean concentrations. <i>Adapted from WHO Air Quality Guidelines - Global Update 2005 (2006)</i> <sup>55,65</sup> .....	12
Table 4: Natural minerals associated with human disease <sup>100</sup> .....	18
Table 5: Nomenclature of common pneumoconiosis by PM source .....	19
Table 6: Histopathology of metal-induced disease <sup>132</sup> .....	21
Table 7: An example of synthetic bronchioalveolar fluid for addition to media (Hank's balanced salt solution) <sup>143</sup> .....	23
Table 8: Characteristics of anthropogenic PM. Adapted from <i>The Impact of Fine Particles on Health</i> <sup>193</sup> .....	32
Table 9: The effects of cytokines in lung tissues, cytokine network type given where available .....	46
Table 10: Factors stimulating either classical or alternative macrophage activation <sup>251</sup> .....	49
Table 11: Satellite imagery of mining sites. Elevation emphasis x3. Supplied by Google Earth, Newman 2005, Yandi 2011, MAC 2011, Pilbara 2012. ....	63
Table 12: Conversion for other particulate concentration to CuO in $\mu\text{g}/\text{cm}^2$ .....	124
Table 13: Animal designation, dosage and weights.....	143
Figure 1: Infographic outlining the major method development steps planned, culture methods to investigate, and inventories of samples. Preliminary samples are deidentified iron ore samples supplied by BHP Billiton prior to characterised samples Mining Area C (MAC), Yandi mine (Yandi) and Newman Hub Mine (Newman) being supplied through ChemCentre (WA) in 2012. ....	7
Figure 2: Human respiratory tract and nominal particle deposition in an adult male at rest as a function of particle size, based on International Commission on Radiological Protection (ICRP) models <sup>56</sup> .....	17
Figure 3: <i>This figure shows the structure of the epithelial layer in the Airways (A) and Alveoli (B). Key: AEPT I: Alveolar epithelium type I; AEPT II: Alveolar epithelium type II; ALL: Aqueous lining layer; AM: Alveolar macrophage; BM: Basal membrane; C: Capillary; CT: Connective tissue; DC: Dendritic cell; EP: Epithelial cell; P: Particle; S: Surfactant; TJ: Tight junction. Adapted from <i>In vitro models of the human epithelial airway barrier to study the toxic potential of particulate matter</i><sup>40</sup>. ....</i>	22
Figure 4: <i>Ultrafine Carbon Black particles are shown in A: standard Phosphate Buffered Saline; B: Mouse bronchioalveolar lavage fluid; C: a sonicated combination of Phosphate Buffered Saline, DPPC and Bovine Serum Albumin</i> <sup>146</sup> .....	24
Figure 5: Top: A picture of the Cultex® system exposure hardware. Bottom: A diagram of cell culture methods enabled by the Cultex® system. Submersed mode replicates classic culture and enables a coculture to be set up, while lifted and dynamic exposure modes allow cell/air interface modelling <sup>161</sup> . ....	26

- Figure 6: A) Normal human bronchial histology. B) Type I collagen seeded with fibroblasts, contracting as it cools. C) Immortalized HBECs attached collagen gel surface. Right: Scanning electron microscope image showing differentiation of HBECs on collagen gel into goblet, ciliated and normal cells <sup>182</sup>. ..... 29
- Figure 7: Interaction between alveolar type II cells and macrophages during inflammation in response to particles <sup>186</sup> ..... 31
- Figure 8: Differences in particle length and rigidity affecting particulate clearance. (left) Successful and frustrated phagocytosis of long asbestos fibres; (right) Successful and frustrated phagocytosis of tangled and rigid carbon nanotubes. .... 35
- Figure 9: Pathways for toxic interactions of CuO and ZnO particles. (a) entry mechanisms into cells through diffusion and pinocytosis; (b) effect of ROS on intracellular particles and DNA breaks; (c) coordination of dissolved Cu<sup>2+</sup> and Zn<sup>2+</sup>; (d) non-homeostasis effect caused by Cu<sup>2+</sup> <sup>209</sup> ..... 36
- Figure 10: Copper release rate per unit surface area from artificial copper patina powder exposed to synthetic biological fluids and PBS. Insert shows results on logarithmic scale <sup>210</sup> ..... 37
- Figure 11: The toxicities of micrometre scale particles (approximately 1 µm) versus nanoscale particles (<0.1 µm) to A549 cells are shown. A: Cytotoxicity after an 18hr exposure at 40 µg/cm<sup>2</sup>; B: DNA damage after a 4 h exposure at 40 µg/cm<sup>2</sup>; C: Oxidative DNA damage after 4 h at 40 µg/cm<sup>2</sup>; D: Mitochondrial damage after a 16h exposure at 40 µg/cm<sup>2</sup>; E: Dose-response of mitochondrial depolarization to CuO after 4 h at 40 µg/cm<sup>2</sup>; F: Comet assays showing DNA damage from CuO with and without the Formamido-Pyrimidine DNA Glycosylase (FPG) DNA repair enzyme which forms DNA adducts in the presence of O<sub>2</sub> after 4 h at 40 µg/cm<sup>2</sup>. Adapted from Size-Dependent Toxicity of Metal Oxide Particles – A Comparison Between Nano- and Micrometer Size <sup>197</sup>. .... 39
- Figure 12: MTT assay interactions with activated carbon, TiO<sub>2</sub>, soot, oxidized soot and diesel particles after 3 h of incubation at 50 µg/mL. a) spectra of particle suspensions and MTT metabolic product (formazan) b) spectra after centrifugation for 10 minutes at 115 g. .... 41
- Figure 13: TEM images of A549 cells, x80000 zoom. A: Unexposed cells; B: TEM image demonstrating TiO<sub>2</sub> nano-particle uptake at 100 µg/mL. Nu denotes the nucleus, NP denotes the particle <sup>227</sup>. .... 44
- Figure 14: Targets of macrophage participation in the termination of acute inflammatory activity and coordination of repair processes in the pulmonary acinus. Recruitment of polymorphonuclear cells (PMN) such as neutrophils and monocytes such as macrophages is inhibited and cell proliferation and repair processes are activated <sup>183</sup>. .... 50
- Figure 15: Hierarchical oxidative stress model showing response tiers related to PM exposure. (Tier 1) Antioxidant enzyme activity restores cellular redox homeostasis. (Tier 2) Proinflammatory responses are induced. (Tier 3) Cellular apoptosis-necrosis is induced. GSH (Glutathione); GSSG (Oxidized Glutathione); NF-κB (Nuclear Factor κB); MAPK (Mitogen Activated Kinase); AP-1 (Activator protein 1) <sup>66</sup> ..... 51
- Figure 16: The proposed effect of transition metals and Polycyclic Aromatic Hydrocarbons (PAH) combustion products on cellular redox homeostasis and gene expression. Increased inflammation and cell

proliferation may affect chronic obstructive pulmonary disease (COPD), asthma, cardiovascular disease and cancer <sup>262</sup> . .....	53
Figure 17: Inflammatory networking in cancer. Cytokines dependent on NF- $\kappa$ B activation pathways are involved in numerous cancer pathways, including genes conferring chemoresistance and increased proliferation and metastatic ability <sup>161</sup> . .....	54
Figure 18: Proposed heirarchy for poorly-soluble coarse particulate matter toxicity .....	60
Figure 19: Outline of cyclone separation apparatus operation and collected sample.....	65
Figure 20: Sieve shaker and ultrasonic ring (left) with ultrasonic wave generator (right). .....	66
Figure 21 Light microscopy 200x magnification of A549 and LL24 cells exposed to CuO and Fe <sub>3</sub> O <sub>4</sub> over 48 h using micron-size standards.....	70
Figure 22: View of A549, LL24 and U937 cells in 6 well plates exposed to 390 $\mu\text{g}/\text{cm}^2$ Fe <sub>2</sub> O <sub>3</sub> . Top row: 96 h post exposure 1X; Bottom Row: Immediately after PBS wash 200x magnification. ....	71
Figure 23: A typical 96-well plate plan for the MTS assay .....	72
Figure 24: Terminal procedure for adapted MTS assay to avoid particulate interference with absorbance assays .....	73
Figure 25: LL24 24 h particle toxicity, using iron ore samples and reference compounds. From a 1:2 serial dilution over 12-1562 $\mu\text{g}/\text{cm}^2$ . .....	75
Figure 26: LL24 48 h particle toxicity, using iron ore samples and reference compounds. From a 1:2 serial dilution over 12-1562 $\mu\text{g}/\text{cm}^2$ . .....	76
Figure 27: LL24 96 h particle toxicity, using iron ore samples and reference compounds. From a 1:2 serial dilution over 12-1562 $\mu\text{g}/\text{cm}^2$ . .....	77
Figure 28: A549 24 h particle toxicity, using iron ore samples and reference compounds. From a 1:2 serial dilution over 12-1562 $\mu\text{g}/\text{cm}^2$ . .....	78
Figure 29: A549 48 h particle toxicity, using iron ore samples and reference compounds. From a 1:2 serial dilution over 12-1562 $\mu\text{g}/\text{cm}^2$ . .....	79
Figure 30: A549 96 h particle toxicity, using iron ore samples and reference compounds. From a 1:2 serial dilution over 12-1562 $\mu\text{g}/\text{cm}^2$ . .....	80
Figure 31: A549 (right) and LL24 (left) experiments examining differences in cytotoxicity when the lung surfactant protein and BSA were used together in combination with ultrasonication against regular media suspensions of particulate matter.....	81
Figure 32: Diagram of 3D spheroid structure within microtitre 96 well plate. ....	82
Figure 33: Images of spheroid cultures after 48 h post seeding: A: A549 cells tended to cluster in a tight spheroid on agar. B: LL24 cells tended to form more diffuse spheroids on agar. C: A549+LL24 cells tended to form very diffuse cell masses on agar. D: A549 cells cultured conventionally on the well surface shown for reference. Magnification 200x. ....	83
Figure 34: A549 3D spheroid, 96 h particle toxicity, Fe <sub>3</sub> O <sub>4</sub> and Iron Ore A at 390-49 $\mu\text{g}/\text{cm}^2$ . Concentration of CuO at 195-24.5 $\mu\text{g}/\text{cm}^2$ , shown in brackets. ....	84
Figure 35: LL24 and A549 Transwell™ insert, 6 well plate culture assay. CuO micron size particles assayed. .	85



Figure 36: Depiction of strategy to avoid optical interference of particles by using top down cytotoxic measurement of a 96-well plate and settled particulate matter.....	95
Figure 37: Distribution of particles ultrasonically sieved with a 10 µm electroformed mesh obtained on a Malvern Mastersizer 2000. ....	96
Figure 38: TEM images of A549 cells after 96 h exposures to the Fe <sub>3</sub> O <sub>4</sub> < 50 nm . Top Left, potential uptake of particles into the cytoplasm. Microvilli and particles are also visible outside the cell. Scale bar 1 µm. Top Right, horizontal membrane structure entrapping clusters of iron ore. Scale bar 2 µm. Bottom: extensive apical surface membrane development and possible internalisation of particulate agglomerates.....	98
Figure 39: TEM image of LL24 cells after 96 h exposures to Fe <sub>3</sub> O <sub>4</sub> < 5 nm samples. Top Left, apical membrane extension interacting with particle agglomerations. Top Right, complex membrane bound inclusions of particles. Scale bars 1 µm. Bottom staining reduces visibility of particle interactions however highlights the rough and complex surface of the LL24 cell membrane surface. Scale bar 3 µm . ....	99
Figure 40: TEM image of A549 cells after 96 h exposures to Yandi (Top Left) and Newman (Top Right) and MAC (Bottom Left) PM <sub>10</sub> and TiO <sub>2</sub> < 50 nm (Bottom Right), showing complex apical membrane interactions including internalisation of particulate agglomerates. Scale bar 1000, 2000 nm. ....	100
Figure 41: ICP-MS detection of free <sup>48</sup> Ti, <sup>56</sup> Fe, <sup>57</sup> Fe <sup>63</sup> Cu and <sup>65</sup> Cu ions using MAC, Yandi, Newman Iron ores, Fe(II,III)O < 5 µm and TiO <sub>2</sub> < 50 nm at 180 µg/mL, CuO < 5 µm at 45 µg/mL. Incubated with A549 cells 37 °C 96 h. ....	101
Figure 42: ICP-MS detection of free Ti, Fe and Cu ions using MAC, Yandi, Newman Iron ores, Fe(II,III)O < 5 µm and TiO <sub>2</sub> < 50 nm at 180 µg/mL, CuO < 5 µm at 45 µg/mL. Incubated with LL24 cells 37 °C 96 h. ....	102
Figure 43: ICP-MS detection of free Ti, Fe and Cu ions using MAC, Yandi, Newman Iron ores, Fe(II,III)O < 5 µm and TiO <sub>2</sub> < 50 nm at 180 µg/mL, CuO < 5 µm at 45 µg/mL. Incubated with U937 cells 37 °C 96 h. ....	103
Figure 44: TEM images of iron-ore samples. Scale Bar: Top Row: 2000 nm; Middle Row 200 nm, Bottom Row: EDS Sample points. ....	104
Figure 45: EDS of MAC, Yandi and Newman ore samples. Differences in spectra height are not necessarily related to stoichiometry, and reflect penetration through the bulk sample. ....	105
Figure 46: LL24 48 h particle toxicity. CuO 39 µg/cm <sup>2</sup> , 156 µg/cm <sup>2</sup> other particulates. ....	107
Figure 47: LL24 48 h + 50 µM B[a]P particle toxicity. CuO 39 µg/cm <sup>2</sup> , 156 µg/cm <sup>2</sup> other particulates.....	108
Figure 48: A549 48 h particle toxicity. CuO 39 µg/cm <sup>2</sup> , 156 µg/cm <sup>2</sup> other particulates.....	108
Figure 49: A549 48 h + 50 µM B[a]P + 5% S9 mix particle toxicity. CuO 39 µg/cm <sup>2</sup> , 156 µg/cm <sup>2</sup> other particulates.....	109
Figure 50: U937 48 h particle toxicity. CuO 39 µg/cm <sup>2</sup> , 156 µg/cm <sup>2</sup> other particulates.....	110
Figure 51: U937 48 h + 50 µM B[a]P particle toxicity. CuO 39 µg/cm <sup>2</sup> , 156 µg/cm <sup>2</sup> other particulates.....	111
Figure 52: AREc32 48 h particle toxicity. CuO 39/10 µg/cm <sup>2</sup> , 156/39 µg/cm <sup>2</sup> other particulates, TBHQ 25 µM/6.25 µM .....	112
Figure 53: ARE element activation as measured by a luciferase reporter in AREc32 cells 48 h exposure, positive control TBHQ 6.25 µM, CuO 10 µg/cm <sup>2</sup> , others 39 µg/cm <sup>2</sup> .....	113

Figure 54: LL24 inflammatory cytokine expression. CuO, at 5 $\mu\text{g}/\text{cm}^2$ , others 156 $\mu\text{g}/\text{cm}^2$ .....	114
Figure 55: A549 inflammatory cytokine expression. CuO, at 5 $\mu\text{g}/\text{cm}^2$ , others 156 $\mu\text{g}/\text{cm}^2$ .....	115
Figure 56: U937 inflammatory cytokine expression. CuO, at 5 $\mu\text{g}/\text{cm}^2$ , others 156 $\mu\text{g}/\text{cm}^2$ .....	116
Figure 57: A549 cumulative toxicity of particles across 5-156 $\mu\text{g}/\text{cm}^2$ dose range, and 1-39 $\mu\text{g}/\text{cm}^2$ dose range for CuO, over 48 h.....	125
Figure 58: LL24 cumulative toxicity of particles across 5-156 $\mu\text{g}/\text{cm}^2$ dose range, and 1-39 $\mu\text{g}/\text{cm}^2$ dose range for CuO, over 48 h.....	126
Figure 59: U937 cumulative toxicity of particles across 5-156 $\mu\text{g}/\text{cm}^2$ dose range, and 1-39 $\mu\text{g}/\text{cm}^2$ dose range for CuO, over 48 h.....	127
Figure 60: U937+A549 coculture cumulative toxicity of particles across 5-156 $\mu\text{g}/\text{cm}^2$ dose range, and 1-39 $\mu\text{g}/\text{cm}^2$ dose range for CuO, over 48 h. ....	128
Figure 61: A549+LL24 coculture cumulative toxicity of particles across 5-156 $\mu\text{g}/\text{cm}^2$ dose range, and 1-39 $\mu\text{g}/\text{cm}^2$ dose range for CuO, over 48 h. ....	129
Figure 62: U937+LL24 coculture cumulative toxicity of particles across 5-156 $\mu\text{g}/\text{cm}^2$ dose range, and 1-39 $\mu\text{g}/\text{cm}^2$ dose range for CuO, over 48 h. ....	130
Figure 63: Right: LL24+U937 coculture (denoted CC) toxicity of particles. Left: Geometric mean of monoculture LL24 and U937 toxicity values. Exposure shown 39 $\mu\text{g}/\text{cm}^2$ for CuO and 156 $\mu\text{g}/\text{cm}^2$ for other particles, over 48 h.....	131
Figure 64: LL24 inflammatory cytokine expression. CuO, at 1 $\mu\text{g}/\text{cm}^2$ , others 39 $\mu\text{g}/\text{cm}^2$ .....	132
Figure 65: U937 inflammatory cytokine expression. CuO, at 1 $\mu\text{g}/\text{cm}^2$ , others 39 $\mu\text{g}/\text{cm}^2$ .....	133
Figure 66: U937+LL24 inflammatory cytokine expression. CuO, at 1 $\mu\text{g}/\text{cm}^2$ , others 39 $\mu\text{g}/\text{cm}^2$ .....	134
Figure 67: Cell lines exposed to 156 $\mu\text{g}/\text{cm}^2$ of $\text{Fe}_3\text{O}_4$ oxide over 96 h, 200x magnification .....	134
Figure 68: TEM of macrophage standard uptake in 12 plates after 96 h culture at 40 $\mu\text{g}/\text{cm}^2$ . Scale bar 5 $\mu\text{m}$ . .....	136
Figure 69: TEM of macrophage standard uptake in 12 plates after 96 h culture at 40 $\mu\text{g}/\text{cm}^2$ . Top: Scale bar 10 $\mu\text{m}$ . Bottom: Scale bar 5 $\mu\text{m}$ .....	137
Figure 70: 28 day exposure, control, Vehicle Control, $\text{Fe}_3\text{O}_4$ , CuO. C57/BL6 lung histology, Masson's Trichrome 200x.....	145
Figure 71: 28 day exposure, MAC, Newman, Yandi, $\text{SiO}_2$ . C57/BL6 lung histology, Masson's Trichrome 200x. ....	146
Figure 72: 28 day exposure, Carbon Black, Bleomycin. C57/BL6 lung histology, Masson's Trichrome 200x. .	146
Figure 73: Analysis of Masson's Trichrome stained mouse lung histological sections. Positive to negative pixel count ratios for blue/green staining indicative of collagen deposition shown.....	147
Figure 74: Linking of key steps and endpoints in the high-throughput assay of poorly-soluble $\text{PM}_{10}$ and $\text{PM}_{2.5}$ .....	153

## List of Abbreviations used in the thesis

<b>M<math>\phi</math></b> : Macrophage	<b>IL-8</b> : Interleukin 8
<b>2D</b> : Two Dimensional (traditional cell culture)	<b>KEAP1</b> : Kelch-like ECH-associated protein 1
<b>3D</b> : Three Dimensional (multilayer cell culture)	<b>mtpa</b> : Million Tonnes per Annum
<b>APAF</b> : Apoptotic Protease Activating Factor	<b>MTS</b> : 3-(4,5-dimethylthiazol-2-yl)-5-(3-carboxymethoxyphenyl)-2-(4-sulfophenyl)-2H-tetrazolium
<b>ARE</b> : Antioxidant Response Element	<b>MTT</b> : (3-(4,5-Dimethylthiazol-2-yl)-2,5-diphenyltetrazolium bromide
<b>B[A]P</b> : Benzo[a]Pyrene	<b>Nrf2</b> : NF-E2-related factor
<b>BD</b> : Becton Dickenson	<b>PBS</b> : Phosphate Buffered Saline
<b>BSA</b> : Bovine Serum Albumin	<b>PM10</b> : Particulate Matter $\leq$ 10 micrometres in diameter
<b>CBA</b> : Cytometric Bead Array	<b>PM2.5</b> : Particulate Matter $\leq$ 2.5 micrometres in diameter
<b>CCWA</b> : Chemistry Centre of Western Australia	<b>PMA</b> : Phorbol Myristate Acetate
<b>DMSO</b> : Dimethyl Sulfoxide	<b>ROS</b> : Reactive Oxygen Species
<b>DPCC</b> : Dipalmitoylphosphatidylcholine	<b>SP-A</b> : Surfactant Protein A
<b>EDS</b> : Energy-dispersive X-ray spectroscopy	<b>TBARS</b> : Thiobarbituric Acid Reactive Substances
<b>FADD</b> : Fas Activated Death Domain	<b>TBHQ</b> : tert-Butylhydroquinone
<b>FasL</b> : Fas Ligand	<b>TEM</b> : Transmission Electron Microscopy
<b>FBS/FCS</b> : Foetal Bovine/Calf Serum	<b>TGF-<math>\beta</math>1</b> : Transforming growth factor beta 1
<b>H<sub>2</sub>DCF-DA</b> : 2',7'-dichlorofluorescein-diacetate	<b>TNF</b> : Tumour Necrosis Factor
<b>HICK</b> : Human Inflammatory Cytokines Kit	<b>TNFR</b> : Tumour Necrosis Factor Receptor
<b>IAP</b> : Inhibitor of Apoptosis	<b>TRADD</b> : Tumour Necrosis Factor Activated Death Domain
<b>IC20</b> : Inhibition Concentration 20, cell viability 20% below control	<b>TSP</b> : Total Suspended Particulate matter, particles of all size in atmospheric sample
<b>IC50</b> : Inhibition Concentration 50, cell viability 50% below control	<b>UFP</b> : Ultrafine Particulate Matter, $\leq$ 0.1 micrometres in diameter
<b>ICP-MS</b> : Inductively coupled plasma mass spectrometry	<b>WA</b> : Western Australia
<b>IL -1<math>\beta</math></b> : Interleukin 1 Beta	<b>XRF</b> : X-Ray Fluorescence
<b>IL-10</b> : Interleukin 10	
<b>IL-12p70</b> : Interleukin 12p70	
<b>IL-6</b> : Interleukin 6	

## 1. Introduction

### 1.1 Fugitive Iron-Rich Dust in Western Australia

Iron ore production and trade in Australia has more than doubled over the past decade making it the world's largest iron ore exporter, fuelled by strong growth in Asian markets. China is the world's largest iron ore consumer and Australia's key import partner, with demand being driven by China's accelerating urbanisation and the development of heavy industries. Australia produced 488 million tonnes (Mt) of iron ore in 2011, a quarter of world production, and this was largely mined and exported from Western Australia. The high grade haematite and haematite goethite ore in WA is sought after amongst steelmakers, and is exported with minimal processing as fines consisting of about 60% iron, netting the state over \$60 billion annually. The WA treasury estimates that by 2015 the state will produce 659 Mt per annum, and forecasts sustained growth for decades to come <sup>1,2</sup>.

Approximately 48 billion tonnes of iron ore resources lie in the Hamersley Basin, in the Pilbara Region of north-western WA. The Pilbara is an arid interior expanse of over 500,000 square kilometres, known for its red earth and rich mineral reserves. Hamersley accounts for an impressive 74% of Australian iron resources, and is a site of many existing high capacity mines as well as projected expansions. The largest of these take the shape of surface or open-pit mines. The overburden (unwanted top layer crustal material) is removed and the ore extracted in a heavily mechanised and large scale process. After crushing, the ore is transported via rail to port cities some 350 km to the west and loaded onto bulk carriers mainly destined for China, but also Japan, Korea and Taiwan <sup>3</sup>.

The intense growth and high volume mining of iron ore has created burgeoning townships associated with mining, shipping and support operations. The town of Port Hedland is one such town and one of the largest settlements in the Pilbara, home to more than 15,000 residents and competing with Port Dampier (over 1,300 residents) as the region's largest port by tonnage. BHP Billiton currently has 199 Mt per annum of iron ore shipping capacity, and has approval to build an outer harbour raising capacity to 240 Mt per annum by 2017. The relatively large population of Port Hedland and high iron ore throughput has brought public and stakeholder attention

towards potential short term and long term health risks associated with the inhalation of elevated levels of fugitive iron-rich particulate matter (PM), which are highest in concentration near port facilities in West End. Here, iron-oxides account for up to 93% of total suspended particulates (TSP) by volume <sup>4-6</sup>.

Arid low rainfall conditions and high tropical winds exacerbate the dust problem, increasing the cost and reducing the effectiveness of dust control methods such as wetting. Port Hedland receives only about 12.3 inches of rainfall per year, with virtually none in the December-June period. Seaspray, inland soil erosion resulting from mine operations and natural crustal dust combine with industrial activity at Port Hedland to create some of the highest ambient particulate levels in Australia <sup>7</sup>. Naturally high levels of PM and problems controlling particulate emissions near loading operations at the port facilities have put pressure on the Department of Environment and Conservation, WA to allow greater leeway for exceeding national guideline values for ambient PM <sup>6</sup>.

The current Australian National Environmental Protection Measures (NEPM) ambient air quality standard was put into effect in 1998 and specifically prescribes limits for < 10  $\mu\text{m}$  (PM<sub>10</sub>) and < 2.5  $\mu\text{m}$  (PM<sub>2.5</sub>) diameter particle fractions (added in 2003). The PM<sub>10</sub> fraction corresponds to particles small enough to invade thoracic small airways of the lung, and the PM<sub>2.5</sub> fraction corresponds to particles small enough to be respirable, contacting the alveoli <sup>8,9</sup>. Setting limits for ambient PM by size is common practice and supported by the World Health Organization (WHO), the US EPA and European regulators, as well as others around the world.

Based on a consensus of epidemiological data, the WHO has determined progressively improving targets for limiting airborne PM mass for both PM<sub>10</sub> and PM<sub>2.5</sub> should be implemented globally. The staggered timeline for reducing ambient levels of these particulates reflects the difficulties developed and developing countries face implementing PM reduction measures. The EU, Australian and US Ambient Air Quality Guidelines (AAQG) are listed in Table 1, some of which are still under development.

Table 1: EU, US and Australian AAQG for PM10 and PM2.5 <sup>10,11</sup>

International Limits on Thoracic and Respirable PM						
	PM10			PM2.5		
Government	Daily Mean Target ( $\mu\text{g}/\text{m}^3$ )	Allowable Excesses (Days/Year)	Yearly Mean Target ( $\mu\text{g}/\text{m}^3$ )	Daily Mean Target ( $\mu\text{g}/\text{m}^3$ )	Allowable Excesses (Days/Year)	Yearly Mean Target ( $\mu\text{g}/\text{m}^3$ )
European Union	50	35	40	-	-	25
United States of America	150	1	-	35	1	15
Australia	50	5	-	25	5	8

Problems controlling PM<sub>10</sub> emissions near loading operations at the port facilities have put pressure on the Department of Environment and Conservation, WA to raise daily mean exposure limits by up to 40% to 70  $\mu\text{g}/\text{m}^3$  with greater leeway for exceeding that value <sup>4</sup>. However, this has raised concerns that NEPM limits may inadequately address the specific toxicological profile of iron-rich PM<sub>10</sub> specific to the geology of WA and other industrial pollutants possibly adsorbed by them, such as Volatile Organic Compounds (VOCs), Polycyclic Aromatic Hydrocarbons (PAHs) and combustion products like Benzene, Toluene, Ethylbenzene – collectively known as BTEX.

## 1.2 Informing Air Quality Regulations through In Vitro Toxicology

Several multi-city epidemiological studies, some including Australian cities <sup>12</sup>, have established clear causal links between respirable particulate matter concentration and subsequent acute and long-term morbidity and mortality. These serve as the basis for the WHO ambient Air Quality Guideline (AQG) which underpins the current framework developed by leading regulatory bodies. The AQG is targeted at the minimum concentration at which health effects are observable to a 95% confidence interval, and is to be reached through a series of phased transitions known as Interim Targets 1-3 followed by the AQG itself.

The guidelines primarily stratify particulate matter by size fractions. Although particles up to 100  $\mu\text{m}$  in diameter are inhalable, most of this fraction is filtered or

cleared rapidly into the gut. TSP limits have not featured in the AQG since 1987, and PM<sub>10</sub> and PM<sub>2.5</sub> penetrating the deeper lung have been more clearly associated with morbidity and mortality than larger fractions. These particles are also more likely to be carried by winds over large distances.

The ambient air quality NEPM makes few distinctions in addition to PM<sub>10</sub> and PM<sub>2.5</sub>, be they aerosols or liquids, nor the respective composition of particulates bar a select few pollutants specified; ozone, sulphur dioxide, nitrogen dioxide, carbon monoxide and lead. The focus has instead been acceptable mean daily and annual concentrations, with chronic exposure recognized as more hazardous than acute exposure. This format works well for urban air pollution from which the epidemiological supporting data is based, although extending the NEPM to environments where the ambient PM profile is very different in composition is not a scientifically validated process.

Given there may be no threshold of effect for PM<sub>10</sub> and PM<sub>2.5</sub> pollutants, specific investigation of particulate matter dominating the airspace of rural and outback communities with ambient PM profiles vastly different to ambient urban PM is logical. In the case of Port Hedland, understanding the risks posed by iron-rich PM<sub>10</sub> clearly carries some urgency as the health effects of ambient iron rich PM<sub>10</sub> under these conditions is not well understood in a chronic exposure civilian setting. Yet stakeholder interests are also mindful of unnecessarily strict regulation and unacceptable economic impacts, therefore limits must be as rational as possible. While the question remains as to the level of absolute protection the public can expect from regulatory measures, without firm data commercial interests and civilian interests may end up at odds with one another.

### 1.3 Aims

The premise of this project is that there is a lack of specific information on the toxicity of iron-rich PM<sub>10</sub> from Port Hedland for accurate Australian air quality policy making, as iron-rich PM<sub>10</sub> is a major component of all PM<sub>10</sub> found in the Port Hedland area, and current regulations are based on meta-studies of urban PM<sub>10</sub> toxicity where the iron-rich component may be insignificant. This is important as substantial

discrepancies in toxicity can arise from the unique chemical compositions and adsorbed species specific to Port Hedland iron-ore. The information gathered from *in-vitro* experiments may therefore warrant the consideration and development of air quality regulations for atmospheric iron-rich PM<sub>10</sub> separate from existing regulations in settlements at risk of high iron-rich PM<sub>10</sub> exposure.

The project aim is therefore:

- To develop the means to comparatively assess the toxicology of iron ore dusts affecting Port Hedland *in-vitro* more effectively than previously possible, so that the risks inhalation of iron ore PM<sub>10</sub> may hold to human health are understood in respect to the effectiveness of current NEPM exposure guidelines.

Because the work involves environmental samples, it is important to not only characterise toxicity but characterise physical properties to know what is being examined. To this end, the project operates in partnership with the Chemistry Centre of Western Australia to physically characterise the particulate matter. Furthermore, the University of Sydney has been involved to conduct a desktop literature review to properly define what is known, unknown and what is relevant in terms of Australian policy making on particulate matter and iron-rich dusts in general.

## 1.2 Objectives

The project objectives are designed to provide a series of deliverables building an understanding of iron-rich PM<sub>10</sub> toxicity under *in-vitro* models of increasing complexity. The comparative component of testing against other metal oxides and materials creates many combinations of results that aid in understanding both the toxicological profiles of the materials and how methodological developments affect these outcomes.

- To determine a sample test set including iron ore samples from mines delivering to Port Hedland and particle standards comparable to the literature and occupational exposure regulations



- To establish an effective high-throughput means of extracting and sterilising the PM<sub>10</sub> component from crushed iron ore fines while minimising changes in aerodynamic-size representation and surface chemistry
- To characterise extracted samples by size, morphology and elemental analysis
- To determine a set of relevant human cell lines to use for use *in-vitro* representing target tissues in lung disease
- To establish appropriate exposure intervals and dosing metrics to build comparative cytotoxic dose-response relationships between samples and standards *in-vitro*
- To establish an oxidative stress profile for samples and standards
- To establish the effect of additional adsorbed organic combustion products
- To assess improvements to *in-vitro* testing by using lung fluid components
- To assess improvements to *in-vitro* testing by using 3D culture techniques
- To assess improvements to *in-vitro* testing by using cocultures
- To assess inflammatory cytokine profiles expressed by monolayer and coculture techniques for samples and standards
- To examine the cellular uptake of particles by lung cells and immune cells
- To conduct an *in-vivo* study on fibrotic changes associated with samples and standards to assess the relationship between biochemical endpoints *in-vitro* and histological changes *in-vivo*

This project entails several iterative stages of method development, and testing, as well as a variety of samples cell lines to be tested as appropriate, outlined in Figure 1. Samples are chosen for their prevalence and importance in lung toxicology literature, while the cell lines are chosen to represent aspects of lung physiology or provide valuable information. A549 cells represent aspects of both Type I and Type II lung epithelial cells, while LL24 fibroblasts are active in the lung basement membrane. Together, they are used to model parts of the gas exchange parenchyma of the lungs. U937 monocytes can be differentiated to macrophages and are useful in modelling immune interactions which are important to the development of respirable particle mediated disease. AREc32 cells are not directly related to lung physiology but are used to model oxidative stress which is an

important aspect of how insoluble transition metals mediate their toxicity *in-vivo*. All cell lines are of human origin. Combinations of extraction methods, characterisation methods, cell culture methods, and samples and cell types will be explored to find the most meaningful data. Polycyclic Aromatic Hydrocarbons (PAH) will be investigated for their effect on toxicity if adsorbed onto iron-rich particles from combustion sources. Animal studies will be conducted to help determine the relationship between *in-vivo* and *in-vitro* data.

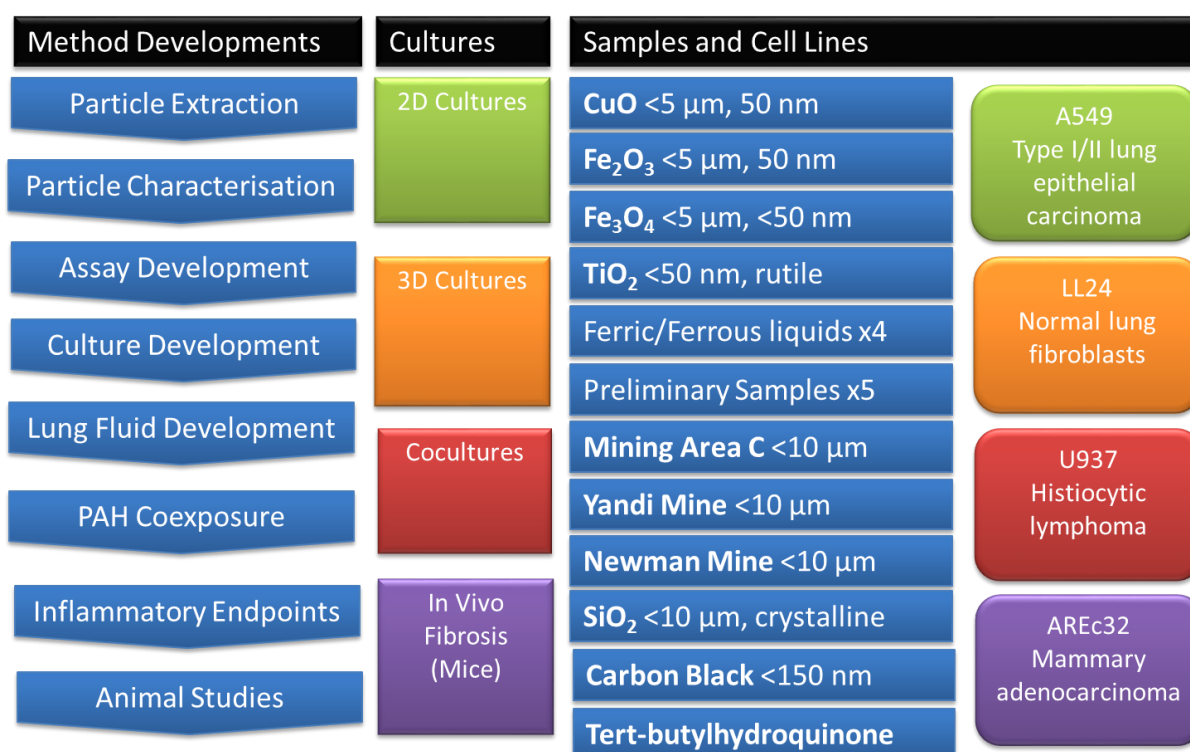


Figure 1: Infographic outlining the major method development steps planned, culture methods to investigate, and inventories of samples. Preliminary samples are deidentified iron ore samples supplied by BHP Billiton prior to characterised samples Mining Area C (MAC), Yandi mine (Yandi) and Newman Hub Mine (Newman) being supplied through ChemCentre (WA) in 2012.

#### 1.4 Thesis format

This thesis is comprised of both thesis chapters and manuscripts to be submitted for review. Chapter 1 introduces the reader to the state of the iron-ore mining industry in Australia, and the iron-ore dust problems that have befallen the industry-associated town of Port Hedland in the shadow of its economic success. Chapter 2 is written as a systematic literature review manuscript discussing the current state of knowledge in the relevant literature and inherent strengths and weaknesses in *in-vitro* inhalable

particulate research. This chapter is purposefully extensive, to bring together aspects of human physiology, the methods available for in-vitro respirable particulate toxicology, as well as regulatory aspects of dealing with particulate pollution, in order to build solid foundations for interpreting project's necessity and direction. Chapters 3 through to 6 are composed of results manuscripts which describe significant methodology developments and the toxicology of the iron-ore samples representative of those affecting Port Hedland, including an *in-vivo* experiment. Chapters 7 and 8 bookend the thesis, discussing the meaning and the importance of the results circumspect of the thesis aims and objectives, as well providing directions for progress given the accomplishments within the framework of the project's original conception. The complex underpinnings of this project benefit from this format, with a mix of technical stages and key iron-ore results having a tightly focused and clear perspective, though some repetition consequently occurs.

## 2. Review: Pathways for Comparative In-Vitro Inhalation Toxicology of Poorly Soluble Mineral Ore Particulate Emissions from Mining Industry

### 2.1 Abstract

The translation of *in-vitro* toxicological data to ambient air quality standards has met little success despite decades of research. In its place, epidemiological data has shaped such standards. However, the need for high-throughput toxicological monitoring of mine-site dusts has not abated, rather increased, due to increasing economies of scale applied to open-pit mines, generating enormous quantities of poorly-soluble inorganic particulate matter, rich in metal-oxides, with relatively unknown toxicological effects from a population health perspective. Successful integration of toxicological data engenders the search for the key drivers of particulate matter toxicity; a task fit for Bellerophon, the hero of Greek mythology whom defeated the Chimera. Particulate matter toxicity is found to depend on size, shape, composition, crystallinity and solubility. The cellular targets of such particles include cytotoxic, metabolic, inflammatory, oxidative, genotoxic and coagulative endpoints. We explore relevant information for each of these factors, and propose that a hierarchical comparative toxicity model may help to determine the differential effects of particulate matter under standardised experimental and dosage conditions.

### 2.2 Introduction

By the early 20<sup>th</sup> century, the toxicology of airborne particulate matter (PM) inhalation had branched into two broad categories; PM associated with pulmonary fibrosis induced morbidity and mortality, and nuisance PM with little evidence for health effects<sup>13</sup>. Varieties of miner's pneumoconiosis, including silicosis, coal worker's pneumoconiosis (CWP) and asbestosis, were recognised as most hazardous and fibrosing for their distinguishable pathologies commonly affecting miners<sup>13-16</sup>. The view that nuisance PM could be ignored as a cause of morbidity and mortality began to change with highly increased occupational exposures to mining dusts such as iron ore, associated with the introduction of the pneumatic drill when used in inadequately ventilated environments, allowing fibrosis to develop<sup>17,18</sup>. More recently, chronic

exposure to low concentrations of ambient PM has been found to affect health outcomes without apparent threshold, suggesting multiple properties independent of composition determine toxicity, requiring the health impact of all significant emission sources to be evaluated <sup>16,19</sup>. Open-pit mining operations are some of the largest industrial contributors to ambient PM concentrations, necessitating closer scrutiny from a toxicological standpoint <sup>20</sup>.

Mechanistic *in-vivo* and *in-vitro* studies of the late 1980s and early 1990s investigating pulmonary pathology resulting from PM inhalation focused on biopersistence as a fundamental aspect of particulate toxicology, finding enhanced inflammation and fibrosis <sup>13,21</sup>. In the resulting models, the clearance rate of PM from the lung parenchyma by pulmonary alveolar macrophages (PAMs) was a central feature in the development of fibrotic pathology <sup>22</sup>. Both PM toxicity and concentration were independently found to exacerbate PAM death, reducing clearance rate and therefore increasing PM retention in the interstitial spaces of the lung. Persistent pro-inflammatory and pro-fibrotic immunological signalling was theorised to then initiate the fibrosing aspects of lung tissue damage and remodelling <sup>13,23–32</sup>. Under this paradigm, experiments were designed to show how otherwise inert PM could exhaust the PAM pool increasing insoluble alveolar PM load and half-life in acute exposures <sup>30,33,34</sup>, demonstrating the importance of volumetric load, in addition particle number alone. Toxicity mediated by particle shape was also investigated. High aspect ratio particles including asbestos and glass fibres were found to cause chronic inflammation and reactive oxygen species (ROS) production, resulting from lysosome dysfunction triggered failure of the phagocytic process, termed frustrated phagocytosis <sup>30,35–39</sup>.

From the 1990s to the present, dose-response relationships derived from epidemiological meta-studies have helped define environmental air quality standards around the world <sup>40</sup>. Findings in major multi-city prospective cohort studies such as the Harvard Six Cities Study <sup>41</sup>, American Cancer Society (ACS) Study <sup>42</sup> and many more recent studies <sup>12,43–54</sup> associate relatively small fluctuations in annual and daily mean PM concentrations to excess morbidity and mortality in the general population. These associations can often be attributed to fluctuations in PM fractions less than  $\leq 10 \mu\text{m}$  ( $\text{PM}_{10}$ ) in nominal diameter, which are able to enter the thoracic portion of the

respiratory tract without being completely filtered, and more strongly with fractions  $\leq 2.5 \mu\text{m}$  ( $\text{PM}_{2.5}$ ) in nominal diameter which can reach the respiratory parenchyma<sup>55</sup>. There can be some variation in the impaction and diffusion of these size fractions throughout the lungs, arising from irregular particle shape, chemical composition, state and environmental characteristics<sup>9,23,26,56</sup>, although the dominance of these factors is toxicologically relevant is unclear<sup>57</sup>. These factors also influence debate over the relative importance of the  $\text{PM}_{10}$ - $\text{PM}_{2.5}$  fraction, with some studies showing negligible  $\text{PM}_{10}$  contribution<sup>49,50</sup> and others similar or greater  $\text{PM}_{10}$  contribution than  $\text{PM}_{2.5}$ <sup>51,53,58,59</sup> to respiratory and cardiovascular morbidity and mortality. Studies from arid climates suggest that coarse dusts can cause acute respiratory distress and long term fibrotic outcomes<sup>60,61</sup>, while urban studies tend to suggest chronic lung diseases are more strongly associated with  $\text{PM}_{2.5}$ <sup>62</sup>. Common classifications and depositions of PM are detailed in Table 2.

**Table 2: Common size classifications describing inhalable PM**

PM Fraction	PM size range ( $\mu\text{m}$ )	Fraction Equivalent
TSP	N/A	Total Suspended Particulate
$\text{PM}_{100}$	$\leq 100$	Inhalable
$\text{PM}_{10-2.5}$	2.5 – 10	Coarse
$\text{PM}_{10}$	$\leq 10$	Thoracic
$\text{PM}_{2.5}$	$\leq 2.5$	Respirable
$\text{PM}_{1.8}$	$\leq 1.8$	Fine
UFP	$\leq 0.1$	Ultrafine

The World Health Organization (WHO) has determined Air Quality Guideline (AQG) and interim targets listed in Table 3<sup>55</sup>, and with US Environmental Protection Agency (EPA) National Ambient Air Quality Standards (NAAQS) provide common benchmarks underlying many national Ambient Air Quality Standards (AAQS)<sup>63</sup>. The 2005 WHO AQG update reflects recent analyses predicting annual concentrations of  $\text{PM}_{2.5}$  above 11-15  $\mu\text{g}/\text{m}^3$  lead to significant increases in all-cause public morbidity and mortality<sup>11,55,64,65</sup>. Increased respiratory and cardiovascular hospitalization events can be expected, most strongly associated with heart disease in adults, asthma in children, and exacerbation of any pre-existing cardiovascular or

respiratory problems <sup>15,58,62,66–76</sup>. Daily increases of PM<sub>10</sub> over 150 µg/m<sup>3</sup> can lead to declines in lung function of up to 7% <sup>67</sup>. Newborn birth weight and mortality may also be affected <sup>59,77–79</sup>. Despite the described risks, global national AAQS average 95 µg/m<sup>3</sup> per 24 h and many do not feature PM<sub>2.5</sub> <sup>63</sup>. This may be a result of practical difficulties in compliance with low values, and occasionally failure to update AAQS or accept cost-effectiveness as a public health measure <sup>15,80–82</sup>. While compliance can be costly, in some implementations potential savings in healthcare costs may dramatically outweigh these costs <sup>65</sup>.

**Table 3: WHO AQG 2005 and US EPA 2013 air quality for particulate matter: annual and 24 h mean concentrations.**  
Adapted from *WHO Air Quality Guidelines - Global Update 2005 (2006)* <sup>55,65</sup>:

Standard		PM <sub>10</sub> (µg/m <sup>3</sup> )	PM <sub>2.5</sub> (µg/m <sup>3</sup> )	Basis for selected annual PM <sub>2.5</sub> concentration limit
WHO Interim target-1 (IT-1)	24 h	150	75	These levels are associated with about a 15% higher long-term mortality risk relative to the AQG level.
	annual	70	35	
WHO Interim target-2 (IT-1)	24 h	100	50	In addition to other health benefits, these levels lower the risk of premature mortality by approximately 6% [2-11%] relative to the IT-1 level.
	annual	50	25	
WHO Interim target-3 (IT-1)	24 h	75	37.5	In addition to other health benefits, these levels reduce the mortality risk by approximately 6% [2-11%] relative to the IT-2 level.
	annual	30	15	
WHO Air quality guideline (AQG)	24 h	50	25	These are the lowest levels at which total, cardiopulmonary and lung cancer mortality have been shown to increase with more than 95% confidence in response to long term exposure to PM <sub>2.5</sub>
	annual	20	10	
US EPA National Ambient Air Quality Standard (US)	24 h	150	35	Provides protection against excess aggravated asthma, chronic bronchitis, non-fatal heart attacks, and premature death in children, elderly, and cardiopulmonary disease sufferers, and those of lower socioeconomic status most at risk.
	Annual	None	12	

Efforts to construct source-apportionment models attributing risk to particulates by chemical components have met considerable challenges in the differentiation of co-pollutant effects, especially in the PM<sub>2.5</sub> size fraction dominated by combustion products in multiple co-existing phases<sup>83–87</sup>. Toxicological input is widely seen as necessary to isolate the driving factors behind PM<sub>10</sub> and PM<sub>2.5</sub> toxicity and biological activity, underscored by lack of an apparent no-effect threshold epidemiologically, to provide convincing AAQS for public health risk management at reasonable cost<sup>15,19,63,88–90</sup>. Major institutions have made concerted effort in answering these questions by various *in-vitro* biochemical and *in-vivo* physiological endpoints<sup>88,91</sup>. Still, the translation of causal mechanisms to clinical outcomes is often considered weak<sup>57,92</sup>. Modern AAQS remain largely independent of *in-vitro* or *in-vivo* literature on PM component toxicology and as such, AAQS dependent on the predominating pollutant source at given geographic locations are unlikely to be defined<sup>92,93</sup>, despite defined occupational exposure limits for mining dust pollutants such as coal and quartz<sup>14,94–96</sup>.

Given the wealth of existing publications on a wide range of PM, it is surprising an increasingly detailed mechanistic understanding has failed to interface with epidemiological data. Aspects of this problem arise from limitations inherent in data provided by each approach. The largest epidemiological studies are unable to disentangle pollutant toxicity drivers<sup>19</sup>, and many criticisms are levelled at the associative conclusions drawn from them<sup>97</sup>. Studies of low population regional centres greatest affected by primary industry emissions may fail to reach significance and suffer greater confounding<sup>70</sup>. From the experimental perspective, the toxicity of PM<sub>10</sub> and PM<sub>2.5</sub> may lie in the effects on vulnerable subpopulations with as yet to be identified genetic factors<sup>75</sup>, and the correlation between acute laboratory models and long-term chronic exposure outcomes is questionable<sup>34,97</sup>. The complexity of unidentified mixtures present in the environment requires PM standards to be validated against captured PM, which can be time-consuming to collect with high-volume air samplers and are nonetheless subject to aerodynamic sizing and spatial resolution limitations<sup>57,90</sup>. As a result, the translation of ambient PM concentrations affecting toxicity endpoints to proportional morbidity and mortality in humans is challenging using both *in-vivo* studies and *in-vitro* studies, with modelling caveats attenuating the scope of even the most complex experimental methods.



Future investigations into the pulmonary toxicology of PM<sub>10</sub> and PM<sub>2.5</sub> generated by mining must follow lines of enquiry carefully drawn to produce ample and robust data, with a view towards compatibility with current AAQS. Comparative *in-vitro* toxicology offers a pathway to draw upon existing occupational exposure limits for PM against crystalline silica, asbestos, coal and materials with similarly quantified exposure risks if acceptable methodology and endpoints can be standardised. An advantage such investigations have over tracing toxicity drivers in urban centres is the relative homogeneity of physical characteristics in PM generated by open-pit mining operations, generally composed of poorly-soluble coarse and fine metal-oxide PM<sup>98</sup>. This reduces the number of possible mixtures interactions with noxious gases, though the potential remains for surface adsorption of active organic and Volatile Organic Compounds (VOC) onto PM<sup>99</sup>. Finding comparative endpoints which functionally describe common and fundamental pathophysiological interactions between PM and the lung parenchyma *in-vitro* that lead to fibrosis would enable development of biosensors to monitor PM for toxicity risks that warrant *in-vivo* studies. A mix of toxicological characterisation in parallel with current PM concentration monitoring hardware would benefit communities subject to high levels of mining dust pollution, forewarning of health risks chronic exposure may cause. The principle challenge is to reach a consensus on the importance of various molecular endpoints to disease outcomes, using a biologically relevant exposure system. This review details toxicity drivers most likely relevant to comparative *in-vitro* toxicology investigations of poorly-soluble PM generated by mining activity, and the methods and endpoints which best capture these drivers.

### 2.3 Generation of Mining Dusts

Impacts of dust generation from surface mining operations are felt at national and international scales, contributing a large proportion of PM to national airborne pollutant inventories and often overwhelming settlements associated with mining activity<sup>20</sup>. The economic success of large-scale open-pit mining processes is tempered by the environmental costs, in terms of displaced crustal material, release of fugitive PM and production of tailings and other waste products<sup>100</sup>. Blasting, crushing and processing of mineral ores produces particulate emissions at different

stages over the mining process, creating variances in PM composition and size distributions. The nature of the mined ore itself may also change over geographic variations by composition, texture and foliation, influencing particle shape and friability<sup>98</sup>. Particles < 75 µm in diameter are considered to be 'dusts' and can remain suspended in the atmosphere long enough to spread over large distances depending on weather conditions, and large open-pit mines can generate dozens of Mt/year<sup>101</sup>. Transportation of mined material to handling and shipping sites can also spread high concentration emissions to areas distal to the mine-site<sup>82</sup>. Typically crustal dust comprises 10-25% of urban PM<sub>2.5</sub><sup>102</sup>, however in arid environments in close proximity to ore processing and shipping operations, ore dust contributions can rise to 80% or more in addition to increased overall concentrations of poorly soluble PM<sup>103,104</sup>. This can create conditions where distal populations in addition to those adjacent to mining sites are chronically exposed to PM<sub>10</sub> and PM<sub>2.5</sub> concentrations higher than WHO AQG IT-1 values<sup>82</sup>.

Increasingly stringent measures are being introduced to control PM emissions in the USA, EU, Australia and other nations with high mining output<sup>100</sup>. Compliance is often not straightforward and can itself have negative environmental impacts, being costly and often putting pressure on water resources for wetting or introducing toxic materials<sup>94,101</sup>. For these reasons, PM limit values must be designed bearing in mind the ability to determine apportionment of PM to mines accurately and whether steps to control emissions will bear measureable improvements in public health.

Toxicological arguments against enforcing limits similar to the WHO AQG centre on the differences between mining particulate emissions and combustion products typical of urban PM pollution that informs much of the AQG. Unlike urban PM the bulk composition of airborne mining dusts is largely poorly-soluble minerals such as metal oxides and silica<sup>101</sup>, having a size-distribution shifted away from the ultrafine fraction, centred on the fine fraction<sup>20,105</sup> or coarse fraction depending on proximity to crushing activity<sup>98</sup>. The morphological distribution of particles can also vary by ore, for example high aspect ratio fibres originating from friable ores in asbestos production<sup>98,105</sup>. These fractions are generally most significant in terms of both particle number and mass, comprising approximately 1/3 of the TSP entrained in the atmosphere dispersed by mining sites<sup>105</sup>.

## 2.4 Inhalation of Particulate Matter

For individuals exposed to mining dusts, the quantity of dust entering the lungs depends on respiration rate, tidal volume and particle size. At resting respiration rates, 10,000-15,000 L of air is exchanged in the lungs every 24 h<sup>106</sup>. Air entering the nasopharyngeal region is humidified and filtered, and particles larger than 4.6 µm are efficiently impacted and prevented from reaching the tracheobronchial region<sup>107</sup>. The airway structure of the trachea then bifurcates, symmetrically branching 16 times creating the bronchial tree of the lungs. The acinar airways branch from generation 17 to 24 terminating in the alveoli at generation 25<sup>108</sup>, where gas exchange takes place over a surface area of approximately 150 m<sup>2</sup><sup>109,110</sup>. Sedimentation of particles between 4.6-2.2 µm occurs in the bronchi and first three generations of bronchioles, while diffusion dominates thereafter<sup>107</sup>. Particles reaching the alveoli are generally smaller than 1.1 µm (see Figure 2)<sup>107</sup>, although deposition may vary based on respiration characteristics which can be computationally modelled<sup>108</sup>. Therefore PM<sub>10</sub> generally corresponds to particle deposition in the upper respiratory tract, and PM<sub>2.5</sub> the lower respiratory tract, with both fractions being subject to immune-mediated clearance to the mucociliary escalator and exiting to the gastrointestinal tract<sup>106</sup>. However soluble or degradable PM may be absorbed, and insoluble PM can also be retained in the parenchyma taking from weeks to years to clear, depending on particle size, morphology, concentration and exposure duration<sup>8,34,111</sup>. It is worth noting that clearance to the gastrointestinal tract does not guarantee complete systemic clearance of inhaled PM, and may increase leaching of metals from mining dusts<sup>112,113</sup>.

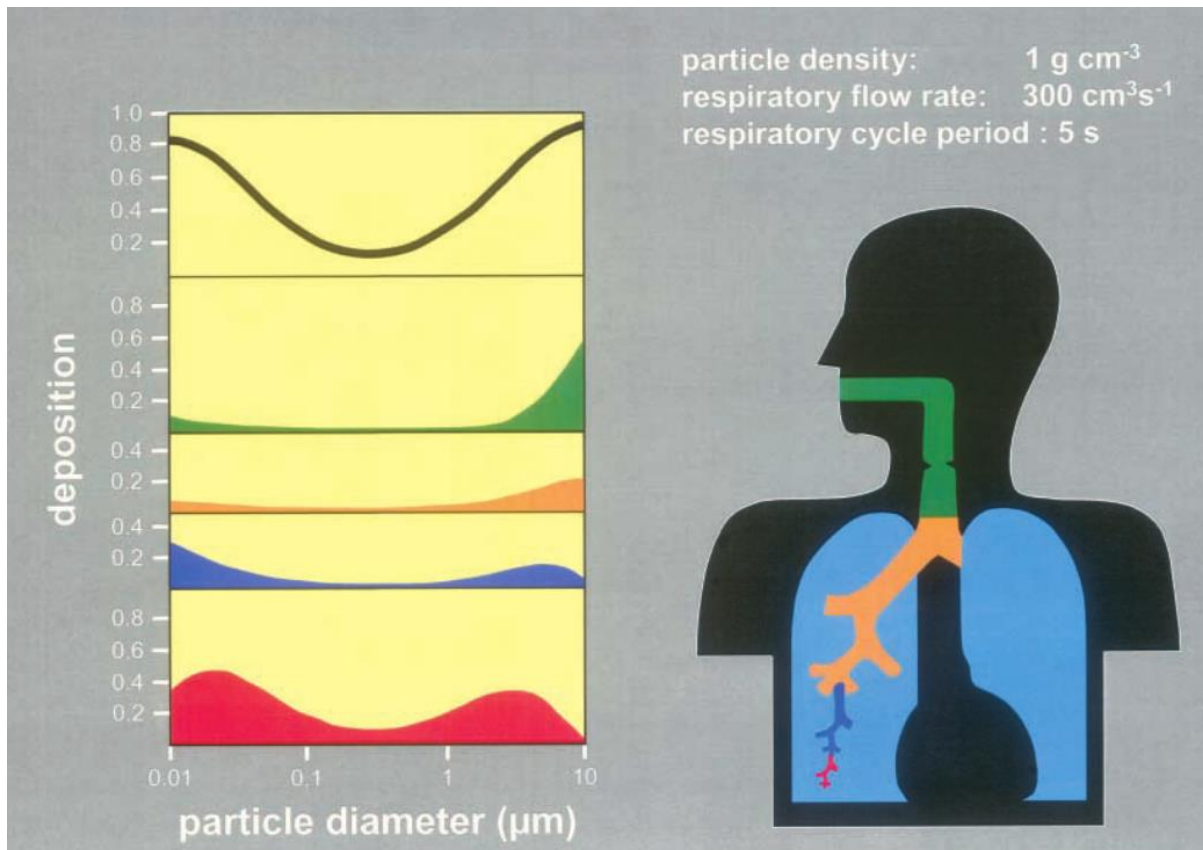


Figure 2: Human respiratory tract and nominal particle deposition in an adult male at rest as a function of particle size, based on International Commission on Radiological Protection (ICRP) models <sup>56</sup>.

## 2.5 Pulmonary Pathologies of Mining Dust Inhalation

A variety of respiratory tract problems arise from acute and chronic exposures to toxins. Severe acute lung injury is likely to manifest as pulmonary oedema, while milder insults can cause bronchitis or asthma. Chronic injuries manifest in a variety of ways, including chronic bronchitis, emphysema, granulomas lung disease, pulmonary fibrosis, pulmonary oedema and cancers of the lung or mesothelium <sup>114</sup>. Inhalation of excessive mineral and coal dusts often occurs through occupational exposure due to mining, drilling, construction and manufacturing activity <sup>115,116</sup>. Mineral dusts generated by mining can also cause systemic toxicity through chemical speciation and free radical generation <sup>117</sup>, provoke hyperplasia and cancer <sup>28,100,118</sup> and elevate cardiovascular risks, likely through inducing systemic inflammation <sup>73</sup>, as well as cause pneumoconiosis with potentially distinctive characteristics on X-ray <sup>100</sup>. Clinical pathologies of excess mineral dust inhalation often take years to manifest, but usually present as a fibrotic pneumoconiosis of

variable granulation, nodulation and opacity with possible complications depending on exposure, as distinguishable on x-ray radiographs (see Table 4) <sup>95,100,119</sup>.

**Table 4: Natural minerals associated with human disease** <sup>100</sup>

<b>Rock type/ore</b>	<b>Human health implications</b>
Chrysotile, crocidolite, anthophyllite etc.	Used as asbestos. Asbestosis, lung cancer; cancer of the gastrointestinal tract; pleural, mesothelioma
Mica group minerals	Pulmonary fibrosis; silicosis; strong association with free silica, likely a major factor in producing fibrosis
Feldspar	Silicosis; often attributed to the included crystalline silica
Fullers earth—Bentonites	Pneumoconiosis without massive fibrosis and nodules; mottled X-ray appearance; some related silicosis
Granite, quartzite, sandstone, slate	Silicosis; silico-tuberculosis; nodular silicosis; fibrosis; enlarged and hardened lymph glands
Limestone, marble, dolomite	Bronchitis, emphysema, some scarring reported; calcinations increases toxicity; caustic burns; dermatitis
Silica, quartz, flint, cristobalite, tridymite	Silicosis; silicotic nodules in spleen; silico-tuberculosis; progressive pulmonary fibrosis; cristobalite-tridymite are more fibrogenic
Talc	Talcosis; talc pneumoconiosis
Bauxite ore; corundum	Aluminosis; lung scarring; pneumoconiosis; emphysema
Chromite	Lung cancer; ore may be associated with chrysotile asbestos
Iron ore (hematite, magnetite, taconite)	Siderosis; reports of increased lung cancer among taconite ore
Lead ore (galena, cerussite, anglesite)	Pneumoconiosis; diseases of the central nervous system; nephritis; anaemia
Uranium, thorium and vanadium ores	Excess lung cancer
Tin, titanium	Severe X-ray changes in miners; tin pneumoconiosis; severe lung scarring; titaniosis

A range of occupational pneumoconiosis conditions are differentiated in name by the causative PM source (see Table 5).

Table 5: Nomenclature of common pneumoconiosis by PM source

<b>Nomenclature of Pneumoconiosis</b>	
<b>Dust Species</b>	<b>Pneumoconiosis</b>
Carbon	Anthracosis
Coal	Coalworker's pneumoconiosis ( <i>black lung</i> )
Asbestos	Asbestosis
Silica	Silicosis ( <i>grinder's disease</i> )
Bauxite	Bauxite fibrosis
Beryllium	Berylliosis
Iron	Siderosis
Cotton	Byssinosis

Airborne silica, asbestos and coal have been subject to extensive study given the ubiquity of these dusts and early recognition of their health impacts<sup>95,120,121</sup>. Silicon constitutes 26% of the earth's crust, making it the second most abundant element to oxygen. It is found in combination with or as a component of many mineral ores and may be partially responsible for shared outcomes resulting from inorganic mineral pneumoconiosis, confusing apportionment of toxicity<sup>95,122</sup>. Acute silicosis can occur from inhalation of high concentration crystalline silica encountered in occupations such as surface drilling and tunnelling. It is characterised by pulmonary oedema, interstitial inflammation, accumulation of proteinaceous fluid and eosinophils in the alveoli, lung lesions and X-ray opacities<sup>95,123</sup>. These effects result in dyspnoea and reduced lung function. Accelerated silicosis and chronic silicosis may include symptoms of acute silicosis combined with pulmonary remodelling including development of fibrotic granulomas. The alveolar sacs become hypertrophic, and hyperplasia of type II epithelial cells occurs causing emphysema. Histopathology of granulomas show nodules with concentric collagen ring development and central hyalinised zones. Calcification and necrosis may occur, with macrophage and lymphocyte build-up on the nodule periphery<sup>95,121</sup>. For a working life of 45 years,

the mortality due to silicosis is estimated to be 1.3% up to age 65, at an occupational exposure level of  $100 \mu\text{g}/\text{m}^3$  per 8 h day, as is currently the US Occupational Safety and Health Administration (OSHA) Permissible Exposure Limit (PEL) standard for quartz<sup>96,124</sup>. The cristobalite form of crystalline silica is thought to be even more fibrogenic than quartz, although it is much less abundant, and PEL of  $50 \mu\text{g}/\text{m}^3$  is set for it<sup>124</sup>.

Asbestos is also a silicon allotrope and has historically found extensive use in industrial, construction and insulation applications until regulatory measures led to restriction or banning of its use in developed nations by the 1980s<sup>125</sup>. Six types of fibrous silicate minerals are defined as asbestos, falling into two classifications; serpentine and amphibole. Only chrysotile, a serpentine asbestos, remains commercially relevant and is considered less toxic than amphibole asbestos. Chrysotile fibres in excess of  $20 \mu\text{m}$  in length can be attacked and cleared by the immune system under non-lung overload conditions<sup>126</sup>. Chrysotile fibres have a half-life of approximately 1 day<sup>127</sup> and a potency at least 100 fold less than amphibole fibres<sup>120</sup>. In contrast, long amphibole fibres are not susceptible to macrophage digestion, persisting in the lungs and penetrating the pleural cavity within 7 days. While the exact mechanism of toxicity is debated, inhalation of amphibole asbestos and very high concentrations of serpentine asbestos is associated with diffuse interstitial pulmonary fibrosis, the formation of asbestos bodies, pleural inflammation, lung cancer and mesotheliomas<sup>126–129</sup>. Symptoms may take up to 40 years to develop after the initial exposure, although in up to a fifth of patients abnormalities such as diffuse interstitial pulmonary fibrosis may not appear on X-ray<sup>129,130</sup>. Exposure to amphibole asbestos carries a 5% risk of lung cancer per excess fibre/ $\text{cm}^3$ , while chrysotile asbestos carries a 0.5% risk<sup>131</sup>. The long lead time, variety of asbestos fibre types and different lengths makes it difficult to determine if a safe threshold exists for exposure. The US OSHA has determined a PEL of 0.1 fibres/ $\text{cm}^3$  over an 8 h/day for fibres that are  $5 \mu\text{m}$  in length and have a 3:1 aspect ratio<sup>130</sup>.

Metal ores are the target prospect of many large-scale mining operations. As with other kinds of pneumoconiosis, metal ore dust is associated with inflammation, fibrosis, granulomas and reduced lung function. However, specific metal ores differ

in systemic effects such as carcinogenesis, neurotoxicity and other acute toxicities unique to the chemistry of the ore<sup>132–134</sup> (see Table 4, Table 6). For example, chronic occupational exposure to manganese over 70 µg/m<sup>3</sup> is associated with the development of neurotoxic symptoms<sup>135</sup>. The variation in ore composition, crystallinity and metal speciation arguably require specific determination of risk and exposure limit on a mine-site by mine-site basis<sup>20,100,136,137</sup>. This is underlined by differences in fibrotic potential when workers are occupationally exposed to manufactured iron oxides, such as limited findings of fibrosis in welder's siderosis, compared to fibrotic outcomes in haematite miners<sup>17,122,138</sup>. Insight into whether compositionally driven differences in metal ore toxicity disproportionately alter toxicity mediated by physical characteristics alone requires is a key challenge for *in-vitro* PM toxicology.

Table 6: Histopathology of metal-induced disease<sup>132</sup>

<b>Agent</b>	<b>Characteristic Histopathology</b>	<b>Other Reported Histopathology</b>
Aluminium	Interstitial fibrosis	Sarcoidlike granulomas; alveolar proteinosis
Beryllium	Sarcoidlike granulomas; diffuse interstitial fibrosis	Tracheitis; bronchitis; acute pneumonitis
Cadmium	Acute pneumonitis; interstitial fibrosis; emphysema	
Cobalt	Giant cell interstitial pneumonia; desquamative interstitial pneumonitis; fibrosis	Sarcoidlike granulomas
Copper	Foreign body granulomas; fibrosis	
Iron	Dust macule; peribronchiolar collections of dust with dust-laden macrophages	Fibrosis



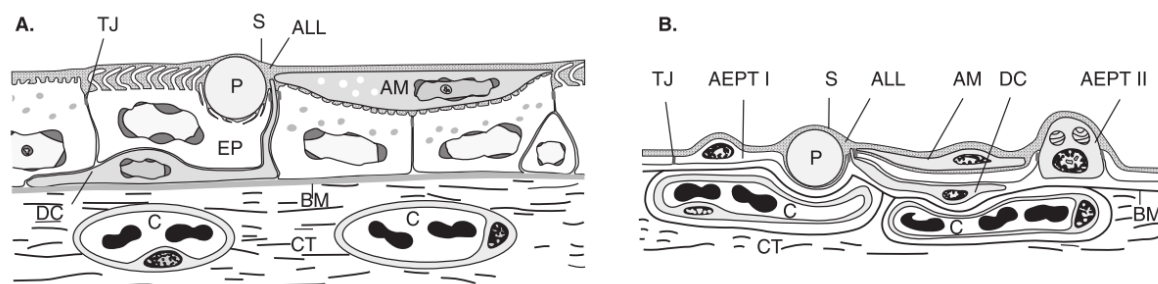
Mercury	Tracheobronchitis; bronchiolitis; pneumonitis; pulmonary oedema; desquamative interstitial pneumonitis (late)	Proteinuria; acute tubular necrosis; neurotoxicity
Nickel	Asthma; epithelial dysplasia; chemical pneumonitis	Nasal septal perforation; chronic rhinitis; hyper- plastic sinusitis; anosmia

## 2.6 In-Vitro Models of Pulmonary PM Exposure

### 2.6.1 Respiratory Structures and PM Interactions

#### 2.6.1.1 Alveolar Structures

Knowledge of the cell types and structure of the respiratory surfaces is essential in choosing appropriate cell lines for *in-vitro* models of inhaled PM<sub>10</sub> and PM<sub>2.5</sub> toxicity<sup>40</sup>. The alveolar surfaces are the thinnest external barrier of the lung parenchyma, only one cell layer thick. Type I alveolar epithelial cells are 5 µm thick allowing gas exchange, while Type II cells are 15 µm thick and secretory. Type I cells are unable to replicate and must be replaced by the differentiation of Type II cells, although this process is slow<sup>139</sup>. The supporting fibroblast and capillary-rich connective tissue is separated from the epithelial layer by the interstitial space<sup>106</sup>. Granulocytes, monocytes and macrophages can migrate between these tissues<sup>140</sup> (see Figure 3). Pulmonary surface tension is reduced by a layer of bronchioalveolar fluid on the surfaces of the conducting airways and pulmonary acinus, allowing inflation. This ‘surfactant’ fluid is composed of large proteins and phospholipids<sup>141</sup>.



**Figure 3:** This figure shows the structure of the epithelial layer in the Airways (A) and Alveoli (B). Key: AEPT I: Alveolar epithelium type I; AEPT II: Alveolar epithelium type II; ALL: Aqueous lining layer; AM: Alveolar macrophage; BM: Basal membrane; C: Capillary; CT: Connective tissue; DC: Dendritic cell; EP: Epithelial cell; P: Particle; S: Surfactant; TJ: Tight

*junction. Adapted from In vitro models of the human epithelial airway barrier to study the toxic potential of particulate matter*<sup>40</sup>.

### 2.6.1.2 Bronchioalveolar Fluid Interactions with PM

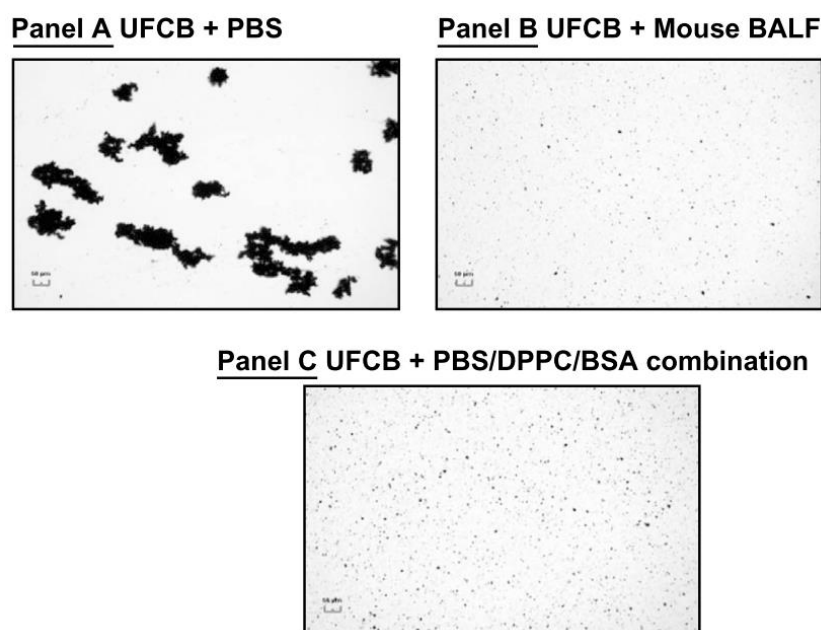
Typically studied toxicants are soluble, forming solutions where the compound dissolves to a molecular level, as is the case with most pharmacological drugs. Poorly-soluble PM however persists as a solid internal phase within a liquid continuous phase, and is therefore a suspension. Suspensions differ from colloids in that they contain larger particles which undergo sedimentation and potentially agglomerate. The effect of bronchioalveolar fluid on particle agglomeration, dispersion and solubility is therefore an important area of study, potentially affecting effective PM size-distribution and toxicity at the acinar surfaces.

Bronchioalveolar fluid can either be obtained by lavage (BALF) from animals or recreated synthetically. Simple synthetic bronchioalveolar fluid can be constituted with a combination of biologically active molecules, featuring albumin and dipalmitoylphosphatidylcholine (DPPC), the most abundant phospholipid, at a physiological alkalinity of pH 7.6<sup>142</sup>. More complex synthetic recipes include a diverse range of enzymes, antioxidant complexes and other minor surfactant phospholipids found in bronchioalveolar fluids<sup>143</sup> (see Table 7), and non-biological fluids depending on design philosophy<sup>144</sup>.

Table 7: An example of synthetic bronchioalveolar fluid for addition to media (Hank's balanced salt solution)<sup>143</sup>.

Component	Concentration
Serum albumin	7.4 mg/mL
Dipalmitoylphosphatidylcholine (DPPC)	10 mg/mL
Lysozyme	2.5 mg/mL
Apotransferrin	0.2 mg/mL
Ascorbic Acid	50 µg/mL
Glutathione	50 µg/mL
Uric Acid	25 µg/mL
Alpha-tocopherol	1 µg/mL

A tenfold increase in serum albumin from 1.5 mg/mL to 15 mg/mL has been shown to reduce the average diameter of TiO<sub>2</sub> nanoparticles approximately 25% at a stock concentration of 2 mg/mL<sup>145</sup>. Improved dispersion characteristics are also reported for ultrafine carbon particles with Bovine Serum Albumin (BSA)<sup>146,147</sup> (see Figure 4) however ultrasonication of the sample is required – a process without biological analogue. While high concentrations of BSA appear to increase particulate dispersion characteristics<sup>148</sup>, its use is cautioned and qualitative data must be evaluated carefully. Concentrations of albumin exceeding *in-vivo* physiological concentrations may cause proteinaceous interference with observed toxicity<sup>149</sup> as well as reduce particle uptake<sup>150</sup>. Albumin also exhibits antioxidant properties which have the potential to diminish redox endpoints<sup>151</sup>, although the oxidative interactions of transition metals has been reported as similar under either BALF or synthetic bronchioalveolar fluid<sup>143</sup>. DMSO finds occasional use as a non-biological dispersant but has inferior performance and interference with oxidative processes is again an issue<sup>147</sup>.



**Figure 4: Ultrafine Carbon Black particles are shown in A: standard Phosphate Buffered Saline; B: Mouse bronchioalveolar lavage fluid; C: a sonicated combination of Phosphate Buffered Saline, DPPC and Bovine Serum Albumin<sup>146</sup>.**

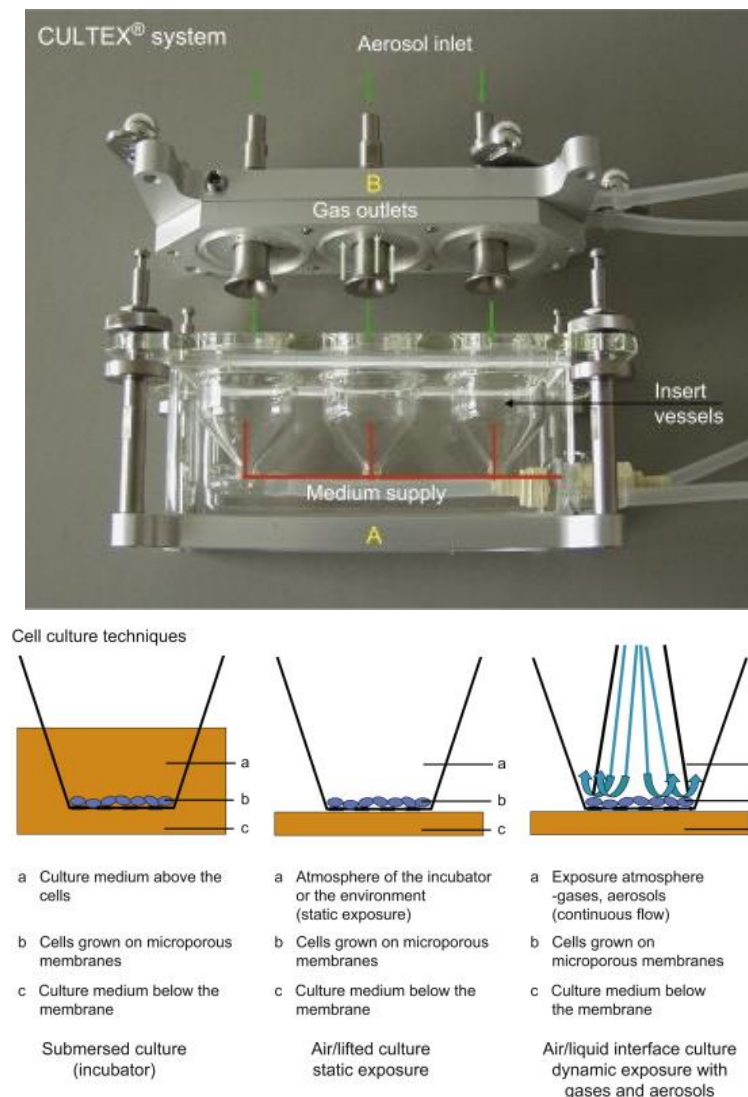
The relevance of forcing the disaggregation of fines and nanoparticles is questioned, as it is not well substantiated that particles are significantly disaggregated *in-vivo*<sup>152</sup>. Theoretical studies indicate that the surfactant properties of DPPC are 2-3 orders of

magnitude weaker than the aggregating forces between fine TiO<sub>2</sub> particles<sup>153</sup>, although newer DPPC preparation methods may improve interactions<sup>146,154</sup>. DPPC may also have effects beyond disaggregation, reducing particle phagocytosis<sup>155</sup>. Other proteins and phospholipids found in bronchioalveolar fluid such as collectins SP-A and SP-D may have important effects to consider when binding to metal oxides, such as particle opsonisation, regulation of histamine release by mast cells and other immunomodulatory effects<sup>142,156,157</sup>.

### 2.6.2 Lung-Air Interface Systems

Given the unique air-liquid interface (ALI) of the lungs, replicating toxicological exposures using an artificial ALI may more closely resemble *in-vivo* conditions and obviate dosing with particle-media suspensions. The increased oxygenation of cells may alter metabolism, the tolerance to oxidative stress, and promote cellular differentiation<sup>158</sup>. Ideally, ALI exposure systems must be able to deliver aerosol doses accurately over time, while keeping cell lines alive. Achieving this in practice presents a number of challenges, including determination of actual dose in contact with cells, resultant particle-size distribution, addressing perfusion and viability of cells, and acquisition of sufficient sample due to deposition efficiencies as low as 2%<sup>159</sup>.

Complex commercial systems exist to perfuse cultures and dose cultures over a thin ALI, although no single system dominates<sup>160</sup>. These include the Cultex® and Minucell® systems<sup>40,159</sup>. Depending on requirements, the submersion of cells into the media and airflow parameters can be adjusted (see Figure 5).



**Figure 5: Top: A picture of the Cultex® system exposure hardware. Bottom: A diagram of cell culture methods enabled by the Cultex® system. Submersed mode replicates classic culture and enables a coculture to be set up, while lifted and dynamic exposure modes allow cell/air interface modelling <sup>161</sup>.**

The ALI can be modelled more simply using porous membranes inserted into multiwell culture plates, allowing cells to grow on an elevated surface much closer to the air while still allowing sufficient media for cell growth underneath. While this does not model airflow and deposition characteristics, Transwell™ culture inserts may be adapted for this purpose and are relatively inexpensive in low-throughput applications <sup>162</sup>.

### 2.6.3 2D Culture Systems

Conventional 2D tissue culture assays lend themselves well to multiwell microtitre tissue culture plates, for which high throughput dose-response assay protocols are well established. In the field of particle toxicology, unique challenges posed by poorly-soluble PM<sub>10</sub> and PM<sub>2.5</sub> require critical analysis and redesign of protocols to account for differences in dosing metrics and assay interference from adsorptive and optical characteristics<sup>163–166</sup>. Successful navigation of these issues will allow detailed comparative toxicology of cellular endpoints which fit in with current toxicological endpoints.

In choosing cell lines, primary cell lines generally allow responses closer to *in-vivo* exposures to be modelled. Immortal cell lines present advantages over primary cell lines in terms of standardisation, and therefore inter-study comparison and cost. Culture of human cell lines can be used alongside animal cell lines to differentiate responses to PM in humans that may not be evident in animal studies, or to model cytokine interactions that may not be completely homologous in animals. To model the respiratory surfaces, the A549 epithelial adenocarcinoma cell line is a common choice, having characteristics of both Type I and Type II cells and is very resilient<sup>167</sup>. The CaLu3 cell line is also used to model the epithelial barrier, while BEAS-2B and 16HBE14o- are popular choices to model the bronchial epithelium<sup>40</sup>. Fibroblast cell lines are frequently used to represent connective tissue responses, such as LL24 and IMR-90<sup>168–170</sup>. However, connective tissue responses are reactive in nature to PM exposure and epithelial cell death in the lungs, making their endpoint selection and interpretation more complicated even if cytotoxic effects appear similar *in-vitro*<sup>171</sup>.

A limited range of macrophage responses including phagocytosis and cytotoxicity can also be modelled using 2D cultures. The mouse macrophage RAW 264.7 cell line is frequently used because of its ease of culture and immortality. Human equivalents such as U937 and THP-1 are cultured as monocytes and then differentiated into monocyte-derived macrophages<sup>172</sup>. This creates some difficulties when using immunological endpoints if the differentiating stimulant, e.g. Phorbol Myristate Acetate (PMA), is not washed completely from the culture before assay as

it can continue to stimulate cytokine production. Washing steps are also required to minimise particle interference before optical assays, although this can be difficult to achieve without altering cell survival if particles have bound to the cell surface <sup>165,166</sup>.

#### 2.6.4 3D Culture Systems and Explants

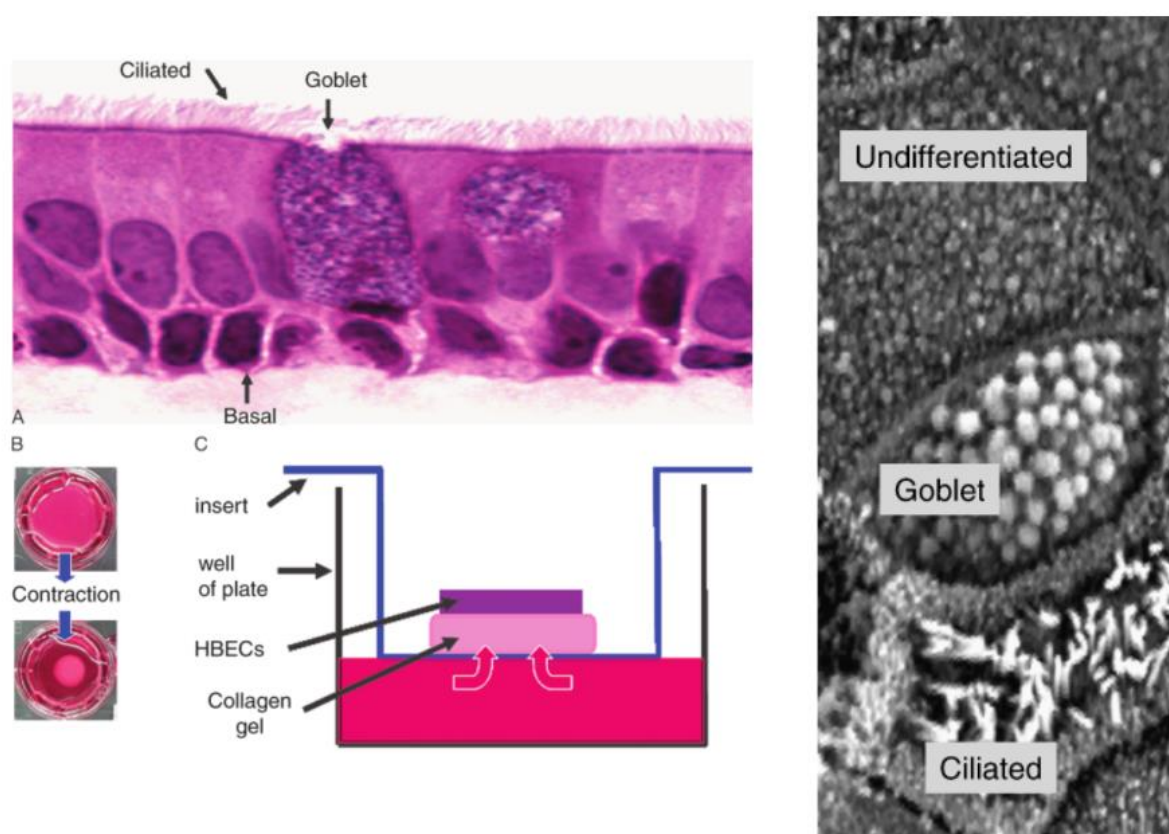
Animal studies by intratracheal instillation of particles often result in toxicity data which is difficult to relate to 2D cell culture models, or may even conflict <sup>173</sup>. If the discrepancies are not due to improperly adapted assay protocols, the poor differentiation of cells in 2D culture may offer an explanation. To remedy this, the use of 3D tissue culture systems has been demonstrated to increase cellular differentiation <sup>174</sup>.

Several systems exist to promote the growth of 3D structures from cellular monocultures. The simplest of these is modification of the tissue-culture growth surface to prevent adherence of cells, which can be achieved through coating with agarose gel, or by using commercially pre-treated surfaces <sup>174</sup>. This allows cells to self-associate and form 3D spheroids which may differentiate, although the process is difficult to control and standardise <sup>175</sup>. A similar method utilises the surface tension of a small amount of media to form a 'hanging drop' when the tissue culture surface is inverted. Cell lines within this hanging drop gravitate to the bottom of the drop and without a surface to interact with form spheroids <sup>176</sup>. The small volume of the drop requires humidity to be controlled to prevent evaporation affecting exposure concentration during incubation <sup>177</sup>. Rotating-wall bioreactors utilize a vessel which is constantly in motion, preventing settling of cells so that they adhere to micro-carrier beads. On these beads collagen I coatings promote cells within the medium to attach and grow into 3D structures <sup>178,179</sup>.

Collagen and Extracellular Matrix (ECM) components have been shown to greatly enhance cellular differentiation, particularly when structured into a 3D scaffold or hydrogel. Scaffold matrices create porous surfaces for cells to adhere to which can then degrade away, although this is not necessary, and common active components in commercial variants include synthetic peptides, hyaluronic acid, collagen, fibrin and reconstituted ECM <sup>180</sup>. New tissue culture technologies such as the UpCell®

system allow 3D tissue cultures to be composited from monolayer sheets released from culture intact without trypsinisation or other enzymatic means<sup>181</sup>. Differential effects of 3D scaffolds on tissue culture endpoints such as inflammatory signalling present relatively unexplored vistas in particle toxicology<sup>174,180</sup>.

Organotypic cultures bridge the gap between *in-vivo* and *in-vitro* experiments, similarly to explants. Immortalised primary cells are grown on fibroblast-seeded collagen I gel which is perfused by media at its base, and can be incubated for up to a month, allowing differentiation and exposure to the cell/air interface<sup>182</sup>. Figure 6 depicts this system and differentiated Human Bronchial Epithelial Cells (HBECs).



**Figure 6: A) Normal human bronchial histology. B) Type I collagen seeded with fibroblasts, contracting as it cools. C) Immortalized HBECs attached collagen gel surface. Right: Scanning electron microscope image showing differentiation of HBECs on collagen gel into goblet, ciliated and normal cells<sup>182</sup>.**

A general drawback of 3D tissue cultures in particle toxicology is the inhibition of drug penetration, as cells may be protected from complete perfusion within the 3D superstructure, especially in spheroidal cultures which resemble tumours<sup>175</sup>. As fine particles cannot diffuse through cells, membrane-contact mediated toxicity will be



completely inhibited. The greatest challenge of 3D tissue cultures is therefore to balance increased complexity with accuracy and sensitivity, in light of reduced cell membrane-particle contact.

### 2.6.5 Co-Culture Systems

While allowing greater differentiation of cell lines, 3D culture systems may not offer a complete picture of complex interactions between unrelated cell-types occurring *in-vivo*. This is especially true of the alveolar surfaces of the lung, where chemotactic and chemokinetic factors are communicated between the underlying vasculature, connective tissue, epithelial cells and immune cells. These communications are critical in orchestrating responses to lung injury, and macrophages play a central role<sup>183–185</sup> (see Figure 7). By establishing cocultures of cell lines representative of these components, important aspects of this interplay can be recreated<sup>186</sup>. Evidence suggests that cocultures of lung epithelial cells and macrophages display differential cytokine expression and cytotoxic sensitivity to monocultures of either, in response to fine silica and metal oxide particles, and these responses do not necessarily proportionally correlate with particle concentration<sup>173,187</sup>. Cocultures have also been successfully combined with other advanced tissue culture techniques, including ALI by Transwell™ insert<sup>186</sup>.

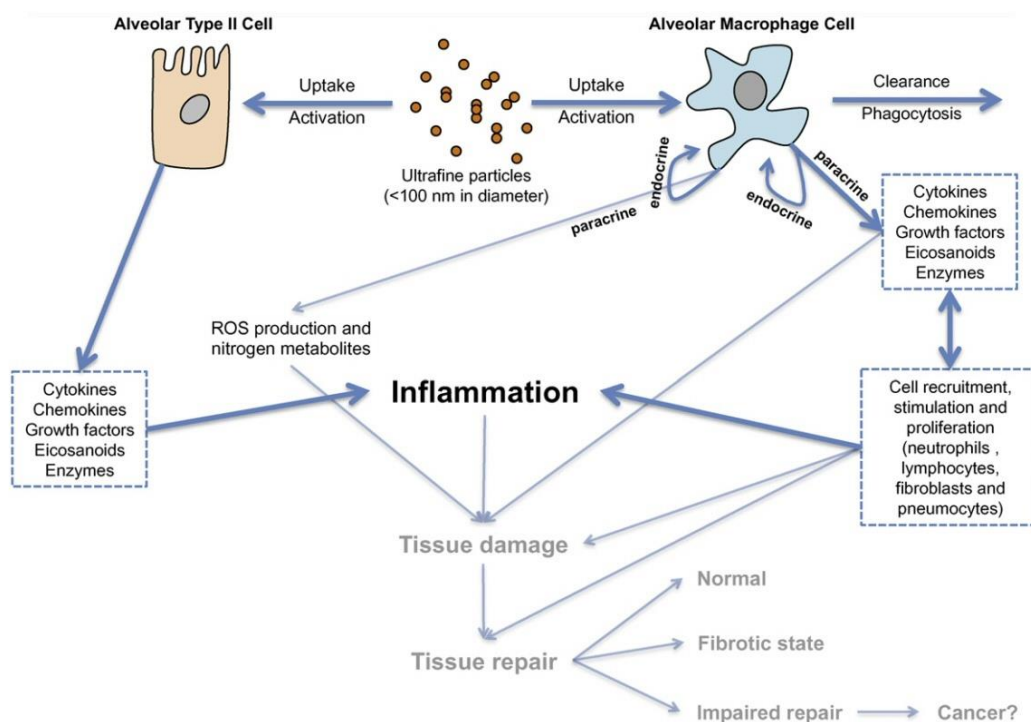


Figure 7: Interaction between alveolar type II cells and macrophages during inflammation in response to particles <sup>186</sup>

## 2.7 Major In-Vitro Endpoints for Determining and Comparing PM Toxicity

### 2.7.1 Particle Characteristics and Toxicity

#### 2.7.1.1 Particle Size

Particle airborne half-life and dispersion is governed by particle size, as are inhalation characteristics described previously. While higher than TSP, the exact toxicity differences between the PM<sub>10</sub> and PM<sub>2.5</sub> fractions are debatable, and factors other than size may take precedence in this range. From a study in Mexico City, TSP levels were found to increase the risk of mortality by 5.8% for every extra 100 µg/m<sup>3</sup> in the atmosphere. However PM<sub>10</sub> and PM<sub>2.5</sub> fractions were found to be significantly more toxic, increasing mortality by 1.83 and 1.48% per 10 µg/m<sup>3</sup>, respectively <sup>188</sup>. This is also reflected in an *in-vivo* study using PM from six different European cities, where the coarse fraction was found to be consistently more inflammatory than the fine fraction, although fines caused greater neutrophil accumulation <sup>189</sup>.

From an *in-vitro* toxicology standpoint, decreasing particle size causes the specific surface-area to mass ratio to increase, and allows cellular uptake of particles to occur more readily. Modern literature explores this relationship frequently <sup>163</sup>, finding increasing free ion release, cytotoxicity, genotoxicity and redox potential with decreasing size within the ultrafine range in metal and metal oxides <sup>173,190–192</sup>. In contrast, inhalation of PM<sub>10</sub> and PM<sub>2.5</sub> mining dust is relatively free of particles in the ultrafine fraction <sup>20</sup>, and therefore the size-dependent toxicity between PM<sub>10</sub> and PM<sub>2.5</sub> is framed by particle composition, lung deposition characteristics and particle clearance rates, more so than surface-area dependent reactivity and intracellular bioactivity <sup>19</sup>. In urban environments, different anthropogenic sources tend to produce particles of different sizes, affecting the composition of particles by size <sup>193</sup>. Table 8 describes the properties of typical urban PM and rate of clearance from the human lung.

Table 8: Characteristics of anthropogenic PM. Adapted from The Impact of Fine Particles on Health <sup>193</sup>

<b>Characteristics of anthropogenic PM</b>		
Particle Size	Solubility	Exposure Mechanism
Coarse thoracic particles (2.5-10 µm)	Large numbers of insoluble minerals and organic material	Enter the ciliated larger bronchi. Cleared within hours or days
Fine particles (< 2.5 µm)	Majority are highly water-soluble inorganic salts, smaller amount of lipid-soluble organic compounds (PAHs, etc) and insoluble soot, organic material and minerals	Enter the small non-ciliated bronchi and alveolar sacs. Solid particles are cleared over a matter of months and sometimes years, by specialized white blood cells or macrophages
Ultrafine Particles (< 0.1 µm)	Solubility varies, depending on nearby emission sources and the chemical composition of emissions (soot, hydrocarbons, sulphuric acid)	Enter the alveolar sacs and the bloodstream to some extent. Large number but small mass. Macrophages do not recognize individual ultrafine particles; they are either cleared as part of the mucous in the mucociliary escalator or taken into the respiratory epithelial cell cytoplasm resulting in very slow clearance.

A 15 week *in-vivo* study using radioactively labelled TiO<sub>2</sub> as a biopersistent particle resistant to physical and chemical breakdown shows that fine (< 2.5 µm) and ultrafine (< 20 nm) particles are cleared from rat alveolar surfaces at similar rates. However, clearance from the interstitial and lymphatic compartments took much longer for ultrafine TiO<sub>2</sub>, as migration to these spaces was higher and macrophage clearance was greatly impaired <sup>194</sup>. Macrophage phagocytic activity has been shown to be less sensitive to ultrafine particles, while neutrophil recruitment appears to be

proportional to the specific surface area of TiO<sub>2</sub> dosed when comparing < 2.5 µm and < 20 nm particle sizes, and therefore ultrafine particles cause greater inflammatory outcomes than macrophage load alone would suggest<sup>137,195</sup>. Increased access to the vasculature by smaller particles may also affect cardiac diseases, as urban epidemiological studies have found ambient fine particle concentrations to be associated with early atherosclerosis<sup>196</sup>.

In a study of fine and ultrafine metal oxide particles, particle composition determined whether a difference was seen between toxicological endpoints. Iron oxides (Fe<sub>2</sub>O<sub>3</sub> and Fe<sub>3</sub>O<sub>4</sub>) were found to differ little by size, having low toxicity. Fine TiO<sub>2</sub> was found to be more toxic than ultrafine TiO<sub>2</sub> causing DNA damage, potentially due to differences in crystallinity. Ultrafine CuO was found to be significantly more toxic than fine CuO, although both showed markedly cytotoxicity and mitochondrial damage than the other samples<sup>197</sup>.

#### 2.7.1.2 Particle Shape

Particle shape has been postulated as central to the toxicity of asbestos, and other particles of high aspect ratio which are biopersistent. While rock crushing techniques in the mining industry produce highly size-heterogeneous particles, they do not generate high aspect ratio particles. It is rather highly foliated rock textures, indicating the possible presence of asbestos or other minerals, which break into fibrous fine particles upon processing<sup>98</sup>.

The size of particles phagocytosed by PAM is limited by cell surface area to ~ 12 µm, and cannot continue past this point even when there is no shortage of phagocytic receptors. If this process fails, PAM may recruit additional monocytes and macrophages. Excess monocytes and macrophages allow multinucleated giant cells involved in granuloma formation to fuse. Frustrated phagocytosis occurs when macrophages enter a continuous state of particle-association which does not resolve against fibres longer than ~ 20 µm<sup>30</sup>. Sequestration of the particle into the lysosome stalls, and the lysosomal protease cathepsin B is released. This triggers the formation of the NALP3 inflammasome which is involved in IL-1β and IL-18 cytokine signalling<sup>37,198</sup>. TNFα expression is also shown to increase with longer fibres<sup>35</sup>.

Increased inflammation is consistently observed with long fibres of multiple compositions, including asbestos, glass, rigid multi-wall carbon nanotubes (MWCNT) and nanoparticles such as TiO<sub>2</sub> engineered into fibres over 15 µm in length<sup>37</sup>. Increased inflammation of this kind in the pulmonary spaces leads to neutrophil and lymphocyte recruitment, and also encourages pleural effusions to develop<sup>36,199</sup>. Pleural inflammation may be linked with the genesis of mesotheliomas. Mechanisms to explain this link include epigenetic silencing of tumour suppressor genes and TNFα mediated cellular transformation, implying all fibrous particulates stimulating TNFα production pose the risk of mesothelioma<sup>200,201</sup>. Furthermore, TNFα receptor knock-out mice are protected from pulmonary asbestosis; a form of diffuse interstitial fibrosis associated with asbestos and formation of ferruginous bodies<sup>130</sup>.

While conventional tissue culture techniques lend themselves to studying inflammatory endpoints of high aspect ratio particle phagocytosis, successful modelling of granulomatous formation using only cell monolayers is doubtful. A study of MWCNT and crocidolite asbestos fibres has successfully created 3D spheroids demonstrating epithelioid granuloma formation by using bone marrow derived macrophages cultured in agarose coated wells. Granuloma formation was determined to correlate better with MWCNT length and complexity than surface-area and iron content. The development of multinucleated giant cells was also observed<sup>202</sup>. Experiments with MWCNT *in-vivo* show increased connective tissue thickness in the alveolar septa of up to 75% in 56 days, in single aspiration doses as low as 80 µg in mice<sup>203</sup>, while nanotubes which are not rigid or are tangled may have diminished fibrotic potential (see Figure 8)<sup>127</sup>.

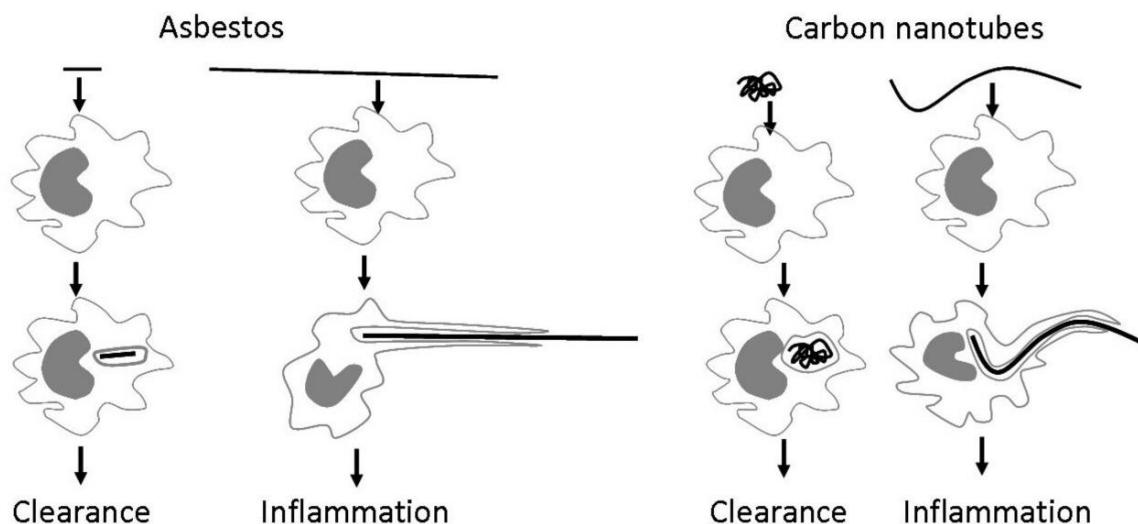


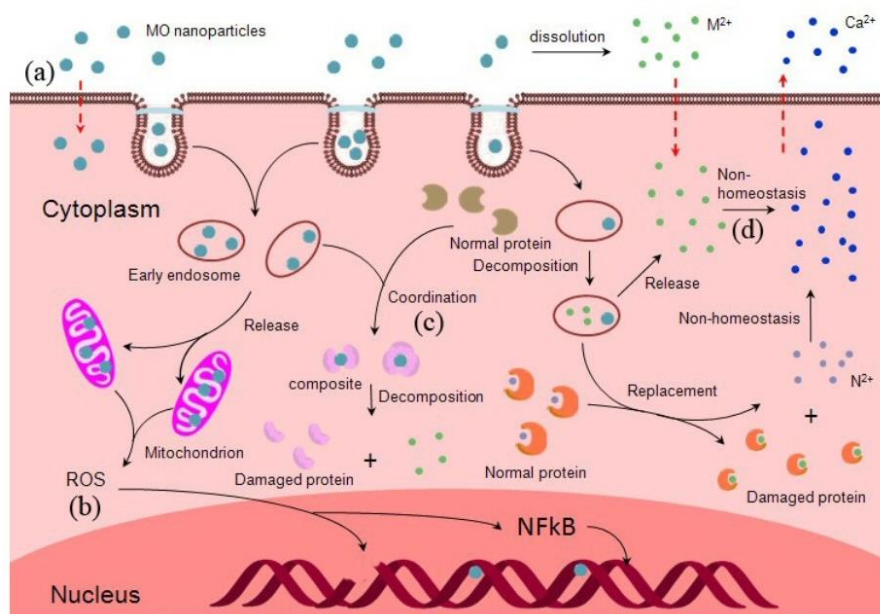
Figure 8: Differences in particle length and rigidity affecting particulate clearance. (left) Successful and frustrated phagocytosis of long asbestos fibres; (right) Successful and frustrated phagocytosis of tangled and rigid carbon nanotubes.

### 2.7.1.3 Particle Composition

Particle composition affects the biochemical interactions available to mediate toxic interactions; the formation of adducts with cellular components, adsorption of nutrients, disruption of ion channels, interference with metabolism, immunogenicity and surface reactivity are dependent on composition<sup>19</sup>. For mining dusts, differences are likely to arise from the solubility of minerals and speciation of metals in bronchioalveolar and lysosomal fluid conditions<sup>204</sup>, as well as surface crystallinity which influences the catalysis of free radicals<sup>205</sup>.

Different mineral crystal structures affect toxicity, and amorphous counterparts are generally less toxic. Changes in toxicity are likely to be reflected by oxidative stress more than cytotoxicity<sup>206</sup>. This is well understood in crystalline silica, the most abundant form of which is quartz and most toxic is cristobalite. Surface modification of quartz has been shown to reduce toxic effects<sup>207</sup>, as free radical generation, hydrogen bonding, surface electric charges and silanol functional groups have been proposed to explain the interactions of silica with proteins, phospholipids and membranes<sup>208</sup>. This is also true of TiO<sub>2</sub> surface crystallization, where the anatase structure has been found to be up to 100 fold more toxic than the rutile structure<sup>168</sup>. Differentiating composition mediated effects on cellular endpoints is a strength of *in-vitro* toxicology, if appropriate endpoints and methodologies are chosen. Of the

common metal oxides found in ores, ZnO and CuO are found to demonstrate markedly higher toxicity. The mechanisms are uncertain, including coordination effects with protein binding, interference with metal ion proteins, generation of free radicals, disruption of homeostasis and the effects of soluble ions (see Figure 9) <sup>209</sup>.



**Figure 9: Pathways for toxic interactions of CuO and ZnO particles. (a) entry mechanisms into cells through diffusion and pinocytosis; (b) effect of ROS on intracellular particles and DNA breaks; (c) coordination of dissolved Cu<sup>2+</sup> and Zn<sup>2+</sup>; (d) non-homeostasis effect caused by Cu<sup>2+</sup> <sup>209</sup>**

#### 2.7.1.4 Particle Solubility

Solubility is fundamental to observation of differences in toxicity amongst poorly-soluble mineral and metal-oxide PM sources. For example, soluble barium compounds cause nervous system toxicity, whereas the insoluble sulphate of barium is ingested in diagnostic medicine with no toxic effect. Silica has been found to be partially soluble, allowing dimensions of silica toxicity to result from biochemical interactions. The dissolving of silicic acid out of quartz, asbestos and other dusts may be enhanced by reactive chemistry occurring at the mineral surface and contact with lysosomal enzymes <sup>208</sup>. Solubility in this way will be increased with increasing particle specific-surface area. The acidic lysosomal fluid compartment of macrophages may also liberate cytotoxic metal ions such as copper with greater efficiency than more neutral fluid compartments such as bronchioalveolar fluid (see Figure 10) <sup>210</sup>, and can be detected by inductively coupled plasma mass spectrometry, atomic absorption spectroscopy and x-ray fluorescence.

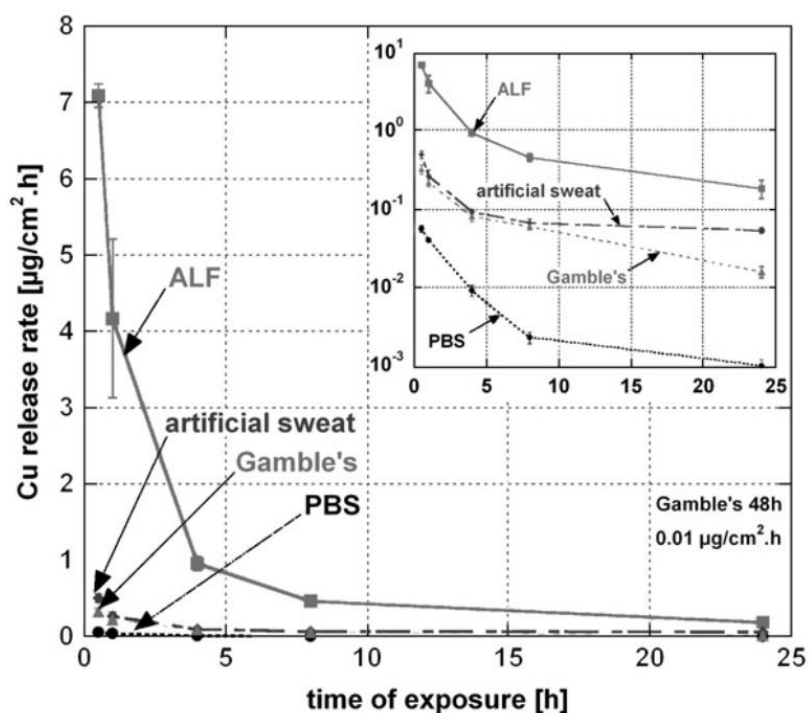


Figure 10: Copper release rate per unit surface area from artificial copper patina powder exposed to synthetic biological fluids and PBS. Insert shows results on logarithmic scale <sup>210</sup>.

## 2.7.2 Cytotoxicity

### 2.7.2.1 Dosing Metrics

Cytotoxicity is the least sensitive measure of toxicity, though a critical point of comparison for assessing other endpoints and data between studies. In measuring differences between PM of different compositions and sizes, an appropriate dosing metric must be decided upon. For completely soluble or liquid toxicants, concentration is usually expressed as solute mass by solvent volume or solute volume by solvent volume. Due to the poorly-soluble nature of mining generated PM<sub>10</sub> and PM<sub>2.5</sub>, particle mass by cell surface area (e.g. LC50 of ZnO in colon cells is 15 µg/cm<sup>2</sup> for 10 nm particles and 29 µg/cm<sup>2</sup> for 44 µm particles <sup>211</sup>) and particle specific surface-area by suspension volume (e.g specific surface area of TiO<sub>2</sub> ultrafine is ~ 50 m<sup>2</sup>/g and fine is ~ 6 m<sup>2</sup>/g <sup>194</sup>) may be more appropriate, if the mass in contact with cell membranes or surface area dependent reactivity are dominant factors in toxicity. Studies have also suggested specific surface area by cell surface area exposed allows better comparisons between *in-vitro* and *in-vivo* results <sup>212</sup>.



For PAM, particle volume by PAM number may better correlate with load-dependent toxicity, as  $60 \mu\text{m}^3/\text{PAM}$  is the approximate threshold for lung overloading, with PAM mediated particle clearance ceasing near  $600 \mu\text{m}^3/\text{PAM}$  <sup>22</sup>. These dosing metrics ease cross-comparisons between studies. For instance, RAW 264.7 rat macrophages are reported to be sensitive to ultrafine  $\text{TiO}_2$  and  $\text{SiO}_2$ , with cell viability at  $100 \mu\text{g}/\text{mL}$  being 20% and 0%, respectively <sup>213</sup>. However, these metrics are unlikely to be consistent if the size distribution of particle suspensions is not identical or different cell seeding densities are used. When measuring poorly-soluble particles of different sizes, sedimentation rates should be considered as this affects particle-cell contact duration, and gentle centrifuging should be considered. In an *in-vivo* study, the innocuous particle-induced lung overload condition was seen to occur at concentrations over  $20 \text{mg}/\text{m}^3$  at an exposure time of 6 h/day for 20 days in rats <sup>91</sup>.

#### 2.7.2.2 Metal and Metal Oxide Cytotoxicity

The cytotoxicity of poorly soluble metal oxides likely to be found as trace or bulk components of mineral ores is usually found to be low when using alveolar cell lines such as A549, with exceptions such as  $\text{ZnO}$ ,  $\text{CuO}$  and anatase  $\text{TiO}_2$  <sup>172,214</sup>. Amongst carbon, carbon nanotubes and a range of metal oxide nanoparticles ( $\text{CuO}$ ,  $\text{ZnO}$ ,  $\text{TiO}_2$ ,  $\text{Fe}_3\text{O}_4$ ,  $\text{Fe}_2\text{O}_3$ ,  $\text{CuZnFe}_2\text{O}_4$ , carbon nanopowder, carbon nanotubes), cytotoxicity was found to be less than 10% at a concentration of  $40 \mu\text{g}/\text{cm}^2$  on A549 cells, except for carbon nanotubes,  $\text{ZnO}$  and  $\text{CuO}$ . Intracellular ROS was difficult to distinguish from control other than  $\text{TiO}_2$  and  $\text{CuO}$ . DNA fragmentation was clearly distinguishable from controls by  $\text{CuO}$ , followed by  $\text{TiO}_2$ ,  $\text{CuZnFe}_2\text{O}_4$  and carbon nanotubes <sup>215</sup>. Another study focusing on size-dependent differences in toxicity found little distinction between fine and ultrafine metal oxides, other than  $\text{CuO}$  cytotoxicity where the ultrafine fraction was more toxic and DNA damage (see Figure 11) <sup>197</sup>. However, pure metals exhibit higher reactivity and cell membrane disruption than oxides <sup>216</sup>, reinforcing the importance of testing with lysosomal fluid to see if leaching occurs in the PAM intracellular fluid compartment <sup>217</sup>.

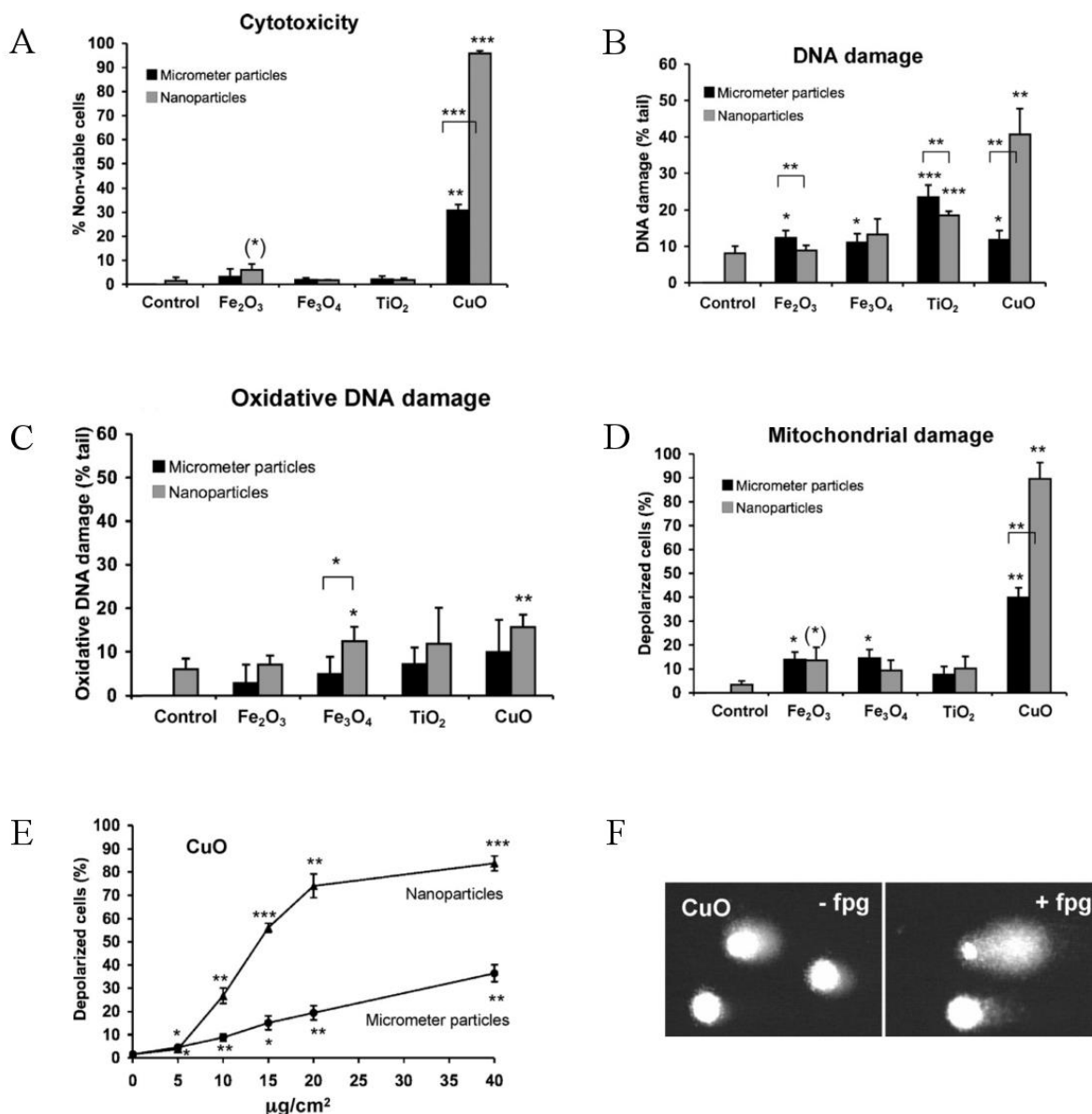


Figure 11: The toxicities of micrometre scale particles (approximately 1  $\mu\text{m}$ ) versus nanoscale particles ( $<0.1 \mu\text{m}$ ) to A549 cells are shown. A: Cytotoxicity after an 18hr exposure at 40  $\mu\text{g}/\text{cm}^2$ ; B: DNA damage after a 4 h exposure at 40  $\mu\text{g}/\text{cm}^2$ ; C: Oxidative DNA damage after 4 h at 40  $\mu\text{g}/\text{cm}^2$ ; D: Mitochondrial damage after a 16h exposure at 40  $\mu\text{g}/\text{cm}^2$ ; E: Dose-response of mitochondrial depolarization to CuO after 4 h at 40  $\mu\text{g}/\text{cm}^2$ ; F: Comet assays showing DNA damage from CuO with and without the Formamido-Pyrimidine DNA Glycosylase (FPG) DNA repair enzyme which forms DNA adducts in the presence of O<sub>2</sub> after 4 h at 40  $\mu\text{g}/\text{cm}^2$ . Adapted from Size-Dependent Toxicity of Metal Oxide Particles – A Comparison Between Nano- and Micrometer Size <sup>197</sup>.

### 2.7.2.3 Assay Considerations and Particulate Interference

Colorimetric metabolic assays such as the MTT and Resazurin assays detect the enzymatic transformation of a substrate by cellular metabolism. These assays do not necessarily distinguish between cellular inhibition and cell death, which may be confirmed by trypan blue staining or the LDH assay for loss of cell membrane

integrity and lysis<sup>218,219</sup>. If long exposure periods are required, media reperfusion and evaporation may make distinguishing small differences in cytotoxicity difficult unless corrected in conventional tissue culture incubations. Furthermore kinetic assays of cell metabolism are not advised with reagents such as MTT due to the formation of cytotoxic crystals<sup>220,221</sup>.

The physiochemical characteristics of PM<sub>10</sub> and PM<sub>2.5</sub> mining dusts interfere with colorimetric assays in a variety of ways. The most apparent interference is through blockage of light over the entire observed spectrum, resulting in false readings. It is also possible that particles catalyse the assay substrate, as demonstrated with diesel particles and MTT, producing formazan which is otherwise indicative of cell metabolism (see Figure 12). Particle adsorption of protein has been shown to be pronounced when assaying soot and oxidised soot particles, resulting in an 85% decline in LDH concentration within 5 minutes at 46 µg/mL<sup>166</sup>. Adsorption of media proteins during incubation may also affect cell growth, although for ultrafine metal oxides this effect becomes significant only at concentrations over 1 mg/mL<sup>149</sup>. Methods of circumventing particulate-assay interference centre on lowering concentrations, identifying when interference occurs during the assay procedure and appropriate centrifugation and media-transfer steps<sup>165,222</sup>.

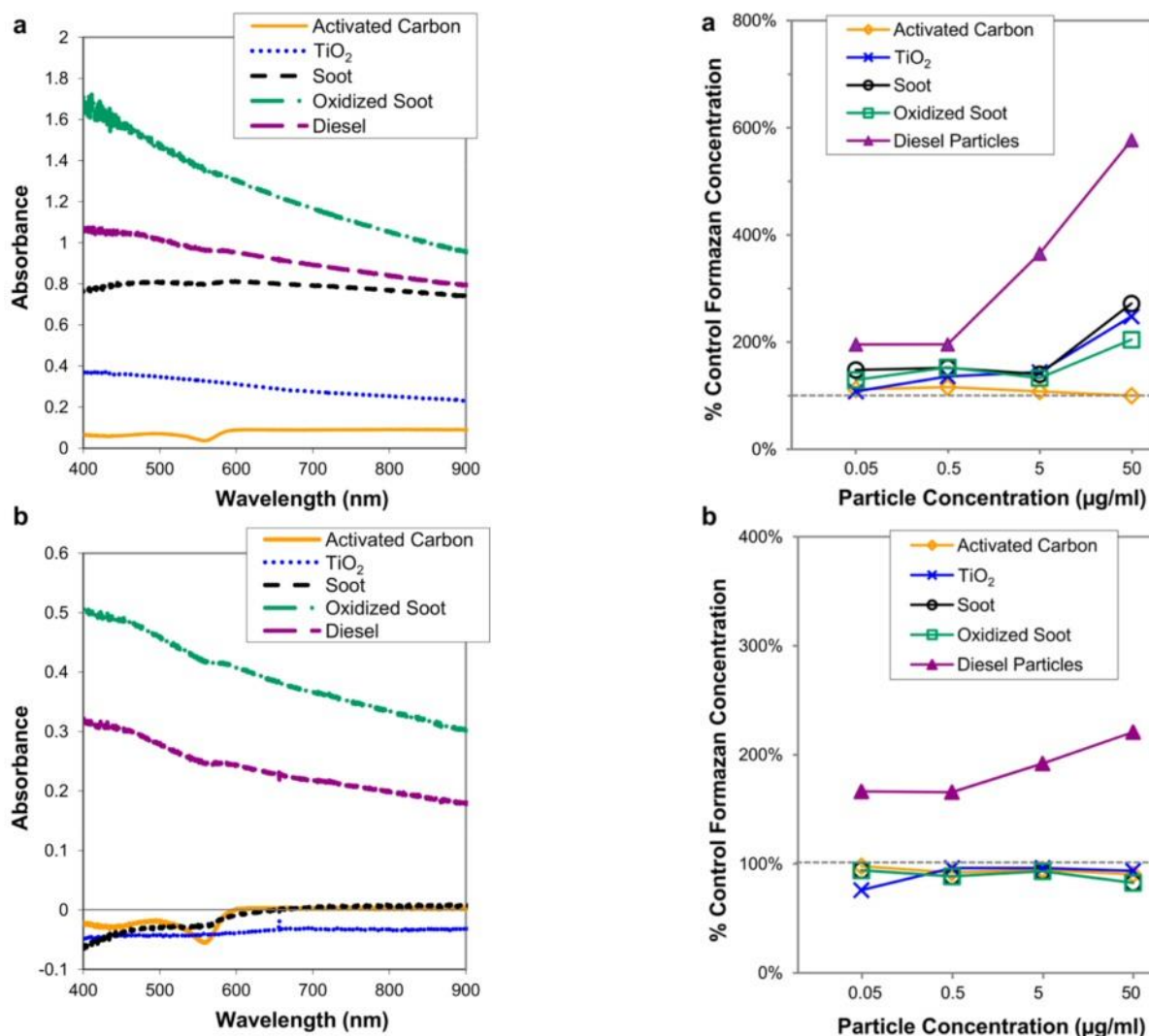


Figure 12: MTT assay interactions with activated carbon, TiO<sub>2</sub>, soot, oxidized soot and diesel particles after 3 h of incubation at 50 µg/mL. a) spectra of particle suspensions and MTT metabolic product (formazan) b) spectra after centrifugation for 10 minutes at 115 g.

#### 2.7.2.4 Reflection of Cytotoxic Outcomes and Pulmonary Pathology

Cytotoxicity may correlate to apoptosis in lung injury and fibrosis, although decreased cytotoxicity does not necessarily indicate milder pathological outcomes. For epithelial, fibroblast and PAM coculture combinations, the immunologically mediated pathways are of particular significance as cell types can differ in their resistance to these signals, and high resistance of fibroblasts to apoptosis is a factor in fibrotic pathogenesis<sup>171</sup>. Incubation of A549 cells with 250 µg/mL ultrafine iron oxide and silica over 72 h was found to induce apoptosis in approximately 15% to 20% of cells measured by annexin V-FITC (green) binding assay<sup>214</sup>. Hyperplasia of Type II epithelial cells is also a pulmonary remodelling response characteristic of

pulmonary disease <sup>139</sup>, implicating increased cell proliferation to be as much a hallmark of disease processes in the lungs as cytotoxicity. Given the complexities affecting cytotoxicity, unexpected results should be expected but investigated, and always accompanied by other cellular endpoints.

### 2.7.3 Immune Mediated Clearance

#### 2.7.3.1 *Physiology of PAM-Mediated Particle Clearance in the Lungs*

Mechanisms of insoluble particulate matter clearance from the tracheobronchial tree differ in the upper respiratory tract and conducting airways to the acinar surfaces. In the upper respiratory tract, the airways are lined with ciliated epithelium which impels a thick, dual-phase mucous fluid layer towards the oropharynx. The cilia move within a low-viscosity hypophase mucosal layer, on which rests a high-viscosity epiphase layer, responsible for removal of most particulate matter from this region. In the bronchioles the bronchioalveolar fluid is composed of only the low-viscosity component and has surfactant properties. The non-ciliated acinar surfaces of the lungs depend on PAM to return particulate matter to the mucociliary escalator, otherwise particles may be collected by PAM after migration into the interstitial spaces and moved to the lymphatic system. Failing this, particles may enter the capillary vasculature spontaneously – particles < 10 nm may diffuse through the air-blood barrier directly <sup>24</sup>.

An experiment on healthy volunteers inhaling 0.2 µm radiolabelled sulphur colloid aerosol found at 100 minutes post exposure macrophage recruitment peaked at 92% of immune cells in sputum, the remainder being neutrophils, monocytes and lymphocytes. It was found that after 40 minutes, collection of sputum cleared ~ 50% of the PM load, although remaining particles had a long half-life <sup>223</sup>. This long-term retention of particles is associated with the proportion of particles which enter the acinar surfaces of the lungs and are not phagocytosed; while there is rapid mucociliary clearance of PM within 48 h, particles which have not been cleared are sequestered. The mechanism of this sequestration is not fully understood but may be related to immobilized particle-laden macrophages in connective tissue, lymphoid foci and other areas <sup>27</sup>. Specifically, ~ 60 % of inhaled fused aluminosilicate particles < 4 µm in were found to be retained in the lungs of healthy volunteers after 7 days,

with a second clearance phase then following a much longer half-life of ~ 500 days<sup>25</sup>.

#### *2.7.3.2 Cellular Mechanisms of PAM-Mediated Particle Clearance*

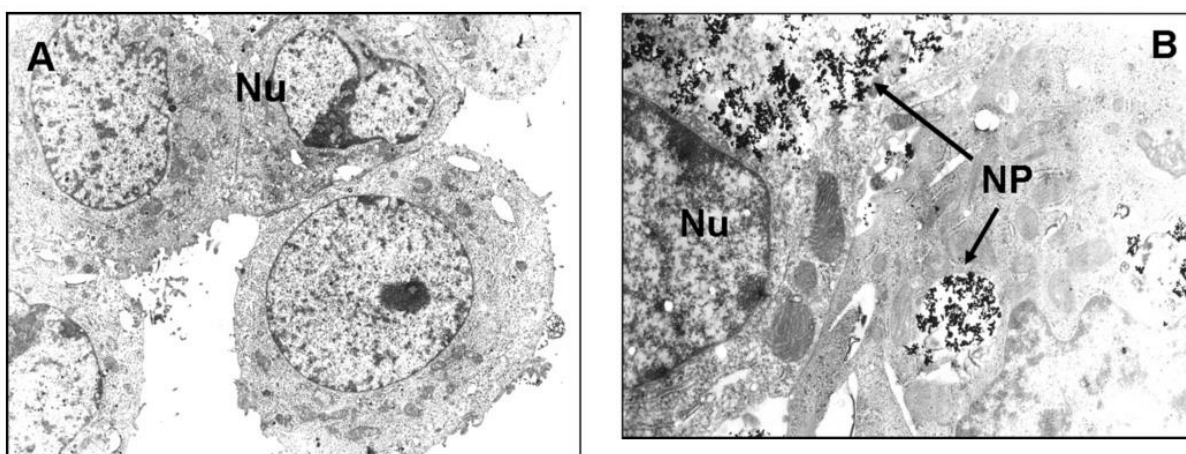
PAM, which typically measure ~ 12  $\mu\text{m}$ , can engulf particles slightly larger in diameter than themselves, a process enhanced by opsonisation<sup>30</sup>. The frequency macrophages associate with particles drops with increasing particle size from 300 nm to 3  $\mu\text{m}$ , slowing clearance of larger particles<sup>224</sup>. The PAM pool of the lung respiratory surfaces have a limited capacity to clear particulates based on maximum carrying volume per cell (~ 60  $\mu\text{m}^3/\text{PAM}$ <sup>22</sup>). Lung overloading also slows down particle clearance, and if severe creates an inflammatory cycle of apoptosis and recruitment<sup>225</sup>, and cessation of clearance at ~ 600  $\mu\text{m}^3/\text{PAM}$ <sup>22</sup>. The most significant problem in overload conditions is the dramatic increase in PAM sequestered particle translocation to the interstitial space, encouraging the development of interstitial granulomas<sup>18,33,226</sup>. In an animal study of ultrafine (20 nm) and fine (250 nm)  $\text{TiO}_2$  particles, it was found that while particle retention in the alveolar spaces was similar between the particle sizes, ultrafine  $\text{TiO}_2$  exhibited increased interstitial retention, inflammatory activity, greater induction of Type II alveolar epithelial cell proliferation and greater total PAM recruitment to the alveolar surfaces during the exposure phase<sup>194</sup>.

#### *2.7.3.3 Intracellular Interactions between PAM, Epithelial Cells and Particles*

The intracellular fluid compartment represented by macrophages has properties distinct from bronchioalveolar fluid, attacking particles at an acidity of pH 4.5. A study of metal and metalloid solubility using ambient  $\text{PM}_{10}$ ,  $\text{PM}_{2.5}$  and  $\text{PM}_1$  acquired from a high-volume sampler found Pb, Cu, As, V and Sb trace metals were markedly more liable to leaching in artificial lysosomal fluid than Gamble's solution, increasing bioavailability of metal ions<sup>217</sup>. Dissolution can be significant and rapid. Ultrafine ZnO will not dissolve in bronchioalveolar fluid at pH 7.4, but dissolution of ~ 90% of the ZnO mass occurs within 24 h of exposure to artificial lysosomal fluid<sup>204</sup>.

The intracellular accumulation of ultrafine metal-oxides by in lung epithelial cell lines has been demonstrated by Transmission Electron Microscopy (TEM) using A549,

with observations as short as 6 h post-exposure showing translocation of  $< 100$  nm  $\text{TiO}_2$  into the cell cytoplasm <sup>227,228</sup> (see Figure 13). This is larger than  $< 10$  nm size limit thought to allow diffusion through the alveolar epithelium, indicating pinocytosis of particles. Ingestion of quartz particles  $< 2$   $\mu\text{m}$  in size by A549 cells has also been observed <sup>229</sup>. Epithelial particle ingestion is theorised to play a significant role in particle migration to the interstitial space, and is enhanced under conditions of lung overload <sup>229</sup>.



**Figure 13: TEM images of A549 cells, x80000 zoom. A: Unexposed cells; B: TEM image demonstrating  $\text{TiO}_2$  nano-particle uptake at  $100 \mu\text{g/mL}$ . Nu denotes the nucleus, NP denotes the particle <sup>227</sup>.**

## 2.7.4 Inflammatory Signalling and Fibrosis

### 2.7.4.1 Cytokines in the Genesis of Fibrosis

Inflammation and tissue remodelling are tightly linked processes in the repair of lung injury, and the disruption of homeostasis between these processes by chronic exposure to mining dusts greatly increases the likelihood of lung fibrosis; the pathological growth of connective scar tissue with an accumulation of fibroblasts and a reduction or elimination of the epithelium <sup>171</sup>. Failure of the immune system to resolve inflammatory processes, or hypersensitive induction of inflammatory processes, are thought to underlie most kinds of fibrosis, including those with idiopathic, autoimmune and foreign material causes. The lung presents as two distinct immunological environments, where inflammation in either is not necessarily intertwined; the bronchial space where inflammation from asthma and bronchitis does not cause changes in the lung interstitium, and the pulmonary space where

interstitial inflammation such as sarcoidosis does not affect the bronchial wall. These compartments are independently vascularised <sup>140</sup>.

During pulmonary inflammation from PM<sub>10</sub> and PM<sub>2.5</sub>, epithelial and macrophage cytokine signalling drive the rapid recruitment and activation of monocytes, granulocytes and lymphocytes. Once cells are recruited, the signalling environment of lungs during becomes complex, creating cytokine networks which under dysregulated chronic inflammatory conditions initialise pulmonary fibrosis. It is postulated that there are at least two kinds of effector cytokine networks involved, Type 1 (non-fibrotic) and Type 2 (fibrotic). In Type 1 inflammation, IFN- $\gamma$  expression leads to mononuclear cell activation, clearing the antigen while mediating antiproliferative and antifibrotic effects. In Type 2 inflammation, IL-4/IL-3 expression leads to effector cell activity encouraging fibroproliferation and matrix deposition <sup>230</sup>.

A wide variety of cytokines drive cell migration, activation, proliferation, apoptosis and extracellular matrix deposition (see Table 9). Particles contacting lung epithelial cells are found to influence the expression of interleukins IL-8 (also known as CXCL8) and IL-6 which have pro-inflammatory and anti-inflammatory effects, respectively, as well as C-Reactive protein and TNF $\alpha$  <sup>231</sup>. Macrophages can also express these interleukins. Increased expression of IL-8 is found in patients suffering from idiopathic pulmonary fibrosis and is chemotactic to neutrophils <sup>29</sup>. Neutrophils do not normally account for a large fraction of cells in bronchioalveolar fluid, however exposure to PM<sub>10</sub> *in-vitro* has been shown to allow neutrophils to accumulate and make up to 15% of cells in bronchioalveolar fluid within 6 h <sup>232</sup>.

Comparisons of PM<sub>2.5</sub> metal-oxides against nanoparticle metal-oxides (Al<sub>2</sub>O<sub>3</sub>, CeO<sub>2</sub>, Fe<sub>2</sub>O<sub>3</sub>, NiO, SiO<sub>2</sub> and TiO<sub>2</sub>) in bronchial epithelial cells have been shown to elicit weak IL-6 and IL-8 expression changes in lung epithelial cells at concentrations where there is no significant cytotoxicity with the exception of micron and nano SiO<sub>2</sub>. A 3-fold induction of IL-8 resulted from SiO<sub>2</sub> exposure at 58  $\mu\text{g}/\text{cm}^2$ , while IL-6 expression was nominal. However, it was demonstrated that low serum concentration below 3% allowed nanoparticle interference to deplete the concentration of an IL-6 standard significantly, raising questions about the accuracy of low induction results <sup>233</sup>. Other studies have shown epithelial cell production of



both IL-8 and IL-6 in response to silica particles being strongly induced<sup>229,231,234</sup>, while coculture with macrophages has been shown to further enhance IL-8 expression. In these cocultures, epithelial cell cytokine expression appears to be regulated by macrophage expression of IL-1 $\beta$ , rather than TNF $\alpha$ <sup>234,235</sup>. Mineral PM<sub>10</sub> induction of cytokine expression in macrophages has been shown to occur independently of apoptotic potential, depending on mineral composition<sup>206</sup>.

Table 9: The effects of cytokines in lung tissues, cytokine network type given where available

Cytokine	Effects in Lung Tissue	Type <sup>230</sup>
<b>PGE<sub>2</sub></b>	Anti-inflammatory <sup>140</sup>	
<b>TGF-<math>\beta</math>1</b>	Anti-inflammatory. Myofibroblast resistance to cell death <sup>236</sup>	
<b>TNF<math>\alpha</math>/TNF</b>	Pro-inflammatory responses, regulation of neutrophil chemotaxis (adhesion molecule ICAM-1 and Eselectin upregulation) <sup>140</sup> , associated with macrophage activation <sup>183</sup> , induction of apoptosis, induction of matrix metalloproteinases <sup>237</sup> , eosinophil recruitment <sup>238</sup>	
<b>Type I IFN</b>	Associated with macrophage activation <sup>183</sup>	
<b>IGF-1</b>	Proliferation of fibroblasts and myofibroblasts, increased collagen matrix synthesis <sup>239</sup>	
<b>IFN-<math>\gamma</math></b>	Macrophage priming <sup>183</sup> , suppression of IGF-1 and fibroblast proliferation and activity <sup>239</sup>	Type 1
<b>IL-1</b>	Regulation of neutrophil chemotaxis (adhesion molecule ICAM-1 and Eselectin upregulation) <sup>140</sup>	
<b>IL-1<math>\beta</math></b>	Associated with macrophage activation <sup>183</sup> , pro-inflammatory responses, collagen deposition, fibroblast proliferation <sup>29</sup> , A549 cell migration, induction of matrix metalloproteinases <sup>240</sup>	
<b>IL-1ra</b>	Down-regulation of neutrophil chemokine MIP-2 <sup>183</sup>	
<b>IL-4</b>	Activation of granulocytes in allergy <sup>140</sup> , stimulation of IGF-1 <sup>239</sup>	Type 2
<b>IL-5</b>	Activation of granulocytes in allergy <sup>140</sup>	

<b>IL-6</b>	Anti-inflammatory <sup>140</sup> , inhibition of fibroblast proliferation <sup>241</sup> , epithelial response to fine particles <sup>233</sup>	
<b>IL-8</b>	Neutrophil chemotactic <sup>29,185</sup> , epithelial response to fine particles <sup>233</sup>	
<b>IL-10</b>	Inhibition of granuloma formation and Th1 recruitment <sup>242</sup> , opposes inflammatory action of TNF, activated during fibrosis <sup>243</sup> , suppression of Type 1 cytokines <sup>230</sup>	Type 2
<b>IL-13</b>	Macrophage priming <sup>183</sup> , stimulation of IGF-1 and fibroblast proliferation and activity <sup>239</sup>	Type 2
<b>IL-12</b>	Inducer of IFN- $\gamma$ <sup>244</sup>	Type 1

#### 2.7.4.2 Modelling Fibrosis

Fibrosis as a result of high ambient PM inhalation or high occupational exposures often takes years to develop. Bleomycin induced lung injury is often used to model interstitial fibrosis, and develops rapidly *in-vivo*; increased collagen deposition is visible 8 days after exposure in histologically stained lung sections <sup>245</sup>. Dendritic cells and macrophages have been suggested to play key roles in bleomycin induced fibrosis, and other forms of fibrosis. Dendritic cells accumulate in fibrotic diseases and may drive damaging effector cell activity in the lungs, as the fibrotic response to bleomycin diminishes when dendritic cells are inactivated *in-vivo* <sup>246</sup>. Mice deficient in macrophage colony-stimulating factor (M-CSF), or treated with IL-12 (an IFN- $\gamma$  inducer) also experience diminished fibrotic response to bleomycin <sup>171,244</sup>. When used *in-vitro*, bleomycin has been shown to cause lung epithelial cell apoptosis, as modelled by A549 cells, as a result of increased free radical production. This damages mitochondrial DNA and nuclear DNA <sup>247</sup>.

#### 2.7.4.3 Tissue Remodelling During Fibrosis

Tissue remodelling during fibrosis involves proliferative and apoptotic processes that create non-functional scar tissue in place of healthy pulmonary tissue. Accumulation of immune cells is accompanied by cellular apoptosis of the alveolar epithelium Type I cells and hypertrophy of Type II cells, characterising denudation of the alveolar surface. Meanwhile, collagenases and matrix metalloproteases degrade the extracellular matrix allowing it to be reshaped by fibroblast activity which respond to

inflammatory signals by resisting apoptosis, causing remodelling of the interstitium<sup>171</sup>, and enhanced epithelial cell migration<sup>248</sup>. The expression of IGF-1 and TGF- $\beta$ 1 by macrophages and monocytes is known to activate fibroblast anti-apoptotic pathways and induce production of matrix metalloproteases<sup>239,249</sup>. The leakage of plasma into damaged alveoli containing lysophosphatidic acid may activate fibroblast migration into the alveolar spaces during fibrosis. Mice deficient for the lysophosphatidic acid-1 G-coupled receptor, which is expressed on the alveolar epithelium, were less affected by bleomycin induced fibrosis than control<sup>250</sup>.

#### 2.7.4.4 *Signalling Models*

The role of the macrophage is multifaceted, and depends upon the mode of activation. Once circulating monocytes are attracted to the site by cytokines and chemokines, they differentiate into macrophages and are activated by a range of factors; immune complexes, lymphocytes, damaged extracellular matrix, opsonised particles and bacterial moieties. The method of activation determines the 'type' of resulting macrophage (see Table 10). Classically activated macrophage types tend to express higher levels of cytokines and chemokines, and generate more free radicals. This leads to apoptotic cell death, anti-microbial activity, phagocytosis of opsonised particles and immune complexes and matrix degradation. Alternatively activated macrophages tend to express anti-inflammatory cytokines. This leads to matrix stabilisation, cell survival and proliferation, angiogenesis and antigen presentation. Both classically and alternatively activated macrophages show enhanced phagocytosis of debris and apoptotic cells. In progressive fibrosis, classically activated macrophages are implicated in causing excess apoptosis. Excess or prolonged activity of alternatively activated macrophages is implicated in TGF- $\beta$ 1 mediated fibrosis<sup>251</sup>.

Table 10: Factors stimulating either classical or alternative macrophage activation <sup>251</sup>.

<b>Mφ activation</b>	<b>Stimulus</b>
<b>Classical</b>	IFN-γ
	Bacterial lipoproteins (TLRs)
	Bacterial DNA (TLRs)
	Parasitic proteins/carbohydrates (TLRs)
	Opsonized particles (FcR, CR)
	Hypoxia
	Abnormal matrix
<b>Alternative</b>	IL-4
	IL-10
	IL-13
	TGF-β
	Glucocorticoids

The balance of macrophage activation states is important in the coordination of the overall inflammatory response, having downstream effects on both immunological and parenchymal cell types in the lungs. After acute inflammatory activity, macrophages must inhibit neutrophil and monocyte chemotaxis and initiate parenchymal repair processes. These include repair of gaps in the acinar epithelium, stabilisation of connective tissue and angiogenesis <sup>183</sup> (see Figure 14).

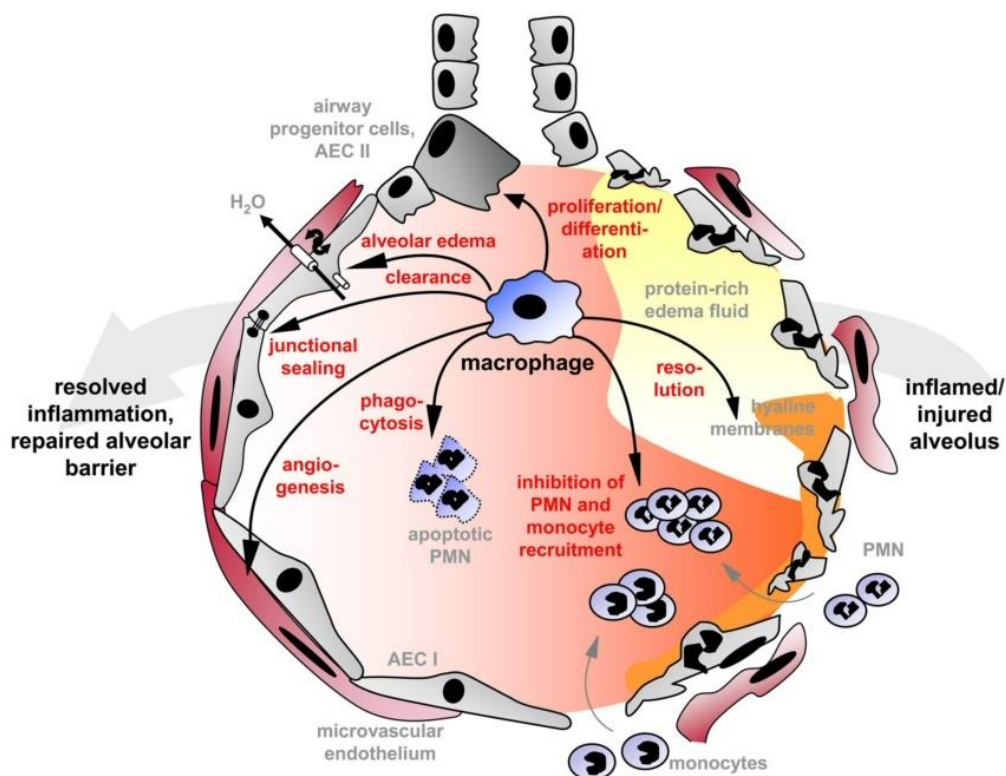


Figure 14: Targets of macrophage participation in the termination of acute inflammatory activity and coordination of repair processes in the pulmonary acinus. Recruitment of polymorphonuclear cells (PMN) such as neutrophils and monocytes such as macrophages is inhibited and cell proliferation and repair processes are activated<sup>183</sup>.

### 2.7.5 Free Radical Generation

Particulate air pollution has repeatedly been shown to increase alveolar epithelial cellular oxidative stress *in-vitro*, and this is linked with increased TNF $\alpha$  expression peaking in the short term (5 h) and increased IL-6 expression peaking in the longer term (72 h)<sup>252</sup>. Decreased concentration of the antioxidant glutathione has also been observed *in-vivo* in response to intratracheal PM<sub>10</sub> instillation in as little as 6 h<sup>232</sup>. Redox imbalance can occur in a variety of ways, both directly due to particle chemistry and surface interactions, and from oxidative bursts by macrophages as part of their antimicrobial defenses which may vary depending on particle surface characteristics<sup>195</sup>. The overall redox imbalance on cells ranges from insults that can be resolved spontaneously, to irreversible cellular DNA damage and ultimately cell death (see Figure 15)<sup>66</sup>.

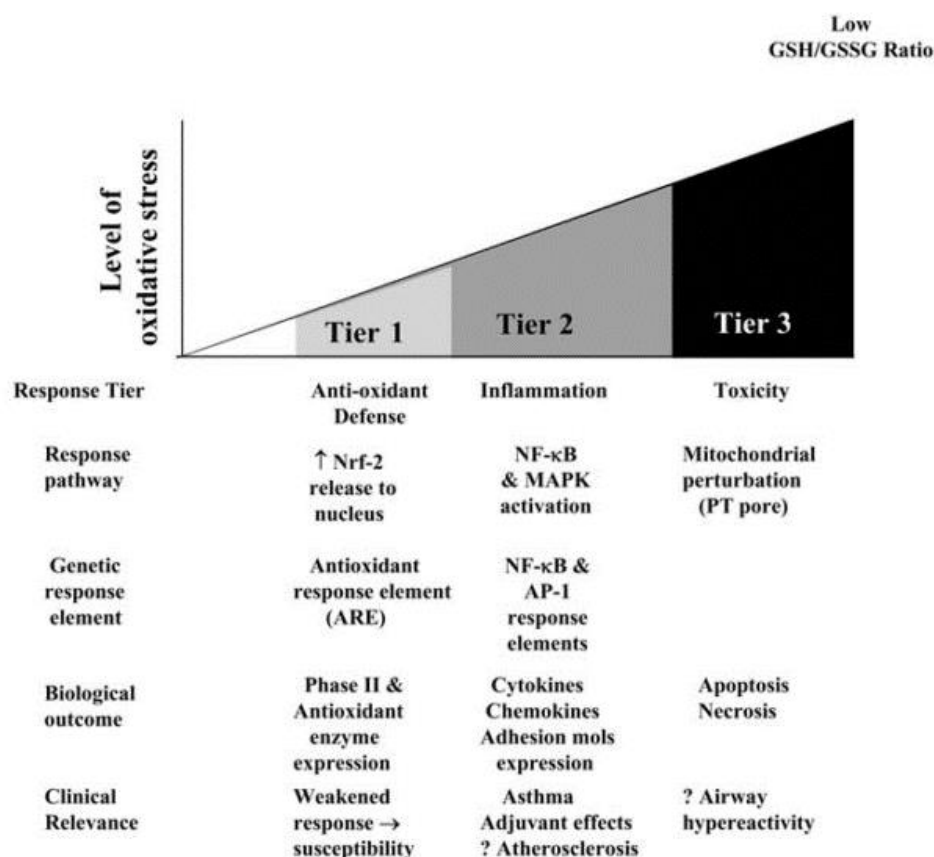


Figure 15: Hierarchical oxidative stress model showing response tiers related to PM exposure. (Tier 1) Antioxidant enzyme activity restores cellular redox homeostasis. (Tier 2) Proinflammatory responses are induced. (Tier 3) Cellular apoptosis-necrosis is induced. GSH (Glutathione); GSSG (Oxidized Glutathione); NF-κB (Nuclear Factor κB); MAPK (Mitogen Activated Kinase); AP-1 (Activator protein 1) <sup>66</sup>.

The nature of contact between particulate matter and epithelial cell membranes likely makes lipid peroxidation an important player in cellular membrane disruption and cytotoxicity. It has been proposed that cell membrane interference activates the protein MKK1 which stimulates an ERK1,2 cascade activating both cPLA1 and sPLA1 proteins, hydrolyzing phospholipids and producing arachidonic acid. This in turn is an additional source of cellular redox imbalance <sup>253</sup>. However, measurements of free radical damage should extend beyond the Thiobarbituric Acid Reactive Substances (TBARS) test for lipid peroxidation to other oxidation products <sup>254</sup>.

Metal-oxides with low cytotoxic effect are also shown to increase oxidative stress, which is associated with microvascular and endothelial permeability <sup>255</sup>. For fine ZnO particles, free radical generation and DNA oxidation has also been cited in lung epithelial cells as the leading toxicological endpoint, and distinctly mediated by the oxide compound whereas equivalent Zn<sup>2+</sup> exposure resulted in less redox activity <sup>192</sup>.

A study on the differential effects of fine and ultrafine TiO<sub>2</sub> particles on RAW 264.7 rat macrophage cells found no significant difference in cytotoxicity between 0 and 200 µg/mL suspensions of the particles after 24 h, however 1.5 to 2.5 fold inductions of free radicals were observed at 4 h <sup>218</sup>. Free iron ions in inhaled particulate matter, Fe<sup>2+</sup> and Fe<sup>3+</sup>, are found to increase hydroxyl radical production and DNA oxidation products through the Fenton reaction:



The presence of metal-oxides and free transition metal ions therefore presents a source of oxidative stress in addition to free radicals associated with inflammation, and may be complicated by cross-reactivity in transition metal mixtures as found in particulate matter <sup>256–259</sup>. However, results may vary depending on the type of oxidative stress assay employed. Using iron oxide and silica ultrafines on A549 cells, dihydrodichlorofluorescein diacetate (H<sub>2</sub>DCF-DA) assay fluorescence was found to only differ by only ~5% from 126-600 µg/mL <sup>214</sup>, while comparisons between ultrafine TiO<sub>2</sub> and fine silica also observed little difference up to 200 µg/mL <sup>227</sup>. It is important to note that the H<sub>2</sub>DCF-DA assays requires either activity by cytochrome c, or both the presence of H<sub>2</sub>O<sub>2</sub> and redox-active transition metals such as iron ions <sup>260</sup>. A study comparing ultrafine TiO<sub>2</sub> effects on fibroblast redox balance found greater sensitivity; concentrations of 300 µg/mL increased H<sub>2</sub>DCF-DA assay fluorescence 50% and depleted glutathione by 25% compared to control. Between 3-600 µg/mL, GSH levels responded in the clearest dose-dependent fashion <sup>261</sup>.

The downstream effects of redox imbalance and resulting oxidative stress initiate cellular responses, affecting overall gene expression within the cell (see Figure 16). It is proposed that ultrafine particle stimulation of oxidative stress can cause disruption of redox homeostasis resulting in positive feedback, as intracellular Ca<sup>2+</sup> both signals macrophage superoxide radical and nitric oxide production and is increased by these free radicals. The expression of TNFα may also be indicative of intracellular Ca<sup>2+</sup> concentration <sup>262</sup>.

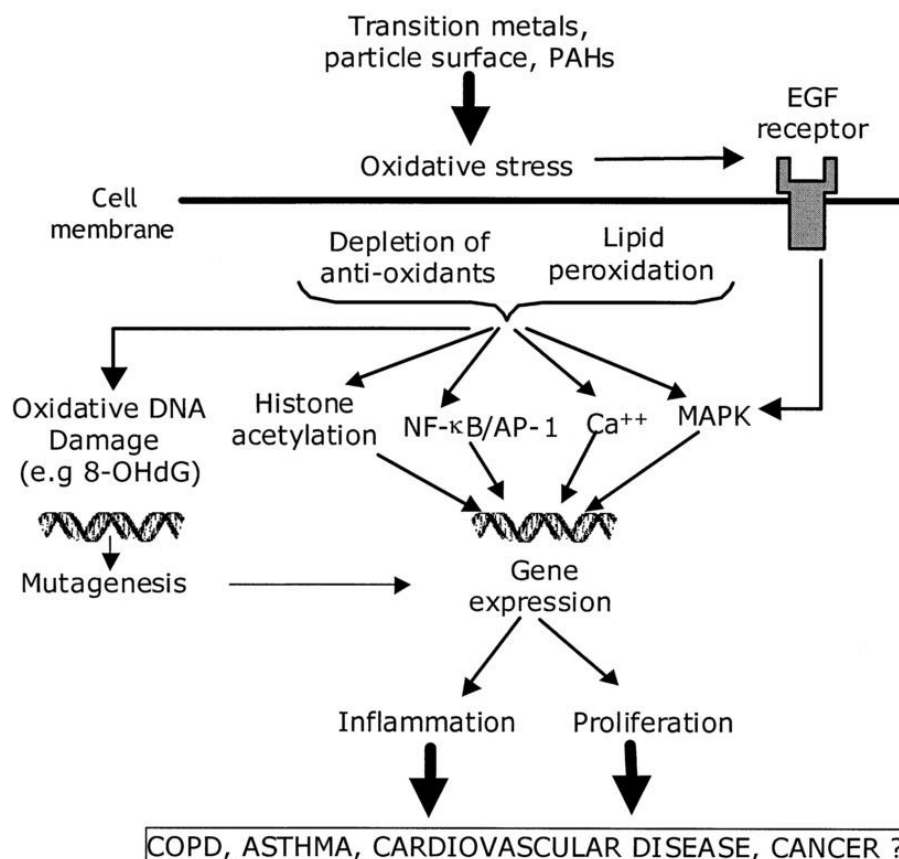


Figure 16: The proposed effect of transition metals and Polycyclic Aromatic Hydrocarbons (PAH) combustion products on cellular redox homeostasis and gene expression. Increased inflammation and cell proliferation may affect chronic obstructive pulmonary disease (COPD), asthma, cardiovascular disease and cancer <sup>262</sup>.

### 2.7.6 Genotoxicity and Carcinogenicity

Genotoxicity bioassays determine a cell's ability to successfully replicate and indicate whether a toxin is mutagenic, carcinogenic or both. Oxidative potential and free radical generation are genotoxic mechanisms, and genotoxicity can similarly be tested by acellular assays as well as *in-vitro* and *in-vivo*, with the added possibility of biomarker studies in humans. Genotoxicity can therefore occur directly because of particle inhalation (primary), or as a result of inflammation (secondary). Therefore, any particle resulting in an inflammatory response, especially those arising from NF-κB regulated pathways, may cause secondary tumours to develop, but some particles may have a primary genotoxic component which can manifest at a low or sub-chronic dose <sup>136,201</sup> (see Figure 17).



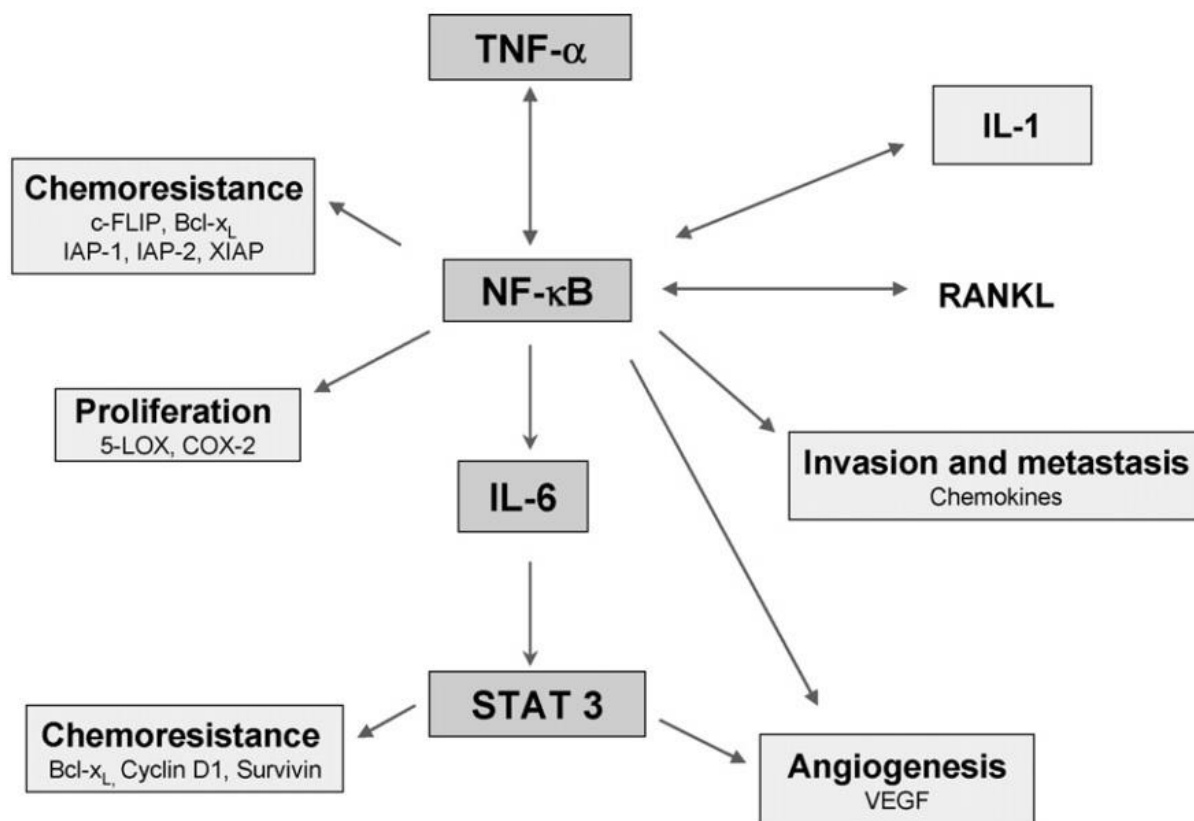


Figure 17: Inflammatory networking in cancer. Cytokines dependent on NF-κB activation pathways are involved in numerous cancer pathways, including genes conferring chemoresistance and increased proliferation and metastatic ability <sup>161</sup>.

As reviewed by Borm et. al. <sup>118</sup>, it has been shown that poorly soluble particulates such as TiO<sub>2</sub>, carbon black and coal mine dust can cause tumours *in-vivo*. While fibrosis is considered a precursor of lung cancer, it has been shown that tumours arise independently. Furthermore, the type of squamous tumour appeared to differ in frequency based on particle size and particle type. The observed tumours were squamous cell carcinoma (SCC), non-keratinizing non-cystic tumour (NKCT), squamous keratinizing cyst (SKC), bronchio-alveolar carcinoma (BAC) and bronchioalveolar adenoma (BAA). Amorphous silica was found to be largely non-tumorigenic. Fine TiO<sub>2</sub> caused mostly SCC, SKC and BAA in mostly equal measure that showed a dose-response relationship. Ultrafine TiO<sub>2</sub> exposure resulted in SKC, BAA and BAC but these did not appear to follow a strong dose-response relationship. However, SCC maintained a dose-response relationship increasing with increasing specific-surface area dosed, in line with fine exposures. Fine carbon black showed a strong dose-response relationship from BAA and BAC, but SKC and SCC responses, while induced, were not as clear. Ultrafine carbon black did not result in a

clear dose-response relationship for any of SKC, SCC, BAA or BAC and seldom resulted in NKCT. Taken together, the results between fine and ultrafine particles indicate there are either problems in dosing ultrafines accurately *in-vivo*, or other effects are at play such as particle agglomeration or particle redistribution away from the interstitial spaces. Despite this, it is informative that insoluble fine inorganic particles are tumorigenic <sup>118</sup>.

In a study of ultrafine anatase TiO<sub>2</sub> and Fe<sub>2</sub>O<sub>3</sub>, intracellular uptake was observed in fibroblasts and bronchioepithelial cells, but not nuclear, mitochondrial or ribosomal uptake. It was found that lung fibroblasts were more sensitive to cytotoxic and genotoxic effects from both particle types. The mechanism of action for TiO<sub>2</sub> appeared to be through generation of free radicals, while Fe<sub>2</sub>O<sub>3</sub> was able to cause DNA strand breaks directly at concentrations of 50 µg/cm<sup>2</sup> in both fibroblasts and bronchioepithelial cells, but required reducing conditions to generate high levels of free radicals <sup>169</sup>.

The measurement of gene expression profiles is also informative of cellular response pathways to particulate matter, providing information about the mode of toxicity and defense mechanisms employed by the cell. One study has found that environmental PM<sub>10</sub> particles and metal-oxide standards differentially induce cytokine and chemokine gene expression based on particle source, size and composition, and that fine particles did not induce changes in gene expression, using bronchial epithelial cells <sup>231</sup>.

It has been shown that environmental PM<sub>2.5</sub> and PM<sub>10</sub> increase the expression of *fos/jun* family proto-oncogenes involved in sarcoma and non-small cell lung carcinomas several fold. Over a 2 h time period, gene expression was most elevated in lung epithelial cells exposed to PM<sub>2.5</sub>, however over a 24 h time period, gene expression was most elevated in cells exposed to PM<sub>10</sub> <sup>263</sup>.

#### 2.7.7 Relationship of Pulmonary Models with Cardiovascular Models *In-Vitro*

Many epidemiological studies have associated PM inhalation with increased cardiovascular risks, indicating it as one of the most important risk factors for

population health at ambient concentrations alongside pulmonary and cancer risks. Furthermore, these risks are evident at much lower concentrations than previously believed possible<sup>90</sup>. Estimates vary, however many studies show a 1% or greater increase in relative risk of cardiovascular mortality per 10  $\mu\text{g}/\text{m}^3$  of daily ambient  $\text{PM}_{10}$  exposure, although some studies on  $\text{PM}_{2.5}$  indicate the risk to be as high as 14%<sup>15,73</sup>.

Bai et al.<sup>264</sup> have identified from the literature five biological pathways to mechanistically explain the association of ambient  $\text{PM}_{10}$  exposure to cardiovascular outcomes; 1) the systemic effects of pulmonary inflammation affecting the vasculature, 2) ultrafine fraction translocation to the vascular and activation, 3) generation of free radicals which enter circulation and affect cardiac function, 4) interference of endothelial function by inflammatory mediators or soluble components of PM, 5) cardiac function changes altered by central nervous system response to  $\text{PM}_{10}$ <sup>264</sup>.

Of the pathways identified, *in-vitro* endpoints discussed in this review are informative of aspects in pathways 1 (PAM and inflammatory endpoints), 2 (particle size endpoints), 3 (free radical generation and oxidative stress endpoints), and 4 (solubility endpoints). Therefore in screening  $\text{PM}_{10}$  sources for pulmonary toxicity and fibrogenicity, samples with high activity in these pathways may also be identified as warranting specific investigation against cardiovascular endpoints.

During inflammation, high alveolar permeability allows pro-inflammatory factors to enter the blood stream and cause endothelial dysfunction in the vasculature and hypercoagulability of the blood which has follow-on negative effects on heart function and health, such as increased risk of infarction<sup>73</sup>. This may also be directly mediated by particle uptake into the lungs and into the circulatory and lymphatic systems<sup>164</sup>.

Well-designed comparative *in-vitro* models must be able to distinguish the nuances of inflammatory and oxidative stress markers which indicate systemic effects able to reach the heart. As the differential influence these factors have on cardiovascular risk has not been quantified, *in-vivo* validation would be required to extrapolate cardiovascular risk from a chosen lung parenchyma model. However, there is clearly

utility for vascular epithelial and myocardial cell lines in addition to erythrocyte lysis and blood coagulability tests.

## 2.8 Discussion

Without a satisfactory mechanistic understanding of why  $PM_{10}$  and  $PM_{2.5}$  influence morbidity and mortality, epidemiologists have begun to pursue ultrafine particulate fractions, supported by some evidence that  $PM_{2.5}$  health impact correlations are stronger than  $PM_{10}$ , and that  $PM_{2.5}$  is dominated by a variety of toxic combustion products in urban environments. However, differential effects between  $PM_{10}$  and  $PM_{2.5}$  do exist, and  $PM_{2.5}$  correlations are not universally accepted as more powerful<sup>49,51,53,62,89,189</sup>. This is especially evident from the pulmonary morbidity associated with increases in coarse fraction mineral  $PM_{10-2.5}$  during dust storms<sup>60,61</sup>, which have similarities to mining dusts. This is a key insight that gives weight to the need for specific monitoring of  $PM_{10}$  produced at different mining sites. Given the knowledge  $PM_{10}$ ,  $PM_{2.5}$  and ultrafine particles have different kinds of interaction with the lungs, it becomes apparent that all three fractions have a place in the monitoring paradigm and cannot yet replace one another.

Environmental regulators around the world are currently in a difficult position. There is increased pressure for risk assessment vs. screening, and the lowest effect levels to ensure the public is free of risk have been determined as extremely low or non-existent. Furthermore the validity of a linear dose-response relationship which is somewhat interpolated from epidemiological studies requires a mechanistic understanding to validate, yet in the past inflection points of reduced proportionality of risk for particles such as smog above a certain concentration have been observed<sup>195</sup>. These considerations raise the question of what 'acceptable' public risk is in the face of increasing compliance costs. It is therefore imperative that *in-vitro* toxicology techniques be marshalled for effective bulk data generation to aid risk assessment in monitoring effect levels on a source-apportioned basis.

While occupational exposure limits exist, they cannot be directly applied to AAQS due to differences in design; such safety standards assume a minimum level of employee personal protective equipment be worn, that employees are not of rare but

vulnerable- population groups and that exposures be time-weighted, following the work week schedule. They do however make excellent points of comparison for poorly-soluble metal-oxide dusts.

It is clear that PM<sub>10</sub> and PM<sub>2.5</sub> inhalation present risks to health through many different mechanistic pathways, none of which may clearly dominate overall due to interdependencies<sup>15</sup>. In determining the factors relevant to *in-vitro* determination of PM<sub>10</sub> and PM<sub>2.5</sub> toxicity, inter-study variability is a distinct problem which further cloud the nature of these interdependencies. Differences in sample preparation, particle size-distribution, crystallinity and dosing metrics can make *in-vitro* comparisons complicated, even when the same compounds, cell types and assays are being used<sup>34</sup>. Standardisation is the greatest strength of *in-vitro* experiments, yet the field of particulate toxicology has had a difficult time in validating results *in-vivo* well enough to settle upon standards<sup>173</sup>.

Critical questions that must be answered to resolve these difficulties centre on whether the impacts of PM<sub>10</sub> and PM<sub>2.5</sub> can be predicted using simple tissue culture methodologies, without introducing even greater complexities associated with advanced exposure systems and 3D tissue culture methodologies. More fundamentally this question resides in whether the major *in-vitro* endpoints discussed deliver enough understanding of particulate toxicity, including their relationships with macroscopic pathological outcomes, and how these outcomes are prioritised by concentration of exposure.

A large amount of poorly-soluble metal-oxide toxicity in the lungs can be understood through inflammatory effects, after accounting for more readily determinable cytotoxic/metabolic, genotoxic and oxidative effects from soluble factors. It is therefore important to understand whether 'nuisance' dusts mediate toxicity through a pulmonary alveolar macrophage 'overload' effect and can thus be predicted by acinar accumulation alone, or if overload is not a physiologically relevant concept in humans and inflammatory risks depend on immobilised interstitial accumulation.

Once such mass-load questions are addressed, inflammatory dependencies of specific-surface area exposed naturally follow, as does the importance of surface

crystallinity and related power of oxidative/genotoxic stressors. Measurement of relevant gene expression profiles offer a unique perspective on this problem, where the activation of differential pathways produce unique signatures of many upregulated and down-regulated genes which may survive systematic particle interference effects that cast doubts on traditional endpoints.

The overabundance of cytotoxic mediators in fibrosis occurs in parallel with macrophage inability to resolve inorganic particles load resistant to break-down and detoxification, and indeed toxicants rendered soluble by the phagocytic response. The acidic pH conditions of the lysosome should therefore receive as much, if not more, attention than the surfactant properties of lung fluid, as the particle dispersion paradigm lacks merit on its occurrence *in-vivo* and its relevance to the clearance process.

The cytokine interactions between co-cultures of lung epithelial cells and macrophages presents an opportunity to dissect the inflammatory system within the lungs in greater detail beyond the interleukins typically produced by epithelial cells alone. There are nevertheless many variables to consider, including greater time-course resolution to track acute and longer term inflammatory cytokine release as well as the differential effects of classically and alternatively activated macrophages. The ratios between cytokine expression networks are also important, as it appears that while suppression of anti-inflammatory cytokines enhances alveolar damage, over expression of anti-inflammatory cytokines in the longer term may be a principle mediator of fibrotic cell proliferation – which is less intuitive.

Based on the information collected, we propose *in-vitro* methodologies may be able to discern toxicity of poorly-soluble particulate matter comparatively to materials with occupational exposures that have similar physical variables, following a hierarchy of effects which terminate in dominant health outcomes (see Figure 18).

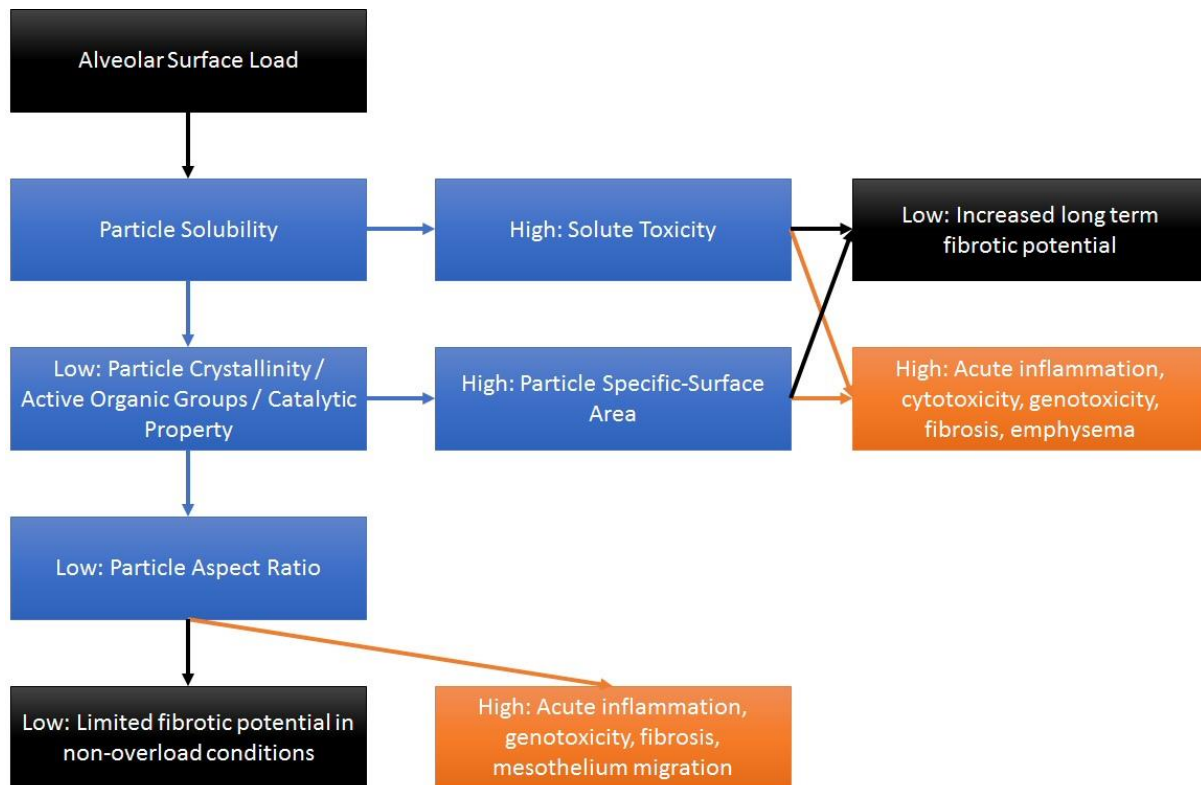


Figure 18: Proposed hierarchy for poorly-soluble coarse particulate matter toxicity

Using such a hierarchy, after adjusting for inflammatory activity due to particle load (assuming the ultrafine component which escapes macrophage uptake is low), current occupational exposure standards that are applicable include, but are not limited to: Low solute toxicity, fine  $\text{SiO}_2$  standards; High solute toxicity, fine  $\text{CuO}$  standards; High particle specific-surface area, ultrafine  $\text{ZnO}$ ; Low particle specific-surface area, fine  $\text{ZnO}$ ; Low particle aspect ratio, fine  $\text{Fe}_2\text{O}_3$  standards; High particle aspect ratio, amphibole asbestos.

The proposed hierarchy would therefore ignore the aspect-ratio of chrysotile asbestos, classifying it as mediating toxic effects through soluble/break-down components, while amphibole asbestos toxicity would still be mediated by particulate length. Development and validation of such hierarchal particulate toxicity systems may allow comparative high-throughput *in-vitro* monitoring of particulate toxicity in the future, and meaningful contributions to AAQS.

### 3. Improving Toxicological Assessment of Poorly-Soluble Coarse Fraction Particulates Relevant to Pulmonary Health *In-Vitro*

#### 3.1 Introduction

Comparative toxicology requires the accurate assessment of cellular endpoints *in-vitro*. For this to occur, the toxicological model must be relevant to the target organ system from which observed health outcomes are to eventuate, and the comparative standards chosen based on similar modes of toxicity. In this regard, when assessing the impact of iron-rich ore particle inhalation on human health, the most immediate concern is damage to lung tissue and inflammatory responses which may lead to asthma, bronchitis, increased respiratory hospital admissions and in severe cases the development of obstructive pulmonary diseases and fibrosis<sup>62</sup>. While there is evidence for systemic cardiovascular risks, it is unclear how they are mediated requiring more investigation *in-vivo* before modelling this phenomenon toxicologically can be validated<sup>73</sup>. Nevertheless, modelling particle interaction with the lungs is also fraught with caveats and complications. With dozens of different cell types, complex 3D structures, airway dynamics affecting particle deposition characteristics by size, a unique air-biofluid interface and a complex immunological environment, the lung far outstrips the ability of current cell culture technology to mimic all factors important in the particle-lung interaction<sup>108,140</sup>. It is therefore not surprising that *in-vitro* toxicology end-points are often thought to correlate poorly with *in-vivo* experimental endpoints<sup>265</sup>. Furthermore, the driving factors behind particulate toxicity of size, shape, composition and crystallinity are not well defined in general<sup>213,265</sup>, with the differences in toxicity between coarse, insoluble metal-oxides of different compositions especially unclear, despite some agreement they are able to cause inflammatory responses<sup>34,212</sup>. Concern over the toxicity of the metal species content in urban PM<sub>10</sub> is also reflected in epidemiological data<sup>259</sup>.

The ambiguities associated with modelling the lungs *in-vitro* as well as the toxic mechanisms of poorly soluble metal-oxides themselves leave the field of *in-vitro* inhalable particulate toxicology in an exploratory state, despite decades of advancements. In reflection of this, several exposure concentration ranges, dosing




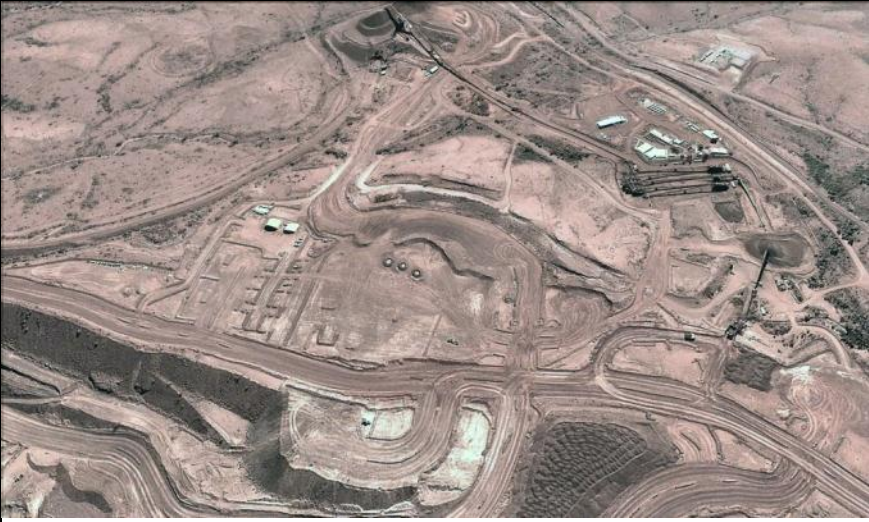
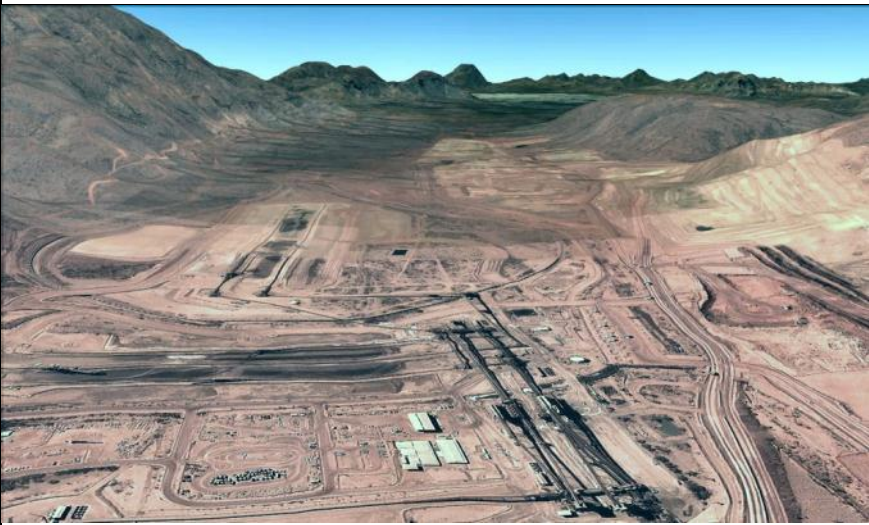
metrics, particulate standards and culture techniques have been trialled throughout the project in search of increased accuracy and greater differentiation between samples. The problems requiring immediate attention include the interference of particulates on assay protocols themselves, which can cause conflicting results between different assays and either exacerbate or reduce perceived particle toxicity unless accounted for <sup>166,222</sup>. Particular care was taken to adapt colorimetric cytotoxicity assays to avoid particle interference, as guaranteeing the similar cytotoxicity profiles between different endpoints is essential to their calibration and interpretation.

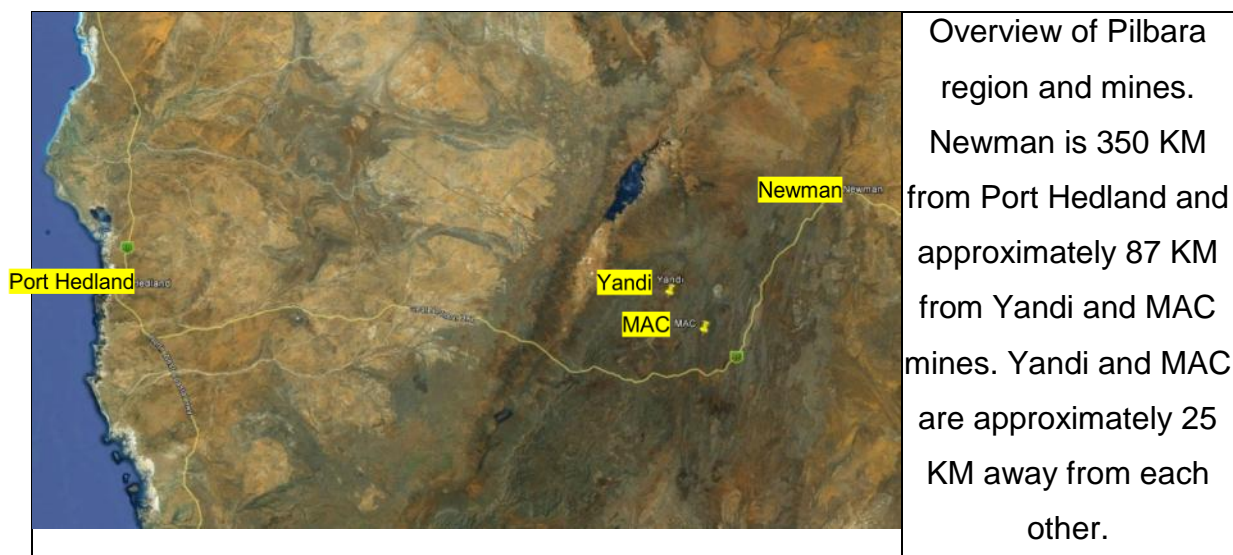
Size dependent toxicity effects between micron and nano-size particles were investigated, as well as the effect of lung surfactant proteins on particulate toxicity which may aid particle disaggregation effects. It is possible that disaggregated particles expose a larger surface area to mediate toxic effects, and have enhanced transmembrane penetrative capability. To assess the effect of cellular differentiation, 3D tissue culture techniques were also employed, and cell contact mediated toxicity assays attempted. As the samples used are of environmental origin, the PM<sub>10</sub> extraction methods have also been refined to increase yield, and sterilisation techniques adapted to reduce changes to surface chemistry which may determine some component of toxicity. However, gentler approaches to sterilisation require caution; environmental samples contaminated with endotoxins may greatly influence toxicological results obtained <sup>266</sup>.

The samples received from the ChemCentre WA for toxicological analysis are sourced from the stockpiles of mining sites producing many megatons of ore per annum and are thus significant sources of PM<sub>10</sub> and PM<sub>2.5</sub> pollution in the immediate region and shipping ports distal to the mines. Mining Area C (MAC, 42 mtpa), the Yandi mine (41 mtpa) and Newman Hub Mt. Whaleback (Newman) mine (37 mtpa) are represented. These mines are all located in the Pilbara region of Western Australia. BHP Billiton owns a majority stake in these mines (85%) and employs some 8,000 people in the region. The town of Newman is adjacent to the Mt. Whaleback mine and is populated by 4,245 residents. Table 11 shows satellite imagery of these mines. Samples directly obtained from BHP Billiton in 2009-2012

were tested, however were suitable for method development only as BHP Billiton could not guarantee the source and purity of the samples.

**Table 11: Satellite imagery of mining sites. Elevation emphasis x3. Supplied by Google Earth, Newman 2005, Yandi 2011, MAC 2011, Pilbara 2012.**

	Newman Hub Mt. Whaleback Mine (Newman)
	Yandi Mine (Yandi)
	Area C Mine (MAC)



## 3.2 Materials and Methods

### 3.2.1 Cyclone Separation

Sampling the air for  $PM_{10}$  and transferring this into lab based experiments is the most direct method to obtain  $PM_{10}$  and  $PM_{2.5}$ . However, investigation into the feasibility of these processes for supplying the project revealed that it presented a major bottleneck, and the Ecotech HIVOL samplers at BHP Billiton would only be able to supply several dozen micrograms of sample per week which would not be sufficiently rapid to sustain all experiments.

Cyclone separation was instead used to extract aerodynamic  $PM_{10}$  and  $PM_{2.5}$  from ore samples prior to 2012. A tangential flow cyclone separator traditionally used as a wearable device for occupational exposures was adapted to extract respirable fraction particles at an airflow rate of 4.21 L/min and 1.61 L/min to extract thoracic fraction particles (see Figure 19). Samples were continually turned over every 30 minutes to ensure the surface mixture contained extractable  $PM_{10}$  and  $PM_{2.5}$ , and filter papers were generally saturated and ready for collection after 4-6 h. Samples were brushed off filter paper into collection tubes for autoclaving before suspension in media, providing some 250-500  $\mu\text{g}$  of sample per week when continuously run. This created delays of several weeks between sample reception and assay.

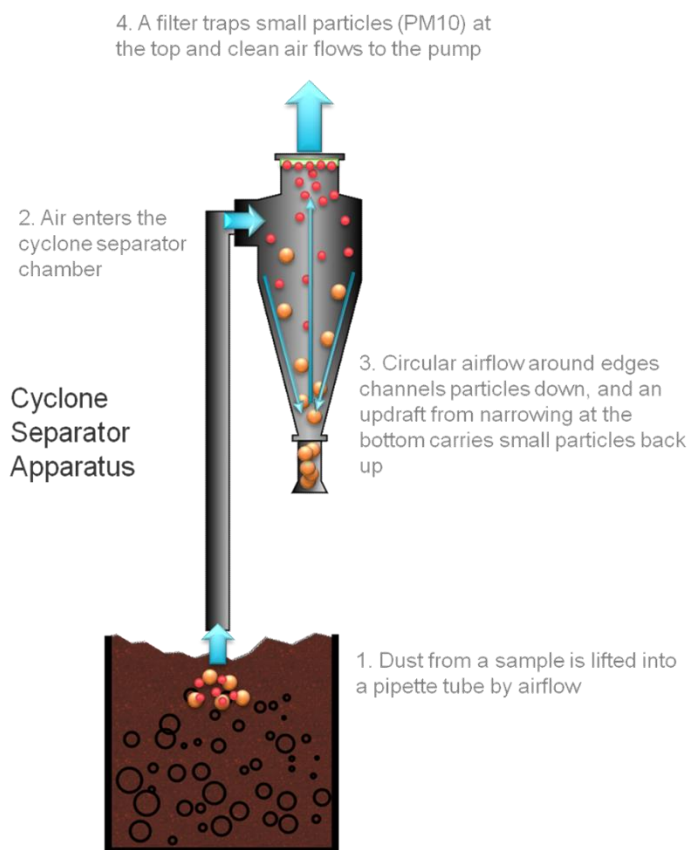


Figure 19: Outline of cyclone separation apparatus operation and collected sample.

### 3.2.2 Ultrasonic Sieving

Despite improvements over atmospheric sampling, the rate of sample collection by cyclone separation remained a limiting factor in the experimental process. Sieving was deemed to be a superior technique for acquiring PM<sub>10</sub> rapidly. However, traditional sieving techniques are best suited to acquiring samples only as small as 45  $\mu\text{m}$ . To sieve below 10  $\mu\text{m}$ , an Ultrasonic Sieve Ring and shaker tower were acquired by 2012, along with custom 10  $\mu\text{m}$  electroformed sieves (Precision Eforming LLC, New York, USA). The ultrasonic burst interval, intensity and shaker intensity were adjusted to provide optimal extraction efficiency and avoid sieve damage. Any sieve damage which occurred was repaired by epoxy resin to avoid collecting unintended size fractions. Placement of the ultrasonic ring below the electroformed sieve and above the collection plate was found to decrease damage to the electroformed sieves. The optimised operation of the apparatus was able to supply 1-2 mg of PM<sub>10</sub> over a 6 hour period of completely automated operation (see

Figure 20). This allowed samples to begin the assay process one day after reception.



Figure 20: Sieve shaker and ultrasonic ring (left) with ultrasonic wave generator (right).

Ultrasonic sieving was used to extract PM<sub>10</sub> from < 45 µm iron ore samples sieved and characterised by ChemCentre WA from the MAC, Yandi and Newman mines as well as Iron-Ore A and B samples. During the sieving procedure, aluminium foil was used to line the collection tray to allow easier transfer of dusts into collection tubes by brushing and prevent contamination from the brass collection tray, while the top sieve was also covered in aluminium foil to avoid dispersion of inhalable material into the laboratory environment. Once sieved onto the collection tray, the sample was brushed off into 5 mL Falcon tubes (BD Biosciences, USA) and fractionally sterilised (see section 3.2.3) for mixture with media or biofluid.

### 3.2.3 Fractional Sterilisation

Steam autoclaving of samples (121 °C, 15 psi, 15 mins) has the potential to solvate adsorbed toxicants on PM samples, while dry autoclaving (170 °C, 60 mins) also has the potential to volatilise adsorbed toxicants. In an effort to reduce changes to surface chemistry, radiative methods such as UV were tested, but penetrated the sample mass insufficiently to guarantee sterilisation. Fractional sterilisation

(tyndallisation) methods were found to be optimal, and introduced to the MAC, Yandi and Newman samples which were ultrasonically sieved. The sample collection tubes (50 mL, BD Biosciences, San Diego, USA) were heated to 60 °c for an hour and allowed to cool each day for three consecutive days. The cooling time allows bacterial and fungal spores surviving the heat sterilisation to germinate and be destroyed by the subsequent sterilisation round, while avoiding extreme changes in heat and humidity brought about during the autoclaving process.

### 3.2.4 Chemicals and Reagents

Poorly-soluble oxide particulate standards (Sigma Aldrich, USA): Copper(II) Oxide <50 nm, Copper(II) oxide <5 µm, Iron(II,III) Oxide <5 µm, Iron(II,III) Oxide <50 nm, Iron(III) Oxide <5 µm, Silicon(IV) Oxide <10 µm, Titanium(IV) Oxide <50 nm. Soluble iron compounds (Sigma Aldrich, USA): Iron(II) Lactate Hydrate, Iron(III) Sulphate Hydrate, Iron(II) D-Gluconate Dihydrate, Iron(III) Chloride on Silica. Other standards: Carbon Black <150 nm powder was obtained from US Research Nanomaterials, Inc., USA. Samples: Iron Ore A and B PM<sub>10</sub> (obtained in 2009-2011, deprecated after BHP Billiton informed these car dumper samples may be contaminated in exchange for samples MAC PM<sub>10</sub>, Yandi PM<sub>10</sub>, Newman PM<sub>10</sub> used in subsequent chapters).

Differentiation of U937 to a mature macrophage-like morphology can be induced by exposure to phorbol esters<sup>267</sup>. For this purpose, differentiation was induced during the seeding period by exposure to 30 ng/mL of Phorbol Myristic Acid (PMA) for 48 h.

Dipalmitoylphosphatidylcholine (DPPC) (#P5911-250MG, Sigma Aldrich, USA) was employed as a surfactant additive in creating a synthetic biofluid, which has been described as successful in dispersing ultrafine carbon black when used in combination with albumin<sup>146</sup>. DPPC was prepared in 100% ethanol stock and added to media for a final concentration of 10 µg/mL (0.1% ethanol v/v), with bovine serum albumin (BSA) 2 mg/mL.

For 3D spheroid culture experiments, 96-well plates were prepared with a mixture of 1.5% v/v agarose gel and F-12K media, 50 µL per well, and allowed to set for 1 hr prior to seeding.

Cell viability was analysed by the 3-(4,5-Dimethylthiazol-2-yl)-5(3-carboxymethoxyphenol)-2-(4-sulfophenyl)-2H-tetrazolium, inner salt (MTS) assay, marketed as the the CellTiter 96<sup>®</sup> Aqueous Non-Radioactive Cell Proliferation Assay (#G5430, Promega, USA)

### 3.2.5 Cell Culture

Cell types cultured: A549 pulmonary type I/II-like epithelial adenocarcinoma (ATCC CCL-185), LL24 pulmonary normal fibroblast (ATCC CCL-151), U937 monoblastic-like histiocytic lymphoma (ATCC CRL-1593.2).

The A549 and LL24 cell lines were cultured in F-12K medium (#21127, Life Technologies, USA) supplemented with 10% foetal bovine serum (FBS), 100 IU/mL penicillin, 100 µg/mL streptomycin, and 10 mg/mL amphotericin B (#A9528-50MG, Sigma Aldrich, USA). U937 was cultured in RPMI 1640 medium (#72400, Life Technologies, USA) supplemented with 10% foetal bovine serum (FBS), and 100 IU/mL penicillin, 100 µg/mL streptomycin, 10 mg/mL amphotericin B (#A9528-50MG, Sigma Aldrich, USA), 2mM L-glutamine, 1mM Sodium pyruvate and 10mM HEPES buffer.

Cells were cultured in 75 cm<sup>2</sup> tissue culture treated flasks (Corning, USA) at 37 °C in humidified 5% CO<sub>2</sub>, 95% air atmosphere. A549 and LL24 medium was changed every 2-3 days and split every 5 days. As they are adherent, cells were harvested for seeding using trypsinization and washing in Phosphate Buffered Saline (PBS). U937 were cultured in suspension and maintained in at 2 x 10<sup>5</sup> to 1 x 10<sup>6</sup> cells/mL by passage every 4 days.

For seeding incubation, cells were plated in clear flat bottom 96-well plates (BD Biosciences, USA) at 70% confluency (100 µl/well, 2x10<sup>5</sup> cells/mL) and incubated for 24 h prior to the particle exposure time period at 37 °C under Breath Easier sealing membrane for multiwell plates (#Z763624, Sigma Aldrich, USA).

For cell contact experiments, 1 µm polycarbonate pore Transwell™ 6 well plate filter inserts (#Z681814, Sigma Aldrich USA) were inserted into 6-well plates (BD Biosciences, USA) after cell incubation, and particulate sample added above the insert.

### 3.2.6 Cytotoxic Endpoint Development

#### 3.2.6.1 *Particle Interference in Spectroscopic Assays*

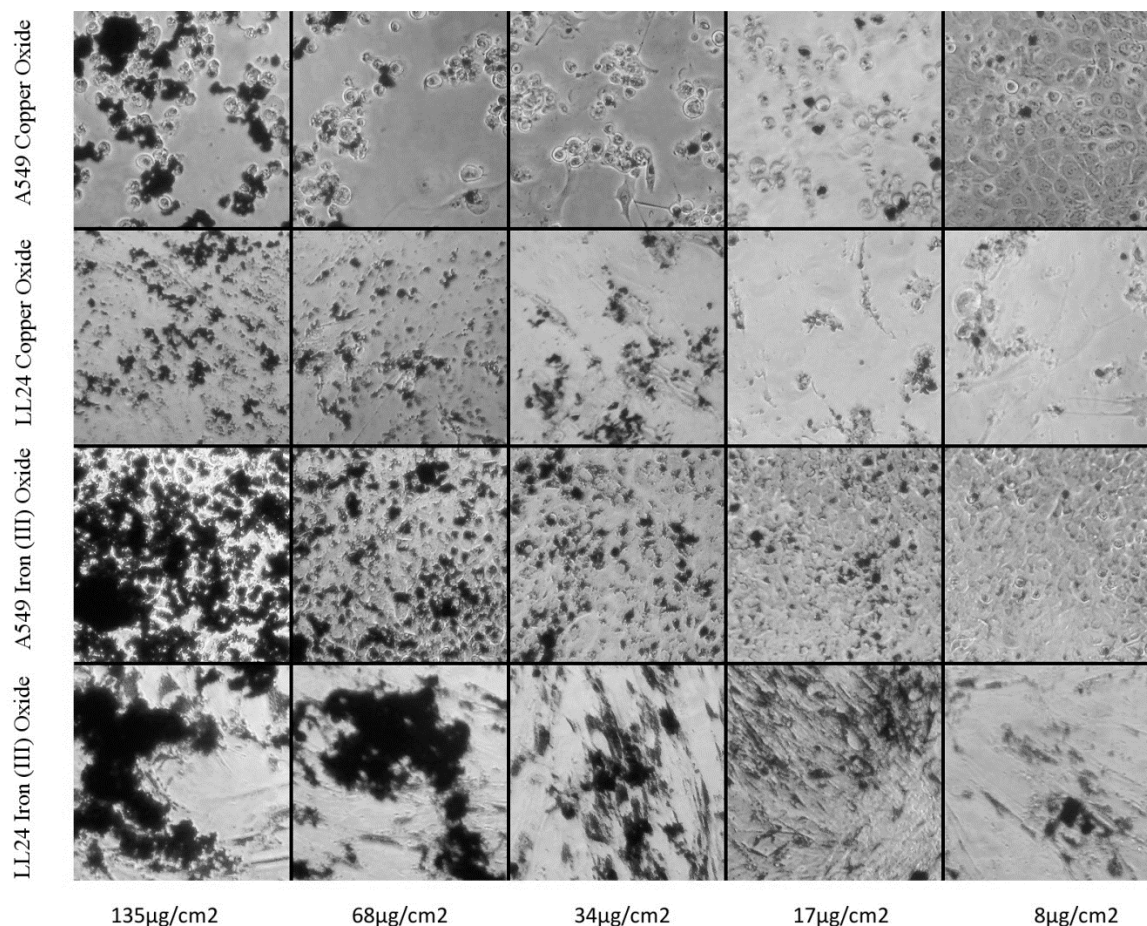
The testing of insoluble particles for cytotoxicity rather than soluble chemicals poses many technical challenges. Both cell surface area exposure to particles as well as the concentration of the suspension must be considered, and the particle number which may vary greatly depending on the weight and size distribution of the particles. Once these are accounted for, traditional bioassays may require substantial adaptation to work with particles. Cell proliferation assays are a major endpoint for cytotoxicity, apoptosis and quiescence. By measuring the metabolic activity of an exposed group of cells against an unexposed control, the loss of metabolism due to exposure is proportional to the loss of cell number or cell function.

A mainstream method to measure cell proliferation is the colorimetric MTS assay, a derivation of the well-established 3-(4,5-dimethylthiazol-2-yl)-2,5-diphenyltetrazolium bromide (MTT) assay. It was initially determined this assay which detects the colour change of a substrate as it is metabolized (MTS+PMS → formazan) should be used on the 96 well assay plates to construct a dose-response relationship using a serial dilution of sample.

Work to optimise the experimental concentrations and durations revealed problems in the MTS assay for cell proliferation in assessing coarse particle toxicity, as well as physical problems in pipetting particle suspensions, preventing the collection of interpretable data. In initial assays, the unmodified MTS assay showed increasing cell proliferation with increasing dose, rather than increasing toxicity with increasing dose as would be expected. As increased absorbance indicates increased cell survival in the MTT assay, absorption or blocking of light by the insoluble iron-ore samples and particulate standards was determined to be the cause of these results. This was confirmed by light microscopy observation, showing that while copper oxide



dispersions did indeed lead to cell apoptosis, iron compounds did not necessarily cause significant cell death at concentrations that were high enough to interfere with visible light (see Figure 21).



**Figure 21** Light microscopy 200x magnification of A549 and LL24 cells exposed to CuO and Fe<sub>3</sub>O<sub>4</sub> over 48 h using micron-size standards.

To remedy this, cells were washed prior to assay in PBS to free them of particulate interference. The effect of the washing step was effective in trending the dose-response relationship along the correct gradient, although results varied significantly between experiments and failed to show any correlation with particle composition. Light microscopy of 6 well plates before and after the washing step revealed that at high concentrations, particles became embedded in all cell lines and therefore could not be washed away without destroying cells (see Figure 22). Trypan blue staining indicated A549 survival rates of at least 85% when exposed to 390 μg/cm<sup>2</sup> of Iron ore A and B samples over 24 h, sans washing step. Therefore cell destruction during the washing step was implicated in the dose-response curves observed, confounding

the determination of coarse particle toxicity. Dramatic macroscopic patterns were also observed at high particulate loads over longer time periods of 96 h, owing to cell-particle interaction characteristics (see Figure 22). In the A549 cell line exposures particle distribution remained similar to that of empty wells, while the cells themselves appeared largely unaffected by the presence of particles and adherent. In contrast the polar and self-aligned growth characteristics of the LL24 cell line was observed to produce a mottled pattern with particulate matter clumping along axes of fibroblast growth. In the U937 cell line a more uniform and granular appearance resulted. This was microscopy observed to be the clearance and concentration of particles by macrophages into clumps, possibly facilitated by phagocytosis to the point of cell overloading and death.

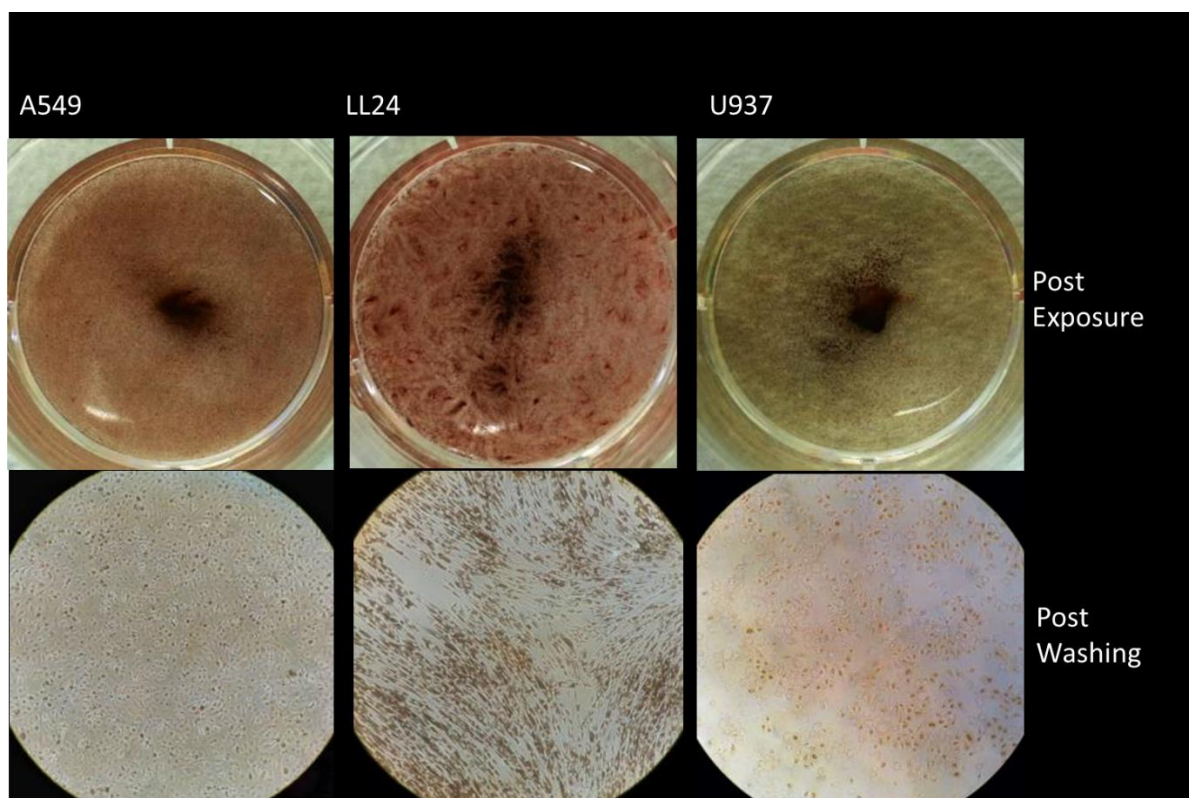


Figure 22: View of A549, LL24 and U937 cells in 6 well plates exposed to 390 µg/cm<sup>2</sup> Fe<sub>2</sub>O<sub>3</sub>. Top row: 96 h post exposure 1X; Bottom Row: Immediately after PBS wash 200x magnification.

### 3.2.6.2 96 Well Plate Layout

In response to these effects, the arrangement of replicates and controls (Figure 23) was designed to compensate for particle interference no longer controlled by a

washing step, by including both traditional no-exposure controls and exposure no-cell controls.

Experiment Tpe		Date														Notes
ID #	# µl/well	Cell Line			Cells/well			Seed # h			Exposure # h					
Friday		Sample 1			Sample 2			Sample 3			Controls					
# µg/ml stock		1	2	3 no cell	4	5	6 no cell	7	8	9 no cell	10	11	12			
1 in 2	A															
1 in 2	B															
1 in 2	C															
1 in 2	D															
1 in 2	E															
1 in 2	F															
1 in 2	G															
1 in 2	H															

Figure 23: A typical 96-well plate plan for the MTS assay

Two sample rows exposed to cells (row mean =  $A_s$ ) at  $1 \times 10^4$  cells/well with a third no cell exposure ( $A_b$ ) form one sample bracket and help counteract the effects of particle opacity while a control bracket of three rows with cells and no exposure (row mean =  $A_c$ ) form the control measurement which is measured against. Three of these plates are used for accuracy (6 replicates at each data point). Survival rate calculation:

$$\text{Survival rate (\%)} = \frac{A_s - A_b}{A_c - A_b}$$

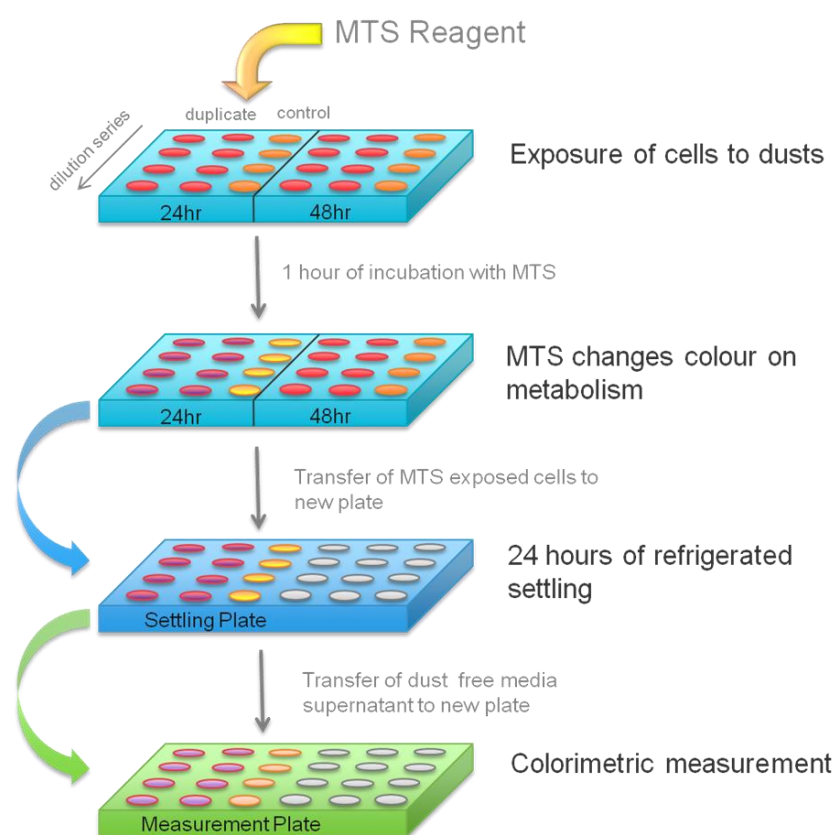
Conversion from mg/mL suspension concentration ( $C_s$ ) to mg/cm<sup>2</sup> surface area concentration ( $C_a$ ) is shown below where  $V_{ws}$  is sample volume in well and  $W_a$  is well area. It is assumed particle settling time is negligible over the exposure period. The resulting figure is multiplied by a thousand for expression as µg/cm<sup>2</sup>:

$$C_a = \frac{C_s \times V_{ws}}{W_a}$$

### 3.2.6.3 Adapted MTS Assay

The final adapted MTS assay carries improvements over the standard protocol to minimise collateral cell death due to particle abrasion and reduce uneven evaporation in multiwell assay plates by using appropriate controls and sealing membranes, a problem that has been previously recognised affecting longer duration, low toxicity exposures<sup>268</sup>. The assay was continued normally without a

washing step until the MTS incubation step with the sample was completed. The reaction was then stopped with ethanol and 75% of the well volume supernatant transferred to a new clean 96 well plate (see Figure 24). This allowed live cells to metabolise the assay substrate normally, and due to the settling properties of the particles, the extracted supernatant for measurement remained low in particulate interference in experimental exposures longer than 24 h. This was corroborated by control rows of particulate matter in serial dilution without cells to be subtracted as described (see section 3.2.6.2), which showed no measurable increase in opacity with higher concentrations.



**Figure 24: Terminal procedure for adapted MTS assay to avoid particulate interference with absorbance assays**

The importance of aligning all sample endpoints by cytotoxicity is underscored by the unknown mode of toxicity for a given PM sample. Repeating these experiments across different laboratories by other alignments, such as mass by suspension volume or mass by surface area, provide less of a guarantee downstream endpoints will bear any relationship because the toxicological action of particulate samples could be mediated either through contact or soluble factors – the ratio of which can

change depending on size distribution and total reactive surface area, extraction method, assay format, media type and reagents used.

Concentrations ranging from 5 mg/mL to 0.1 mg/mL for a 1:2 serial dilution into 96 well plates were used to determine initial cytotoxic parameters. The preferred stock concentration subsequent to initial experiments was found to be 1 mg/mL, with the exception of copper oxide stock at 0.25 mg/mL due to its much greater toxicity.

### 3.3 Monolayer Cytotoxicity Results

The toxicity of the iron ore samples (Iron Ore A, B, and MAC, Yandi and Newman samples) were measured against several standards. The  $\text{SiO}_2 < 10 \mu\text{m}$  standard was chosen to compare against silica dusts, which are abundant in many industrial activities as silica compounds compose 28% of the earth's crust. The U.S. Occupational Safety and Health Administration's permissible exposure limit is  $100 \mu\text{g}/\text{m}^3$  in an 8 h work day, to protect against known pulmonary disease outcomes<sup>95</sup>. Iron is also abundant, composing 5.6% of the earth's crust. The  $\text{CuO} < 5 \mu\text{m}$  standard was chosen as a relatively cytotoxic control given its use as a sterilising agent<sup>216</sup> and the  $\text{CuO} < 50 \text{ nm}$  standard for determination of size-dependent toxicity<sup>190</sup>. The  $\text{Fe}_3\text{O}_4 < 5 \mu\text{m}$  and  $\text{Fe}_2\text{O}_3 < 5 \mu\text{m}$  standards were used as magnetite and haematite iron oxide references with the  $\text{Fe}_3\text{O}_4 < 50 \text{ nm}$  sample also being used for size dependent toxicity tests. The  $\text{TiO}_2 < 50 \text{ nm}$  standard was chosen for reference to existing *in-vitro* literature where it is extensively studied in relation to nanomaterial containing consumer goods<sup>269</sup>.

While soluble iron compounds were assayed, comparing solubilised weight to volume ratios of the various soluble iron compounds to particulate matter was not found to produce informative comparisons. As the particulate samples assayed were highly insoluble in nature, the weight to cell surface area exposed convention was adopted. This more accurately reflects changes in cell behaviour mediated by particulate surface contact with the cell membrane as the particles rapidly settle within the exposure well, and is applied in the literature for *in-vitro*  $\text{PM}_{10}$  and  $\text{PM}_{2.5}$  exposures<sup>202,229,233,270,271</sup>, although the w/v relationship holds proportionally so long as the well area and media volume are constant.

### 3.3.1 LL24 Monolayer Toxicity

Analysis of cytotoxicity using the adapted MTS assay showed that insoluble PM had very little effect on cell viability despite high concentrations used. Once a maximum effect level was reached, likely indicating saturation contact of cells with PM, cytotoxic changes were minimal and did not follow a traditional dose-response relationship. Standards  $\text{Fe}_3\text{O}_4 < 5 \mu\text{m}$ ,  $\text{Fe}_2\text{O}_3 < 5 \mu\text{m}$ ,  $\text{TiO}_2 < 50 \text{ nm}$ , Iron Ore A  $< 10 \mu\text{m}$ , and Iron Ore B  $< 10 \mu\text{m}$  were tested. Over 24 h, neither of the micron-size iron oxide standards, iron ore samples, nor  $\text{TiO}_2$  achieved an  $\text{IC}_{50}$  value in the LL24 cell line (see Figure 25)

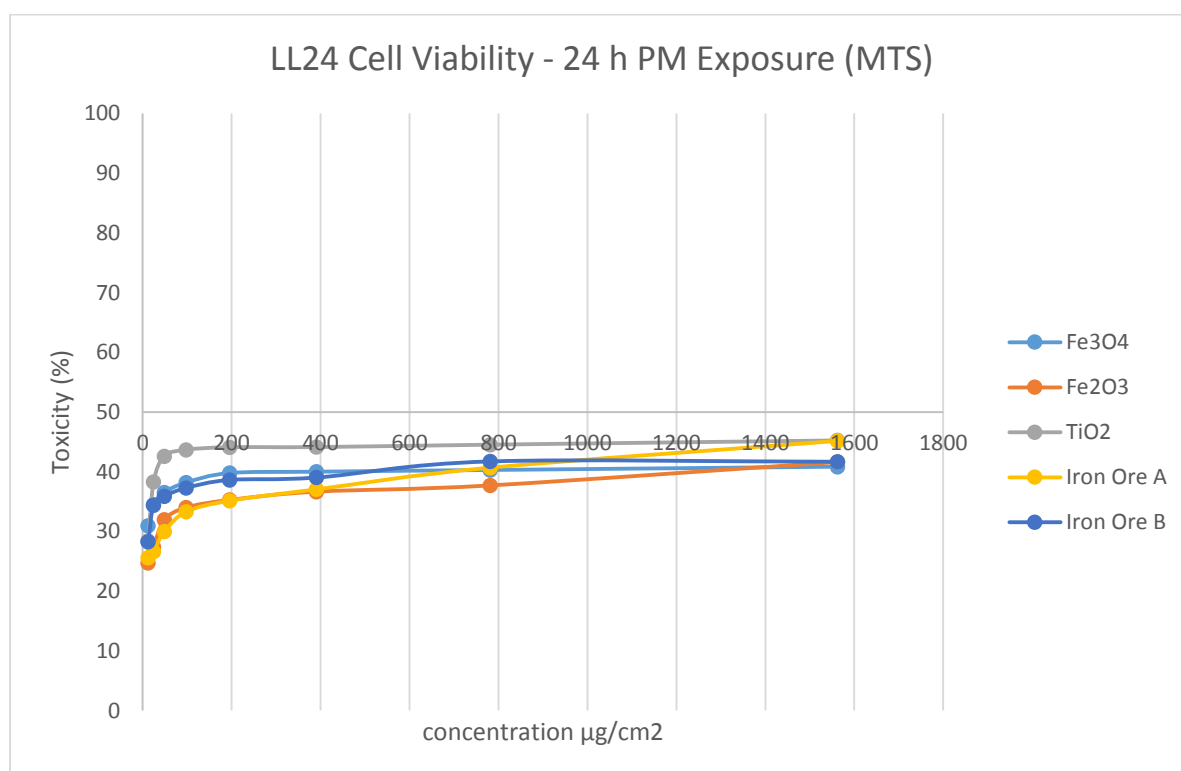
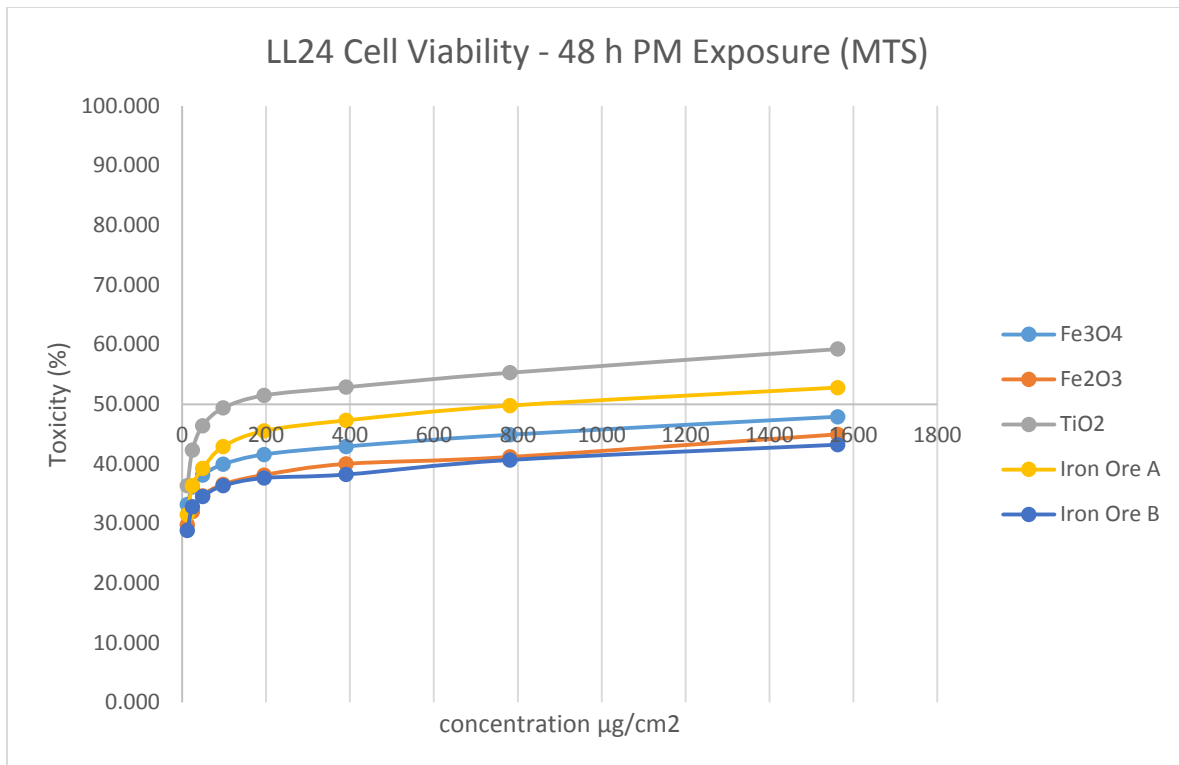


Figure 25: LL24 24 h particle toxicity, using iron ore samples and reference compounds. From a 1:2 serial dilution over 12-1562  $\mu\text{g}/\text{cm}^2$ .

Over a 48 h long exposure period, the maximum cytotoxicity is increased (see Figure 26). However, the nature of this increase in cytotoxicity may be confounded by adsorption of protein and obstruction of media diffusion in addition to direct cytotoxic effects <sup>166</sup>.



**Figure 26: LL24 48 h particle toxicity, using iron ore samples and reference compounds. From a 1:2 serial dilution over 12-1562 µg/cm².**

Over a 96 h long exposure period (see Figure 27), the dose-response relationships had largely moved through the IC50 toxicity level. However, there was remarkably little movement in the maximum cytotoxicity despite increased separation between sample toxicities.

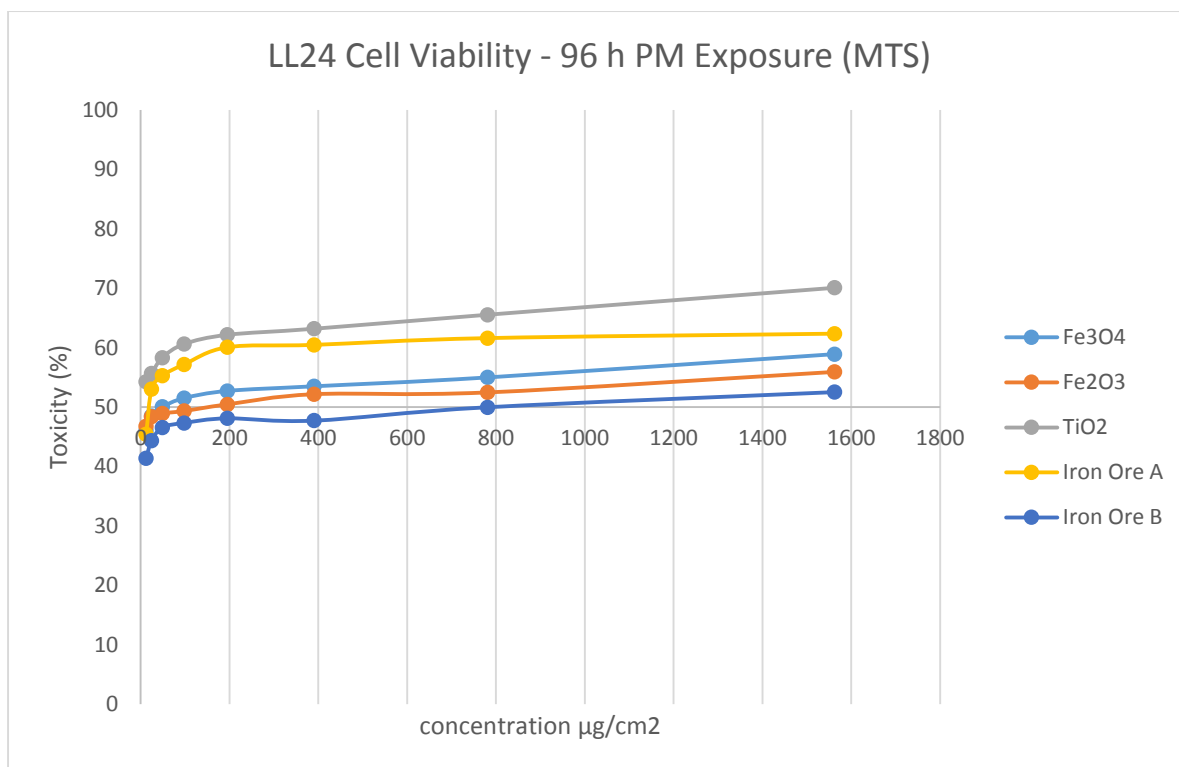
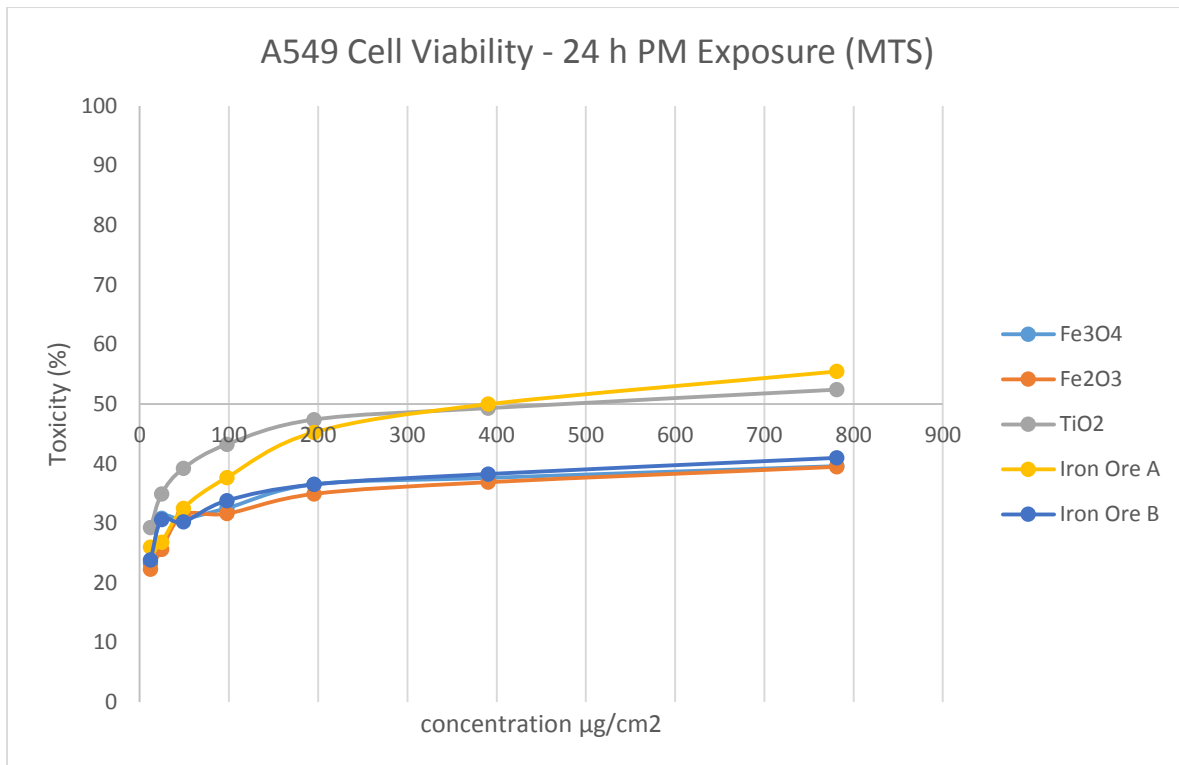


Figure 27: LL24 96 h particle toxicity, using iron ore samples and reference compounds. From a 1:2 serial dilution over 12-1562 µg/cm<sup>2</sup>.

### 3.3.2 A549 Monolayer Toxicity

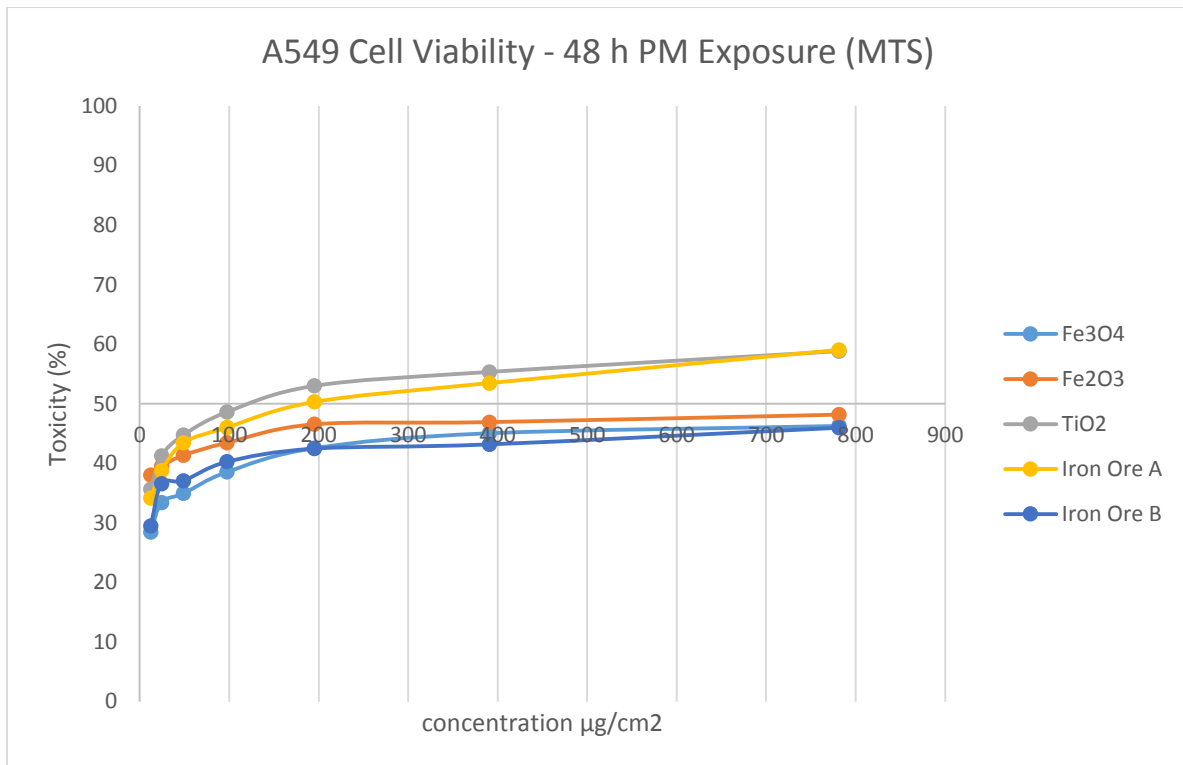
The A549 cell line responded similarly to the LL24 cell line in terms of the ranking of toxicity of particulates, showing greater divergence in the 24 h period (see Figure 28). Interestingly, the Iron Ore A and TiO<sub>2</sub> sample were again found to have a similar toxicity, approaching an IC<sub>50</sub> of 390 µg/cm<sup>2</sup> after 24 h, while Iron Ore B and the micron-size iron oxides remained largely indistinguishable and less cytotoxic. The similarity of the Fe<sub>3</sub>O<sub>4</sub> and Fe<sub>2</sub>O<sub>3</sub> standards allows to the former to be substituted for the latter if room is required for additional standards to be compared on the same plate.





**Figure 28: A549 24 h particle toxicity, using iron ore samples and reference compounds. From a 1:2 serial dilution over 12-1562 µg/cm<sup>2</sup>.**

Over a 48 h long exposure period, the maximum cytotoxicity is increased and some differentiation of the particulates occurred at the lower concentrations (see Figure 29). For this reason, the 48 h interval was considered optimal for differentiation of particle cytotoxic effect while minimising error due to evaporative and other effects accruing over time.



**Figure 29: A549 48 h particle toxicity, using iron ore samples and reference compounds. From a 1:2 serial dilution over 12-1562  $\mu\text{g}/\text{cm}^2$ .**

Over a 96 h long exposure period, the maximum cytotoxicity responded in an inelastic fashion in comparison to lower dose exposures, although greater differentiation also occurred at the lower doses (see Figure 30). This differentiation appeared maximum within a range of 24-94  $\mu\text{g}/\text{cm}^2$ .

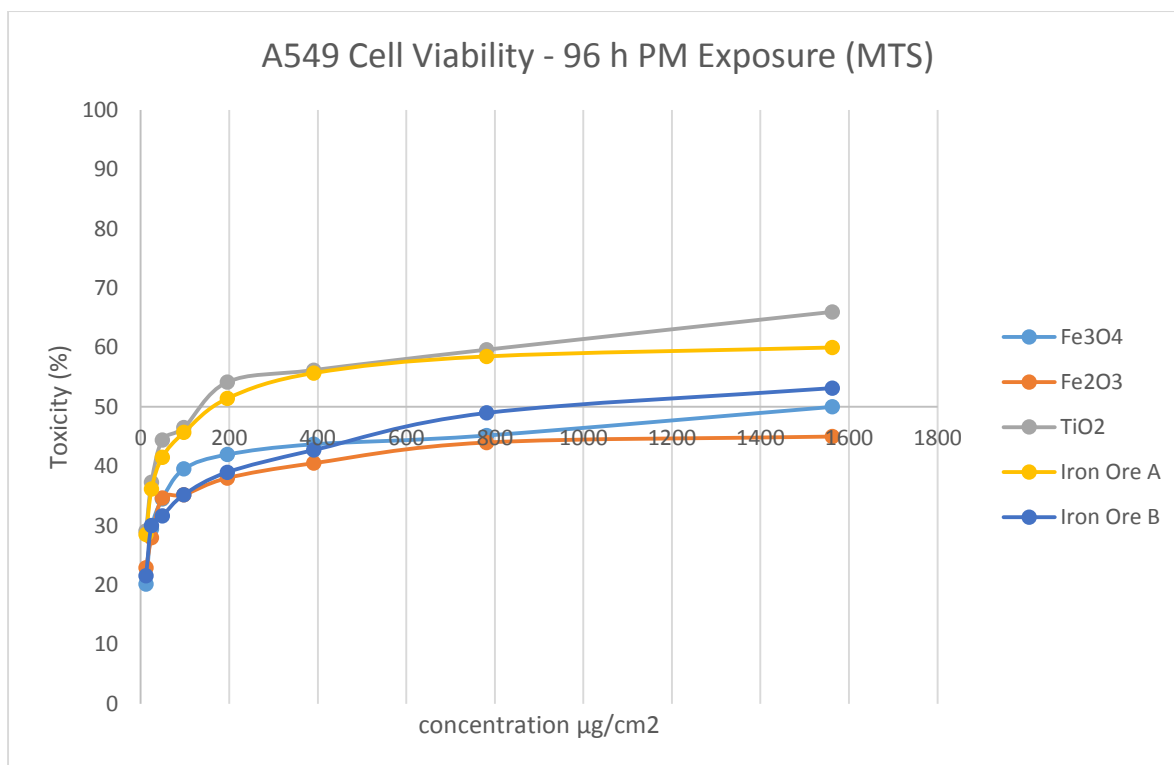


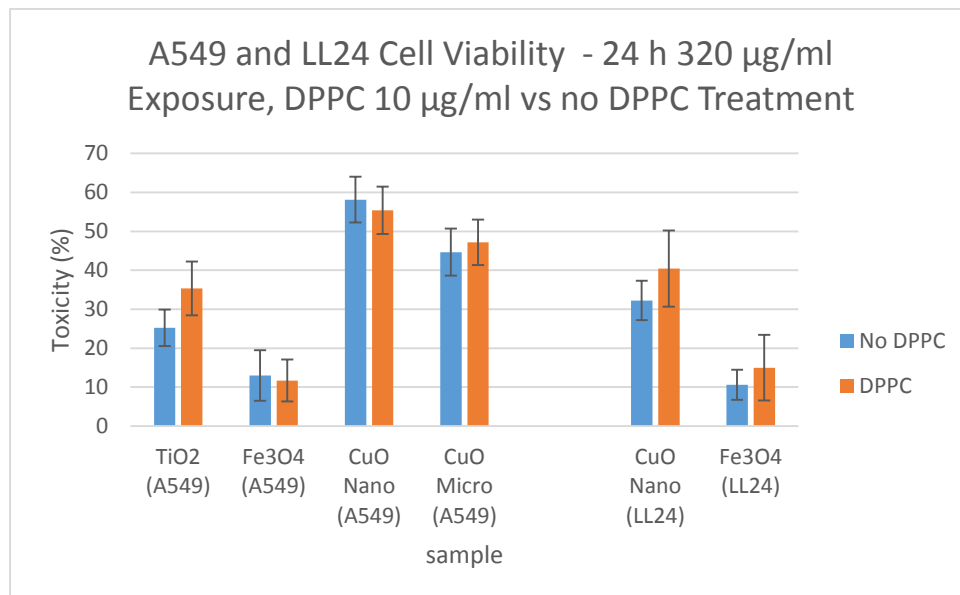
Figure 30: A549 96 h particle toxicity, using iron ore samples and reference compounds. From a 1:2 serial dilution over 12-1562 µg/cm<sup>2</sup>.

The dose-response relationship between low and high cytotoxic effects of the particle exposures suggest that a return on effect diminishing towards zero approached in the toxicity mode active at the upper end of the dose range. While the level of agreement between the A549 and LL24 cell lines added to the robustness of the observed effect, the sensitivity limit of the assay appears to be inadequate to truly differentiate the insoluble metal-oxide samples types observed at lower doses which would be of greater physiological relevance.

### 3.3.3 Lung Surfactant and Size-Dependent Effects

The addition of DPPC 10 µg/mL and BSA 2 mg/mL to culture media was used to create a synthetic biofluid with lung surfactant and disaggregation effects described by experiments in the literature<sup>148,154</sup>, for assessing whether such biofluids alter cytotoxicity. Surfactant added media was used in both sample suspension and assay culture. Prior to dosing, sample tubes were ultrasonicated for 30 minutes and vortexed immediately before pipetting. The TiO<sub>2</sub> < 50 nm, Fe<sub>3</sub>O<sub>4</sub> < 50 nm, CuO < 50 nm and CuO < 5 µm samples were used in the cytotoxicity analysis, and compared to identically prepared samples without DDPC or increased BSA concentration using

the A549 cell line. CuO and Fe<sub>3</sub>O<sub>4</sub> was also compared in the LL24 cell line (see Figure 30).



**Figure 31: A549 (right) and LL24 (left) experiments examining differences in cytotoxicity when the lung surfactant protein and BSA were used together in combination with ultrasonication against regular media suspensions of particulate matter.**

The results indicate there is very little or no effect as a result of the addition of surfactant protein and ultrasonication steps as no significant differences were observed between the exposure groups. Evidence in the literature supports this finding, as it has been calculated the force required to overcome particle aggregation cannot be overcome by the protein-particle interactions which occur in the production of surfactant effects<sup>153</sup>. This is emphasised by the relatively modest difference between the toxicity of nanoscale and micron size CuO particles, which was not enhanced by the surfactant proteins. If disaggregation were a significant effect, it is presumed cytotoxicity would be increased by increased specific surface area of particulate exposed to cells. Furthermore, under light microscopy no surfactant mediated disaggregative effects were distinguishable from controls.

While albumin concentrations as high as 15 mg/mL are shown to be required to stabilise some nanoparticle suspensions<sup>145</sup>, the resulting increased specific surface area of the suspension may be counteracted by reduced catalytic activity in the

generation of ROS. Such concomitant effects are undesirable, compounded by the questionable physiological relevance of such high albumin concentrations. It has been shown using BSA that albumin carries antioxidant effects, which may interfere with the oxidative stress mechanism of cellular damage <sup>151</sup>, and further reduce intracellular nanoparticle uptake <sup>150</sup>.

### 3.4 3D Cytotoxicity Results

#### 3.4.1 A549 Spheroid

Cytotoxicity studies were performed to establish the utility of spheroid cell culture methodology as a suitable 3D cell culture system. Seeding of cultures was performed at normal 2D culture densities, onto well surfaces coated with a 1.5% agar-media mix which had been allowed to set and brought to room temperature (see Figure 32).

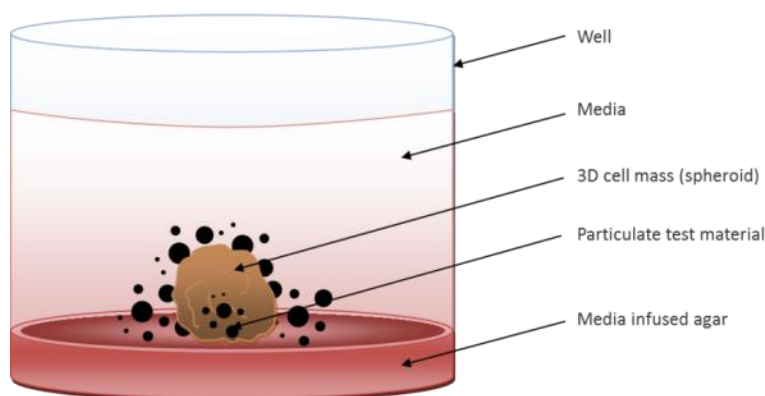
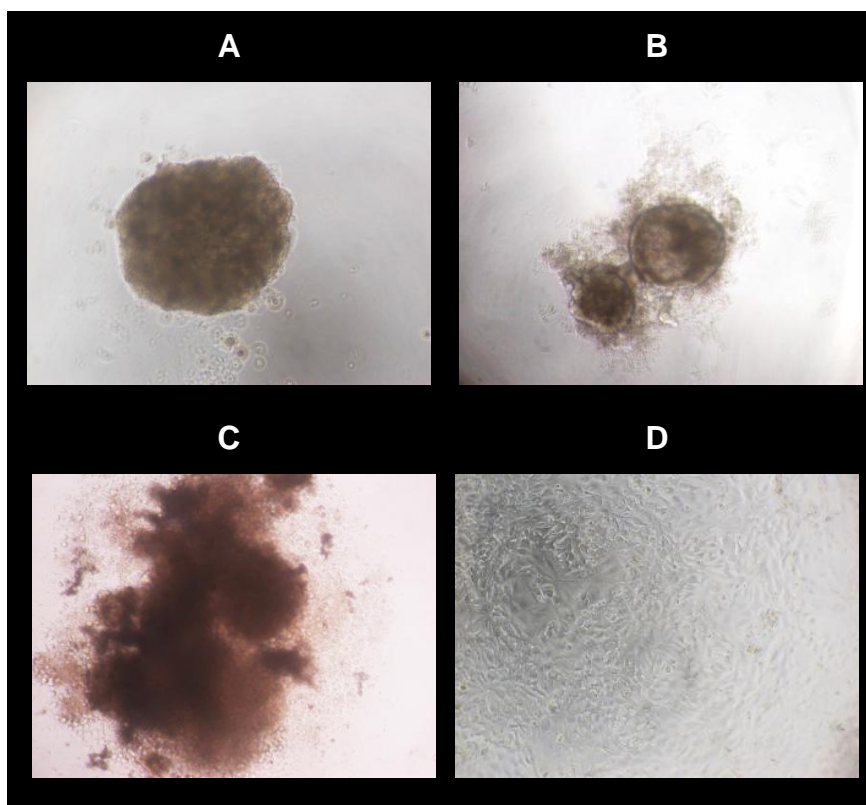


Figure 32: Diagram of 3D spheroid structure within microtitre 96 well plate.

Different cell lines were examined for the construction of the spheroid, shown in Figure 33, panels A-D, after 48 hours of incubation. The regularity in shape of spheroid clusters was dependent on cell type. Monocyte differentiated macrophages (U937) were found to be incompatible with spheroid culture techniques, as they were unable to form spheroids through self-adherence and hence remained settled on the well surface.



**Figure 33: Images of spheroid cultures after 48 h post seeding: A: A549 cells tended to cluster in a tight spheroid on agar. B: LL24 cells tended to form more diffuse spheroids on agar. C: A549+LL24 cells tended to form very diffuse cell masses on agar. D: A549 cells cultured conventionally on the well surface shown for reference. Magnification 200x.**

In particle exposure experiments, the A549 spheroid system demonstrated reduced sensitivity compared to 2D systems. However the nature of this reduced sensitivity was helpful in determining the transmission of cytotoxic action for a given particulate sample; as spheroids reduce the cell surface area available for contact with particles for a given cell number, it is expected that particles with soluble toxic components will maintain cytotoxic power better than those solely exerting cytotoxicity through cell contact or uptake. If so, this most clearly supported by the observation of CuO exposures compared to the other particles. At a dose of 0.138 mg/mL (24.5  $\mu\text{g}/\text{cm}^2$ ) a toxicity of 24% continues to be exerted where no significant toxicity is observed in the other sample types at 0.276 mg/mL (49  $\mu\text{g}/\text{cm}^2$ ), as show in Figure 34.

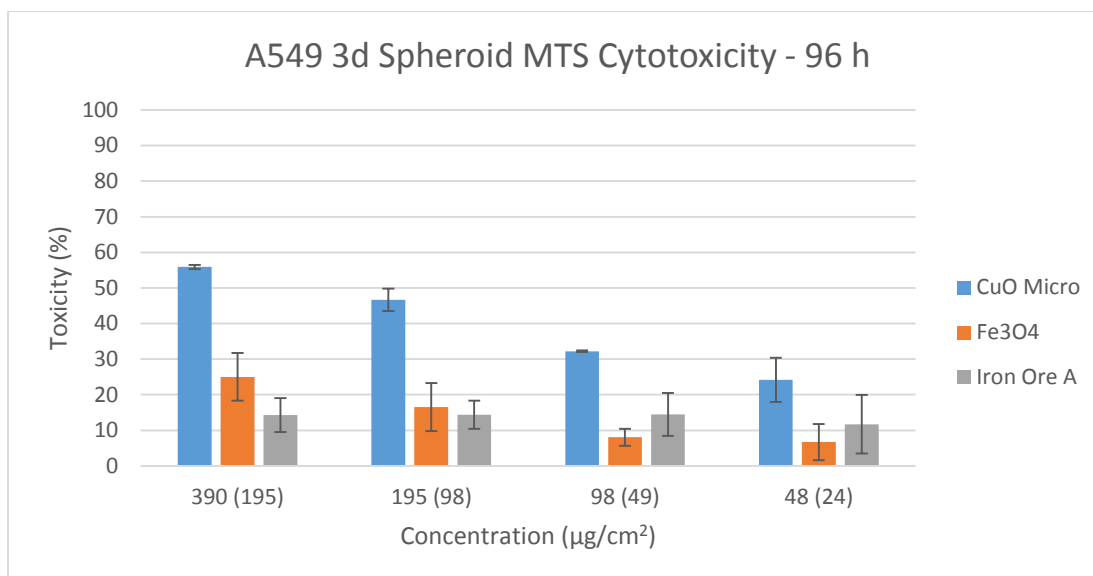


Figure 34: A549 3D spheroid, 96 h particle toxicity, Fe<sub>3</sub>O<sub>4</sub> and Iron Ore A at 390-49  $\mu\text{g}/\text{cm}^2$ . Concentration of CuO at 195-24.5  $\mu\text{g}/\text{cm}^2$ , shown in brackets.

As particles settle over the 96 h exposure period, the surface area of the spheroid in contact with particles will be far less in practice, as most particles will rest at the well bottom not in contact with the spheroid. The potency of CuO cytotoxicity at the lowest dose therefore suggests that the catalysis of ROS or effusion of a soluble intermediate occurs. While CuO is considered insoluble, limited production of soluble species may still occur and the concomitant cytotoxic activity of these species has previously been intimated in the literature<sup>133,272</sup>.

### 3.5 Cell Contact Cytotoxicity Results

#### 3.5.1 Insert Culture

To further investigate the role of cell contact, 1  $\mu\text{m}$  pore filter inserts were used to investigate whether cytotoxicity could be mediated without direct contact using 6-well plates. This was achieved by separately layering the particulate exposure material on top of inserts after cells had been seeded at the bottom of the well normally (Figure 35). Using the 6 well plates posed additional challenges, causing particles to settle in the middle of the well rather than disperse evenly, increasing the error of results. It can be observed however that CuO is able to mediate toxicity similar to positive controls despite insert separation, and this further supports the possibility that soluble species, redox catalysis or to a lesser extent (given the 2 mL well volume), nutrient adsorption affects cell survival.

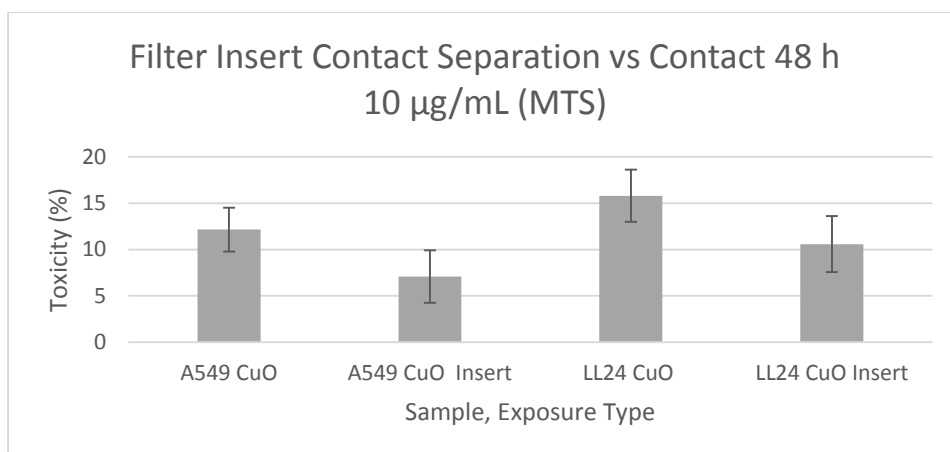


Figure 35: LL24 and A549 Transwell™ insert, 6 well plate culture assay. CuO micron size particles assayed.

### 3.6 Discussion

The experiments in this chapter reflect adaptations towards dealing with particulate matter in a manner that is aware of the limitations in directly applying current biochemistry and cell biology methodologies to poorly soluble micron-size particles. Similar investigations in the literature *in-vitro* increasingly are finding that once effective endpoints and metrics of toxic interactions with lung cells are found, the epidemiological assumptions about toxicity as a function best predicted by particle size and inhaled mass are inadequate to explain toxicity<sup>222</sup>. The wide range of toxic interactions requires comprehensive analysis of biological endpoints, while accounting for adsorbed toxicants and immunological interactions as well as size-distribution<sup>163</sup>. As found in the cell proliferation experiments, dose response curves become difficult to construct when dealing with poorly soluble particulates such as metal oxides where cytotoxicity can range from high, as seen in the CuO standard, to having a maximum cytotoxic effect, as seen with other samples. Yet, particle number alone can begin to overwhelm the immunological clearance of particles independent of cytotoxicity in chronic exposures<sup>91</sup>. At the size ranges investigated, differences between micron and nanometer size particles were also difficult to distinguish, driven by the effect of agglomeration. Particle size differences at these ranges may require dynamic immunological interactions to effectively observe, otherwise constrained by strong agglomeration<sup>266</sup>.



Attempts to elicit more dynamic effects through emulating a more complex lung structure or increasing cellular differentiation also have a limited impact on discriminating which toxic modes a given poorly soluble particle is active in. The spheroid experiment may offer clues to a particle's solubility, however this may be redundant as insolubility is indicated by particles with an apparent maximum level of effect in monolayer experiments and filter based experiments offer a more targeted way to approach this problem. A typical spheroid 1.4 mm in diameter has an approximate surface area of 6.2 mm<sup>2</sup>, compared to a surface area of 25 mm<sup>2</sup> for an 80% confluent 96 well microplate monolayer. This is some 3 fold less surface area exposed. If cytotoxic responses were mediated solely by surface interaction, it follows that a sphere would exhibit only a fraction of the effect. Spheroids are also unsuitable to high sensitivity or long term assays and develop necrotic cores if exceeding 400 µm in diameter. Their non-adherent nature also poses additional challenges in serial dilutions or other exercises requiring media transfer.

Despite these problems, determining the cytotoxicity of a particle is not a problem that can be ignored, as it has traditionally been a source of discrepancies between *in-vivo* and *in-vitro* experiments of haematite dusts <sup>273</sup>. Given the variability of the effect of other measures of differentiating particles including size-distribution and particle number, to reasonably expect downstream endpoints to be comparable such as oxidative stress and cytokine signalling profiles, cell death must be matched as closely as possible. It must also be expected that many insoluble particulates will be poorly distinguishable in effect <sup>167</sup>, even when acting through a multitude of pathways <sup>205</sup>. However, the general findings presented in this chapter suggesting a toxicity hierarchy of CuO > TiO<sub>2</sub> > Fe<sub>2</sub>O<sub>3</sub> and iron ore samples is consistent with similar experiments in the literature <sup>214,215</sup>.

A newer reagent, PrestoBlue (Life Technologies) resazurin based assay, replaces the MTS assay (Promega) in subsequent chapters, based on the findings in this chapter. The MTS assay requirement for two 96 well plates to complete one assay increased error due to multiple pipetting steps. The difficulty of obtaining IC<sub>50</sub> data also led to high concentrations of particulate sample being used. These experiments have established that the amount of sample required to reach IC<sub>50</sub> is not only physiologically irrelevant to environmental exposure but brings about model specific

limitations not present in the biology. For example, it is possible the particle layer affecting diffusion of media to cells may have been a major contributor to the IC50 values found. Therefore, the IC20 concentration data is more relevant. For these, exposures are started at 1000  $\mu\text{g}/\text{ml}$  ( $312 \mu\text{g}/\text{cm}^2$  for 100  $\mu\text{l}$  1:2 dilutions in a 0.32  $\text{cm}^2$  well) and therefore less optically dense. The IC20 concentrations while still high in mass terms, allow comparative toxicology of oxidative stress and cytokine responses to scale on a more accurate measure of interaction<sup>212</sup>. Secondly, laboratory upgrades from the FLUOStar Optima to the FLUOStar Omega (BMG Labtech) allow multiple measurements per well in an orbital track and the opportunity to perform top-down fluorescence measurements.

Given that the resazurin assay responds in both absorbance (600 nm) and fluorescence (excitation 540-570 nm, emission 580-610 nm) ranges, the selection of the fluorescence measurement and top-down optic emission reading provides the advantage of being less susceptible to the interference of particles, where individual particles or agglomerations obscure the bottom reading optic absorbance measurements. In the FLUOStar Omega, top-down a xenon flash lamp provides the excitation emission which passes through a filter into the clear bottom well. The diffuse light of this flash is blocked only by the average opacity of the suspended dust in the well and causes the fluorescence emission to occur throughout the media. When the top-down optic measures the fluorescence, there is little or no impact on the measurement from particles as they are at the bottom of the well.

Another significant advantage presented by the resazurin based assay as opposed to the MTS assay is that it is minimally cytotoxic by comparison, subsequently allowing downstream assays. The MTS-formazan product in the MTS assay is insoluble in water, causing purple needle shaped crystals to form in the cells unless an organic solvent is part of the assay kit, and the test is somewhat cytotoxic. PrestoBlue can therefore be used prior to both the Cytometric Bead Array Human Inflammatory Cytokines Kit (CBA HICK, BD Biosciences, USA) and the Luciferase assay (Promega) used to detect oxidative stress in AREc32 cells. Assay multiplexing in this way allows cell viability to be tied directly with these endpoints so that values can be normalized.

## 4. In-Vitro Comparative Toxicology of Inhalable Iron-Rich Particles from Mining Industry in Western Australia

### 4.1 Introduction

Australia exported approximately 505 million tonnes (Mt) of iron ore in 2012, placing it as the world's largest exporter. The industry's scope and growth has significant economic and environmental ramifications, largely affecting Western Australia where exports have doubled over the last five years to 2012 and continued growth is projected. In towns associated with iron ore export activity in Australia, fugitive dust has become a prevailing air quality hazard owing to semi-arid conditions and encroachment of housing development toward high volume shipping terminals. The town of Port Hedland is one such settlement, home to over 15,000 residents and is the region's largest port by tonnage, exporting 240 Mt per annum of material mined from the productive Pilbara region. Iron-rich particles account for up to 93% of total suspended particulates (TSP) in the town by volume <sup>2,4</sup>.

The current regulatory framework adopted by leading international bodies including the World Health Organization (WHO), US Environmental Protection Agency (USEPA) and the EU makes few distinctions between the health burdens of aerosols and liquids, nor their respective compositions bar a select few pollutants; ozone, nitrous oxides and sulphuric oxides. The focus has instead been to stratify particulate matter (PM) by size and set guideline limits governing the acceptable mean daily and annual concentrations. This format works well for urban air pollution and is targeted at the minimum concentration at which health effects are observable to a 95% confidence interval, known as the Air Quality Guideline (AQG) which is set by the WHO, although a threshold value which eliminates health burdens entirely may not exist <sup>12,48</sup>.

Meta-analyses of urban epidemiological studies serve as the basis for the AQG, and show smaller particles are more clearly associated with morbidity and mortality than larger fractions. The Australian Ambient Air National Environmental Protection Measure (NEPM) specifically governs PM<sub>10</sub> and < 2.5 µm diameter particles (PM<sub>2.5</sub>)

separately. PM<sub>10</sub> is not to exceed a 24 h mean concentration of 50 µg/m<sup>3</sup> and the PM<sub>2.5</sub> component is not to exceed a 24 h mean concentration of 25 µg/m<sup>3</sup>, nor a mean of 8 µg/m<sup>3</sup> per annum. Because of difficulties meeting these requirements, especially in proximity to the port facilities, the WA state government has proposed an interim lifting of site-specific PM<sub>10</sub> limits to 70 µg/m<sup>3</sup> in Port Hedland <sup>4</sup>.

Increasing the annual mean PM 2.5 concentration by 10 µg/m<sup>3</sup> may be expected to increase pulmonary, cardiovascular and all-cause morbidity and mortality by up to 10%, whereas the same mean increase limited to a 24 hour period can be expected to increase morbidity and mortality just 1% <sup>15</sup>. While dust storms occur with regularity in Port Hedland requiring exceptions in the NEPM air quality guidelines for natural events, the fibrotic potential of iron-rich particles must be assessed for residents and authorities to be aware of health risks mediated by ambient fine particulate matter. Lung fibrosis and obstructive diseases <sup>15,28,95,96,122,194,274</sup>, inflammatory responses <sup>189,212,232,275,276</sup> and cardiovascular <sup>45,73,117,277,278</sup> implications have all been associated with PM<sub>10</sub> and PM<sub>2.5</sub> inhalation, although prediction of long term health outcomes remains unclear by any other metric than size, though various factors have been proposed as indicators of fibrotic potential <sup>57,73,196,279</sup>. Inorganic transition metal such as iron may have unique modes of action and catalytic potentials <sup>132</sup>. New toxicological data specific to the area benefits both prediction of long term health outcomes and may shed light on contributors to acute toxicity to vulnerable populations, as well as rationalise dust mitigation actions which have their own environmental and economic costs <sup>80</sup>.

Before personal protective equipment was commonplace in the workforce, occupational lung disease, or siderosis, had been well associated with iron ore mining for the better part of a century <sup>17,122</sup>, and similar afflictions were also seen in steelmakers and welders <sup>138,280,281</sup>. Surface miners were found to be less afflicted by lung diseases than underground miners, whom inhaled extremely high quantities of dust when pneumatic drills came into use <sup>17</sup>. Unlike air pollution in large urban centres, epidemiological associations between industrial air pollution and morbidity and mortality in the general population have been harder to establish <sup>70,282</sup>, hindered by small population sizes and confounding factors such as smoking <sup>82,282</sup>.

This study aims to comparatively assess the *in-vitro* effects of iron-rich PM<sub>10</sub> derived from three major Pilbara mines; Newman, Mining Area C (MAC) and Yandi which deliver crushed ore to Port Hedland. Commercially available < 5 µm Iron(II,III) Oxide, Copper(II) Oxide, < 10 µm Silicon(IV) Oxide, < 50 nm Titanium(IV) Oxide, and 150 nm carbon black (CB) have been chosen as standards to compare against existing literature<sup>172,209,283</sup>. Benzo[a]Pyrene (B[a]P) has been included in cytotoxicity studies, being a potent aerosol carcinogen<sup>284</sup> and having the potential to be adsorbed onto particles<sup>285</sup> from industrial combustion sources<sup>286</sup>. Four human cell lines bearing relevance to the development of pulmonary disease were selected to carry out toxicity tests; the A549 lung epithelium-like adenocarcinoma, LL24 fibroblast like normal cell line, U937 monoblastic-like histiocytic lymphoma and the AREc32 transfected Antioxidant Response Element (ARE) reporter adenocarcinoma.

The development of high-throughput *in vitro* models that can predict pulmonary disease is sought after to supplement conventional analytical techniques that predict toxicological characteristics based on chemistry and minimise animal use<sup>162</sup>. *In-vitro* modelling is advantageous in its standardisation, use of human cell lines, cost-effectiveness and speed in comparison to animal studies and epidemiological studies. However, inconsistencies observed between *in-vitro* and *in-vivo* literature require some form of resolution<sup>91</sup>. To this end, we construct *in-vitro* experiments focusing on the limitations of modelling the lung parenchyma and associated phagocytic and inflammatory activity in response to long term particle residence. We find sensitivity is key in attempting to bridge the interpretation of cellular level biochemistry to tissue level disease using comparative toxicology, and that proliferative effects should be investigated more thoroughly. It is anticipated further data collection by high throughput bioassays with this understanding can allow meaningful risk assessment of ambient inorganic particulates with reduced ambiguity.

## 4.2 Materials and Methods

### 4.2.1 Chemicals and Reagents

As standard compounds the following from Sigma Aldrich, USA were obtained: Copper(II) oxide <5 µm, Iron(II,III) Oxide <5 µm, Iron(III) Oxide <5 µm, Silicon(IV)

Oxide <10 µm, Titanium(IV) Oxide <50 nm. Carbon Black < 150 nm powder was obtained from US Research Nanomaterials, Inc., USA. Benzy[a]Pyrene (B[a]P) (#B1760-100MG, Sigma Aldrich, USA) was used as a carcinogenic potentially adsorbed combustion product standard. Tert-Butylhydroquinone (TBHQ) (Sigma Aldrich, USA) was used as the NRF2 (Nuclear factor (erythroid-derived 2)-like 2) positive control in oxidative stress experiments. The S9 male rat liver enzyme mix (Sigma Aldrich S2067-1VL) was used to emulate normal metabolism of PAH compounds.

The PrestoBlue reagent (#A-13261, Life Technologies, USA) was obtained for cell viability experiments. The Luciferase Assay System experimental reagents were acquired as kit (#E4030, Promega USA) for identifying response to oxidative stress in the AREC32 cell line. The Human Inflammatory Cytokine Kit was used to detect interleukin expression (#551811, BD Biosciences, USA). Cells were fixed in glutaraldehyde prior to electron microscopy (Sigma Aldrich, USA).

#### 4.2.2 Particle Extraction and Sterilisation

Representative iron ore stockpile samples were supplied from three major mining sites in the Pilbara region in Western Australia courtesy of BHP Billiton; Newman Hub Mine (Newman), Mining Area C (MAC) and Yandi Mine (Yandi). The supplied samples were sieved to < 45 µm by ChemCentre WA (CCWA). To sieve the samples further down to PM<sub>10</sub>, an ultrasonic sieve tower and accompanying custom 10 µm electroformed sieve was used (Precision Eforming LLC, New York, USA).

To preserve as much surface chemistry as possible while reducing bacterial and fungal interference, sterilization was carried out based on fractional sterilization methodology. Sieved material was collected into 50 mL Falcon conical tubes (BS Biosciences, USA) and heated to 60 °C for 15 minutes before being allowed to cool at room temperature for 24 hours, repeated over three successive days. This negates the need for high temperature, pressure and moisture conditions under traditional autoclaving which may remove VOC and or other organic compounds. However, experiments conducted at CCWA show VOC are unlikely to remain adsorbed onto the iron ore samples naturally.

#### 4.2.3 Particle Size Distribution Analysis

Particle size profiles for the sieved PM<sub>10</sub> iron ore samples were obtained on a Malvern Mastersizer 2000 (Malvern, UK) located at the Department of Chemical Engineering, The University of Queensland. Approximately 200 mg of PM<sub>10</sub> was dispersed in water and a particle Refractive Index of 2.94 and Absorption of 0.1 assumed. Size measurement ranged between 0.02 and 2000 µm.

#### 4.2.4 Particle Solubility Analysis

To assess particulate solubility in culture medium and the effect of cell type on metal ion leaching, particulates were exposed to cell cultures before extraction of media for measurement. Cells were plated at 70% confluence in 6 well plates over 48 h in 400 µL of media, at a concentration of 45 µg/mL for copper (II) oxide and 180 µg/mL for all other samples. A 1 mL sample of media was then extracted using a 0.22 µm filter and diluted to 5 mL with PBS. Inductively coupled plasma mass spectrometry (ICP-MS) was then performed to analyse for free metal ion isotopes. The isotopes detectable by this method were <sup>48</sup>Ti, <sup>56</sup>Fe, <sup>57</sup>Fe, <sup>63</sup>Cu and <sup>65</sup>Cu.

#### 4.2.5 Electron Microscopy

Cells were grown on 12 well plates and incubated for 96 hours with samples. Media was drained from the cells and fixed with glutaraldehyde. Post fixation cells were cured with osmium tetroxide and baked in resin for four hours, then left to solidify overnight. Resin was then mounted and cut on an ultramicrotome (Lecia UC61, Germany) to 40 nm for observation by transmission electron microscopy (JEOL 1010, Japan) on 400 square mesh copper grids (ProSciTech, Australia).

#### 4.2.6 Electron Density Spectroscopy

The local chemistry of the particle microstructures were investigated by Energy-dispersive X-ray spectroscopy (EDS) using an FEI Tecnai-F20 FEG TEM equipped with a Gatan image filter. Particles were suspended in ethanol and ground with a mortar and pestle to achieve fines small enough for analysis. The particles were then transferred to lacey carbon grids for analysis.

#### 4.2.7 Cell Culture

The A549 pulmonary type I/II-like epithelial adenocarcinoma (ATCC CCL-185), LL24 pulmonary normal fibroblasts (ATCC CCL-151) and U937 monoblastic-like histiocytic lymphoma (ATCC CRL-1593.2) were used to represent lung epithelial, connective and immunological cells, respectively. A transgenic cell line to indicate electrophilic and oxidative potential *in vivo* was also employed; AREc32 (CXR Biosciences, Scotland), a transgenic Nrf2 mediated Antioxidant Response Element (ARE) luciferase reporter, based on the MCF7 mammary adenocarcinoma cell line.

The A549, LL24 and AREc32 cell lines were cultured in F-12K medium (#21127, Life Technologies, USA) supplemented with 10% foetal bovine serum (FBS), 100 IU/mL penicillin, 100 µg/mL streptomycin, and 10 mg/mL amphotericin B (#A9528-50MG, Sigma Aldrich, USA). U937 was cultured in RPMI 1640 medium (#72400, Life Technologies, USA) supplemented with 10% foetal bovine serum (FBS), and 100 IU/mL penicillin, 100 µg/mL streptomycin, 10 mg/mL amphotericin B (#A9528-50MG, Sigma Aldrich, USA), 2mM L-glutamine, 1mM Sodium pyruvate and 10mM HEPES buffer.

Cells were cultured in 75 cm<sup>2</sup> tissue culture treated flasks (Corning, USA) at 37 °C in humidified 5% CO<sub>2</sub>, 95% air atmosphere. A549 and LL24 medium was changed every 2-3 days and split every 5 days. As they are adherent, cells were harvested for seeding using trypsinization and washed in Phosphate Buffered Saline (PBS). U937 was cultured in suspension and maintained in at 2 x 10<sup>5</sup> to 1 x 10<sup>6</sup> cells/mL by passage every 4 days.

For seeding and exposure incubation, cells were plated onto opaque flat bottom 96-well plates (Becton Dickinson, USA) at 70% confluency (100 µl/well, 2x10<sup>5</sup> cells/mL) and incubated for 24 h prior to the particle exposure time period at 37 °C under sealing film (Corning, USA).

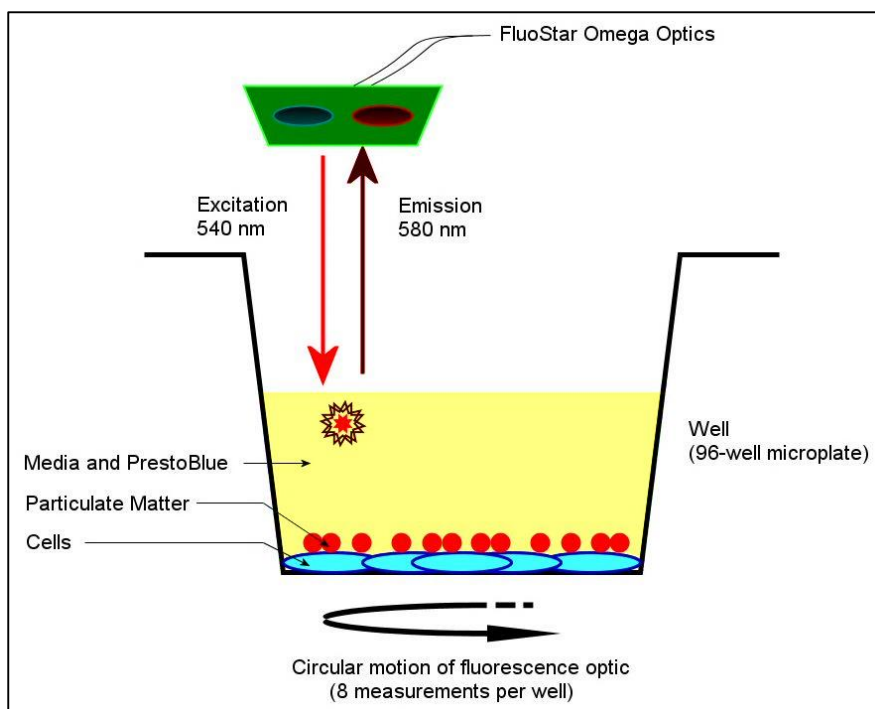
Differentiation of U937 to a mature macrophage-like morphology can be induced by exposure to phorbol esters<sup>267</sup>. For this purpose, differentiation was induced during the seeding period by exposure to 30 ng/mL of Phorbol Myristic Acid (PMA) for 48 h.



#### 4.2.8 Cell Proliferation Assay

Cytotoxicity of particulate matter was measured using a cell survival resazurin assay, PrestoBlue. After seeding incubation, cells were exposed to a 2 x serial dilution of particulate matter suspension down 8 rows. To achieve the first well concentration expressed as  $312.5 \mu\text{g}/\text{cm}^2$  (unless CuO, at  $78.1 \mu\text{g}/\text{cm}^2$ ),  $100 \mu\text{L}$  of  $2 \text{ mg}/\text{mL}$  (CuO,  $0.5 \text{ mg}/\text{mL}$ ) suspension was added to  $100 \mu\text{L}$  of media per well of an area  $0.32 \text{ cm}^2$ . Incubation with particulate matter was then continued until measurement for up to 96 h, again under sealing film. For measurement,  $10 \mu\text{L}/\text{well}$  of PrestoBlue reagent was added to the plates and incubated for 1 h (LL24) or 30 minutes (A549, U937) at  $37^\circ\text{C}$ . Spectrophotometric analysis was then conducted using the FluoStar Omega microplate reader (BMG Labtech, Germany), using the top-down fluorescence optic ( $540 \text{ nm}$  excitation,  $580 \text{ nm}$  emission) configured to average 8 pulses in a circular pattern per well.

This particular method was developed to minimize particulate matter interference. The elimination of washing reduced toxicity false-positive effects caused by the mechanical abrasion of cells by the particulate matter during washing. To negate optical interference by dusts, the top down fluorescence approach avoids the requirement for a clear optical path through the bottom of the plate, where particulate matter effectively settles due to the extended exposure times. This is described in Figure 36.



**Figure 36:** Depiction of strategy to avoid optical interference of particles by using top down cytotoxic measurement of a 96-well plate and settled particulate matter.

#### 4.2.9 Oxidative Stress Assay

Gently, cell media was removed from the 96 well sample plate. Cells were rinsed in PBS and 20  $\mu\text{L}$ /well of Luciferase Assay System lysis agent was added and incubated at room temperature for 10 minutes. Briefly, 100  $\mu\text{L}$  of luciferase assay reagent was then added to the wells and immediately analysed on the FluoStar Omega plate reader in fluorescence mode.

#### 4.2.10 Flow Cytometric Cytokine Quantification

Cytokine standards were prepared as follows; each vial of lyophilized Human Inflammatory Cytokine Standards was reconstituted with 0.2 mL of Assay Diluent to prepare a 10x bulk standard. This was equilibrated for at least 15 minutes before making dilutions. Dilutions were mixed by pipetting. Serial dilutions were then performed from 1:1 through 1:256 in a 2x serial dilution, starting with 900  $\mu\text{L}$  of Assay Diluent and 100  $\mu\text{L}$  of 10x bulk standard in the Top Standard tube and 300  $\mu\text{L}$  transferred to successive tubes thereafter.

After cytotoxic measurement, 20  $\mu\text{L}$  was taken from each sample well on the 96-well microplate into Eppendorf tubes. This was mixed with 8  $\mu\text{L}$  per sample of CBA beads

comprised of the 6 detection bead types, after an equal amount of PE detection reagent to the CBA beads was added and vortexed. The mixture was then incubated at room temperature away from light for 3 hours. 150  $\mu\text{L}$  of wash buffer was then added to each sample and centrifuged at 400 x g for 3 minutes. Precipitate was resuspended in 200  $\mu\text{L}$  wash buffer. This was then analysed on the Accuri C6 flow cytometer to count over 1,000 events. Data was then processed on BD's FCAP Array v3 software.

### 4.3 Results

#### 4.3.1 Sample Size Distribution

Ultrasonically sieved iron ore samples (MAC, Yandi and Newman) were analysed for particle size distribution. The sieving method was found to be effective in extracting  $\text{PM}_{10}$ , particles of 7-10  $\mu\text{m}$  made up the bulk of the sample, while sub-micrometre particles were present in all samples (Figure 37) and most numerous. This indicates both  $\text{PM}_{10}$  and  $\text{PM}_{2.5}$  mediated effects are present in the ore samples.

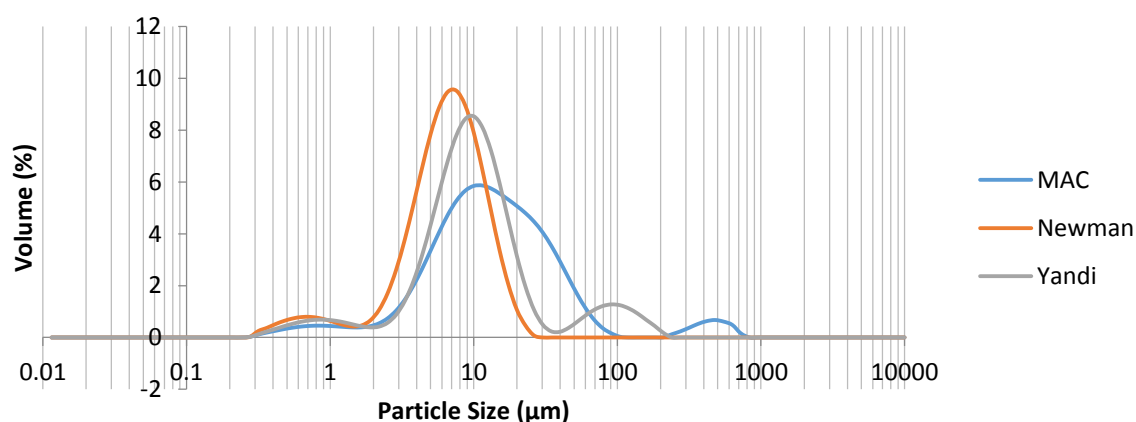


Figure 37: Distribution of particles ultrasonically sieved with a 10  $\mu\text{m}$  electroformed mesh obtained on a Malvern Mastersizer 2000.

#### 4.3.2 Sample and Standard Electron Microscopy

Electron microscopy was performed on the  $\text{Fe}_3\text{O}_4 < 50 \text{ nm}$  sample, and ore samples with cells. Large size heterogeneity is apparent in all the particle standards, and the ore samples as is expected from size distribution analysis. No fibre-like morphologies were seen in the ore samples, indicating the sieving process is less likely to cause significant distortions in inertial aerodynamic settling of particles which

differ in higher aspect ratio particles. Particles under 1  $\mu\text{m}$  begin to be dominated by diffusive effects and are unaffected by aerodynamic shape <sup>26</sup>.

The interaction between the  $\text{Fe}_3\text{O}_4$  standard and the lung epithelial A549 cell line in Figure 38 and lung fibroblast LL24 cell line in Figure 39 show particles intersecting with the cells and being internalised into the cytoplasm. Figure 38, top left, shows opacities around a particle within the cell, possibly indicating a vesicle. The most common observation is as seen in Figure 38, right, where particles become entrapped by elongated membrane structures. Similar results with haematite particles have been regarded as cytoplasmic uptake in the literature <sup>187</sup>.

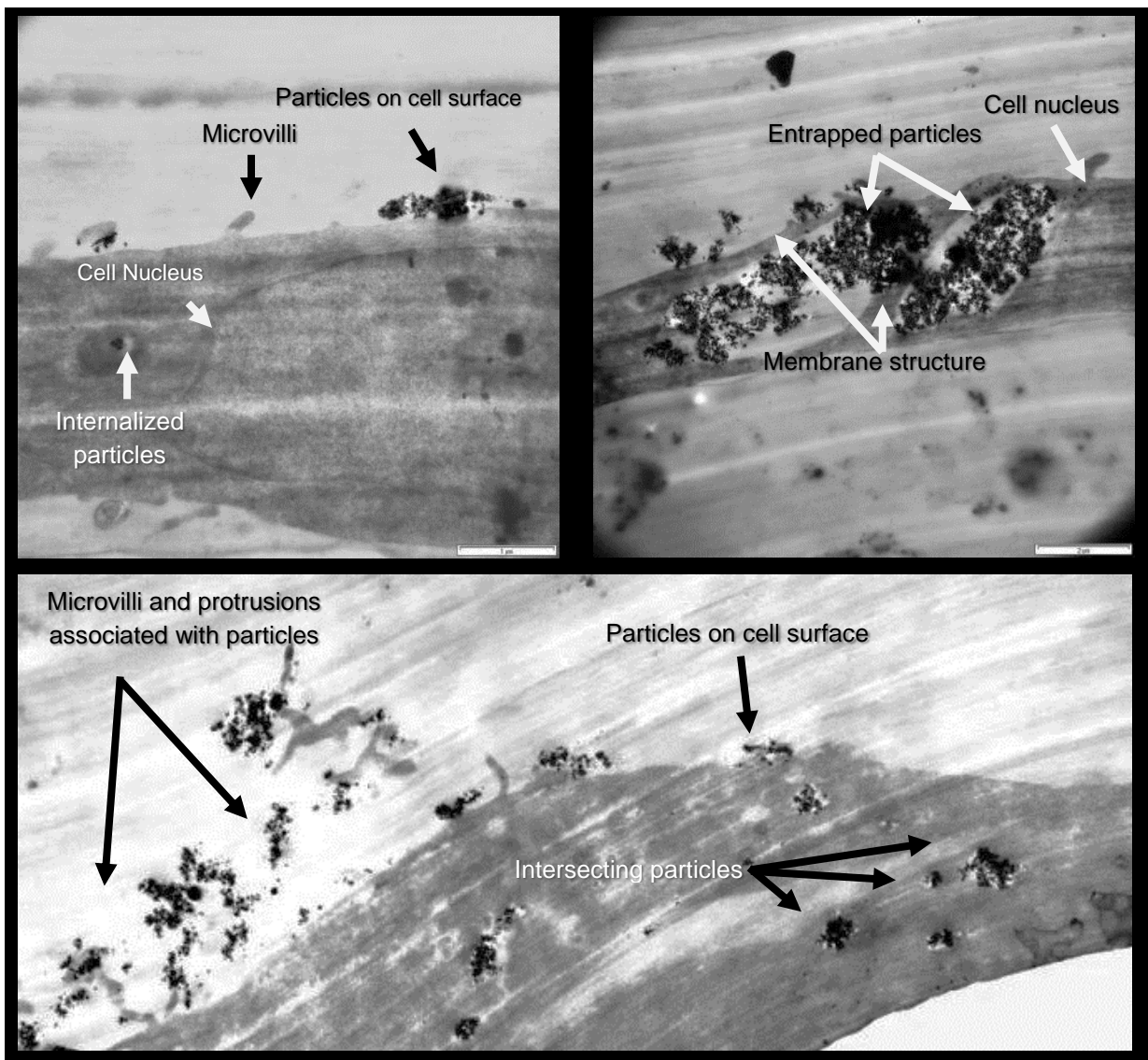


Figure 38: TEM images of A549 cells after 96 h exposures to the  $\text{Fe}_3\text{O}_4 < 50 \text{ nm}$ . Top Left, potential uptake of particles into the cytoplasm. Microvilli and particles are also visible outside the cell. Scale bar  $1 \mu\text{m}$ . Top Right, horizontal membrane structure entrapping clusters of iron ore. Scale bar  $2 \mu\text{m}$ . Bottom: extensive apical surface membrane development and possible internalisation of particulate agglomerates.

In the LL24 cells, similar membrane structures where particles intersect the cells were observed but how this process occurs is ambiguous, as seen in Figure 39. However, this form of uptake still likely to be driven by membrane bound endosomes if it is not membrane extension around the particles, with little resultant biochemical interaction<sup>287</sup>. The recurrent development of this structure supports literature findings that particulate loads stimulate apical membrane extension in epithelial lung cells and may also apply to fibroblasts<sup>288</sup>.

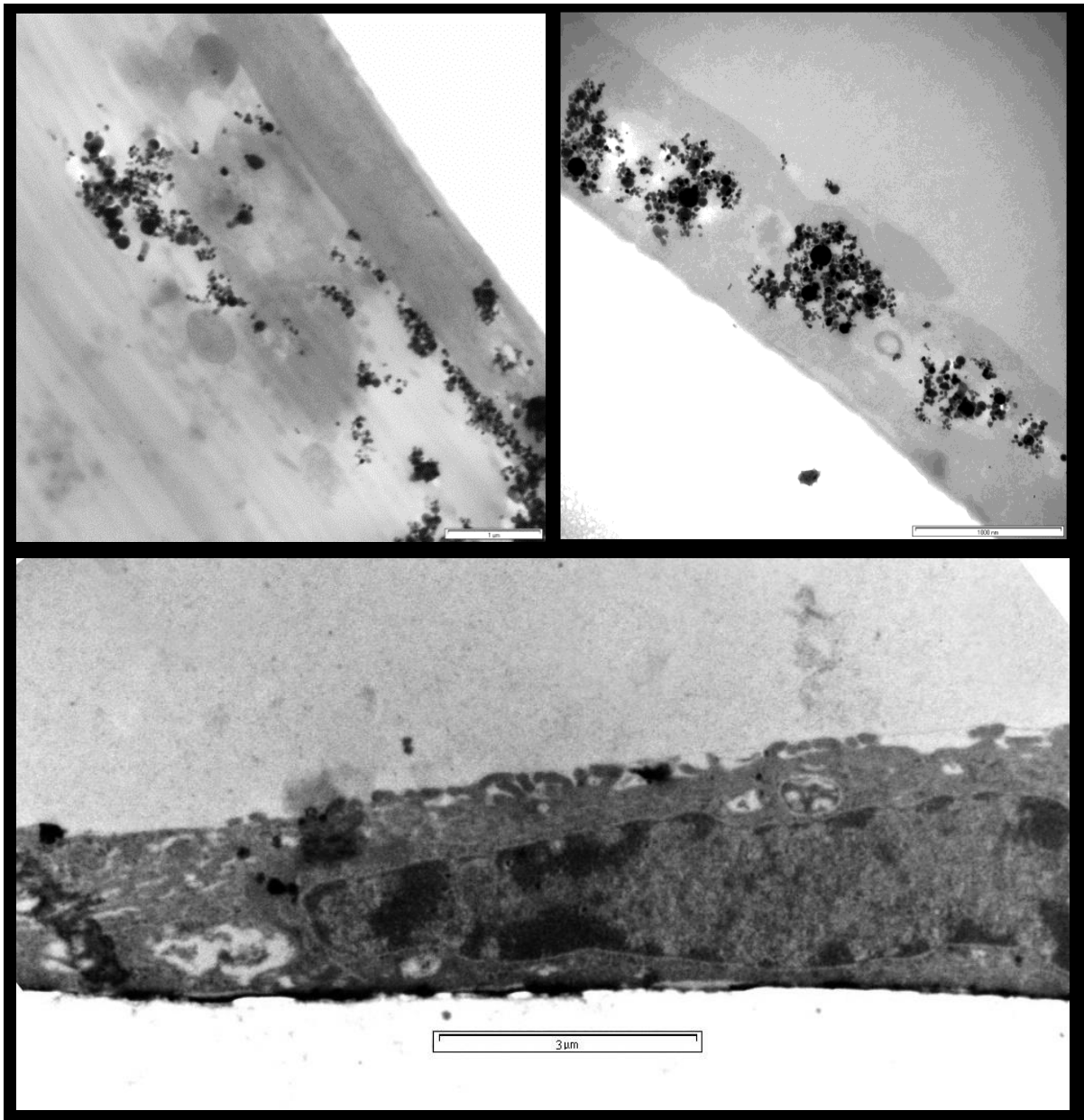


Figure 39: TEM image of LL24 cells after 96 h exposures to  $\text{Fe}_3\text{O}_4 < 5 \text{ nm}$  samples. Top Left, apical membrane extension interacting with particle agglomerations. Top Right, complex membrane bound inclusions of particles. Scale bars  $1 \mu\text{m}$ . Bottom staining reduces visibility of particle interactions however highlights the rough and complex surface of the LL24 cell membrane surface. Scale bar  $3 \mu\text{m}$ .

Exposure of A549 cells to MAC, Yandi and Newman ores and  $\text{TiO}_2$  is shown in Figure 40. The ore sample sizes varied containing considerably larger somewhat irregular chunks than the standards. These agglomerated particles were nonetheless found to interact closely with the cell membrane, although fewer clear examples of cytoplasmic internalisation could be found.

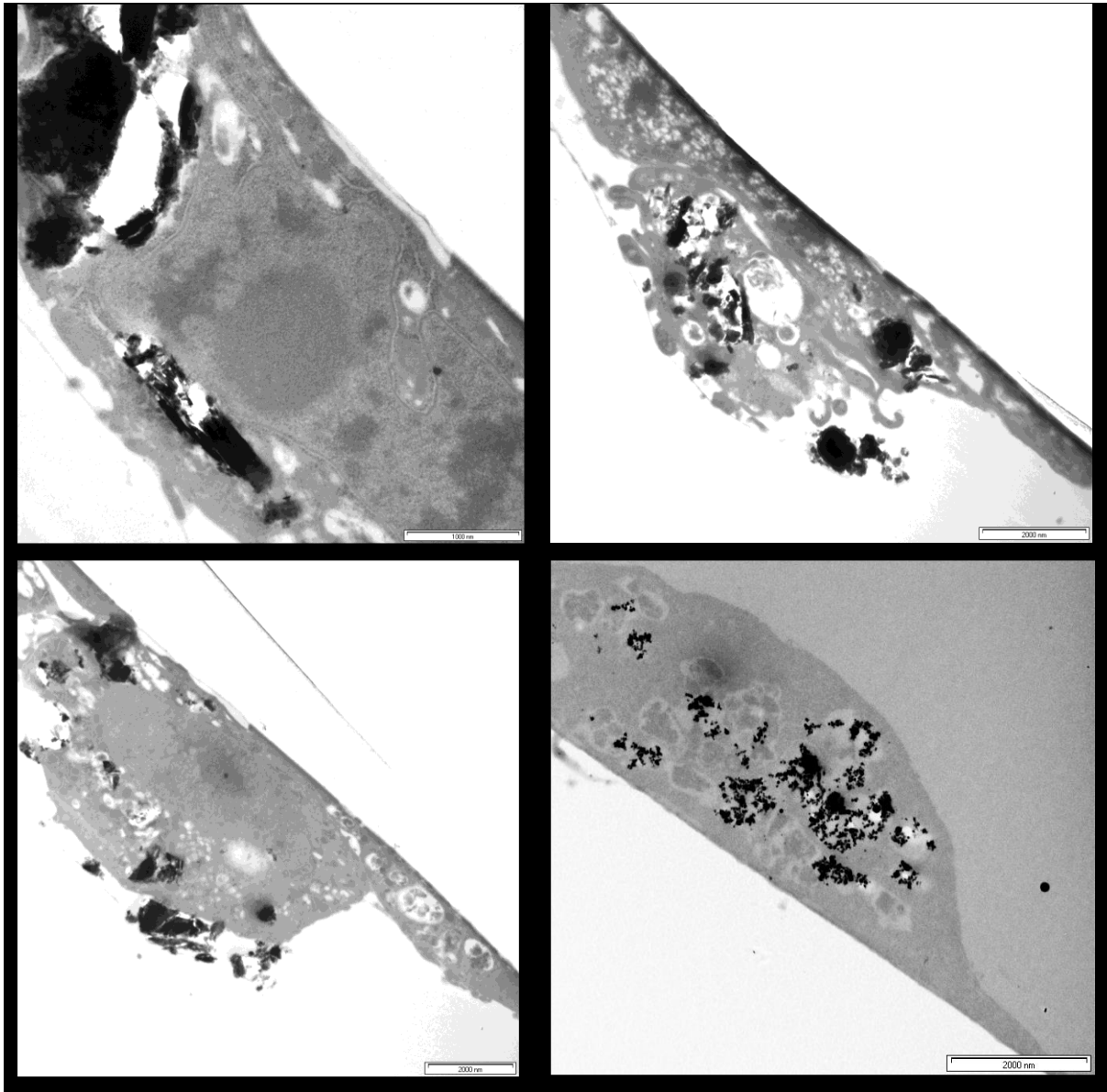
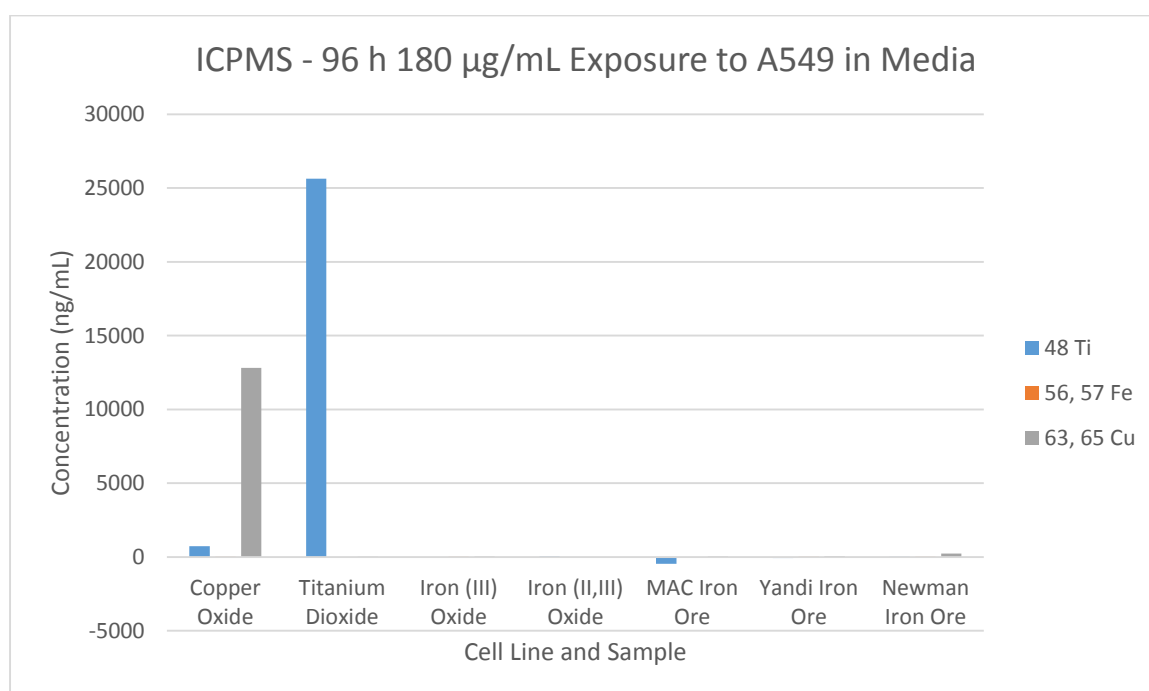


Figure 40: TEM image of A549 cells after 96 h exposures to Yandi (Top Left) and Newman (Top Right) and MAC (Bottom Left)  $PM_{10}$  and  $TiO_2 < 50$  nm (Bottom Right), showing complex apical membrane interactions including internalisation of particulate agglomerates. Scale bar 1000, 2000 nm.

#### 4.3.3 Sample and Standard Solubility

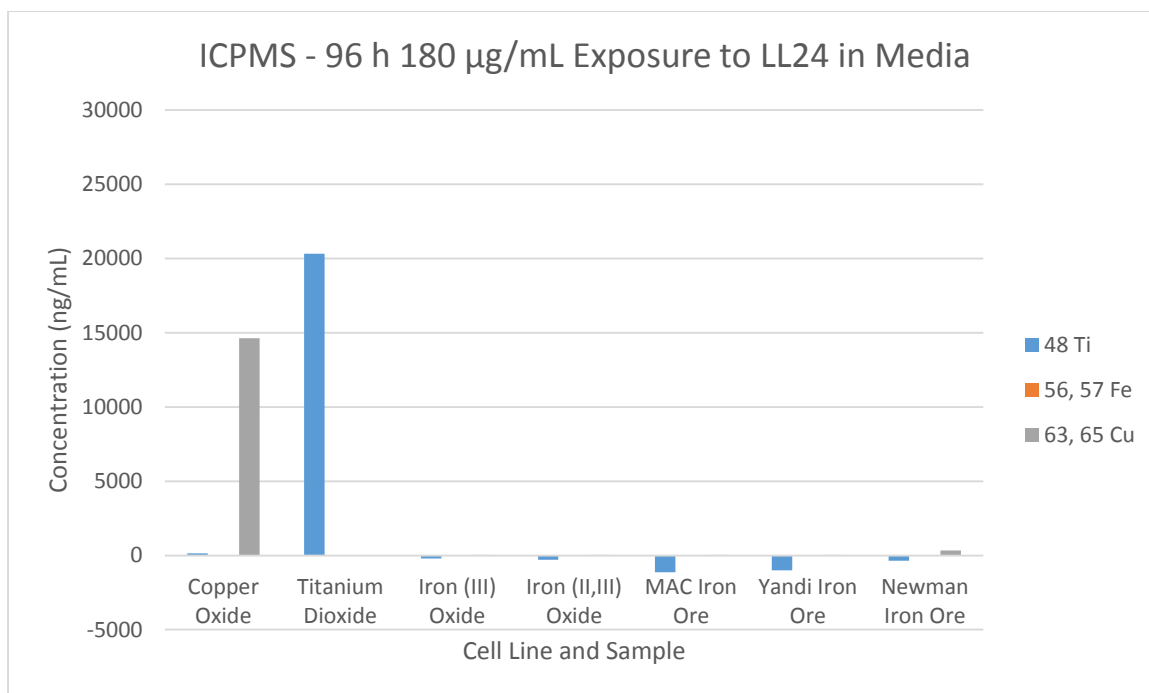
Solubility analysis was carried out on samples using ICP-MS which had been exposed to cell lines for 96 h, and then resuspended in PBS for analysis. This helped determine if intracellular compartment conditions played a role in the solubilisation of metal oxides. Samples prepared with A549 cells showed that TiO<sub>2</sub> and CuO were the only samples tested with an appreciable free-ion component (see Figure 41), once isotope counts were normalised by abundance and background concentrations subtracted.



**Figure 41:** ICP-MS detection of free <sup>48</sup>Ti, <sup>56</sup>Fe, <sup>57</sup>Fe <sup>63</sup>Cu and <sup>65</sup>Cu ions using MAC, Yandi, Newman Iron ores, Fe(II,II)O < 5 µm and TiO<sub>2</sub> < 50 nm at 180 µg/mL, CuO < 5 µm at 45 µg/mL. Incubated with A549 cells 37 °C 96 h.

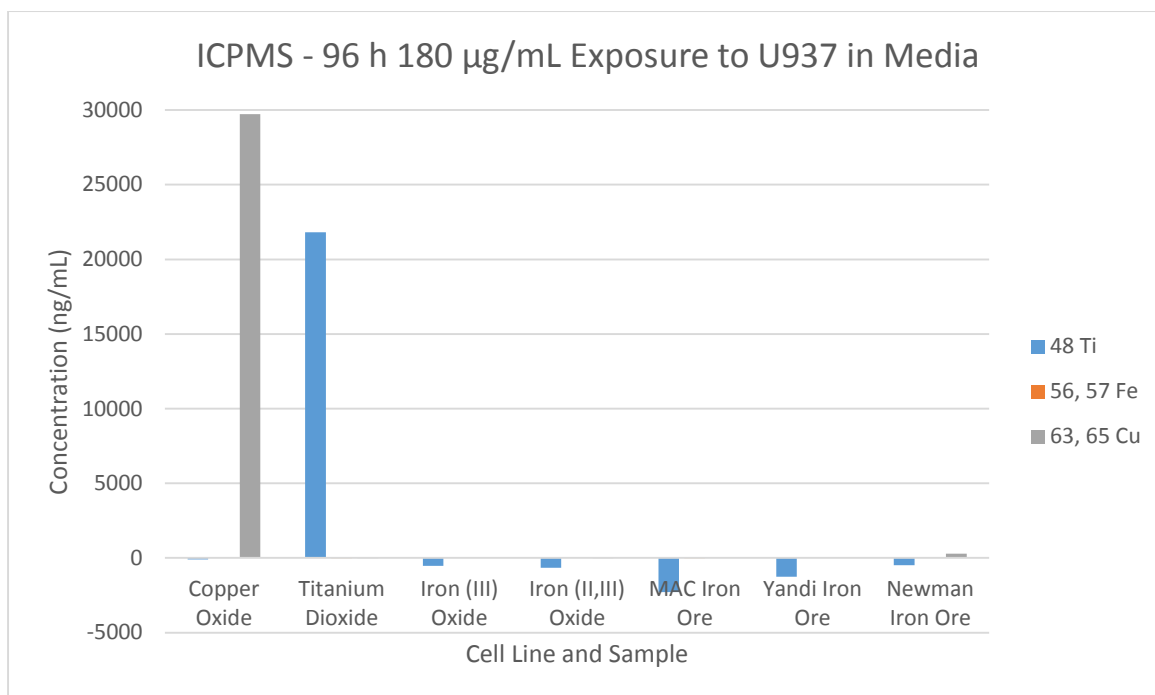
The solubility of TiO<sub>2</sub> and CuO did not change when cultured with LL24 cells, with differences being within limits of differences caused by the error in cell proliferation and viability (Figure 42).





**Figure 42:** ICP-MS detection of free Ti, Fe and Cu ions using MAC, Yandi, Newman Iron ores, Fe(II,II)O < 5 µm and TiO<sub>2</sub> < 50 nm at 180 µg/mL, CuO < 5 µm at 45 µg/mL. Incubated with LL24 cells 37 °C 96 h.

Incubation of particles with U937 cells, while failing to liberate any iron ions, dramatically increased the release of Cu ions by 230%, relative to A549 (see Figure 43). This implies immunological activity towards CuO inhalation would greatly increase the toxicity of the compound, independent of effects caused by biofluids. Moreover, the solubility of TiO<sub>2</sub> and iron oxides was unaffected, making this form of screening useful in discriminating against particulates which may unexpectedly be solubilised in the lysosomal environment of the macrophage.



**Figure 43:** ICP-MS detection of free Ti, Fe and Cu ions using MAC, Yandi, Newman Iron ores, Fe(II,II)O < 5 µm and TiO<sub>2</sub> < 50 nm at 180 µg/mL, CuO < 5 µm at 45 µg/mL. Incubated with U937 cells 37 °C 96 h.

The sparing solubility demonstrated by CuO and TiO<sub>2</sub> in culture media is appreciable, though still far lower than quartz and its polymorphs which range from 3-40 mg/L<sup>289</sup>. Nevertheless, it is a significant finding, as in water CuO is insoluble at physiological temperatures and pressure<sup>290</sup>. While occasionally observed, the solubility of CuO in media is often not addressed<sup>210</sup>.

#### 4.3.4 Elemental Analysis

EDS was carried out to ascertain the composition of particles seen to interact with cells under TEM (see Figure 44). Elemental analysis aids in confirming particle identity, where images may contain interfering materials with similar electron density<sup>291</sup>. The sharper imagery of the FEI Tecnai-F20 in comparison to the JEOL 1010 also allowed better visualization of the particles. One or more points were scanned by EDS to identify the bulk material as opposed to silica and other minor compounds.

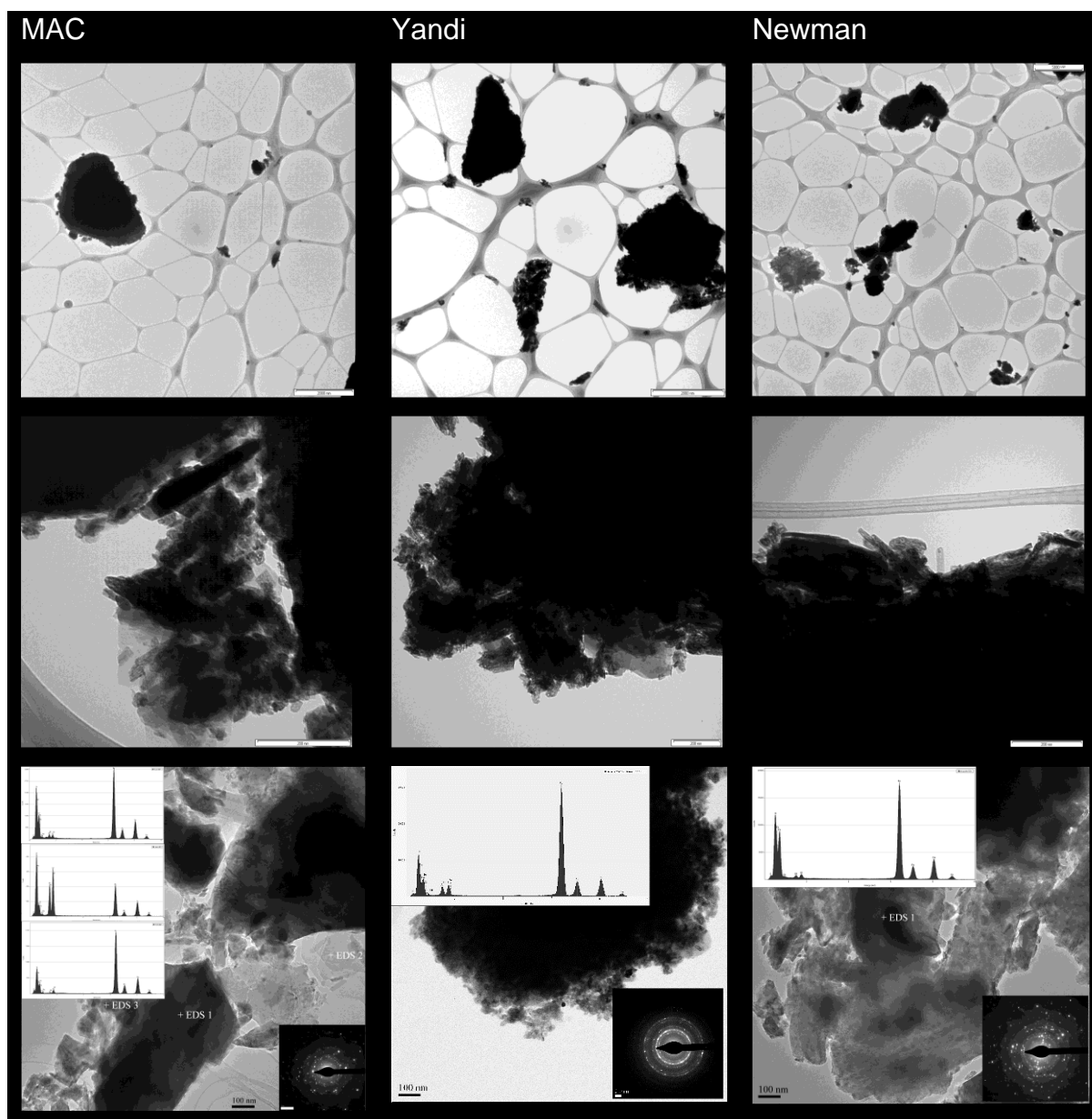


Figure 44: TEM images of iron-ore samples. Scale Bar: Top Row: 2000 nm; Middle Row 200 nm, Bottom Row: EDS Sample points.

The spectra produced by the EDS measurement indicated a very similar iron oxide composition for all three samples, with minor compounds of aluminosilicates and cupric oxides as would be expected from rock samples (see Figure 45).

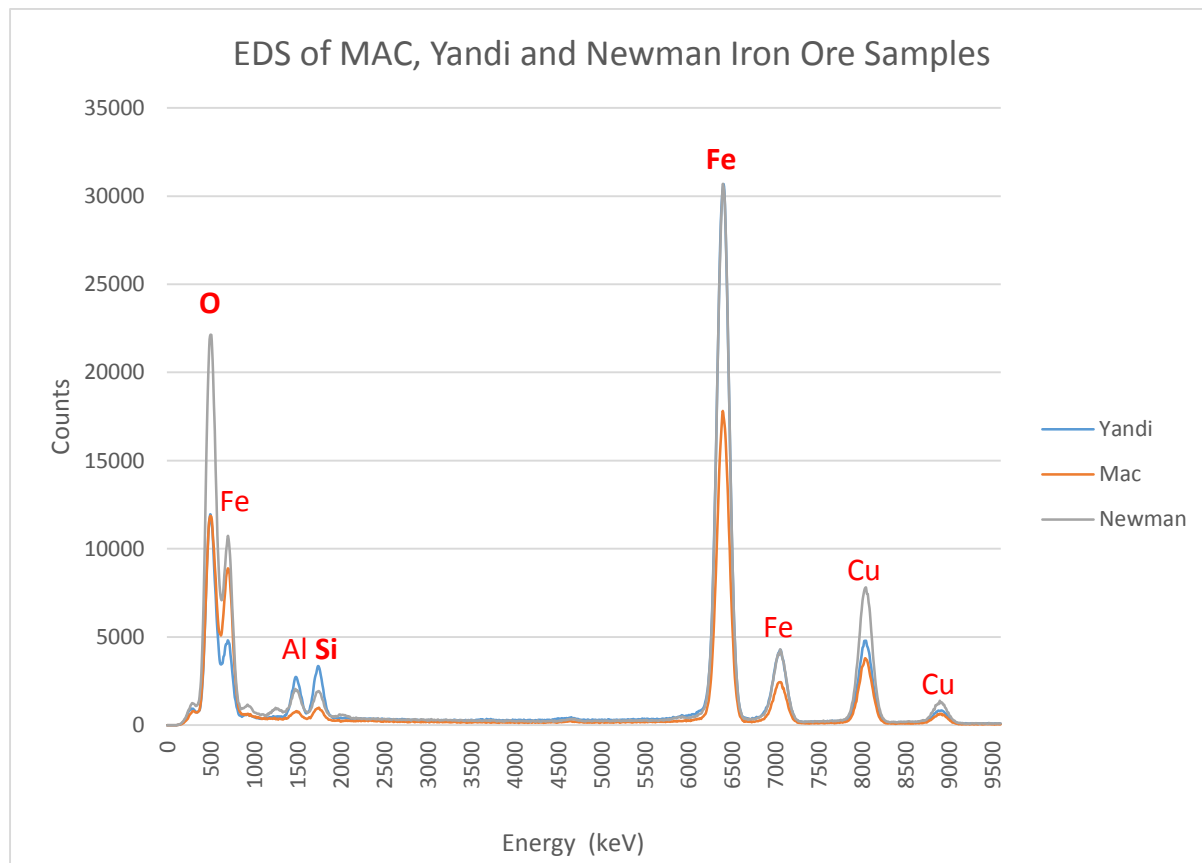


Figure 45: EDS of MAC, Yandi and Newman ore samples. Differences in spectra height are not necessarily related to stoichiometry, and reflect penetration through the bulk sample.

#### 4.3.5 Cell Proliferation

The interference of particulate matter in the proper functioning of *in-vitro* assays is quickly becoming a recognized problem<sup>165,166,222</sup>, however the development of mitigation strategies is still to gain traction in nano and micron-size particle *in-vitro* research. Failure to take interference into account leads to problems, in the form of overestimated toxicity in formazan MTT assays and underestimation in Lactate Dehydrogenase (LDH) assays<sup>166</sup>.

The iron ore samples and other particulate standards were found to interfere with optical assays, presenting opaque solid phase agglomerations blocking correct absorbance values in the popular formazan MTT assay. The inextricability of particle

agglomerations and cells shown in TEM (Figure 38-Figure 40) provided evidence that washing steps would not be able to remove particles without destroying the cell membrane, creating false positives. Instead, a 96 well plate format resazurin based fluorescence assay was used with modifications. The washing step was discarded, and the wells assayed directly using only the top-down fluorescence optic. This ensured particulate matter settled at the bottom of the well did not block excitation and emission light in the upper volume of the well. Plate sealers were also used during cell culture incubations to eliminate evaporative edge effects over long exposure periods, which was found to impact sensitive assays over 24 h. This method allowed high sensitivity despite maintaining a high throughput measurement process in long exposure, high PM concentration conditions.

There is ongoing discussion about suitable dosing metrics for nano and micrometre size particles, as which metric is chosen depends on how toxicity is assumed to be mediated. For completely soluble compounds, the relationship between mass by volume concentration and toxicity remains constant. For insoluble particles, this is not necessarily the case if toxicity is mediated by particle-cell contact. Assuming even distribution is achieved, mass by cell surface area exposed can rectify this to some degree, though significant surface adsorption/desorption kinetics and catalytic effects can make material surface area by cell surface area the most desirable measure for a given material. For the purposes of this study  $\mu\text{g}/\text{cm}^2$  is used, providing sufficiently consistent relationships between samples and particle standards. Using particle mass by surface area also provides a compromise in comparing cell biochemistry mediated interactions to macrophage phagocytic interactions, which are influenced by mass load, and enhances throughput for biomonitoring purposes where the impact of airborne  $\text{PM}_{10}$  and  $\text{PM}_{2.5}$  particulate surface areas may not be cost effective to characterise.

The particle standards used were  $\text{Fe}_3\text{O}_4 < 5 \mu\text{m}$ ,  $\text{TiO}_2, < 50 \text{ nm}$ ,  $\text{SiO}_2 < 10 \mu\text{m}$  and carbon black  $< 150 \text{ nm}$  (CB).  $\text{CuO} < 5 \mu\text{m}$  was also compared as a standard at  $\frac{1}{4}$  the given concentration of the other standards. Ultrasonically sieved  $\text{PM}_{10}$  iron ore samples MAC, Yandi and Newman were tested alongside. The same samples and standards were used in conjunction with exposure to B[a]P, a carcinogenic Polycyclic Aromatic Hydrocarbon (PAH), to understand the toxicity of potentially

adsorbed organic combustion products. Samples were prepared in media as suspensions, before serial dilution in 96 well plates.

It was found that low acute cytotoxicity was elicited by all samples and particulate standards, in comparison to typical mass concentrations for soluble toxicants. Despite different morphological and metabolic characteristics, similar profiles were obtained both from LL24 (Figure 46) and A549 cells (Figure 48). Amongst the samples, the iron-ore samples,  $\text{Fe}_3\text{O}_4$  and  $\text{TiO}_2$  toxicity was mediocre at this dose range, with  $\text{SiO}_2$  demonstrating some 50% greater toxicity. CuO exhibited an order of magnitude higher cytotoxicity and was therefore compared at a quarter of the standard concentration of the other particulates.

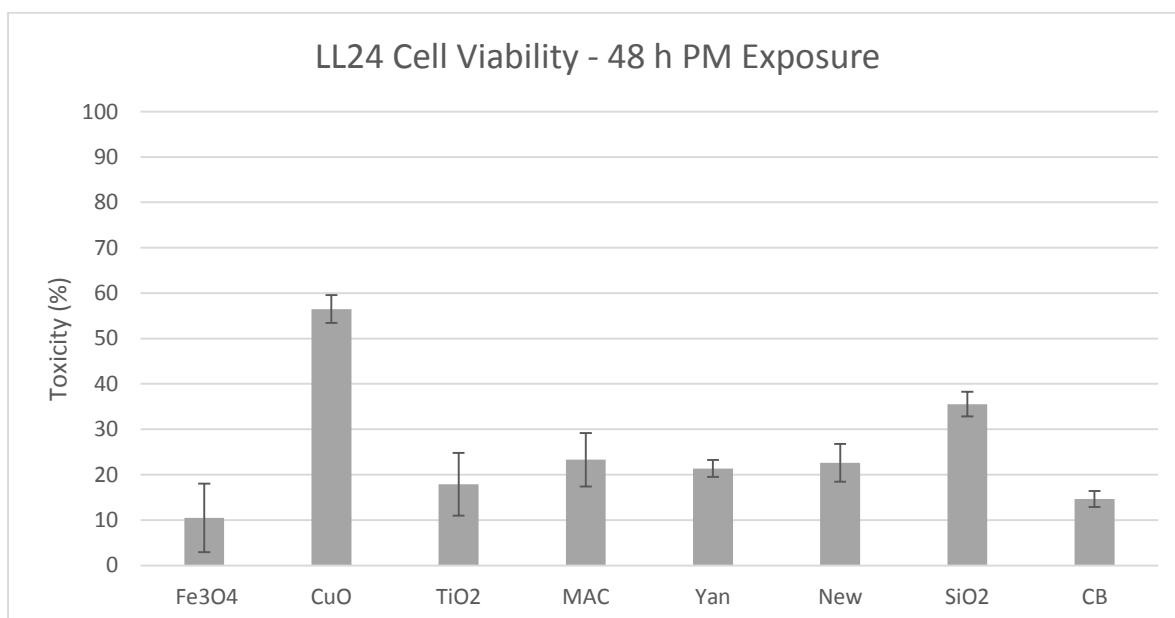


Figure 46: LL24 48 h particle toxicity. CuO  $39 \mu\text{g}/\text{cm}^2$ ,  $156 \mu\text{g}/\text{cm}^2$  other particulates.

Cytotoxic response is increased similarly across all particles in LL24 in response to coexposure with  $50 \mu\text{M}$  B[a]P, shown in Figure 47. There does not appear to be any difference in interaction specifically tied to a given particle.

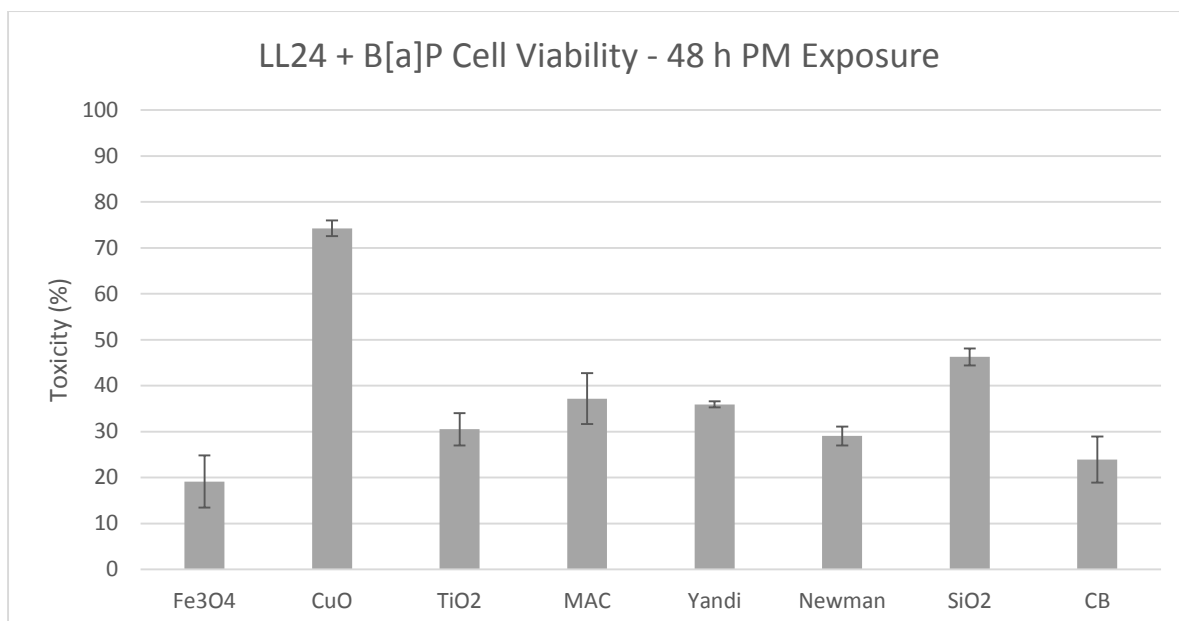


Figure 47: LL24 48 h + 50  $\mu\text{M}$  B[a]P particle toxicity. CuO 39  $\mu\text{g}/\text{cm}^2$ , 156  $\mu\text{g}/\text{cm}^2$  other particulates

The differences in cytotoxicity between samples remained similar in the A549 cells, although greater sensitivity to CB was observed. SiO<sub>2</sub> demonstrated up to 90% greater toxicity than the iron-ore sample, TiO<sub>2</sub> and Fe(II,II)O band (see Figure 48). The toxic response to CuO was marginally less.

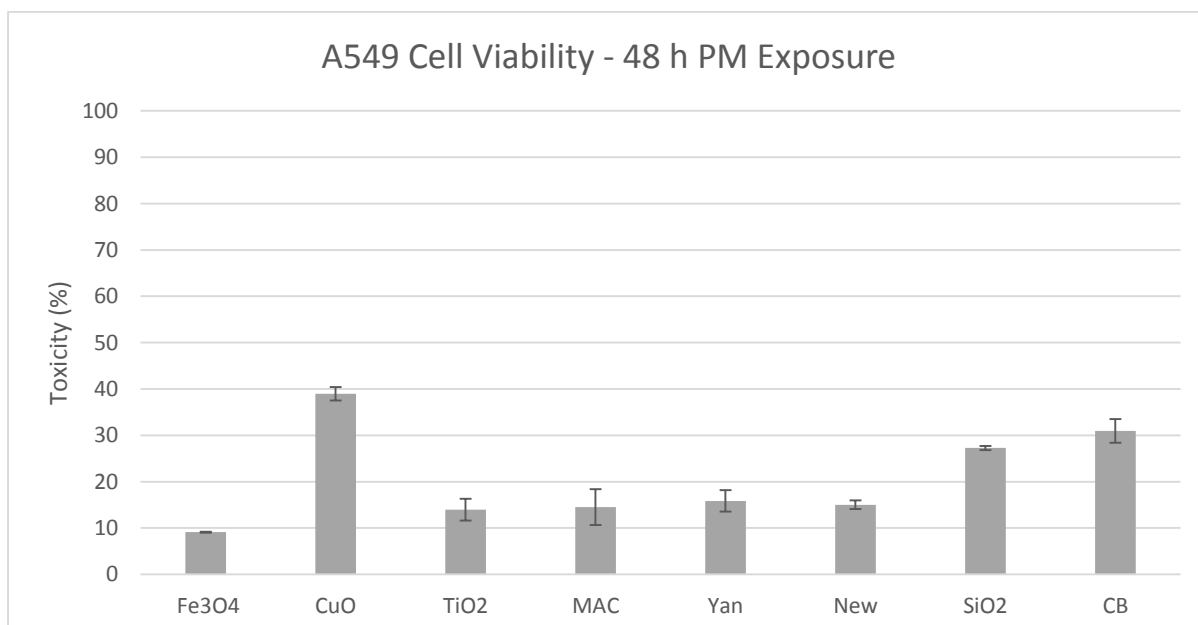


Figure 48: A549 48 h particle toxicity. CuO 39  $\mu\text{g}/\text{cm}^2$ , 156  $\mu\text{g}/\text{cm}^2$  other particulates

The metabolic activity of A549 cells is limited, and it has been shown that metabolites are an important factor in B[a]P mediated toxicity, therefore 5% S9 rat liver enzyme mix was added. While S9 has been previously shown not to increase the toxicity of iron oxide nanoparticles<sup>292</sup>, its presence has been shown to enhance the DNA damage potential of organics in airborne particulate matter<sup>293</sup>. It appeared that CuO toxicity was enhanced to a similar level shown by the LL24 cell line (Figure 49), however the iron-ore samples and SiO<sub>2</sub> remained relatively unchanged.

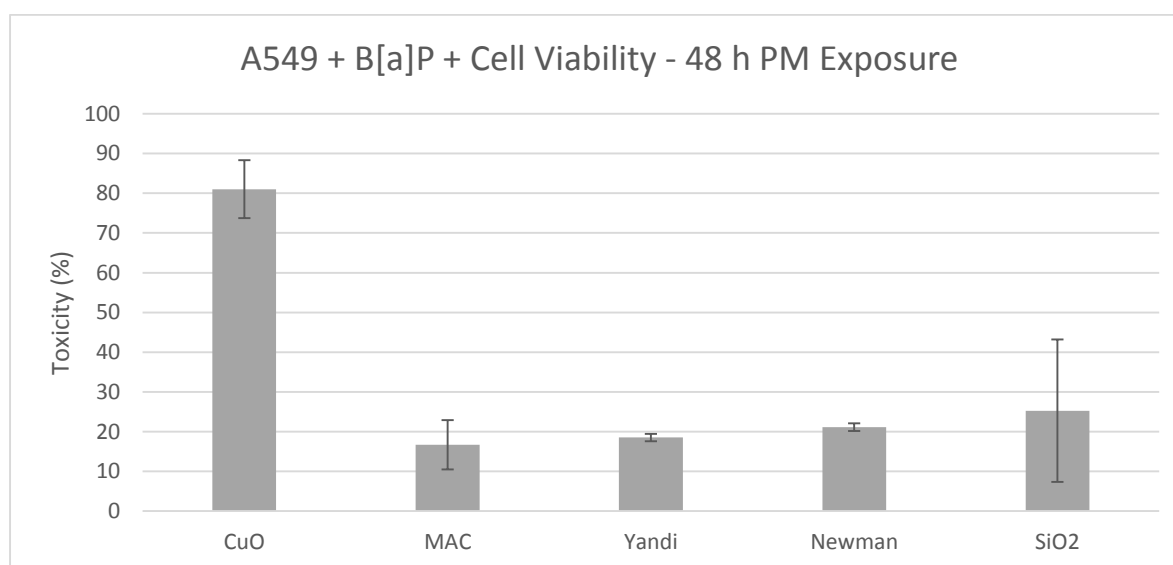


Figure 49: A549 48 h + 50  $\mu$ M B[a]P + 5% S9 mix particle toxicity. CuO 39  $\mu$ g/cm<sup>2</sup>, 156  $\mu$ g/cm<sup>2</sup> other particulates

The monocyte derived macrophage cell line, U937 behaved in a similar fashion to the LL24 and A549 cell lines. The dynamics between the monocytes to macrophages differentiation process may play a role, if the process can continue to occur after seeding. Controls help to account for differences in particle number accrued by non-adherent monocytes being transferred from well to well during sample serial dilution, but does not counteract differences stimulated by macrophage cytokine signalling during phagocytosis – if this is a contributing factor. In the dose range tested, SiO<sub>2</sub> showed a highly positively proliferative effect across a wide range of concentrations. Carbon black caused an even greater positively proliferative effect (down to -20% toxicity) until 156  $\mu$ g/cm<sup>2</sup>, after which the cytotoxic effect prevailed increasing to 28% at 312  $\mu$ g/cm<sup>2</sup>. This form of response may be a result of phagocytosis induced proliferative signalling or differentiation of remaining monocytes, then cytotoxic overloading. However, it masks cytotoxicity, requiring



U937 cell viability assays be used in conjunction with other cell lines to help ascertain the extent of this effect.

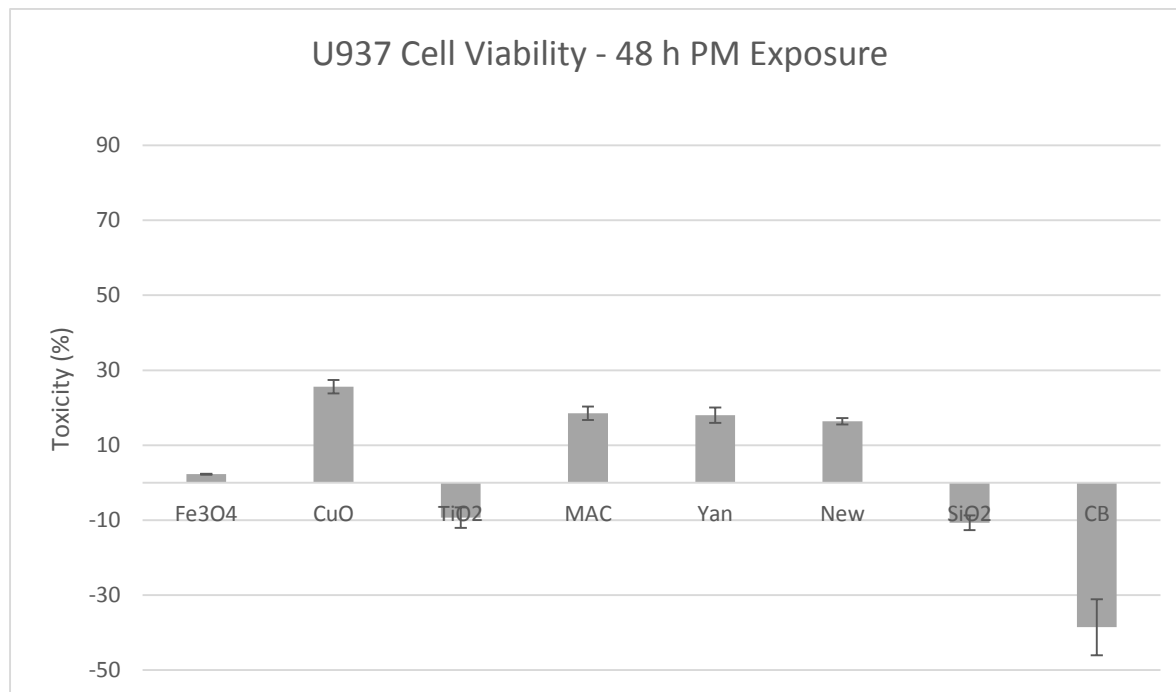


Figure 50: U937 48 h particle toxicity. CuO 39  $\mu\text{g}/\text{cm}^2$ , 156  $\mu\text{g}/\text{cm}^2$  other particulates

The effect of B[a]P on U937, paradoxically tended to equalize toxic effects (Figure 51). This confounds what toxic effect co-inhalation of both particulate matter and B[a]P will have, at the least suggesting immune recruitment will be enhanced. However, the proliferative effect of CB remained very strong at the lower doses, reaching -27% toxicity at 10  $\mu\text{g}/\text{cm}^2$ . Both enhanced cytotoxicity and enhanced immune recruitment are signs of increased inflammatory activity and fibrotic potential.

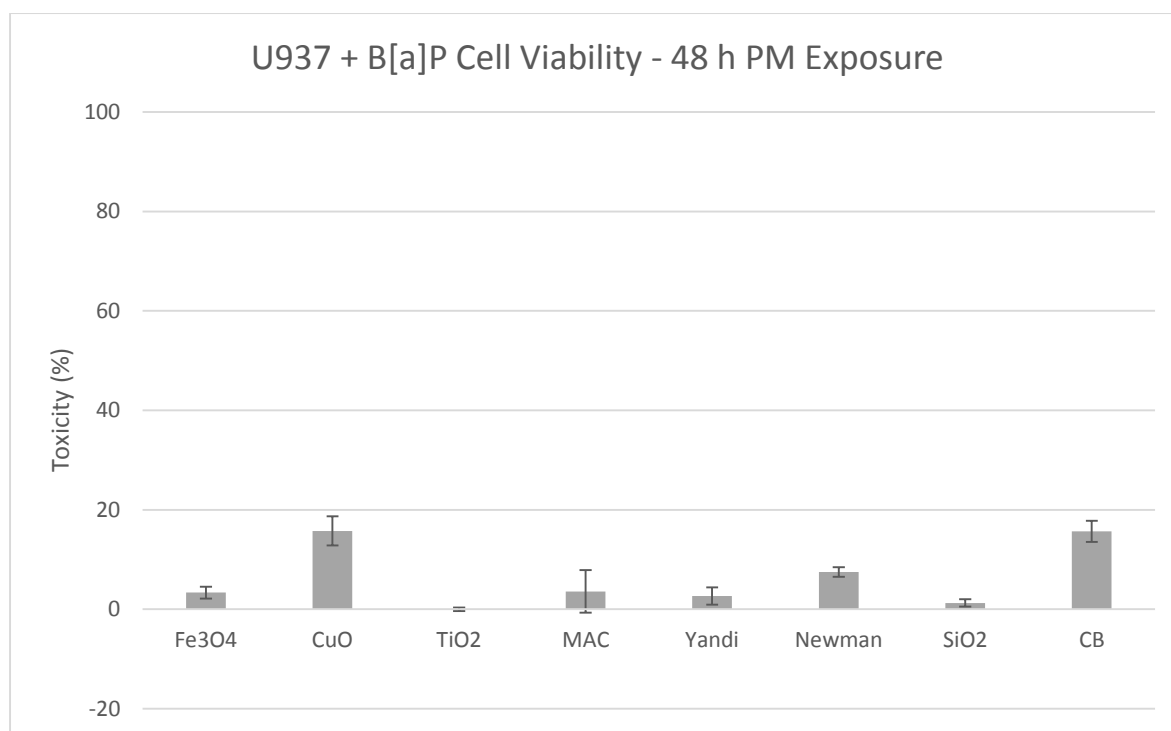


Figure 51: U937 48 h + 50  $\mu$ M B[a]P particle toxicity. CuO 39  $\mu$ g/cm<sup>2</sup>, 156  $\mu$ g/cm<sup>2</sup> other particulates.

#### 4.3.6 Oxidative Stress

To preface the antioxidant reporter element (ARE) luciferase reporter activation test in AREc32 cells, cytotoxicity tests were conducted to ensure that it responded similarly to the lung cell lines and to ensure testing occurred near the IC20 level for each of the particulates, minimizing the effect of cell death on expression of the reporter. The AREc32 system was chosen as it is a measure of intracellular activation of antioxidant response pathways, which are often linked with the Nrf2 transcription factor, and as a more robust method less vulnerable to artifacts<sup>254</sup>. AREc32 was found to respond to particles similarly to lung cell lines, and Figure 52 graphs the toxicity of the samples and standards at 156  $\mu$ g/cm<sup>2</sup> as described for the other cell lines, and 39  $\mu$ g/cm<sup>2</sup> as chosen for the AREc32 luciferase reporter assay. While not strictly part of the lung cells examined for cytotoxic effect, the electrophile sensitisation of the AREc32 cell appeared to make it particularly vulnerable to CuO and SiO<sub>2</sub> toxicity, while leaving the iron-ore samples and Fe<sub>3</sub>O<sub>4</sub> and Fe<sub>2</sub>O<sub>3</sub> responding similarly to LL24 and A549.

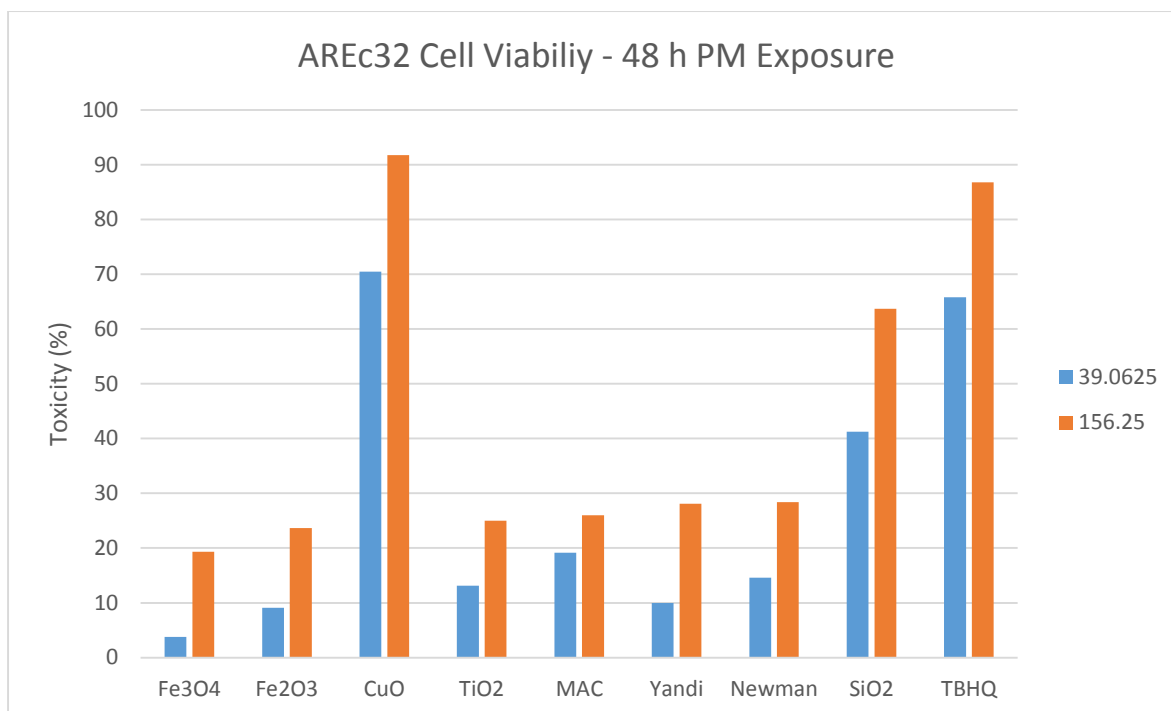
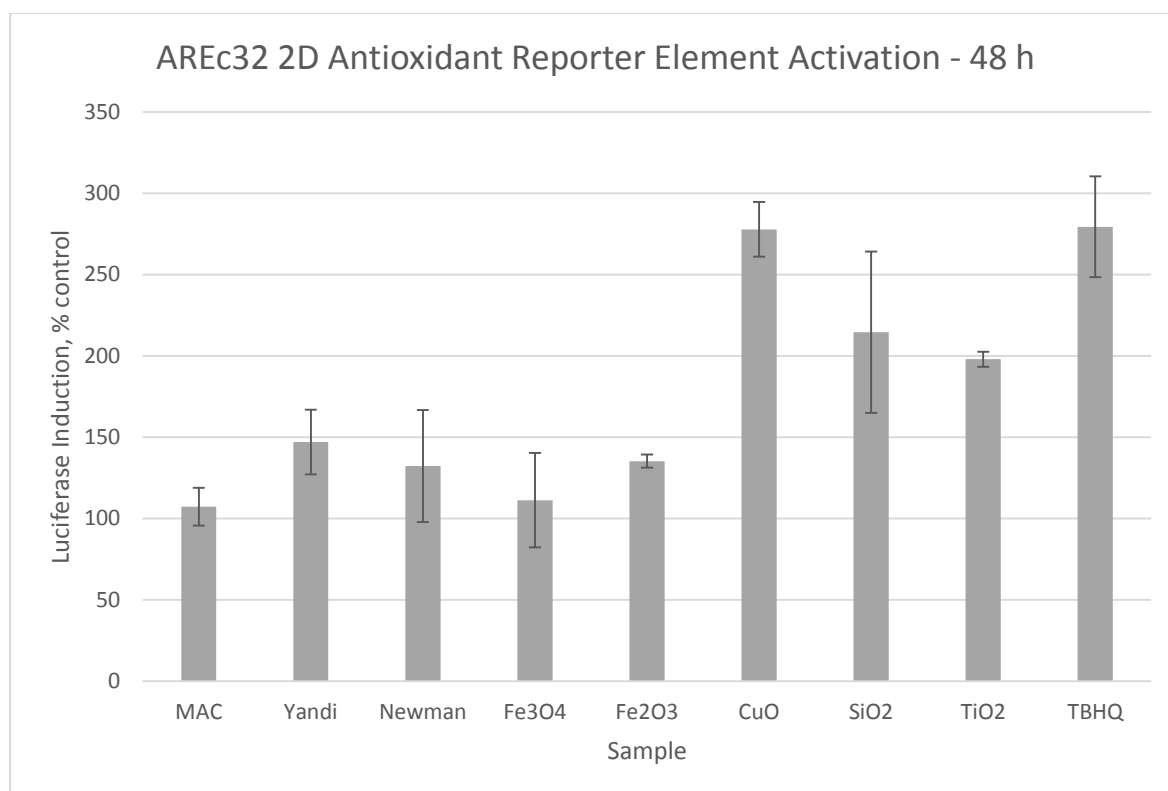


Figure 52: AREc32 48 h particle toxicity. CuO 39/10  $\mu\text{g}/\text{cm}^2$ , 156/39  $\mu\text{g}/\text{cm}^2$  other particulates, TBHQ 25  $\mu\text{M}$ /6.25  $\mu\text{M}$

Aside from tert-Butylhydroquinone (TBHQ) as the positive control, the AREc32 luciferase reporter assay showed activation highest with CuO followed by SiO<sub>2</sub>, followed by TiO<sub>2</sub> and Fe<sub>2</sub>O<sub>3</sub>, described in Figure 53. The iron ore samples had reduced oxidative potential in comparison. Surprisingly, while TiO<sub>2</sub> did not play a major role in cytotoxicity, it caused almost the equivalent Nrf2 mediated activation as SiO<sub>2</sub>.



**Figure 53: ARE element activation as measured by a luciferase reporter in AREc32 cells 48 h exposure, positive control TBHQ 6.25  $\mu$ M, CuO 10  $\mu$ g/cm<sup>2</sup>, others 39  $\mu$ g/cm<sup>2</sup>**

#### 4.3.7 Inflammatory Cytokine Induction

The nature of inflammatory cytokine signalling is complex, and often the ratio of a range of cytokine signals ultimately determine inflammatory outcomes in extension to sheer concentration. In choosing the experimental process to pursue it was therefore important to measure as many cytokines as possible. While ELISA is a popular choice, it measures a single interleukin at a time. The Human Inflammatory Cytokine cytometric bead assay kit (BD Biosciences) was chosen as it simultaneously measures 6 inflammatory cytokines and eliminates inter-experiment variability individual ELSIA measurements of cytokines would introduce, so that the ratios between interleukins are accurate. Quantitatively, IL-6 and IL-8 were most strongly expressed in LL24 (see Figure 54). Simplistically, on the left inflammatory cytokines are represented (IL-8, TNF, IL-1 $\beta$ ) and on the right anti-inflammatory cytokines are represented (IL-10, IL-12p70 and IL-6) <sup>237,241</sup>, although the actual impact of cytokine activity is highly varied. While induction was overall mild, the iron ore samples

appeared to clearly induce cytokine induction similar to SiO<sub>2</sub>, although CuO and SiO<sub>2</sub> engendered the greatest IL-8 response, closely followed by the MAC sample.

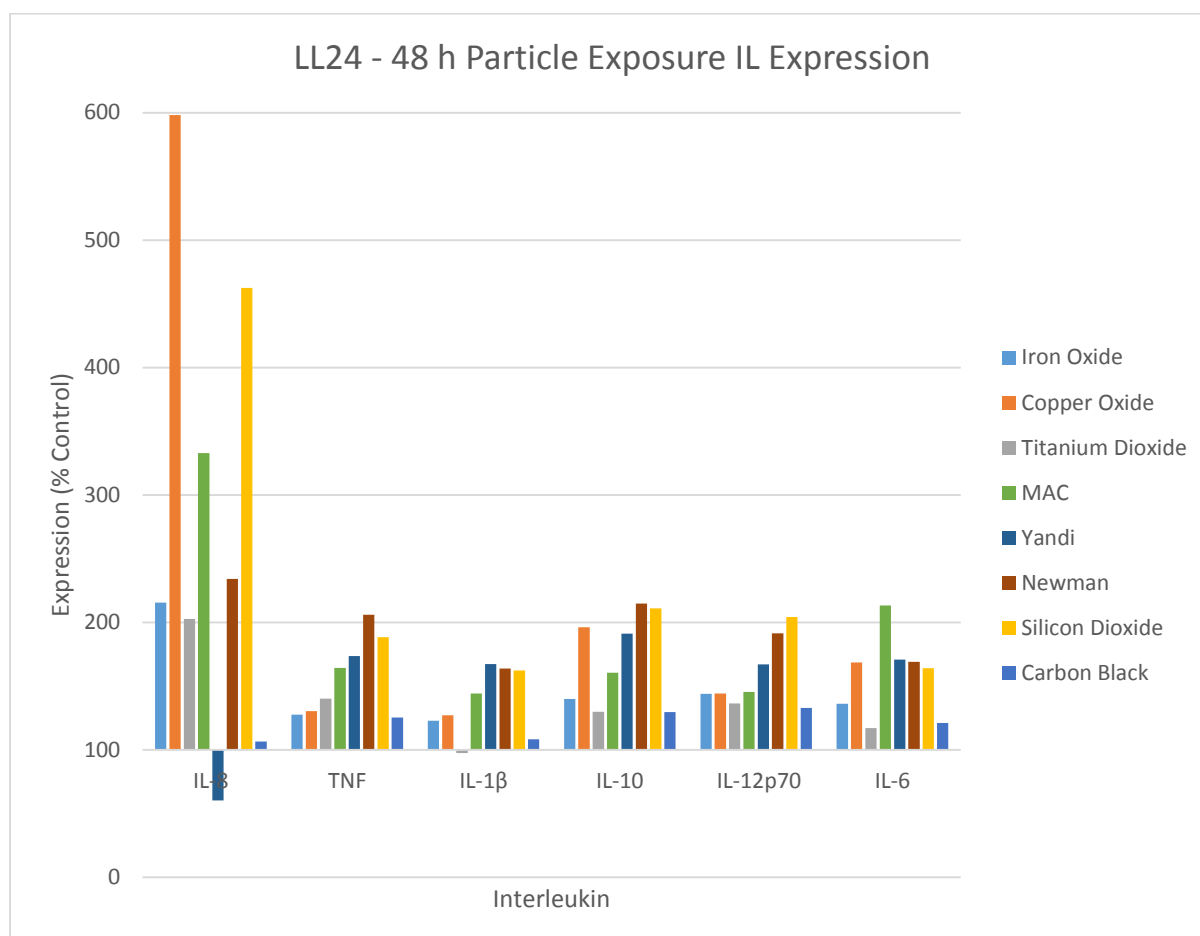


Figure 54: LL24 inflammatory cytokine expression. CuO, at 5  $\mu\text{g}/\text{cm}^2$ , others 156  $\mu\text{g}/\text{cm}^2$ .

IL-8 is typically reported as being expressed in A549 cells<sup>185</sup>, allowing immune recruitment to epithelial cells in airways experiencing injury. Commensurate with this, A549 expressed IL-8 in higher quantities than LL24 cells, and interestingly also showed the most potent TNF, IL-1 $\beta$  and IL-12p70 expression on average. IL-1 $\beta$  has also been associated with fibroblast proliferation<sup>294</sup>. IL-12p70 expression is associated in the development of Th1 lymphocytes and is suppressed in dendritic cells by fibroblasts<sup>295</sup>. IL-10 expression was near that of U937. IL-10 is thought to be a respiratory sensitiser, leading to humoral immunity and allergic responses<sup>186</sup>. Elevated IL-10 has also been suggested as a key diagnostic factor in patients with idiopathic pulmonary fibrosis (IPF)<sup>243</sup>. The Yandi and Newman samples appeared to repress most interleukins, other than IL-6 in which expression was induced, possibly

having elicited an anti-inflammatory feedback mechanism (see Figure 55). SiO<sub>2</sub>, CB and the MAC sample however appeared to be inflammatory and induce IL-8.

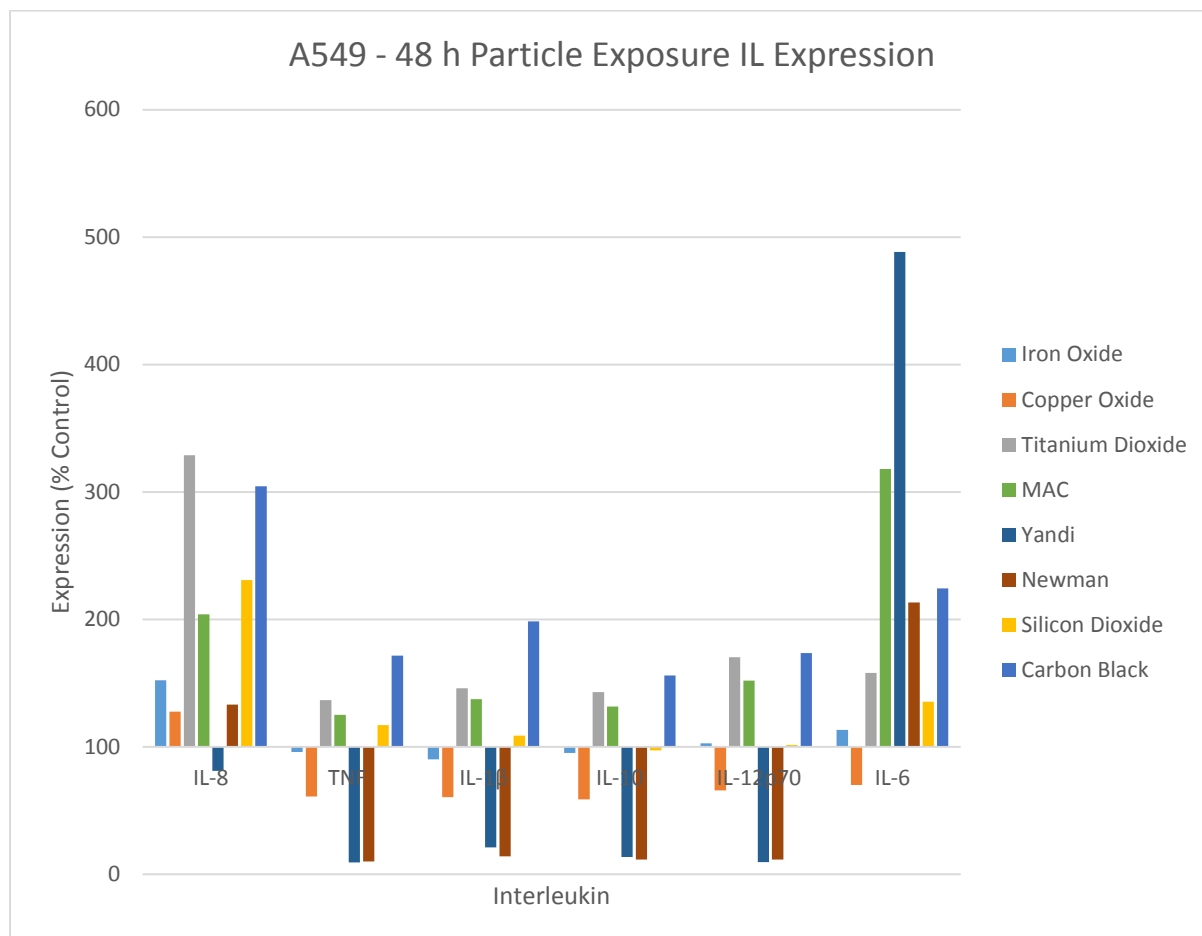


Figure 55: A549 inflammatory cytokine expression. CuO, at 5  $\mu\text{g}/\text{cm}^2$ , others 156  $\mu\text{g}/\text{cm}^2$ .

Quantitatively, U937 was found to express the highest quantity of IL-8 and IL-10, and appeared to express as much TNF as A549, although the addition of PM appeared to greatly suppress TNF expression, and other interleukins (see Figure 56). TNF has been shown to orchestrate many types of other inflammatory responses including cancer<sup>201</sup>. Suppressed TNF expression, with the exception of SiO<sub>2</sub>, would suggest an anti-inflammatory effect, however an alternative explanation would be that culture conditions without stimulus affecting the control samples were relatively pro-inflammatory. Nevertheless, this effect highlights SiO<sub>2</sub> represented as being especially pro-inflammatory, leading to increased TNF expression. The unusually high induction of IL-6 by TiO<sub>2</sub> also suggests it may be problematic to immune function.

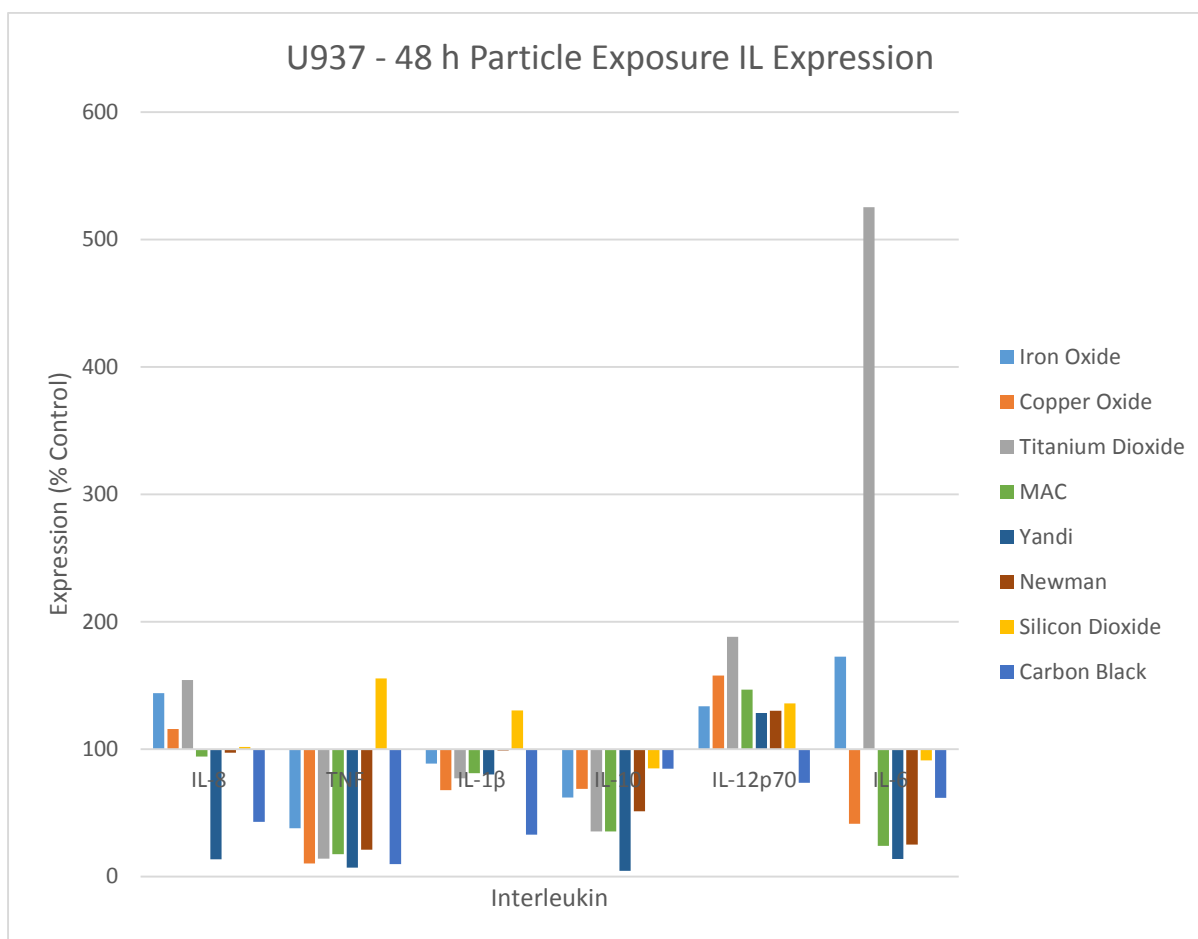


Figure 56: U937 inflammatory cytokine expression. CuO, at 5  $\mu\text{g}/\text{cm}^2$ , others 156  $\mu\text{g}/\text{cm}^2$ .

#### 4.4 Discussion

At the particle loads illustrated (Figure 46-Figure 51), the overall order of cytotoxicity is determined to be  $\text{CuO} > \text{SiO}_2 > \text{Newman PM}_{10} = \text{MAC PM}_{10} = \text{Yandi PM}_{10} > \text{TiO}_2 = \text{CB} > \text{Fe}_3\text{O}_4$ , although the differences vary between cell types. While CuO presents the greatest concern all around being highly cytotoxic, the responses to  $\text{SiO}_2$ , CB and  $\text{TiO}_2$  present as compounds with tangential toxic aspects more sinister than the  $\text{Fe}_3\text{O}_4$  sample. The strong proliferative effect of  $\text{SiO}_2$  and CB on U937 monocyte differentiated macrophages suggests greater inflammatory potential, reflected by potent induction of IL-8 in A549 cells.  $\text{SiO}_2$  also prominently induced IL-8 in LL24 cells and TNF in U937 cells. High  $\text{TiO}_2$  induction of IL-6 in U937 and IL-8 in A549 was also unexpected given the relatively low toxicity of the compound. The iron-ore samples themselves displayed some of the most dynamic induction of IL responses,

with the MAC sample being highly represented in IL-8 induction in A549 and LL24 cells, while the Newman and Yandi samples displayed peculiar suppression of interleukins bar IL-8 in the LL24 sample and potentially induced IL-6 along with the MAC sample. It is of note that the environmental iron-ore samples may carry endotoxins or other organic matter, influencing cytokine responses towards them.

The addition of B[a]P showed an additive affect to the inorganic particulates, and its bioavailability may be limited rather than enhanced by inorganic particulate adsorption <sup>296</sup>. The effect of B[a]P on U937 was also unexpected, and may hint at changes in cell metabolism in U937 cells when undergoing stress, or stress caused by control overgrowth compared to sample exposures where particle uptake activity may limit growth. Oxidative stress results showed correlation with CuO and SiO<sub>2</sub> cytotoxicity, but implicated TiO<sub>2</sub> to have more oxidative stress potential than Fe<sub>3</sub>O<sub>4</sub> and the iron-ore samples.

The experimental results show that proliferative, or inverse cytotoxic interactions *in-vitro*, can affect cell lines in the investigation of lung fibrosis and inflammation. While hyperplasia is frequently noted in histological *in-vivo* samples, it is discussed infrequently in *in-vitro* toxicology or dismissed as an artefact caused by effects such as protein adsorption <sup>266,273</sup>. In these experiments, particulate interference of this kind fails to explain differences between cell lines observed, and biological explanations are better suited to answering questions such as why U937 is disproportionately affected. The interpretation of proliferative effects of low toxicity particles may therefore be a source of discrepancy in translating *in-vitro* research to *in-vivo* outcomes.

Determining such effects requires high sensitivity and tolerance to noise and error, as the lack of cytotoxicity creates difficulty in distinguishing between systematic error and actual responses, which are always clearer with the CuO standard having been shown to have a soluble cytotoxic component giving it much greater toxicity that follows a traditional dose-response relationship <sup>289</sup>. The high toxicity of CuO has been noted previously in the literature in comparison inorganic particulates and carbon based particles <sup>215</sup>, and has been shown to cause increased oxidative stress and cytotoxicity relative to iron oxides and SiO<sub>2</sub>, which this study confirms <sup>283</sup>.



Despite limited cytotoxicity of the iron-ore samples, extensive work in analysing particulate burden *in vivo* over the past three decades<sup>18,22,24,25,27,225,274</sup> has shown that even inert particles can cause obstructive and fibrotic changes if the particle clearance limit of pulmonary alveolar macrophages is reached<sup>280</sup>, and can occur over time as the half-life of particles reaching the acinar surfaces of the lungs is long; some 500 days<sup>25</sup>. An important characteristic of particle uptake underscoring the need for particle shape characterisation by electron microscopy is that particle uptake is also morphology dependent, and high-aspect ratio particles such as asbestos, glass fibre and multi-walled carbon-nanotubes (MWCNT) have been repeatedly shown to induce frustrated phagocytosis<sup>30,35,127,213</sup>. Incomplete phagocytosis of long particles leads to ineffective clearance, prolonged inflammation and potentially penetration into the mesothelium, causing carcinogenic effects<sup>35,127</sup>. Successful particle uptake is also able to liberate metal ions, as demonstrated by ICP-MS, making the immunological compartment of cell uptake even more significant. A limitation of the ICP-MS technique is that it was not able to detect Si ions for this comparison.

The uptake of silica particles by U937 monocyte differentiated macrophages has previously been shown to occur through binding of immunoglobulin to plasma treated silicates and internalization via FcγRI – a known trigger of cellular ROS production<sup>297</sup>. This has the potential to aggravate pulmonary inflammation. The AREc32 transgenic reporter relies on activation by the Nrf2 transcription factor, and this pathway has been shown to be involved in oxidative stress caused by atmospheric pollutants<sup>298</sup>. This establishes the pathway as relevant to in-situ oxidative stress measurement within the cell, in response to particulate matter. Cytotoxicity is often attributed to redox catalytic properties in metals and metal oxides<sup>167,172,222,233,261,299–303</sup>. Whether or not ROS or cytotoxicity itself is a key driver for all metal oxide mediated lung disease, the assessment of standards and samples using AREc32 provides an additional way to rank particle hazard and bore resemblance to inflammatory cytokine comparisons.

Taken together, from our experiments it can be seen regulating airborne particulate in Port Hedland matter solely on the basis of dimensional fractions carries an

inherent assumption that limits are protective against the net toxicity of any size distribution and chemical composition reasonably expected to occur within a given fraction. However, given the nature of epidemiological studies on which regulations are based, arguments can be made for and against the stringency of current standards in all scenarios, based on the perceived statistical strength of associations and that no distinction is made between particulate types <sup>80</sup>. For this reason, the low solubility and concomitant weak acute toxicity of the studied iron-ore PM<sub>10</sub> may place it within the bound of these regulations.

In this study, cytotoxic differences between SiO<sub>2</sub> and the iron-ore samples are shown to be minimal, however proliferative effects, increased oxidative stress and increased inflammatory properties point to SiO<sub>2</sub> as having a fibrotic potential. This is consistent with occupational exposure data showing chronic exposure to silica over 45 years still poses unacceptable mortality risk (6/1000) <sup>96</sup>. Nevertheless, the iron-ore samples are not shown to be inert, and cellular responses towards them indicate they should be treated as an equal hazard.

In practice, an informed balance between public health risk and cost-effective dust mitigation strategies must be achieved; a requirement complicated by the volume of material handled and the scarcity of fresh water for wetting based dust suppression or the environmental impact of chemical methods <sup>94</sup>.

## 5. Comparative Toxicology of Inhalable Particulate Matter to Human Lung Cell and Macrophage Cocultures

### 5.1 Introduction

As inflammatory activity is a central mediator of fibrosis, further investigation into the scope and breadth of immunological reactions to iron-ore PM<sub>10</sub> and standards was required. To achieve this simply without creating further uncertainties to account for when comparing data, coculture methods were developed based on combining two cell types at half their monolayer seeding volume and proceeding with the monolayer methodologies established.

This effectively allows some of the immunological cell to cell communication inherent in the *in-vivo* system to occur *in-vitro*. As each cell type (A549 lung epithelial, LL24 fibroblast, U937 monocyte derived macrophage) has been found to have different cytokine responses when challenged with particulate matter, it is possible that coculture can provide immunomodulatory feedback and grant some clues as to the dysregulation of this process during respirable particle challenges. Dysregulation of the inflammatory cycle could result in continued inflammation and prevent a return to homeostasis, leading to fibrosis, and is dependent on input from both lung parenchymal cells and immune cells<sup>140</sup>.

Furthermore, the uptake of particles into U937 monocyte differentiated macrophages was crucial to examine, based on the importance of the lysosomal compartment of the macrophage. The acidic environment of the lysosomal compartment may play a crucial role in liberating metal ions, and when combined with increased immunological recruitment, create positive feedback. This could in turn create bioavailability conditions which exceed those that would otherwise be determined from pH 7.4 lung biofluid experiments alone, when examining otherwise insoluble metal-oxides. Electron microscopy of U937 macrophages to observe the extent of particle uptake and loading was therefore performed.

## 5.2 Materials and Methods

### 5.2.1 Chemicals and Reagents

As standard compounds the following from Sigma Aldrich, USA were obtained: Copper(II) oxide <5  $\mu\text{m}$ , Iron(II,III) Oxide <5  $\mu\text{m}$ , Iron(III) Oxide <5  $\mu\text{m}$ , Silicon(IV) Oxide <10  $\mu\text{m}$ , Titanium(IV) Oxide <50 nm. Carbon Black < 150 nm powder was obtained from US Research Nanomaterials, Inc., USA. Representative iron ore stockpile samples were supplied from three major mining sites in the Pilbara region in Western Australia courtesy of BHP Billiton; Newman Hub Mine (Newman), Mining Area C (MAC) and Yandi Mine (Yandi)

The PrestoBlue reagent (#A-13261, Life Technologies, USA) was obtained for cell viability experiments. The Human Inflammatory Cytokine Kit was used to detect interleukin expression (#551811, BD Biosciences, USA). Cells were fixed in glutaraldehyde prior to electron microscopy (Sigma Aldrich, USA).

### 5.2.2 Particle Extraction and Sterilisation

The supplied iron ore samples were sieved to < 45  $\mu\text{m}$  by ChemCentre WA (CCWA). To sieve the samples further down to  $\text{PM}_{10}$ , an ultrasonic sieve tower and accompanying custom 10  $\mu\text{m}$  electroformed sieve was used (Precision Eforming LLC, New York, USA).

The prepared samples were sterilised using fractional sterilisation. Sieved material was collected into 50 mL conical Falcon tubes (BS Biosciences, USA) and heated to 60 °C for 15 minutes before being allowed to cool at room temperature for 24 hours, repeated over three successive days.

### 5.2.3 Electron Microscopy

Cells were grown on 12 well plates and incubated for 96 hours with samples. Media was drained from the cells and fixed with glutaraldehyde. Post fixation cells were cured with osmium tetroxide and baked in resin for four hours, then left to solidify overnight. Resin was then mounted and cut on an ultramicrotome (Lecia UC61, Germany) to 40 nm for observation by transmission electron microscopy (JEOL 1010, Japan) on 400 square mesh copper grids (ProSciTech, Australia).

#### 5.2.4 Cell Culture

The A549 pulmonary type I/II-like epithelial adenocarcinoma (ATCC CCL-185), LL24 pulmonary normal fibroblasts (ATCC CCL-151) and U937 monoclonal-like histiocytic lymphoma (ATCC CRL-1593.2) were used to represent lung epithelial, connective and immunological cells, respectively.

The A549, LL24 and AREc32 cell lines were cultured in F-12K medium (#21127, Life Technologies, USA) supplemented with 10% foetal bovine serum (FBS), 100 IU/mL penicillin, 100 µg/mL streptomycin, and 10 mg/mL amphotericin B (#A9528-50MG, Sigma Aldrich, USA). U937 was cultured in RPMI 1640 medium (#72400, Life Technologies, USA) supplemented with 10% foetal bovine serum (FBS), and 100 IU/mL penicillin, 100 µg/mL streptomycin, 10 mg/mL amphotericin B (#A9528-50MG, Sigma Aldrich, USA), 2mM L-glutamine, 1mM Sodium pyruvate and 10mM HEPES buffer.

Cells were cultured in 75 cm<sup>2</sup> tissue culture treated flasks (Corning, USA) at 37 °C in humidified 5% CO<sub>2</sub>, 95% air atmosphere. A549 and LL24 medium was changed every 2-3 days and split every 5 days. As they are adherent, cells were harvested for seeding using trypsinization and washed in Phosphate Buffered Saline (PBS). U937 was cultured in suspension and maintained in at 2 x 10<sup>5</sup> to 1 x 10<sup>6</sup> cells/mL by passage every 4 days.

For seeding and exposure incubation, cells were plated onto opaque flat bottom 96-well plates (Becton Dickinson, USA) at 70% confluency (100 µl/well, 2x10<sup>5</sup> cells/mL). In an effort to mitigate the effects of inflammatory activity by the PMA induced U937 differentiation step and minimise variance, cell cultures were left to incubate and settle for twice the normal duration. Cells were incubated for 48 h after seeding, prior to the particle exposure time period at 37 °C under sealing film (Corning, USA).

Differentiation of U937 to a mature macrophage-like morphology can be induced by exposure to phorbol esters<sup>267</sup>. For this purpose, differentiation was induced during the seeding period by exposure to 30 ng/mL of Phorbol Myristic Acid (PMA) for 48 h.

### 5.2.5 Cell Proliferation Assay

Cytotoxicity of particulate matter was measured using a cell survival resazurin assay, PrestoBlue. After seeding incubation, cells were exposed to a 2 x serial dilution of particulate matter suspension down 6 rows. To achieve the first well concentration expressed as  $156 \mu\text{g}/\text{cm}^2$  (unless CuO, at  $39 \mu\text{g}/\text{cm}^2$ ),  $100 \mu\text{L}$  of  $1 \text{ mg}/\text{mL}$  (CuO,  $0.25 \text{ mg}/\text{mL}$ ) suspension was added to  $100 \mu\text{L}$  of media per well of an area  $0.32 \text{ cm}^2$ . Incubation with particulate matter under sealing film was then continued until measurement. For measurement,  $10 \mu\text{L}/\text{well}$  of PrestoBlue reagent was added to the plates and incubated for 30 minutes at  $37^\circ\text{C}$ . Spectrophotometric analysis was then conducted using the FluoStar Omega microplate reader (BMG Labtech, Germany), using the top-down fluorescence optic ( $540 \text{ nm}$  excitation,  $580 \text{ nm}$  emission).

### 5.2.6 Flow Cytometric Cytokine Quantification

Cytokine standards were prepared as follows; each vial of lyophilized Human Inflammatory Cytokine Standards was reconstituted with  $0.2 \text{ mL}$  of Assay Diluent to prepare a 10x bulk standard. This was equilibrated for at least 15 minutes before making dilutions. Dilutions were mixed by pipetting. Serial dilutions were then performed from 1:1 through 1:256 in a 2x serial dilution, starting with  $900 \mu\text{L}$  of Assay Diluent and  $100 \mu\text{L}$  of 10x bulk standard in the Top Standard tube and  $300 \mu\text{L}$  transferred to successive tubes thereafter.

After cytotoxic measurement,  $20 \mu\text{L}$  was taken from each sample well on the 96-well microplate into Eppendorf tubes. This was mixed with  $8 \mu\text{L}$  per sample of CBA beads comprised of the 6 detection bead types, after an equal amount of PE detection reagent to the CBA beads was added and vortexed. The mixture was then incubated at room temperature away from light for 3 hours.  $150 \mu\text{L}$  of wash buffer was then added to each sample and centrifuged at  $400 \times g$  for 3 minutes. Precipitate was resuspended in  $200 \mu\text{L}$  wash buffer. This was then analysed on the Accuri C6 flow cytometer to count over 1,000 events. Data was then processed on BD's FCAP Array v3 software.

### 5.3 Results

To understand the effects of coculture on cell proliferation and cytokine signalling, experiments were performed with 1:1 combinations of A549:LL24, U937:A549 and LL24:A549. Parallel monolayer cultures of A549, LL24 and U937 cells alone were exposed to identical conditions and examined concomitantly, to ensure the accurate interpretation of the coculture results.

The U937:LL24 combination was chosen for cytokine investigation, to provide the most direct information about the cytokine signalling responses of fibroblasts to inflammatory activity. These results were compared to U937 and LL24 cytokine signalling alone.

Electron microscopy investigations were carried out on U937 monocyte differentiated macrophages to show the effectiveness of the differentiation process and examine uptake activity, apoptosis and self-recruitment on a range of particulate standards.

#### 5.3.1 Cell Proliferation

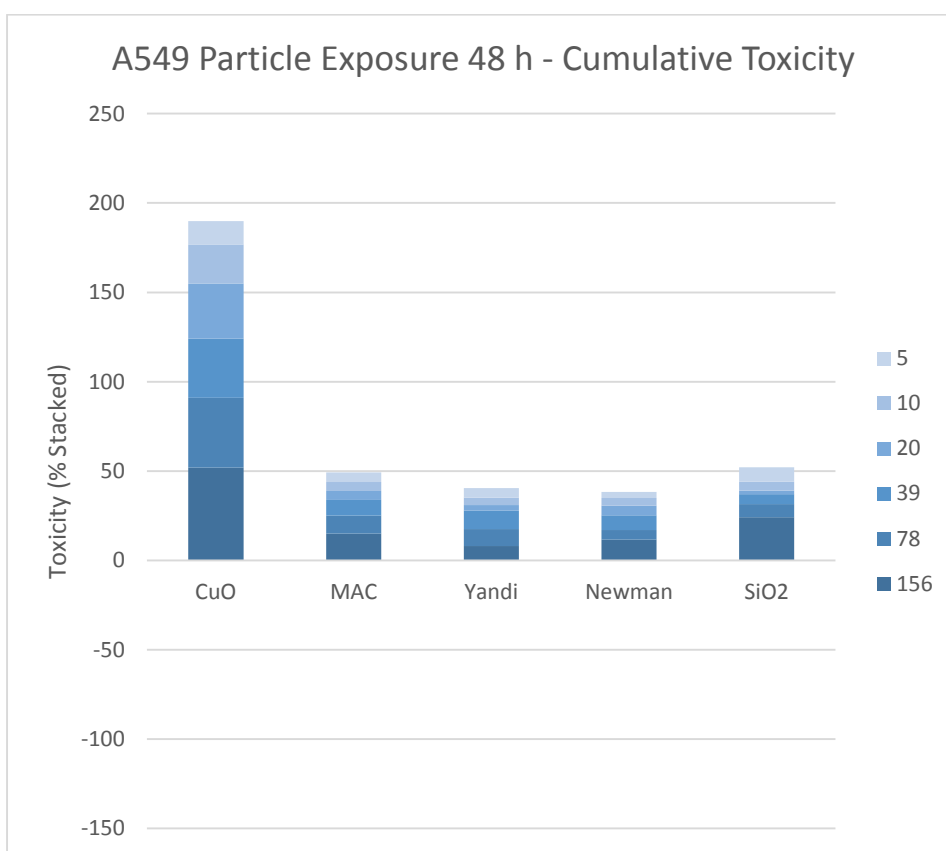
The following set of cell proliferation assays are presented as stacked bar graphs in this chapter. This provides more information across the concentration ranges exposed than single concentration bar charts. Scatter plots, while useful in observing dose-response relationships, are less able to convey the nature of low maximum toxicity exposure information across dose ranges by exhibited by the insoluble particulates examined. Furthermore, proliferative effects were easily interpreted in this format, which may be indicative of hyperplasia potential *in-vivo*. The CuO < 5  $\mu\text{m}$ , and PM<sub>10</sub> MAC, Yandi, Newman and SiO<sub>2</sub> samples and standards were used. As the CuO sample is  $\frac{1}{4}$  the concentration of the other particulate standards, conversions are provided on Table 12.

Table 12: Conversion for other particulate concentration to CuO in  $\mu\text{g}/\text{cm}^2$

Other	CuO
156	39
78	20

39	10
20	5
10	2
5	1

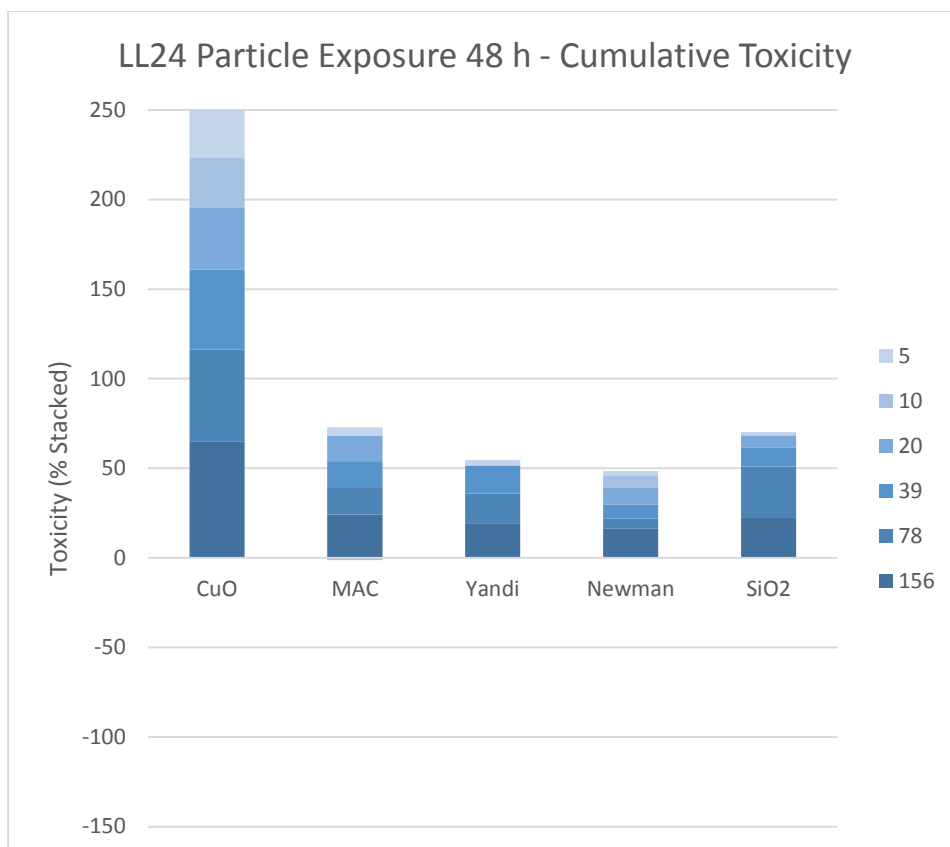
The cumulative toxic effect across the dose range on A549 monoculture cells showed high cytotoxicity from CuO as expected, while the MAC and SiO<sub>2</sub> samples narrowly exceeded the toxicity of Yandi and Newman ores (see Figure 57).



**Figure 57: A549 cumulative toxicity of particles across 5-156 µg/cm<sup>2</sup> dose range, and 1-39 µg/cm<sup>2</sup> dose range for CuO, over 48 h.**

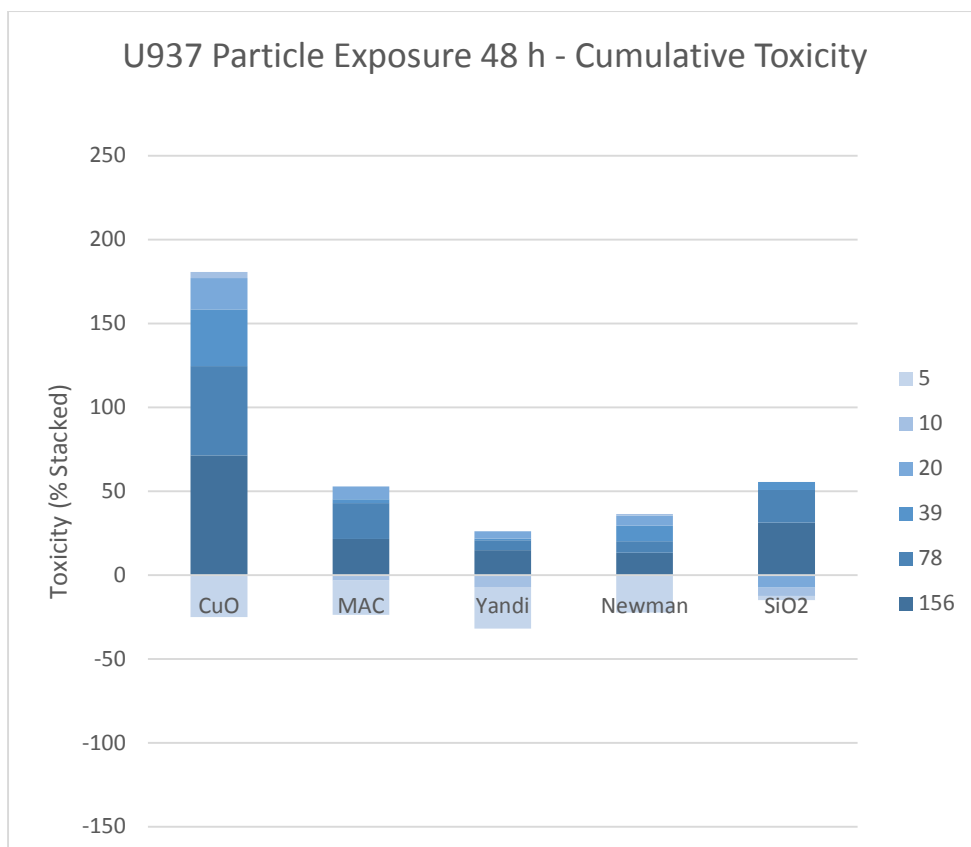
The LL24 monolayer culture showed similar relationships between the toxicity of samples and standards to the A549 cell line, and similar sensitivity in Figure 58.





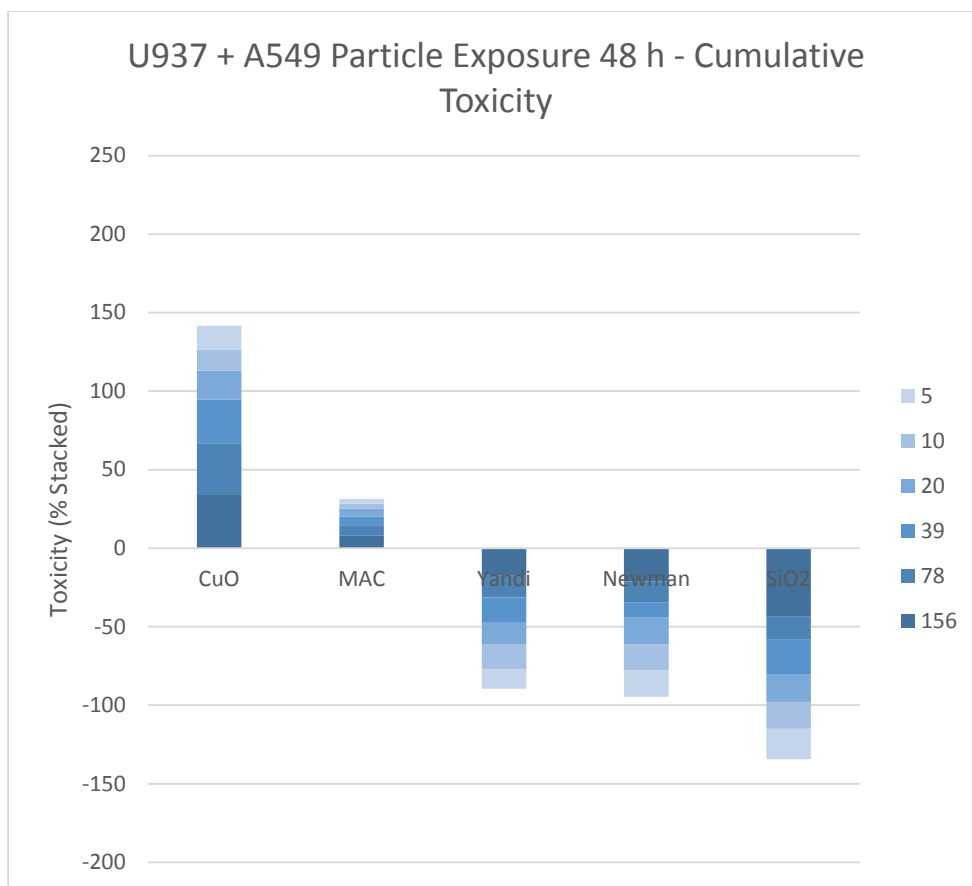
**Figure 58:** LL24 cumulative toxicity of particles across 5-156 µg/cm<sup>2</sup> dose range, and 1-39 µg/cm<sup>2</sup> dose range for CuO, over 48 h.

While the cumulative toxic effects of samples and standards on the U937 monolayer showed similar relationships in comparison to LL24 and A549 (see Figure 59), the toxic effect reversed at lower concentrations becoming a proliferative effect. It is possible that this is caused by induction of undifferentiated U937 monocytes to more metabolically active macrophages in response to cytokines produced during the phagocytosis of particulate matter, or that it is related to greater metabolic activity within the cells.



**Figure 59: U937 cumulative toxicity of particles across 5-156  $\mu\text{g}/\text{cm}^2$  dose range, and 1-39  $\mu\text{g}/\text{cm}^2$  dose range for CuO, over 48 h.**

Interaction between the epithelial layer of the pulmonary acinus and macrophages forms represents the acute immunological recruitment phase in response to particle contact with the respiratory surfaces of the lung. This was modelled as U937 in coculture with A549 cells. Relative to the monolayer responses, this drastically altered the toxicity profile, causing all samples other than CuO and MAC to show large proliferative effects (see Figure 60). As the cumulative cytotoxicity of CuO was reduced relative to the monolayer cultures, a possible explanation for this phenomenon is that the control samples have not performed as well as the exposure samples, although it is unclear what could cause this effect systematically. It would also be expected that underperforming control samples would not differentially affect the sample types. Alternatively, the presence of or uptake of particles and their characteristics may have a modulatory effect on A549 proliferation and U937 differentiation. In this regard, it appears that  $\text{SiO}_2$  is the most potent inducer of proliferation for this coculture.



**Figure 60: U937+A549 coculture cumulative toxicity of particles across 5-156 µg/cm<sup>2</sup> dose range, and 1-39 µg/cm<sup>2</sup> dose range for CuO, over 48 h.**

The coculture of A549 and LL24 represents investigation of connective tissue proliferation in response to epithelial layer signalling, or vice versa, during particle exposure. The toxicity profile of this coculture resembled the U937+A549 coculture more than any of the monolayer experiments (see Figure 61). However, the effect of SiO<sub>2</sub> was not as extremely proliferative, and higher doses showed a slight return to toxicity. The toxicity of MAC also remained resistant to reversal, while Yandi and Newman samples showed very low but somewhat reversed toxicity.

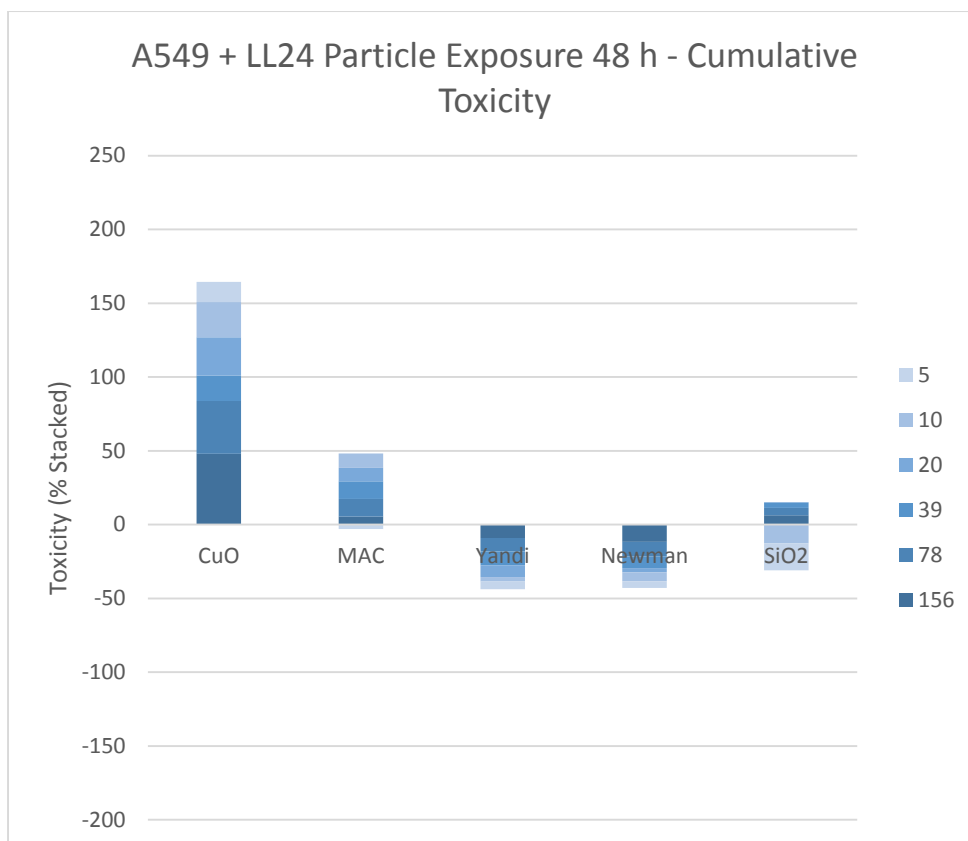
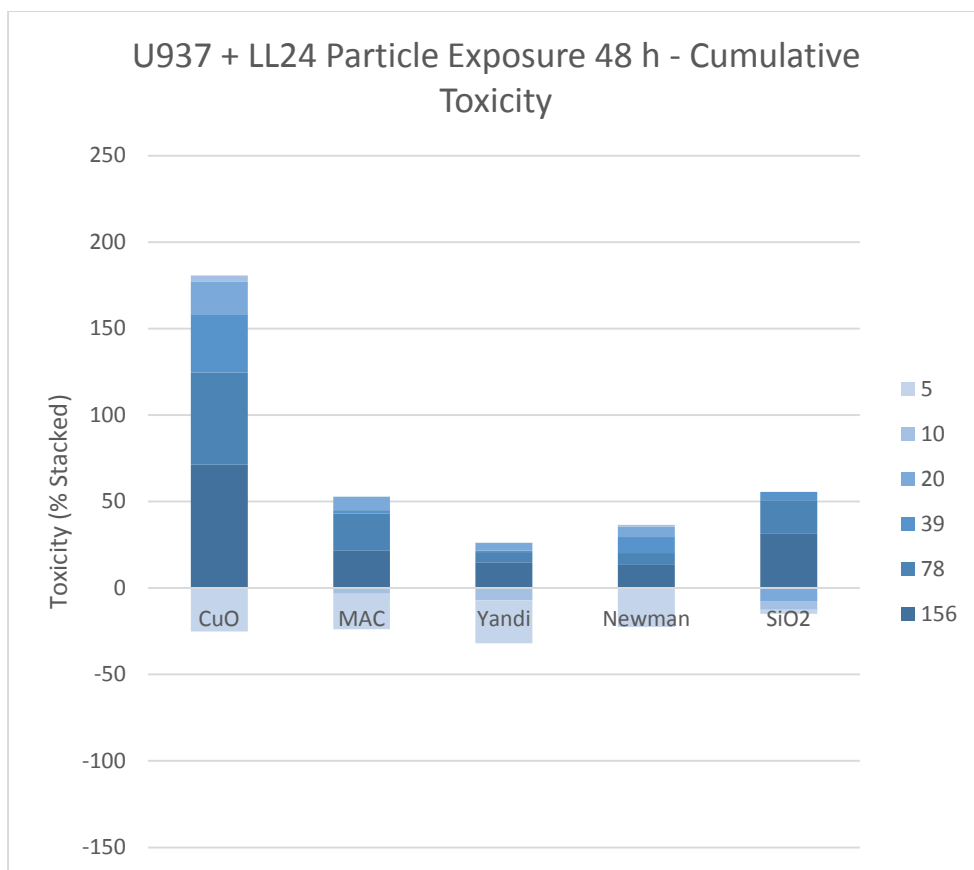


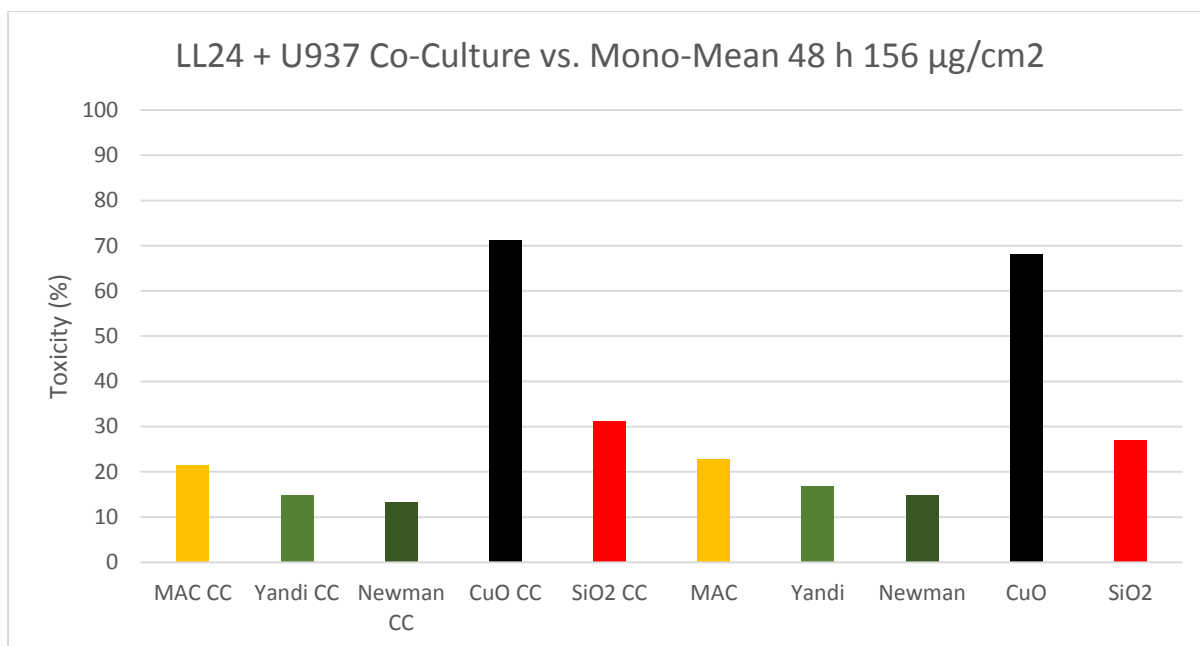
Figure 61: A549+LL24 coculture cumulative toxicity of particles across 5-156  $\mu\text{g}/\text{cm}^2$  dose range, and 1-39  $\mu\text{g}/\text{cm}^2$  dose range for CuO, over 48 h.

The coculture of U937 and LL24 examines a crucial slice of the immunological puzzle. Dysregulation of fibroblast growth by inflammatory mediators from the immune response to particulate matter is implicated as a major factor in fibrotic disease<sup>171</sup>. The cumulative toxic effects and relationships of particulates and standards resembled monoculture experiments more closely than the other coculture experiments Figure 62. At low doses, a proliferative effect was still observed. The weakness of this effect suggests it is mediated by the U937 response alone and does not greatly affect LL24 proliferation, unlike the U937+A549 coculture experiment.



**Figure 62: U937+LL24 coculture cumulative toxicity of particles across 5-156  $\mu\text{g}/\text{cm}^2$  dose range, and 1-39  $\mu\text{g}/\text{cm}^2$  dose range for CuO, over 48 h.**

The LL24+U937 coculture toxicity response to samples and standards was charted alongside the mean response of the individual LL24 and U937 cultures at 156  $\mu\text{g}/\text{cm}^2$  (CuO 39  $\mu\text{g}/\text{cm}^2$ ). The comparison shows little difference in toxicities between these two culture methods at the given concentration (see Figure 63).



**Figure 63:** Right: LL24+U937 coculture (denoted CC) toxicity of particles. Left: Geometric mean of monoculture LL24 and U937 toxicity values. Exposure shown 39  $\mu\text{g}/\text{cm}^2$  for CuO and 156  $\mu\text{g}/\text{cm}^2$  for other particles, over 48 h.

### 5.3.2 Interleukin Data

Interleukin expression was measured at 39  $\mu\text{g}/\text{cm}^2$  for particles other than CuO, which was measured at 1  $\mu\text{g}/\text{cm}^2$ , in order to detect any changes in expression near concentrations where particulate proliferative effects may dominate over cytotoxic effects (see Figure 64). While the cell monolayer toxicity profiles largely corroborated with monolayer toxicity profiles presented in Chapter 4, the cytokine induction is markedly different, potentially due to higher concentrations used previously (156  $\mu\text{g}/\text{cm}^2$  for particles other than CuO at 5  $\mu\text{g}/\text{cm}^2$ ) and shorter seeding incubation times. The expression profile of LL24 was muted in comparison, although differences in the overall profile are also emergent. Expression of IL-8 was highly attenuated, whereas IL-10 expression remained comparable. IL-6 showed the greatest inducibility, responding with a two-fold increase upon SiO<sub>2</sub> exposure.

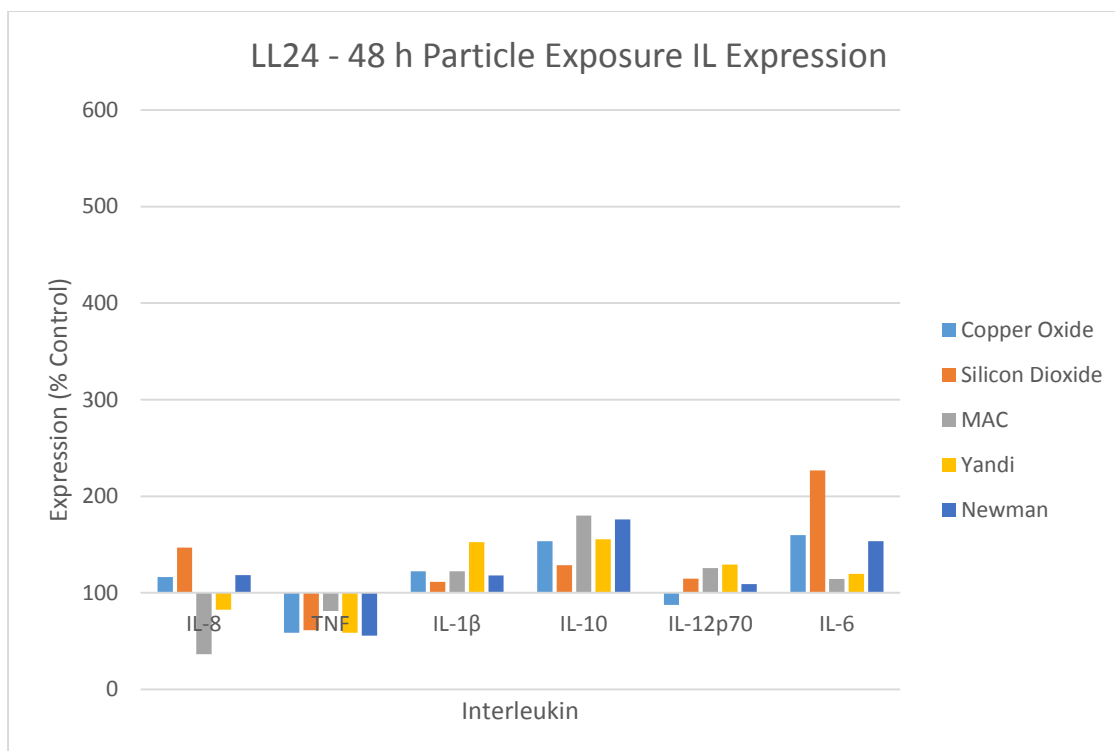


Figure 64: LL24 inflammatory cytokine expression. CuO, at 1  $\mu\text{g}/\text{cm}^2$ , others 39  $\mu\text{g}/\text{cm}^2$ .

Changes in the expression profile of U397 were also evident, and with induction of IL-1 $\beta$  and IL-10 becoming prominent (see Figure 65). Overall repression of other cytokines remained in the same order of magnitude, translating to a relatively more dynamic expression pattern than the previous experiment for the concentration. A two-fold increase in IL-6 expression was stimulated by MAC exposure.

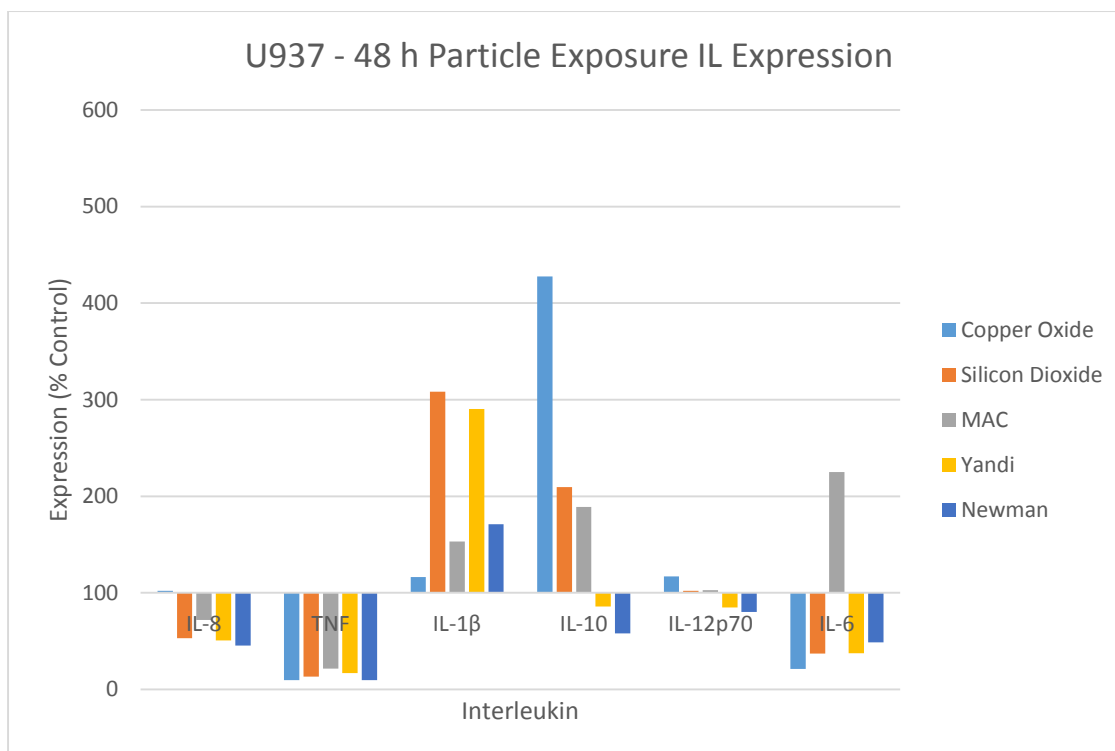


Figure 65: U937 inflammatory cytokine expression. CuO, at 1  $\mu\text{g}/\text{cm}^2$ , others 39  $\mu\text{g}/\text{cm}^2$ .

The U937+LL24 coculture experiment showed near complete suppression of cytokine responses to particles (see Figure 66). Although quantitatively compared to the monocultures, IL-8 expression was close to mean, U937 TNF expression was completely inhibited, U937 IL-1 $\beta$  expression was inhibited, IL-10 expression was inhibited, IL-12p70 expression did not occur in either the monolayer cells or coculture, and IL-6 expression was enhanced.

Why particle responses are not apparent despite continued expression of some cytokines may be due to experimental factors. This includes the 48 h time of assay being too delayed to detect a brief inflammatory reaction, or the balance of cell types being too far weighted in U937 representation. In such a scenario, the anti-inflammatory response by LL24 to too many U937 cells may be overriding any other response, mediated by IL-6. Expression of TNF- $\alpha$  on lung endothelial cells has been shown to have a repressive effect and also induce IL-6<sup>234</sup>, therefore it is possible constitutive expression levels of TNF by U937 are causing a similar suppressive feedback effect.



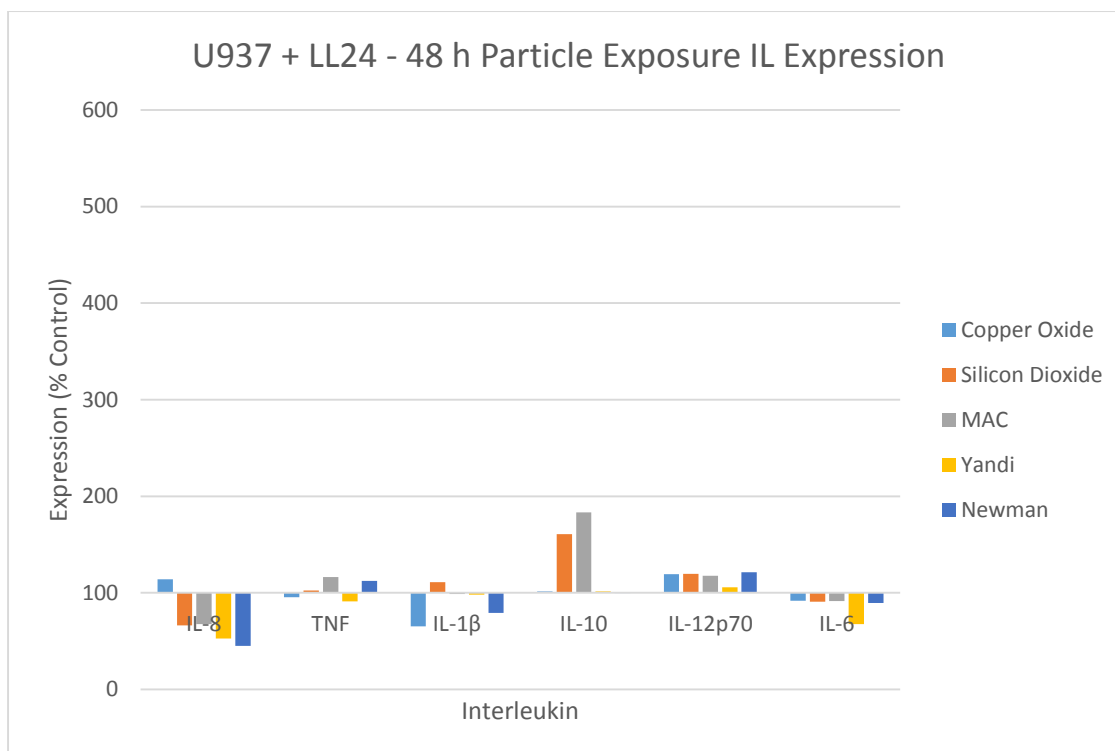


Figure 66: U937+LL24 inflammatory cytokine expression. CuO, at 1  $\mu\text{g}/\text{cm}^2$ , others 39  $\mu\text{g}/\text{cm}^2$ .

### 5.3.3 Macrophage Uptake

Previous TEM of A549 cells and LL24 cells revealed that while by light microscopy, cells appeared to take up particles into the cytoplasm, this was not necessarily the case and significant amounts of particulate matter were associated with cells but were outside the cytoplasm. Light microscopy of differentiated U937 cells confirmed particulate uptake, and unique clearance patterns (see Figure 67). The efficacy of particle uptake and macrophage behaviour was further evaluated using TEM.

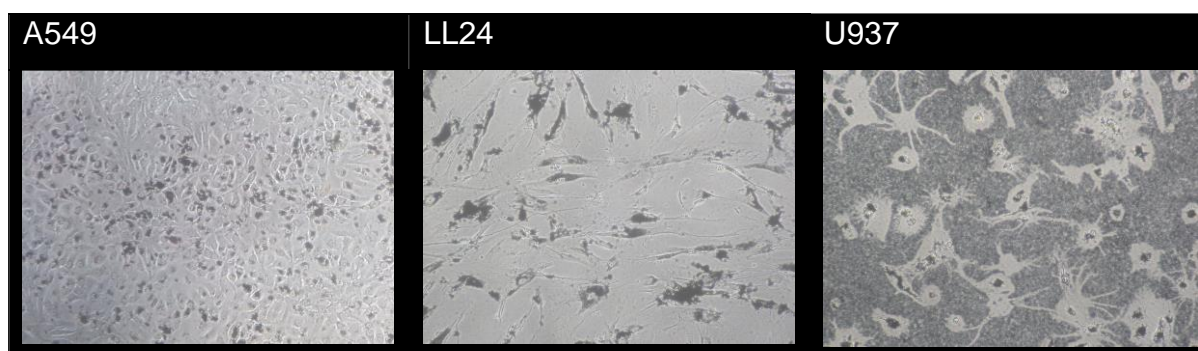


Figure 67: Cell lines exposed to 156  $\mu\text{g}/\text{cm}^2$  of  $\text{Fe}_3\text{O}_4$  oxide over 96 h, 200x magnification

Panel one shows the particle standards, cultured in 12 well plates for 96 h. Ultramicrotomy of the U937 resin samples was complicated by the hardness of the material chipping the glass knife, exacerbated by dense accumulations of particulate matter accrued by the macrophage cells. This led to thick resin sections being required reducing contrast and streaks from glass knife damage were usually visible. However, the image quality is sufficient to reveal particle-cell interactions. The carbon black sample presented with few intact macrophage cells, where instead remains of cells filled with blocky accumulations of carbon black were frequent. The low electron density made free carbon black otherwise difficult to detect. Macrophages interacting with metal-oxide particulates tended to accumulate particles around themselves, and this activity appeared to attract large clusters of macrophages. Complex cytoplasmic extensions and fine processes were seen to reach out in exploration or mediating some form of particle-cell or cell-cell contact.

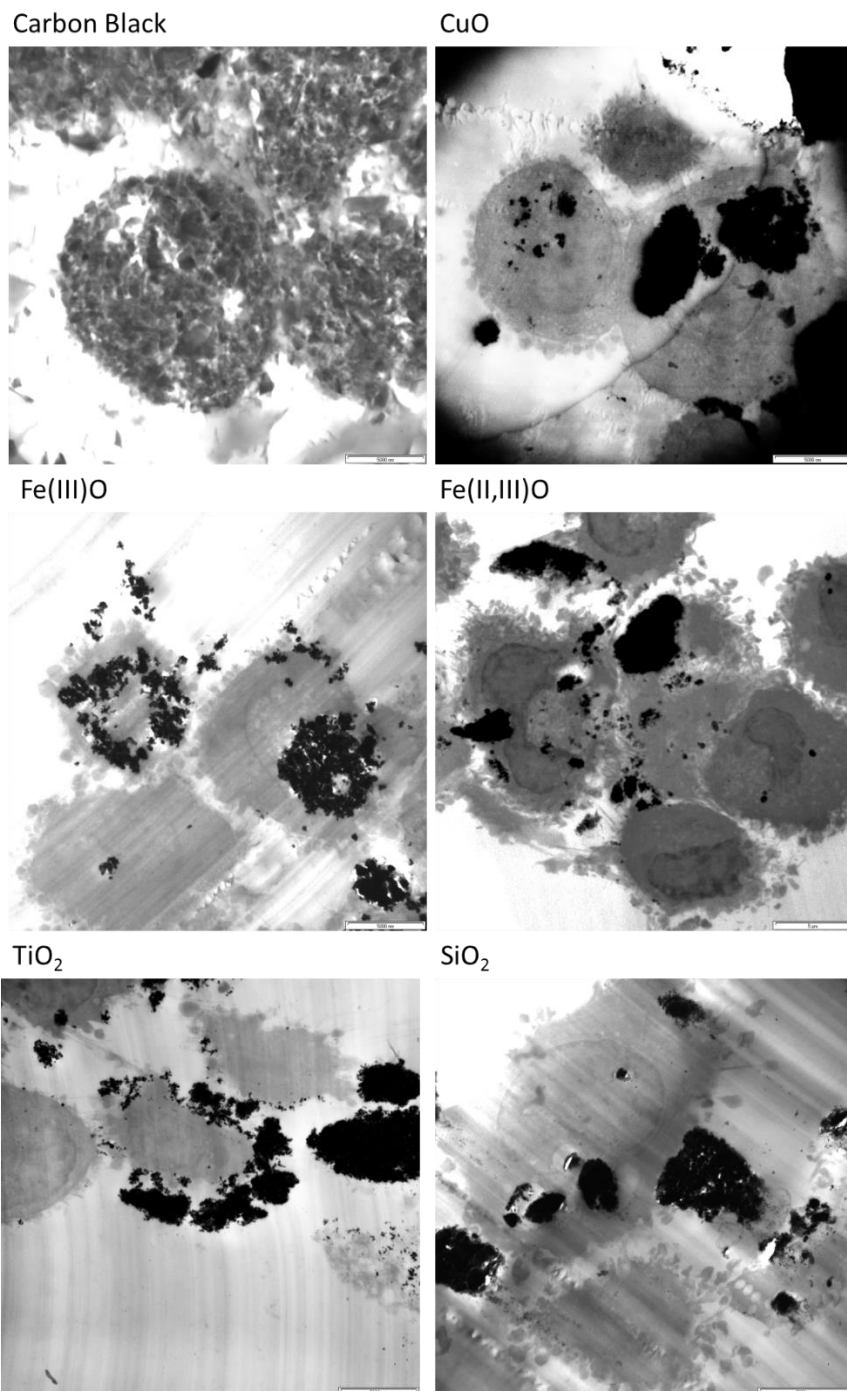
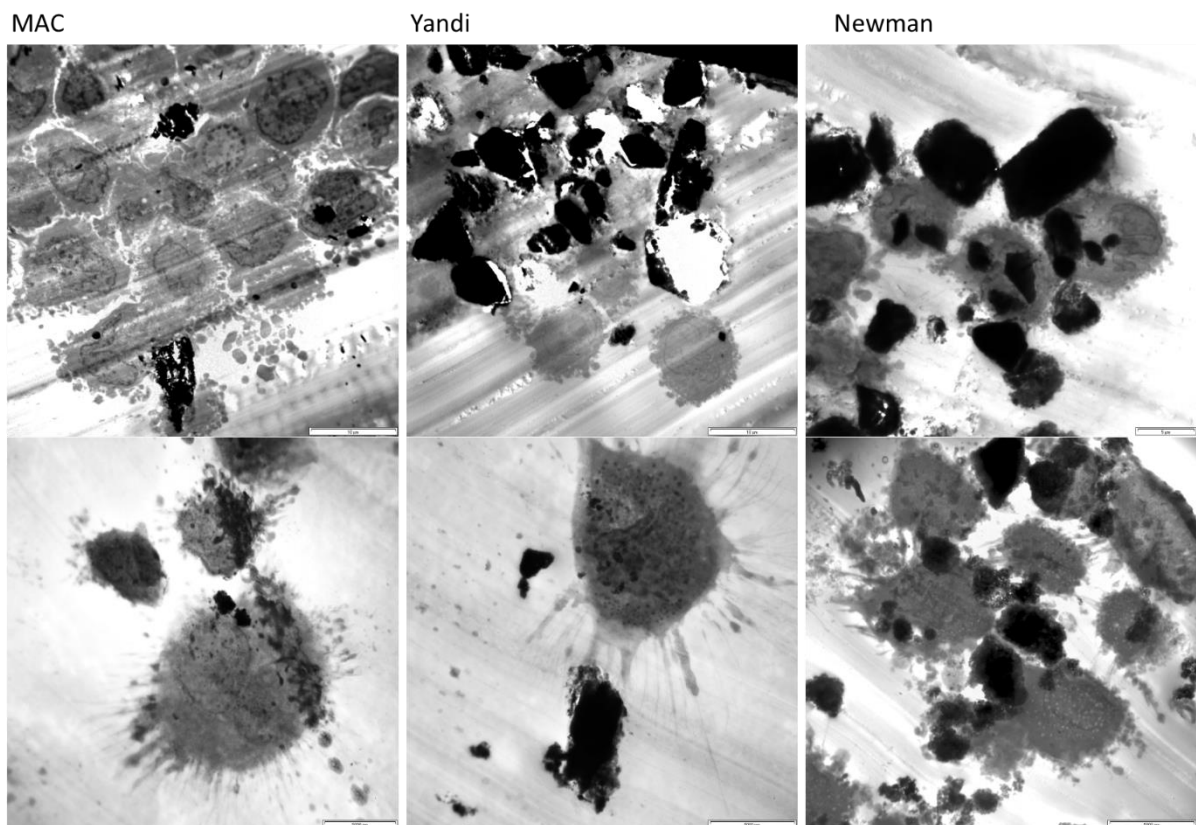


Figure 68: TEM of macrophage standard uptake in 12 plates after 96 h culture at  $40 \mu\text{g}/\text{cm}^2$ . Scale bar  $5 \mu\text{m}$ .

Panel two shows U937 differentiated macrophages interacting with iron-ore  $\text{PM}_{10}$  standards (see Figure 69). The large size of the particles tended to recruit very large masses of cells in response. Finer particles were also present and possibly accumulated cytoplasmically. The increased difficulty of particles larger than  $\sim 2 \mu\text{m}$  attracting these accumulations may implicate differential responses to the respirable fraction particulates than the fine fraction particulates which could influence toxicity.



## 5.4 Discussion

In the cell proliferation data, while the parenchymal cells cultured alone reinforce the message of a toxicity profile for insoluble particulates that is characteristic of being limited to cell membrane contact, the phagocytic cell line and different coculture combinations present an unexpected mix of new information. The shift towards a proliferative effect at concentrations of sample below  $20 \mu\text{g}/\text{cm}^2$  in the U937 cell line is interesting although unlikely to be a true proliferation as only the monocyte progenitor is known to undergo cell division in this cell line, although it may stimulate other lung cells to proliferate<sup>251</sup>. Hence, the effect is mild and likely tied to increased differentiation of remaining undifferentiated monocytes, or metabolic and cytoplasmic expansion related to macrophage phagocytic activity. At higher concentrations, the exhaustive and cytotoxic effect of phagocytosis appears to override any proliferation. When the U937 cell line is paired with the LL24 cell line, the proliferative effect continues to be limited to what is observed of the U937 cell line alone and therefore this coculture pair appears to have no alternate modulation of cytotoxicity. However, when the U937 cell line is paired with the A549 cell line, dramatic increases in cell proliferation are observed. This enhanced proliferation is furthermore discriminative, not affecting CuO or MAC exposures, yet being highly responsive to Yandi, MAC and SiO<sub>2</sub> exposures. When the A549 and LL24 cell lines are paired, the cell proliferation profile most closely resembles the U937 and A549 pairing, albeit with proliferative effects roughly halved. This pattern suggests that only in the presence of cytokine signalling from either the U937 or LL24 cell lines, A549 cells will undergo cell proliferation at moderate particulate concentrations if exposed to certain particulates, and the strength of this effect is modulated by cytokine expression differences between U937 and LL24. Immunomodulatory effects between lung epithelial cells and monocyte differentiated macrophages have been previously observed in the literature, causing differential IL-6 and IL-8 signalling when in coculture to quartz particles<sup>186</sup>.

While such observations are too limited to draw absolute conclusions of the interaction between lung epithelial, fibroblast and macrophage cells, they do show that cocultures in combination with accurate cell proliferation profiling are powerful in discriminating against the toxicity of different particulates. It has long been

understood that hyperplasia is a response to foreign material *in-vivo*, however the recognition of such effects *in-vitro* are investigated infrequently as this conflicts with the acquisition of an IC50 value. Indeed, such a situation juxtaposes opposite values as equitable measures for toxicity; while it is clear that the cytotoxicity of CuO micron-size dusts will cause cytotoxic harm to the lung parenchyma upon inhalation<sup>283</sup>, it is also known that prolonged SiO<sub>2</sub> PM<sub>10</sub> inhalation causes lung fibrosis and this is proliferative harm<sup>21</sup>.

Investigation of immunomodulatory effects using the LL24 and U937 cell line combinations were unable to derive a universal pattern of dysregulation attributable to metal-oxide microparticle exposure. Nevertheless, monoculture experiments show CuO and SiO<sub>2</sub> which are particulates of greater concern leave distinct and differential signatures, eliciting some of the strongest cytokine inductions. By the same token, the MAC and Yandi samples also left competitive signatures. It is possible that minor changes in experimental procedure can cause marked differences in cytokine expression in situations where the cytotoxicity profiles remain similar. The down-regulation of cytokines in the presence of macrophage cells also suggest that self-limiting regulatory systems may have been activated in the fibroblast-macrophage combination. There are many variables that can affect the cytokine representation of particle induced dysregulation. Of greatest concern are the method of U937 cell differentiation, presence of extracellular matrixes, exposure duration and measurement time, and which cytokines are observed<sup>163</sup>. Compounding these uncertainties, as cytokine signalling is a highly acute and transient phenomenon, marrying cytokine signalling profiles in long exposure experiments to mechanistic effects is a necessarily difficult task. In monoculture and coculture scenarios in which dysregulation is occurring it is therefore most important to look for patterns of abnormality to flag particle compositions of concern, then corroborate particle characteristics and other bioassay results in determining the toxicity driver until these issues can be resolved.

Macrophage activity is a key driver of pathological responses to particulates that occurs vigorously, independent of the poor cytotoxicity characteristics of insoluble metal oxide particles. The observation of macrophage behaviour under electron microscopy shows that the U937 monocyte differentiated macrophages are indeed

highly active against micron-size insoluble particulate matter, and will both engorge particulates until cell death occurs and recruit more macrophages while doing so, without the need for mediation by an intermediate cell type. This behaviour is associated with a slowing of particle clearance *in-vivo*<sup>304</sup>. The overall nature of this activity and recruitment appeared similar amongst the different metal-oxide samples. Such particles accrued in agglomerations of similar size that were both internalised and spatially clustered to a high degree. The carbon black nanoparticles produced a minor differential effect, packing more diffusely into the macrophage cells. Once particles had been accumulated by groups of macrophages, recruitment activity continued resulting in large numbers of surrounding cells. If this process is extrapolated to an *in-vivo* setting, it could be expected that pulmonary alveolar macrophages are likely to cause prolonged inflammatory activity against particulate matter if concentrations are high enough or aggregations large enough to prevent rapid clearance to the lymphatic system – a model which is supported in *in-vivo* literature findings<sup>186,251</sup>.

## 6. Comparative Toxicity of Acute Inhalation of Respirable Iron-Rich Particles from Mining Industry In-Vivo

### 6.1 Introduction

Validation of *in-vitro* data through an *in-vivo* experiment was sought to guide interpretation of the data and the most valuable endpoints to follow. Using mice and for intratracheal installation of iron oxides to measure lung fibrosis is an established technique from which biochemical and histological results from which fibrotic potential can be determined<sup>305</sup>. Although developing dose-response relationships in an animal model requires hundreds of animals, as only a comparative assessment of fibrotic potential is required as few as 56 animals were necessary in these experiments.

Selected samples of particulate matter (CB < 150 nm, Fe<sub>3</sub>O<sub>4</sub>, CuO < 5 µm, MAC, Yandi, Newman and SiO<sub>2</sub> PM<sub>10</sub>) and bleomycin were instilled in a single acute dose in 56 female C57BL/6J mice intratracheally. The mice were then observed for a 28 day period. The length of exposure was chosen to allow the development of fibrotic responses after instillation for observation<sup>28</sup>. Instillation was delivered by a DP-4M Dry Powder Insufflator™ (PennCentury, USA) to two groups; 10 mg/kg and 50 mg/kg. This method was chosen as it did not require a liquid bolus for aerosolization, and therefore has a more symmetrical dispersion profile to the right and left lungs, allows administration of larger doses and reduces the risk of asphyxiation. Lung tissue was harvested and split into three parts for histology (fixed in formalin), homogenisation and biochemistry (cryogenically stored in liquid nitrogen), and lastly electron microscopy (fixed in glutaraldehyde). Heart, kidney and liver tissues were also stored in formalin. At least 300 µL of blood was taken and stored cryogenically. Histological staining was performed on the mouse lungs using Masson's Trichrome for detecting collagen deposition as a marker of fibrosis. Due to time constraints and the sufficiency of histological data for comparative purposes, further experimental work was not integrated. However, lung biochemistry and blood work are available to future investigations. Specifically, these are the corroboration of histological lung fibrosis with lung homogenate collagen content through the hydroxyproline assay, analysis of systemic inflammation from blood using the Mouse Inflammation Kit



cytometric bead assay (BD, USA) and electron microscopy of particle-lung interaction *in-situ*.

## 6.2 Materials and Methods

### 6.2.1 Particulates and Reagents

Particle standards: Carbon Black < 150 nm, Fe<sub>3</sub>O<sub>4</sub> < 5 µm, CuO < 5 µm, MAC PM<sub>10</sub>, Yandi PM<sub>10</sub>, Newman PM<sub>10</sub>, SiO<sub>2</sub> PM<sub>10</sub>. Positive control: bleomycin. Particulate vehicle: fine cornflour. Belomycin vehicle: PBS. Anaesthetic: ketamine. Electron microscopy fixative: glutaraldehyde. Biochemistry reagents: Hydroxyproline (#MAK008-1KT, Sigma Aldrich), Mouse Inflammation Kit (552364, Sigma Aldrich).

### 6.2.2 Animal Selection and Handling

The use of animals in this experiment was approved by the Queensland Health Animal Ethics Committee. Female 6 week old C57BL/6J mice were purchased from Cerberus Sciences, Australia. The mice were acclimatised for 1 week before separation into cages of 6 by groupings.

### 6.2.3 Animal Dosing

Animals were restrained on a Mouse Intubation Platform (Penn-Century, USA) and anaesthetised with intraperitoneal injection of ketamine before intratracheal instillation of sample. Dosage was calculated to meet specification (10 mg/kg or 50 mg/kg) using cornflour as a bulking agent, according to their initial weight (see Table 13). The Dry Powder Insufflator™ (Penn-Century, USA) was loaded with 3.5 mg of vehicle and sample mixture and connected to the hand driven air pump. The vehicle mixture dosage were calculated in recognition of an estimated efficiency of 0.8 mg of solid material dosed per 200 µL air volume puff of the device. A small animal laryngoscope (Penn-Century, USA) was used to open the mouth for dosing. Only one puff was used per mouse before reloading.

After dosing, the animals were left to recover, with special observation made three times per day for 3 days to ensure no adverse effects were occurring. Thereafter, the animals were maintained as per usual for 28 days before sacrifice.

**Table 13: Animal designation, dosage and weights**

<i>Material</i>	<i>Dosage</i>	<i>Designation</i>	<i>Initial Weight</i>	<i>End Weight</i>
<i>Carbon Black</i>	10 mg/kg	CB-1B	18.32	21.1
<i>Carbon Black</i>	10 mg/kg	CB-2B	17.66	19.89
<i>Carbon Black</i>	10 mg/kg	CB-3B	19.92	22.12
<i>Carbon Black</i>	50 mg/kg	CB-1R	18.48	22.02
<i>Carbon Black</i>	50 mg/kg	CB-2R	18.75	21.67
<i>Carbon Black</i>	50 mg/kg	CB-3R	17.58	22.76
<i>Iron(II,III) Oxide</i>	10 mg/kg	Fe-1B	18.46	20.63
<i>Iron(II,III) Oxide</i>	10 mg/kg	Fe-2B	19.02	20.35
<i>Iron(II,III) Oxide</i>	10 mg/kg	Fe-3B	17.27	21.16
<i>Iron(II,III) Oxide</i>	50 mg/kg	Fe-1R	18.28	21.71
<i>Iron(II,III) Oxide</i>	50 mg/kg	Fe-2R	19.68	21.63
<i>Iron(II,III) Oxide</i>	50 mg/kg	Fe-3R	19.92	22.28
<i>Newman</i>	10 mg/kg	NM-1B	18.15	21.62
<i>Newman</i>	10 mg/kg	NM-2B	18.11	20.28
<i>Newman</i>	10 mg/kg	NM-3B	17.16	21.06
<i>Newman</i>	50 mg/kg	NM-1R	18.54	21.88
<i>Newman</i>	50 mg/kg	NM-2R	17.71	18.68
<i>Newman</i>	50 mg/kg	NM-3R	18.61	21.51
<i>MAC</i>	10 mg/kg	MC-1B	18.94	21.3
<i>MAC</i>	10 mg/kg	MC-2B	19.13	21.09
<i>MAC</i>	10 mg/kg	MC-3B	17.68	20.21
<i>MAC</i>	50 mg/kg	MC-1R	20.56	23.46
<i>MAC</i>	50 mg/kg	MC-2R	18.86	20.73
<i>MAC</i>	50 mg/kg	MC-3R	19.52	22.3
<i>Yandi</i>	10 mg/kg	YN-1B	18.95	20.35
<i>Yandi</i>	10 mg/kg	YN-2B	17.07	20.46
<i>Yandi</i>	10 mg/kg	YN-3B	19.03	20.86
<i>Yandi</i>	50 mg/kg	YN-1R	19.15	23.53
<i>Yandi</i>	50 mg/kg	YN-2R	17.88	20.1
<i>Yandi</i>	50 mg/kg	YN-3R	18.82	21.46
<i>Silicon Dioxide</i>	10 mg/kg	Si-1B	18.33	21.52
<i>Silicon Dioxide</i>	10 mg/kg	Si-2B	18.58	20.84
<i>Silicon Dioxide</i>	10 mg/kg	Si-3B	18.82	20.22
<i>Silicon Dioxide</i>	50 mg/kg	Si-1R	19.85	23.46
<i>Silicon Dioxide</i>	50 mg/kg	Si-2R	19.86	22.88
<i>Silicon Dioxide</i>	50 mg/kg	Si-3R	17.26	21.62
<i>Copper Oxide</i>	10 mg/kg	Cu-1B	18.4	21.36
<i>Copper Oxide</i>	10 mg/kg	Cu-2B	18.35	19.67
<i>Copper Oxide</i>	10 mg/kg	Cu-3B	19.09	20.6

<i>Copper Oxide</i>	50 mg/kg	Cu-1R	17.69	20.67
<i>Copper Oxide</i>	50 mg/kg	Cu-2R	17.71	20.65
<i>Copper Oxide</i>	50 mg/kg	Cu-3R	17.76	21.3
<i>Bleomycin</i>	5 mg/kg	BL-1B	18.83	20.56
<i>Bleomycin</i>	5 mg/kg	BL-2B	18.84	21.19
<i>Bleomycin</i>	5 mg/kg	BL-3B	19.54	22.48
<i>Bleomycin</i>	10 mg/kg	BL-1R	19.68	21.05
<i>Bleomycin</i>	10 mg/kg	BL-2R	19.04	20.43
<i>Bleomycin</i>	10 mg/kg	BL-3R	17.2	19.69
<i>Vehicle Control</i>	10 mg/kg	VC-1B	18.92	20.52
<i>Vehicle Control</i>	10 mg/kg	VC-2B	20.53	21.6
<i>Vehicle Control</i>	10 mg/kg	VC-3B	18.83	20.23
<i>Blank Control</i>	0 mg/kg	NO-1R	18.02	23.26
<i>Blank Control</i>	0 mg/kg	NO-2R	18.91	22.18
<i>Blank Control</i>	0 mg/kg	NO-3R	17.75	21.36

#### 6.2.4 Animal Sacrifice

Animals were sacrificed using O<sub>2</sub>:CO<sub>2</sub> overdose at a 50:50 ratio to first anaesthetise the animal, before 100% CO<sub>2</sub> was applied after 5 minutes to ensure death had occurred.

#### 6.2.5 Histological Methods

Lung histology was carried out on right lobe lung tissue fixed in formalin and paraffinized using the Masson's Trichrome stain. Approximately 275 slides were prepared (5 slides per lung) with 4 sections each, allowing the statistical power of analysis to be increased if necessary. Slides were recorded digitally on an Aperio slide scanner. Aperio ImageScope v11 was used to calculate the positive pixel count values. The settings used were: Positive Pixel Count v9 Algorithm, Hue 0.936 (red, not used), Hue 0.536 (blue/green), Hue Width 0.5, Color Saturation Threshold 0.04.

### 6.3 Results

#### 6.3.1 Lung Histology

The lung histological sections obtained show that the vehicle control (cornflower) did not appear to cause any fibrotic changes above the no exposure control (see Figure

70). However as the lungs were not filled with agarose prior to fixing to preserve lung biochemistry and net weight, morphological changes are difficult to gauge as some collapse of structure is apparent. This may also be affected by the sacrifice method, causing interference with breathing and lung function. The appearance of the  $\text{Fe}_3\text{O}_4$  sample is similar to the vehicle control, while significant increases in collagen deposition from the CuO exposure are visible, affecting the bronchioles and alveoli.

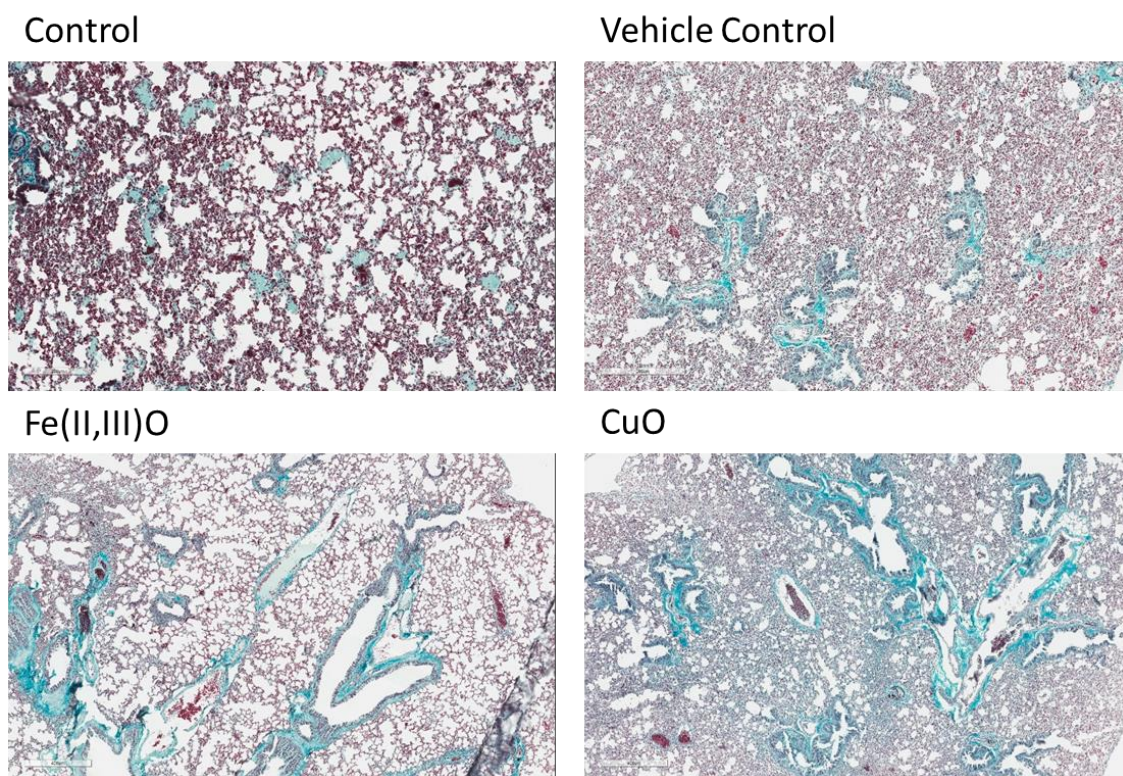
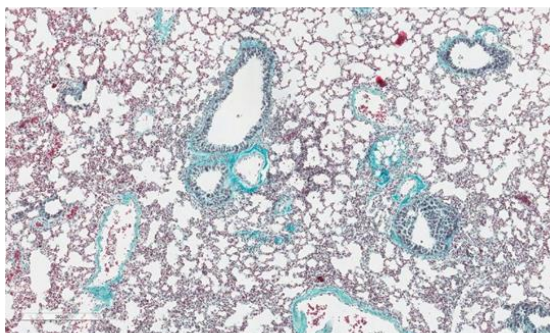


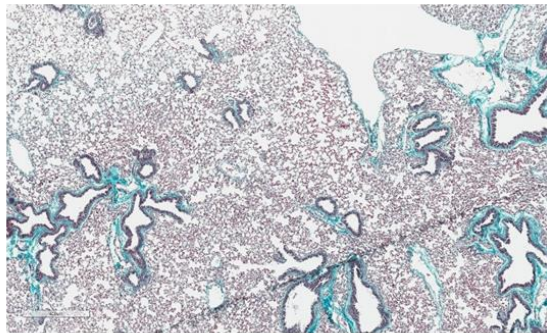
Figure 70: 28 day exposure, control, Vehicle Control,  $\text{Fe}_3\text{O}_4$ , CuO. C57/BL6 lung histology, Masson's Trichrome 200x.

Increases in collagen deposition in the lungs using Masson's Trichrome has been described in the literature previously, showing increases in collagen deposition by  $\text{SiO}_2$  at 10 mg/kg and 50 mg/kg and  $\text{TiO}_2$  only at 50 mg/kg after 28 days<sup>28</sup>. This corroborates well with observations in this study, as collagen staining is visibly higher in the  $\text{SiO}_2$  samples. A pervasive increase in collagen deposition is observed both in the bronchiole walls and in the alveolar spaces. The appearance of collagen in the iron-ore samples is less, similar to the control and  $\text{Fe}_3\text{O}_4$  standard (see Figure 71).

MAC



Newman



Yandi

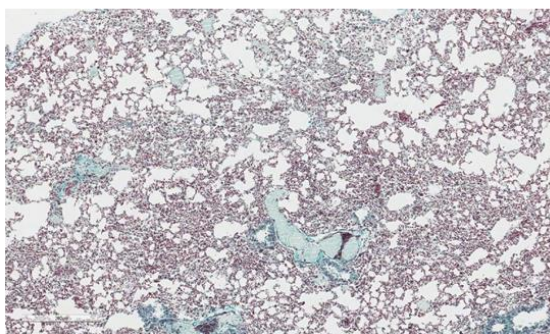
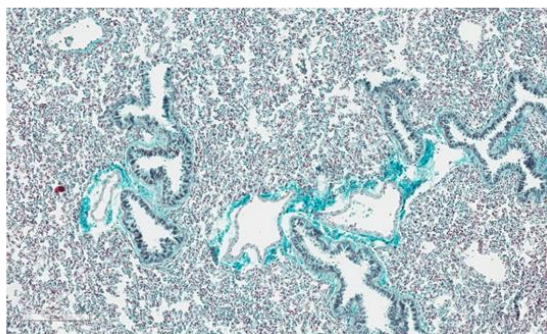
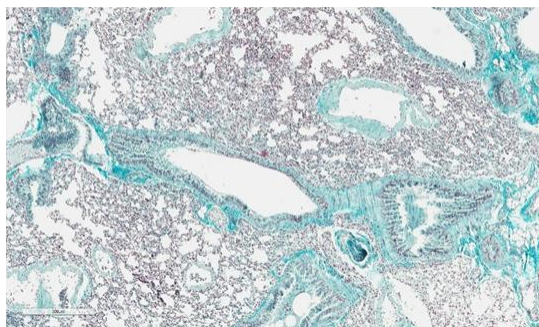
SiO<sub>2</sub>

Figure 71: 28 day exposure, MAC, Newman, Yandi, SiO<sub>2</sub>. C57/BL6 lung histology, Masson's Trichrome 200x.

The pulmonary and systemic inflammatory properties of carbon black<sup>306</sup> are well studied, as are the fibrotic effects of bleomycin from both *in-vivo* and clinical studies due to its use as a cytotoxic antineoplastic drug<sup>246</sup>. The effects of these particles are demonstrated clearly in the observed increase of collagen deposition (see Figure 72).

Carbon Black



Bleomycin

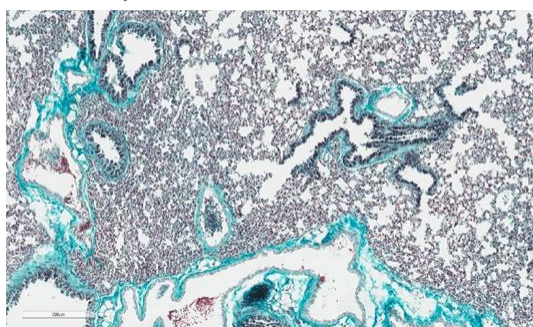
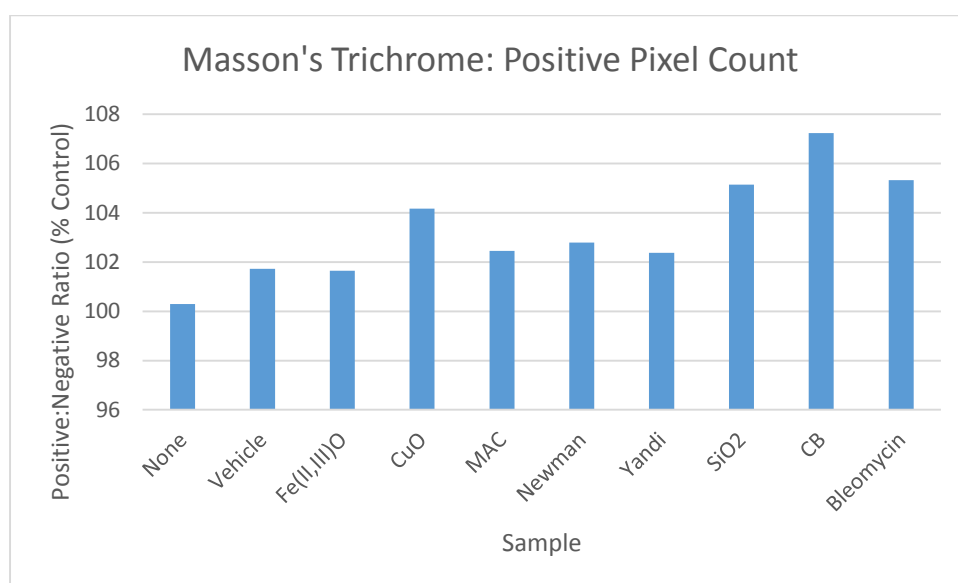


Figure 72: 28 day exposure, Carbon Black, Bleomycin. C57/BL6 lung histology, Masson's Trichrome 200x.

A computational analysis of the higher effect dosage of sample on mouse lung staining is shown in Figure 73. Areas not containing bronchial structures were

chosen for analysis, with 3 different sections per sample used and the mean of the 3 replicates taken. While the short time period produced a very mild fibrotic effect, improvements to the hue values selected in the colour matching algorithm may be able to strengthen the results. The results confirm what is visible by eye, and despite low cytotoxicity *in-vitro*, SiO<sub>2</sub> and carbon black were the most fibrotic compounds assayed as implied by collagen deposition, matching or surpassing bleomycin as the positive control. However, CuO was also confirmed as highly fibrotic, while the pattern between the Fe<sub>3</sub>O<sub>4</sub> standard and iron-ore samples closely resembled *in-vitro* results.



**Figure 73: Analysis of Masson's Trichrome stained mouse lung histological sections. Positive to negative pixel count ratios for blue/green staining indicative of collagen deposition shown.**

The level of effect was on the order of several percent in this analysis, and continued development will be required to allow the algorithm to differentiate the effects more clearly. Nevertheless, the histological samples provide comparative relationships between samples, and do indeed highlight the particulate standards suspected or known to be causes of pulmonary fibrosis. Additional unique parameters, including interleukin expression profiles, redox activity, proliferative effects and solubility. Integration with biochemistry techniques will further enhance these findings in the future.

## 6.4 Discussion

Crystalline silica PM<sub>10</sub> is frequently used in conjunction with mouse models in determining the nature and histological profile of lung fibrosis, often with a trichrome stain, in exposure durations as short as three weeks<sup>307</sup>. Interest in such experiments is typically driven by investigations of silicosis pathology which is a hazardous component of many of mine dusts<sup>95</sup>. It is therefore expected that in iron oxide inhalation experiments *in-vivo* of a similar concentration and size fraction will involve some or all of the mechanisms involved in silicosis, and possibly novel ones. As there are established occupational limits for silicon dioxide inhalation by regulatory agencies around the world<sup>100</sup>, it is therefore useful to compare iron-ore mine site samples predominantly to crystalline silica dioxide by suitable endpoints such as lung fibrosis pathology.

In a review of *in-vivo* and *in-vitro* research on crystalline silica and coal dust, which under occupational exposure settings cause the clinically distinct presentations of silicosis and anthracosis, Castranova et. al. propose four basic toxicity mechanisms; direct cytotoxicity, activation of immunological ROS production, activation of immunological recruitment mediators, and activation of fibrotic mediators<sup>95</sup>. All four mechanisms directly or indirectly mediate the process of fibrosis, through inflammatory and proliferative processes. Fibrosis is therefore a key marker of particulate driven lung toxicity that captures a broad range of the proposed toxic mechanisms, and the lung pathology that it is associated with. However, it must be noted that other systemic complications are possible and restrictive lung disease is irreversible, increasing mortality from infections and other diseases. Cardiovascular disease resulting from chronic hypoxia is also a common cause of death in patients with lung fibrosis<sup>95</sup>. With exception to some particulate types, fibrosis of the lung is generally only mildly associated with cancer outcomes when considering poorly soluble particles and silica, when concomitant inhalation of known carcinogens is accounted for<sup>118</sup>. In coal workers, gastric cancer is increased, the risk of lung cancer is not, potentially reflecting bioactivation or bioavailability in the stomach that does not occur in the lungs<sup>95</sup>.

An epidemiological study of urban ambient particle composition highlights the transition metals Ni and V as most strongly associated with mortality (risk coefficient > 0.5), followed by elemental carbon, Zn, SO<sub>4</sub>, Cu, PB, organic carbon and total PM<sub>2.5</sub><sup>259</sup>. As these transition metals are largely associated with fuel oil combustion they may not necessarily represent the risk pure metal oxides pose, although it is clear attributes beyond particle shape and size account for toxic effects. Solubility, crystallinity, ROS catalysis and associations with VOC and PAH are key modulators<sup>308</sup>. This is not to say insoluble metal oxides are otherwise invariant in toxicity; it has been shown that the cytotoxicity of CuO particles is an order of magnitude higher than corresponding doses of TiO<sub>2</sub> and Fe<sub>3</sub>O<sub>4</sub> *in-vitro*<sup>215</sup>.

Insoluble metal oxides also exhibit greater biopersistence, although this is not strongly indicative of adverse effects. In a study of TiO<sub>2</sub> and crystalline SiO<sub>2</sub> nano and submicron-size particles on rats after a 12 week ambient exposure period, it was found that SiO<sub>2</sub> submicron-size particles caused post-exposure radiolabelled test particle clearance rates to slow by 28 fold. In comparison, the TiO<sub>2</sub> exposures accumulated a 15 fold higher mass in the lungs over the exposure period and TiO<sub>2</sub> nanoparticles caused a slowing of 8 fold, while TiO<sub>2</sub> submicron particles caused a relatively mild 2 fold slowing<sup>33</sup>. It is likely that given the highly extended nature of SiO<sub>2</sub> mediated impairment, the reduced clearance rates are related to fibrotic changes to the lungs which are not limited to temporary immunological depletion. It is also important to note that high particle loads reaching the lung parenchyma appear to have relatively little effect on lung function unless such particles are highly inflammatory or toxic, either by nature of size or biochemical reactivity. These loads must also be consistently applied to reach a critical mass if clearance is to fail, after which the combination of impaired macrophage mediated transport and continued cytokine signalling can cause acceleration of fibrosis, clinically seen as progressive massive fibrosis which can complicate silicosis, anthracosis and other pneumoconiosis diseases<sup>205</sup>.

The subdued differences in collagen deposition between the particulate types observed in Figure 73 may partially be a reflection of the single-dose short duration experiment. Over a longer term 90 day experiment in the literature, rats lung weight resisted change compared to controls when challenged with welding fume



concentrations of 67 mg/m<sup>3</sup> for 2 hours per day, whereas 118 mg/m<sup>3</sup> caused progressive accumulation and fibrosis. Furthermore, fibrotic changes were limited to perivascular and peribronchiolar regions by day 30, and interstitial fibrosis had only begun to develop by day 60<sup>242</sup>. A shorter term 28 day experiment failed to show TiO<sub>2</sub> as fibrogenic at concentrations less than 50 mg/kg<sup>28</sup>, suggesting the 10 mg/kg maximum dose of Fe<sub>2</sub>O<sub>3</sub> and iron ore samples may not be enough to elicit a strong response. However, comparable studies of bleomycin show increases of over two fold in collagen deposition which was not reflected in the positive pixel count<sup>245</sup>. The exclusion of bronchiolar structures in the count, as well as the effects of outliers where instillation has failed may also reduce the observed differences due to the small number of animals used. Nevertheless, the visible changes in staining between exposures (see Figure 70-Figure 72) do serve to draw attention to the increased collagen deposition of bleomycin, carbon black, SiO<sub>2</sub> and CuO – all compounds with known proliferative, fibrotic and cytotoxic potency in the literature. In contrast, Fe<sub>2</sub>O<sub>3</sub> remains similar in appearance to the control, as do the iron-ore samples, strongly supporting to the in-vitro findings mirroring this toxicity profile.

## 7. General Discussion

It is increasingly becoming clear that metal oxide particles pose an imminent health threat to not only settlements associated with mining activity, but major centres especially in developing nations where airborne industrial pollutants are rich in metal oxides whose inhalation toxicity is poorly understood<sup>49</sup>. Regulators are left with inadequate toxicity information specifically relating to such pollutants, and potentially inadequate guidelines and metrics to deal with these issues. Disharmony in the measurement of toxicity doubly affects air quality regulation by eroding the confidence in its enforcement<sup>97</sup>.

Great strides have been made in the development of *in-vitro* particulate matter toxicology assays in an effort to produce reliable toxicity data, however mechanistic uncertainties and conflicting *in-vivo* data have led to a poor translation of experimental data to regulatory air quality guidelines. Fundamentally, *in-vitro* experiments can highlight differential cytotoxicity between insoluble metal-oxides<sup>283</sup>, and with further development complete the mechanistic picture and monitoring applications which epidemiological studies and *in-vivo* studies alone cannot.

A multifaceted approach to both the application and interpretation of *in-vitro* toxicological data is therefore required to reach accurate conclusions for the toxicity of PM<sub>10</sub> and PM<sub>2.5</sub> in the lungs. It is not sufficient to equate cytotoxicity *in-vitro* to fibrotic potency *in-vivo*, or vice versa. The complex interactions between particles, immune system and the lung parenchyma present a system that requires not only a unique approach to modelling disease outcomes but also a strategy for management of complexity itself, observant of the weight of evidence from all sources.

Specifically, emphasis must be given to comparing responses of lung epithelial and fibroblast cells with phagocytic cells and in coculture, as immunological activity occurs against particulate matter regardless of its toxicity and it is this activity which is key in the initiation of fibrosis and the systemic effects that increase the likelihood

of cardiovascular events which shape morbidity and mortality in the population comparably to pulmonary disease <sup>265</sup>.

While unconventional, the interpretation of reverse-toxicity signalling a proliferative immune responses correctly associates SiO<sub>2</sub> and CB with increased inflammatory and cytotoxic potential, in relation to the *in-vivo* study. It is notable that SiO<sub>2</sub> and CB inhalation is also billed as potent fibrotic agents in the literature, and that titanium dioxide also exhibits unique inflammatory characteristics <sup>212</sup>. Similar effects in cocultures help examine and define the proliferative potential of particulates and simultaneously establish important relationships between macrophage and lung cell mediated pro-fibrotic changes which would otherwise require *in-vivo* experiments to detect.

Hyperplasia in fibrotic lung disease is associated with cytokine signalling changes <sup>243</sup>, necessitating the analysis of inflammatory cytokines, which provides data essential to interpretation of particle toxicity. However, such analyses carry several caveats. Interleukin expression may be time-dependent, and has self-regulating properties in coculture. The intricacy of suppressive and stimulatory interactions between different cytokines, as well as differences in acute and prolonged expression characteristics requires further study to develop the most informative and reliable assay protocols. Mitigating these effects requires careful correction for cytotoxicity, an advantage of the multiplexed assays used, and gathering a large volume of data. The flow cytometric bead array process used lends itself to high data throughput and minimizes intra-sample error, as thousands of counts are compiled to report concentration.

In the absence of all other considerations of particulate characteristics, a weight of evidence based approach to determining a Derived No-Effect Levels (DNEL) of exposure for insoluble particulates hinges on particle displacement volume retained in the lungs <sup>34</sup>. Overload of the alveolar macrophage pool by a sufficient volume (approximately 1 µL/g of lung tissue) of particle reduces clearance time, which is on the order of 500 days for particles reaching the acinar surfaces <sup>25,274</sup>. Reduced clearance and increased inflammation aggravates fibrotic processes, with the implication is that increased toxicity reduces the concentration for overload-like

symptoms to occur<sup>18,22</sup>. For residents of mining towns, this raises concerns on the cumulative effect of any chronic exposure to PM<sub>10</sub> and PM<sub>2.5</sub>, and places importance on toxicities that may amplify over time<sup>309</sup>.

To achieve a better understanding of the toxicity of metal-oxide PM<sub>10</sub> and PM<sub>2.5</sub>, large amounts of data must be gathered. The analyses within this thesis are pointed towards integration and reduction of bottlenecks in analysis, suitable to this objective. Figure 74 summarises the most productive endpoints found in the project and how they are linked to one another, as a platform for future studies to assess environmental samples in the future.

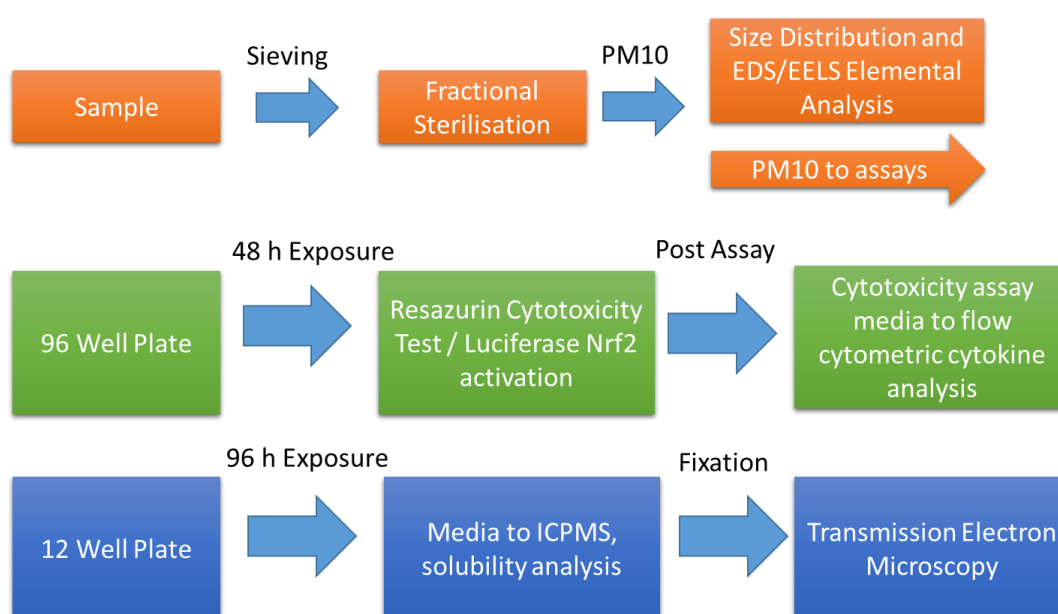


Figure 74: Linking of key steps and endpoints in the high-throughput assay of poorly-soluble PM<sub>10</sub> and PM<sub>2.5</sub>

The current data resulting from this process suggests very similar effects from the MAC, Yandi and Newman PM<sub>10</sub> samples to general haematite and magnetite PM<sub>10</sub> inhalation. The cytotoxic, oxidative, immunological and physical endpoints employed validate this comparison. While this is unsurprising given the nature of the ore, it is important in that it is possible to compare iron ore dusts from multiple regions across the world, and perform epidemiological studies with greater understanding of any site-specific exposure differences. A less conservative approach would be to model toxicity directly as a fraction against the standards tested, creating a composite picture of toxicity using existing epidemiological data of standards such as CuO,

crystalline SiO<sub>2</sub>, CB and micron-size glass fibre to frame cytotoxic, pro-fibrotic, pro-inflammatory and carcinogenic endpoints. In relation to these standards, patterns such as high solubility combined with high cytotoxicity, or moderate cytotoxicity combined with proliferative potential in co-culture and strong induction of inflammatory, or high aspect ratio and insolubility, are warning signs to look for in this regard.

High throughput *in-vitro* analysis is extremely useful to minimise risk through detection of dangerous particulate emission sources early. What such a strategy depends on is good epidemiological data on the translation of very specific material exposures at a subacute, chronic dose, over very long periods of time. Thus, a careful marriage of epidemiological data sets informed by toxicological data will over time produce more direct translations of ambient exposure concentrations and durations to fibrotic and systemic health outcomes.

## 8. Future Work

Further work with *in-vivo* samples is necessary to build a thorough picture of how comparative data *in-vivo* links to *in-vitro* data. Specifically, lung biochemistry can be performed as another measure of inflammatory response and collagen deposition, while electron microscopy may confirm parenchymal and macrophage particle-interactions *in-vivo*.

In the future, more detailed identification of inflammatory responses between cocultures of different cell types needs to be conducted, in addition to optimisation. Experiments with asynchronous coculture, where media supernatant is transferred from one cell line to another after an exposure time interval, may help to clarify the responses and timings of interleukin expression between cell types.

Whether the fibrotic potential of high aspect ratio particles such as asbestos and glass fibres can be detected *in-vitro* is important. Warning of the toxicity of such compounds is currently implied through TEM observation, although a biochemical endpoint would be preferable.

## 9. Bibliography

1. Wilson, J. BHP Billiton Iron Ore: Value through productivity and growth. in *Australian Journal of Mining Global Iron Ore and Steel Forecast Conference* 1–19 (BHP Billiton, 2014). at <[http://www.bhpbilliton.com/home/investors/reports/Documents/2014/140311\\_AustralianJournalofMiningConference.pdf](http://www.bhpbilliton.com/home/investors/reports/Documents/2014/140311_AustralianJournalofMiningConference.pdf)>
2. Ashby, I. BHP Billiton Iron Ore - Growth and Outlook. in *Australian Journal of Mining Global Iron Ore and Steel Conference* 1–21 (BHP Billiton, 2012). at <[http://www.bhpbilliton.com/home/investors/reports/Documents/2012/120320\\_AJMConference.pdf](http://www.bhpbilliton.com/home/investors/reports/Documents/2012/120320_AJMConference.pdf)>
3. Geoscience Australia. Australian Atlas of Minerals Resources, Mines and Processing Centres. *Iron Ore* 1–6 (2013). at <[http://www.australianminesatlas.gov.au/aimr/commodity/iron\\_ore.html](http://www.australianminesatlas.gov.au/aimr/commodity/iron_ore.html)>
4. Government of Western Australia Department of State Development. *Port Hedland Air Quality and Noise Management Plan*. (2010). at <<http://www.dsd.wa.gov.au/documents/000991a.denise.lazenby.pdf>>
5. Sinclair Knight Merz. *Port Hedland Cumulative Impact Study*. (2007). at <<http://www.dsd.wa.gov.au/documents/000247.Denise.LAZENBY.pdf>>
6. Department of Environment and Conservation. *A guideline for managing the impacts of dust and associated contaminants from land development sites , contaminated sites remediation and other related*. (2011).
7. Landcorp. *Port Hedland/South Hedland Pilbara Vernacular Handbook Part 4-29*. (2008). at <[http://www.landcorp.com.au/Documents/Corporate/Pilbara Vernacular/Part-4-PORT-HEDLAND\\_Part3.pdf](http://www.landcorp.com.au/Documents/Corporate/PilbaraVernacular/Part-4-PORT-HEDLAND_Part3.pdf)>
8. Churg, a & Brauer, M. Human lung parenchyma retains PM2.5. *Am. J. Respir. Crit. Care Med.* **155**, 2109–11 (1997).
9. Asgharian, B., Price, O. T. & Hofmann, W. Prediction of particle deposition in the human lung using realistic models of lung ventilation. *J. Aerosol Sci.* **37**, 1209–1221 (2006).
10. Künzli, N. & Perez, L. Evidence based public health - the example of air pollution. *Swiss Med. Wkly. Off. J. Swiss Soc. Infect. Dis. Swiss Soc. Intern. Med. Swiss Soc. Pneumol.* **139**, 242–50 (2009).
11. Grant, L. D., Kotchmar, D. J. & National Center for Environmental Assessment. *Air Quality Criteria for Particulate Matter. Environmental Protection I*, (2004).
12. Morawska, L., Moore, M. R., Ristovski, Z. D. & Review, D. L. *Health Impacts of Ultrafine Particles. Measurement* (2004). at

<<http://www.environment.gov.au/atmosphere/airquality/publications/health-impacts/index.html>>

13. Donaldson, K. & Seaton, A. A short history of the toxicology of inhaled particles. *Part. Fibre Toxicol.* **9**, 13 (2012).
14. Heppleston, a G. Coal workers' pneumoconiosis: a historical perspective on its pathogenesis. *Am. J. Ind. Med.* **22**, 905–23 (1992).
15. Pope, C. A. & Dockery, D. W. Health effects of fine particulate air pollution: lines that connect. *J. Air Waste Manag. Assoc.* **56**, 709–42 (2006).
16. Borm, P. J. A. Particle toxicology: from coal mining to nanotechnology. *Inhal. Toxicol.* **14**, 311–24 (2002).
17. Stewart, M. J. & Faulds, J. S. The pulmonary fibrosis of hæaematite miners. *J. Pathol. Bacteriol.* **39**, 233–253 (1934).
18. Stöber, W., Morrow, P. E., Koch, W. & Morawietz, G. Alveolar clearance and retention of inhaled insoluble particles in rats simulated by a model inferring macrophage particle load distributions. *J. Aerosol Sci.* **25**, 975–1002 (1994).
19. Harrison, R. M. & Yin, J. Particulate matter in the atmosphere: which particle properties are important for its effects on health? *Sci. Total Environ.* **249**, 85–101 (2000).
20. Csavina, J. *et al.* A review on the importance of metals and metalloids in atmospheric dust and aerosol from mining operations. *Sci. Total Environ.* **433**, 58–73 (2012).
21. Fisher, G. L. & Placke, M. E. In vitro models of lung toxicity. *Toxicology* **47**, 71–93 (1987).
22. Morrow, P. E. Dust overloading of the lungs: Update and appraisal. *Toxicol. Appl. Pharmacol.* **113**, 1–12 (1992).
23. Stuart, B. O. Deposition and clearance of inhaled particles. *Environ. Health Perspect.* **55**, 369–90 (1984).
24. Schlesinger, R. Clearance from the respiratory tract\*1. *Fundam. Appl. Toxicol.* **5**, 435–450 (1985).
25. Bailey, M. R., Fry, F. A. & James, A. C. Long-term retention of particles in the human respiratory tract. *J. Aerosol Sci.* **16**, 295–305 (1985).
26. ASGHARIAN, B. & YU, C. P. Deposition of Inhaled Fibrous Particles in the Human Lung. *J. Aerosol Med.* **1**, 37–50 (1988).

27. Stöber, W., Morrow, P. E. & Hoover, M. D. Compartmental modeling of the long-term retention of insoluble particles deposited in the alveolar region of the lung. *Fundam. Appl. Toxicol.* **13**, 823–42 (1989).
28. DRISCOLL, K. Respiratory tract responses to dust: Relationships between dust burden, lung injury, alveolar macrophage fibronectin release, and the development of pulmonary fibrosis. *Toxicol. Appl. Pharmacol.* **106**, 88–101 (1990).
29. Carré, P. C. *et al.* Increased expression of the interleukin-8 gene by alveolar macrophages in idiopathic pulmonary fibrosis. A potential mechanism for the recruitment and activation of neutrophils in lung fibrosis. *J. Clin. Invest.* **88**, 1802–10 (1991).
30. Cannon, G. J. & Swanson, J. a. The macrophage capacity for phagocytosis. *J. Cell Sci.* **101** ( Pt 4, 907–13 (1992).
31. Schmidt, J. A., Oliver, C. N., Lepe-Zuniga, J. L., Green, I. & Gery, I. Silica-stimulated monocytes release fibroblast proliferation factors identical to interleukin 1. A potential role for interleukin 1 in the pathogenesis of silicosis. *J. Clin. Invest.* **73**, 1462–72 (1984).
32. Ferin, J. *et al.* Increased pulmonary toxicity of ultrafine particles? I. Particle clearance, translocation, morphology. *J. Aerosol Sci.* **21**, 381–384 (1990).
33. Oberdorster, G. *et al.* Increased Pulmonary Toxicity of Inhaled Ultrafine Particles: Due to Lung Overload Alone? *Ann. Occup. Hyg.* **38**, 295–302 (1994).
34. Pauluhn, J. Poorly soluble particulates: searching for a unifying denominator of nanoparticles and fine particles for DNEL estimation. *Toxicology* **279**, 176–88 (2011).
35. Ye, J. *et al.* Critical role of glass fiber length in TNF-alpha production and transcription factor activation in macrophages. *Am. J. Physiol.* **276**, L426–34 (1999).
36. Kroegel, C. & Antony, V. B. Immunobiology of pleural inflammation: potential implications for pathogenesis, diagnosis and therapy. *Eur. Respir. J.* **10**, 2411–2418 (1997).
37. Hamilton, R. F. *et al.* Particle length-dependent titanium dioxide nanomaterials toxicity and bioactivity. *Part. Fibre Toxicol.* **6**, 35 (2009).
38. Jay, S. M., Skokos, E. A., Zeng, J., Knox, K. & Kyriakides, T. R. Macrophage fusion leading to foreign body giant cell formation persists under phagocytic stimulation by microspheres in vitro and in vivo in mouse models. *J. Biomed. Mater. Res. A* **93**, 189–99 (2010).



39. Møller, P. *et al.* Role of oxidative damage in toxicity of particulates. *Free Radic. Res.* **44**, 1–46 (2010).
40. Rothen-Rutishauser, B., Blank, F., Mühlfeld, C. & Gehr, P. In vitro models of the human epithelial airway barrier to study the toxic potential of particulate matter. *Expert Opin. Drug Metab. Toxicol.* **4**, 1075–89 (2008).
41. Dockery, D. W. *et al.* An association between air pollution and mortality in six U.S. cities. *N. Engl. J. Med.* **329**, 1753–9 (1993).
42. Pope, C. A. *et al.* Particulate air pollution as a predictor of mortality in a prospective study of U.S. adults. *Am. J. Respir. Crit. Care Med.* **151**, 669–74 (1995).
43. Jervis, R. E., Tan, P. V & Evans, G. J. Measurement of PM<sub>10</sub>/2.5 fractionated respirable particles in urban Toronto by INAA, PIXE, ICP-AES, and LAMS. A comparison. *Biol. Trace Elem. Res.* **71-72**, 223–32 (1999).
44. Pryor, S. C. & Barthelmie, R. J. PM<sub>10</sub> in Canada. *Sci. Total Environ.* **177**, 57–71 (1996).
45. Samet, J. M., Dominici, F., Curriero, F. C., Coursac, I. & Zeger, S. L. Fine particulate air pollution and mortality in 20 U.S. cities, 1987-1994. *N. Engl. J. Med.* **343**, 1742–9 (2000).
46. Murayama, T. *et al.* Ground-based network observation of Asian dust events of April 1998 in east Asia. *J. Geophys. Res.* **106**, 18345–18359 (2001).
47. Alfaro-Moreno, E. *et al.* Biologic effects induced in vitro by PM<sub>10</sub> from three different zones of Mexico City. *Environ. Health Perspect.* **110**, 715–20 (2002).
48. Medina, S., Plasencia, A., Ballester, F., Mücke, H. G. & Schwartz, J. Apheis: public health impact of PM<sub>10</sub> in 19 European cities. *J. Epidemiol. Community Health* **58**, 831–6 (2004).
49. Kan, H. *et al.* Differentiating the effects of fine and coarse particles on daily mortality in Shanghai, China. *Environ. Int.* **33**, 376–84 (2007).
50. Chen, R. *et al.* Coarse particles and mortality in three Chinese cities: the China Air Pollution and Health Effects Study (CAPES). *Sci. Total Environ.* **409**, 4934–8 (2011).
51. Meister, K., Johansson, C. & Forsberg, B. Estimated short-term effects of coarse particles on daily mortality in Stockholm, Sweden. *Environ. Health Perspect.* **120**, 431–6 (2012).
52. Samoli, E. *et al.* Associations between fine and coarse particles and mortality in Mediterranean cities: results from the MED-PARTICLES project. *Environ. Health Perspect.* **121**, 932–8 (2013).

53. Malig, B. J. & Ostro, B. D. Coarse particles and mortality: evidence from a multi-city study in California. *Occup. Environ. Med.* **66**, 832–9 (2009).
54. Golub, A. & Strukova, E. Evaluation and identification of priority air pollutants for environmental management on the basis of risk analysis in Russia. *J. Toxicol. Environ. Health. A* **71**, 86–91 (2008).
55. WHO. *Air quality guidelines: global update 2005*. (2006).
56. Heyder, J. Deposition of inhaled particles in the human respiratory tract and consequences for regional targeting in respiratory drug delivery. *Proc. Am. Thorac. Soc.* **1**, 315–20 (2004).
57. Sloss, L. PM10 and PM2.5: an international perspective. *Fuel Process. Technol.* **65-66**, 127–141 (2000).
58. Chang, H. H., Peng, R. D. & Dominici, F. Estimating the acute health effects of coarse particulate matter accounting for exposure measurement error. *Biostatistics* **12**, 637–52 (2011).
59. Host, S. *et al.* Short-term associations between fine and coarse particles and hospital admissions for cardiorespiratory diseases in six French cities. *Occup. Environ. Med.* **65**, 544–51 (2008).
60. Perez, L. *et al.* Coarse Particles From Saharan Dust and Daily Mortality. *Epidemiology* **19**, 800–807 (2008).
61. Szema, A. M. *et al.* Iraq dust is respirable, sharp, and metal-laden and induces lung inflammation with fibrosis in mice via IL-2 upregulation and depletion of regulatory T cells. *J. Occup. Environ. Med.* **56**, 243–51 (2014).
62. Brunekreef, B. & Forsberg, B. Epidemiological evidence of effects of coarse airborne particles on health. *Eur. Respir. J.* **26**, 309–18 (2005).
63. Vahlsing, C. & Smith, K. R. Global review of national ambient air quality standards for PM(10) and SO(2) (24 h). *Air Qual. Atmos. Health* **5**, 393–399 (2012).
64. Krzyzanowski, M. WHO Air Quality Guidelines for Europe. *J. Toxicol. Environ. Health. A* **71**, 47–50 (2008).
65. Esworthy, R. *Air Quality : EPA's 2013 Changes to the Particulate Matter (PM) Standard*. (2013). at <<http://www.fas.org/sgp/crs/misc/R42934.pdf>>
66. Bernstein, J. a *et al.* Health effects of air pollution. *J. Allergy Clin. Immunol.* **114**, 1116–23 (2004).
67. Pope, C. A., Bates, D. V & Raizenne, M. E. Health effects of particulate air pollution: time for reassessment? *Environ. Health Perspect.* **103**, 472–480 (1995).

68. Poulos, L. M., Toelle, B. G. & Marks, G. B. The burden of asthma in children: an Australian perspective. *Paediatr. Respir. Rev.* **6**, 20–7 (2005).
69. Liu, L. *et al.* Acute effects of air pollution on pulmonary function, airway inflammation, and oxidative stress in asthmatic children. *Environ. Health Perspect.* **117**, 668–74 (2009).
70. Samet, J. M., Bishop, Y., Speizer, F. E., Spengler, J. D. & Ferris, B. G. The relationship between air pollution and emergency room visits in an industrial community. *J. Air Pollut. Control Assoc.* **31**, 236–40 (1981).
71. Lippmann, M. & Chen, L.-C. *Health effects of concentrated ambient air particulate matter (CAPs) and its components. Critical reviews in toxicology* **39**, (2009).
72. Pope, C. A. Mortality effects of longer term exposures to fine particulate air pollution: review of recent epidemiological evidence. *Inhal. Toxicol.* **19 Suppl 1**, 33–8 (2007).
73. Simkhovich, B. Z., Kleinman, M. T. & Kloner, R. A. Air pollution and cardiovascular injury epidemiology, toxicology, and mechanisms. *J. Am. Coll. Cardiol.* **52**, 719–26 (2008).
74. Environment Protection and Heritage Council. *Expansion of the multi-city mortality and morbidity study.* (2010). at <http://www.scew.gov.au/sites/www.scew.gov.au/files/resources/220add0d-0265-9004-1d22-0c312998402c/files/aq-rsch-multi-city-mm-executive-summary-sept-final-201009.pdf>
75. Bateson, T. F. & Schwartz, J. Who is Sensitive to the Effects of Particulate Air Pollution on Mortality? *Epidemiology* **15**, 143–149 (2004).
76. Ling, S. H. & van Eeden, S. F. Particulate matter air pollution exposure: role in the development and exacerbation of chronic obstructive pulmonary disease. *Int. J. Chron. Obstruct. Pulmon. Dis.* **4**, 233–43 (2009).
77. Faiz, A. S. *et al.* Ambient air pollution and the risk of stillbirth. *Am. J. Epidemiol.* **176**, 308–16 (2012).
78. Darrow, L. a, Klein, M., Strickland, M. J., Mulholland, J. a & Tolbert, P. E. Ambient air pollution and birth weight in full-term infants in Atlanta, 1994-2004. *Environ. Health Perspect.* **119**, 731–7 (2011).
79. Woodruff, T. J., Parker, J. D. & Schoendorf, K. C. Fine Particulate Matter (PM<sub>2.5</sub>) Air Pollution and Selected Causes of Postneonatal Infant Mortality in California. *Environ. Health Perspect.* **114**, 786–790 (2006).
80. Green, L. What's Wrong with the National Ambient Air Quality Standard (NAAQS) for Fine Particulate Matter (PM<sub>2.5</sub>)? *Regul. Toxicol. Pharmacol.* **35**, 327–337 (2002).

81. Lippmann, M. Particulate matter (PM) air pollution and health: regulatory and policy implications. *Air Qual. Atmos. Heal.* **5**, 237–241 (2011).
82. Thompson, P. *et al.* *Literature Review and Report on Potential Health Impacts of Exposure to Crustal Material in Port Hedland.* (2007). at <<http://www.dsd.wa.gov.au/documents/000245.Denise.LAZENBY.pdf>>
83. Stanek, L. W., Sacks, J. D., Dutton, S. J. & Dubois, J.-J. B. Attributing health effects to apportioned components and sources of particulate matter: An evaluation of collective results. *Atmos. Environ.* **45**, 5655–5663 (2011).
84. Wang, Y. *et al.* Source apportionment of airborne particulate matter using inorganic and organic species as tracers. *Atmos. Environ.* **55**, 525–532 (2012).
85. Sturtz, T. M., Adar, S. D., Gould, T. & Larson, T. V. Constrained source apportionment of coarse particulate matter and selected trace elements in three cities from the multi-ethnic study of atherosclerosis. *Atmos. Environ.* **84**, 65–77 (2014).
86. Tecer, L. H. *et al.* Metallic composition and source apportionment of fine and coarse particles using positive matrix factorization in the southern Black Sea atmosphere. *Atmos. Res.* **118**, 153–169 (2012).
87. Nadadur, S. S. *et al.* The complexities of air pollution regulation: the need for an integrated research and regulatory perspective. *Toxicol. Sci.* **100**, 318–27 (2007).
88. Lippmann, M. *et al.* The U.S. Environmental Protection Agency Particulate Matter Health Effects Research Centers Program: a midcourse report of status, progress, and plans. *Environ. Health Perspect.* **111**, 1074–92 (2003).
89. Schwartz, J., Dockery, D. W. & Neas, L. M. Is Daily Mortality Associated Specifically with Fine Particles? *J. Air Waste Manage. Assoc.* **46**, 927–939 (1996).
90. Williams, M. L. Air quality risk management. *J. Toxicol. Environ. Health. A* **71**, 9–12 (2008).
91. Pauluhn, J. Inhalation toxicology: methodological and regulatory challenges. *Exp. Toxicol. Pathol.* **60**, 111–24 (2008).
92. Dreher, K. L. PARTICULATE MATTER PHYSICOCHEMISTRY AND TOXICOLOGY: In Search of Causality-A Critical Perspective. *Inhal. Toxicol.* **12**, 45–57 (2000).
93. Lippmann, M. Targeting the components most responsible for airborne particulate matter health risks. *J. Expo. Sci. Environ. Epidemiol.* **20**, 117–8 (2010).

94. Kissel, F. N. *Handbook for Dust Control in Mining (IC 9465)*. (National Institute for Occupational Safety and Health, 2003). at <http://www.cdc.gov/niosh/mining/UserFiles/works/pdfs/2003-147.pdf>
95. Scarisbrick, D. Silicosis and coal workers' pneumoconiosis. *Practitioner* **246**, 114, 117–9 (2002).
96. 't Mannetje, A. *et al.* Exposure-response analysis and risk assessment for silica and silicosis mortality in a pooled analysis of six cohorts. *Occup. Environ. Med.* **59**, 723–8 (2002).
97. Phalen, R. F. The particulate air pollution controversy. *Nonlinearity Biol. Toxicol. Med.* **2**, 259–92 (2004).
98. Belardi, G., Vignaroli, G., Plescia, P. & Passeri, L. The assessment of particulate matter emitted from stone-crushing industry by correlating rock textures with particles generated after comminution and dispersed in air environment. *Environ. Sci. Pollut. Res. Int.* (2013). doi:10.1007/s11356-012-1434-7
99. Adelroth, E. *et al.* Airway inflammation in iron ore miners exposed to dust and diesel exhaust. *Eur. Respir. J. Off. J. Eur. Soc. Clin. Respir. Physiol.* **27**, 714–9 (2006).
100. Petavratzi, E., Kingman, S. & Lowndes, I. Particulates from mining operations: A review of sources, effects and regulations. *Miner. Eng.* **18**, 1183–1199 (2005).
101. Huertas, J. I., Camacho, D. a & Huertas, M. E. Standardized emissions inventory methodology for open-pit mining areas. *Environ. Sci. Pollut. Res. Int.* **19**, 2784–94 (2011).
102. Götschi, T. *et al.* Elemental composition and reflectance of ambient fine particles at 21 European locations. *Atmos. Environ.* **39**, 5947–5958 (2005).
103. Shashi, A., Misso, N., Sutton, J. & Thompson, P. *The Effect of Port Hedland Crustal Dust on Lung Cell Biology. Most* (2009). at <http://www.dsd.wa.gov.au/documents/000317.Denise.LAZENBY.pdf>
104. Cattle, S. R., Hemi, K., Pearson, G. L. & Sanderson, T. Distinguishing and characterising point-source mining dust and diffuse-source dust deposits in a semi-arid district of eastern Australia. *Aeolian Res.* **6**, 21–29 (2012).
105. Huertas, J. I., Huertas, M. E. & Solís, D. a. Characterization of airborne particles in an open pit mining region. *Sci. Total Environ.* **423**, 39–46 (2012).
106. Harkema, J. R., Nikula, K. J. & Haschek, W. M. in *Haschek and Rousseaux's Handbook of Toxicologic Pathology 1935–2003* (Academic Press, 2013). doi:10.1016/B978-0-12-415759-0.00051-0

107. Wang, G., Huang, L., Gao, S., Gao, S. & Wang, L. Measurements of PM10 and PM2.5 in urban area of Nanjing, China and the assessment of pulmonary deposition of particle mass. *Chemosphere* **48**, 689–95 (2002).
108. Hofmann, W. Modelling inhaled particle deposition in the human lung—A review. *J. Aerosol Sci.* **42**, 693–724 (2011).
109. Sznitman, J. Respiratory microflows in the pulmonary acinus. *J. Biomech.* **46**, 284–98 (2013).
110. Gehr, P., Bachofen, M. & Weibel, E. R. The normal human lung: ultrastructure and morphometric estimation of diffusion capacity. *Respir. Physiol.* **32**, 121–40 (1978).
111. Geiser, M. & Kreyling, W. G. Deposition and biokinetics of inhaled nanoparticles. *Part. Fibre Toxicol.* **7**, 2 (2010).
112. Gray, J. E. *et al.* In vitro studies evaluating leaching of mercury from mine waste calcine using simulated human body fluids. *Environ. Sci. Technol.* **44**, 4782–8 (2010).
113. Bruce, S., Noller, B., Matanitobua, V. & Ng, J. In vitro physiologically based extraction test (PBET) and bioaccessibility of arsenic and lead from various mine waste materials. *J. Toxicol. Environ. Health. A* **70**, 1700–11 (2007).
114. Manhattan, S. E. *Toxicological Chemistry and Biochemistry*. (CRC Press, 2003).
115. SEATON, A. Occupational lung disease: an international perspective. *Occup. Environ. Med.* **57**, 844b–844 (2000).
116. Weir, N. A., Gulati, M. & Redlich, C. *Textbook Of Clinical Occupational And Environmental Medicine. International Classification* (WB Saunders, 1994).
117. Araujo, J. a. Particulate air pollution, systemic oxidative stress, inflammation, and atherosclerosis. *Air Qual. Atmos. Health* **4**, 79–93 (2010).
118. Borm, P. J. a, Schins, R. P. F. & Albrecht, C. Inhaled particles and lung cancer, part B: paradigms and risk assessment. *Int. J. Cancer* **110**, 3–14 (2004).
119. Examination, P. *Clinical Features and Diagnosis. International Classification* doi:10.1016/B978-0-7216-8974-6
120. Lenters, V. *et al.* A meta-analysis of asbestos and lung cancer: is better quality exposure assessment associated with steeper slopes of the exposure-response relationships? *Environ. Health Perspect.* **119**, 1547–55 (2011).

121. Environmental Protection Agency. *Ambient Levels and Noncancer Health Effects of Inhaled Crystalline and Amorphous Silica: Health Issue Assessment*. (1996). at <<http://cfpub.epa.gov/ncea/cfm/recorddisplay.cfm?deid=12999>>
122. Teculescu, D. & Albu, a. Pulmonary function in workers inhaling iron oxide dust. *Int. Arch. Arbeitsmed.* **31**, 163–70 (1973).
123. Diseases associated with exposure to silica and nonfibrous silicate minerals. Silicosis and Silicate Disease Committee. *Arch. Pathol. Lab. Med.* **112**, 673–720 (1988).
124. Wagner, G. R. & Hearl, F. J. *Textbook of Clinical Occupational and Environmental Medicine (Second Edition)*. *Textbook of Clinical Occupational and Environmental Medicine* (Elsevier Inc., 2005). doi:10.1016/B978-0-7216-8974-6.50050-6
125. Mullins, S. & Gatof, J. *Chapter 3. Are We Willing to Heed the Lessons of the Past? Nanomaterials and Australia's Asbestos Legacy*. *Nanotechnology Environmental Health and Safety* (Elsevier Inc., 2014). doi:10.1016/B978-1-4557-3188-6.00003-7
126. Bernstein, D. *et al.* Health risk of chrysotile revisited. *Crit. Rev. Toxicol.* **43**, 154–83 (2013).
127. Donaldson, K., Murphy, F. a, Duffin, R. & Poland, C. a. Asbestos, carbon nanotubes and the pleural mesothelium: a review of the hypothesis regarding the role of long fibre retention in the parietal pleura, inflammation and mesothelioma. *Part. Fibre Toxicol.* **7**, 5 (2010).
128. Craighead, J. E., Mossman, B. T. & Bradley, B. J. Comparative studies on the cytotoxicity of amphibole and serpentine asbestos. *Environ. Health Perspect.* **34**, 37–46 (1980).
129. Kipen, H. M., Lilis, R., Suzuki, Y., Valciukas, J. a & Selikoff, I. J. Pulmonary fibrosis in asbestos insulation workers with lung cancer: a radiological and histopathological evaluation. *Br. J. Ind. Med.* **44**, 96–100 (1987).
130. Kamp, D. W. Asbestos-induced lung diseases: an update. *Transl. Res.* **153**, 143–52 (2009).
131. Gamble, J. F. & Gibbs, G. W. An evaluation of the risks of lung cancer and mesothelioma from exposure to amphibole cleavage fragments. *Regul. Toxicol. Pharmacol.* **52**, S154–86 (2008).
132. Kelleher, P., Pacheco, K. & Newman, L. S. Inorganic dust pneumonias: the metal-related parenchymal disorders. *Environ. Health Perspect.* **108 Suppl** , 685–96 (2000).
133. Leonard, S. S., Harris, G. K. & Shi, X. Metal-induced oxidative stress and signal transduction. *Free Radic. Biol. Med.* **37**, 1921–42 (2004).

134. Carter, J. D., Ghio, A. J., Samet, J. M., Devlin, R. B. & Pharmacol, A. Cytokine Production by Human Airway Epithelial Cells after Exposure to an Air Pollution Particle Is Metal-Dependent. **188**, 180–188 (1997).
135. Karmakar, A., Zhang, Q. & Zhang, Y. Neurotoxicity of nanoscale materials. *J. food drug Anal.* **22**, 147–60 (2014).
136. Schins, R. P. F. Mechanisms of genotoxicity of particles and fibers. *Inhal. Toxicol.* **14**, 57–78 (2002).
137. Oberdörster, G., Oberdörster, E. & Oberdörster, J. Nanotoxicology: An Emerging Discipline Evolving from Studies of Ultrafine Particles. *Environ. Health Perspect.* **113**, 823–839 (2005).
138. Doig, A. T. & Mclaughlin, A. I. G. CLEARING OF X-RAY SHADOWS IN WELDERS' SIDEROSIS. *Lancet* **251**, 789–791 (1948).
139. Ahn, M.-H. *et al.* Titanium dioxide particle-induced goblet cell hyperplasia: association with mast cells and IL-13. *Respir. Res.* **6**, 34 (2005).
140. Poulter, L. W. Basic concepts in lung immunology. *Res. Immunol.* **148**, 8–13 (1997).
141. Zasadzinski, J. ., Ding, J., Warriner, H. ., Bringezu, F. & Waring, A. J. The physics and physiology of lung surfactants. *Curr. Opin. Colloid Interface Sci.* **6**, 506–513 (2001).
142. Johansson, J., Curstedt, T. & Robertson, B. The proteins of the surfactant system. *Eur. Respir. J.* **7**, 372–391 (1994).
143. Sun, G. *et al.* Oxidative interactions of synthetic lung epithelial lining fluid with metal-containing particulate matter. *Am. J. Physiol. Lung Cell. Mol. Physiol.* **281**, L807–15 (2001).
144. Notter, R. H., Shapiro, D. L., Ohning, B. & Whitsett, J. A. Biophysical activity of synthetic phospholipids combined with purified lung surfactant 6000 dalton apoprotein. *Chem. Phys. Lipids* **44**, 1–17 (1987).
145. Bihari, P. *et al.* Optimized dispersion of nanoparticles for biological in vitro and in vivo studies. *Part. Fibre Toxicol.* **5**, 14 (2008).
146. Sager, T. M. *et al.* Improved method to disperse nanoparticles for in vitro and in vivo investigation of toxicity. *Nanotoxicology* **1**, 118–129 (2007).
147. Buford, M. C., Hamilton, R. F. & Holian, A. A comparison of dispersing media for various engineered carbon nanoparticles. *Part. Fibre Toxicol.* **4**, 6 (2007).
148. Vippola, M. *et al.* Preparation of nanoparticle dispersions for in-vitro toxicity testing. *Hum. Exp. Toxicol.* **28**, 377–85 (2009).



149. Horie, M. *et al.* Protein adsorption of ultrafine metal oxide and its influence on cytotoxicity toward cultured cells. *Chem. Res. Toxicol.* **22**, 543–53 (2009).
150. Baier, G. *et al.* BSA adsorption on differently charged polystyrene nanoparticles using isothermal titration calorimetry and the influence on cellular uptake. *Macromol. Biosci.* **11**, 628–38 (2011).
151. Kouoh, F. *et al.* Antioxidant properties of albumin: effect on oxidative metabolism of human neutrophil granulocytes. *Farmaco* **54**, 695–9 (1999).
152. Levy, L., Chaudhuri, I. S., Krueger, N. & McCunney, R. J. Does carbon black disaggregate in lung fluid? A critical assessment. *Chem. Res. Toxicol.* **25**, 2001–6 (2012).
153. Maier, M., Hannebauer, B., Holldorff, H. & Albers, P. Does lung surfactant promote disaggregation of nanostructured titanium dioxide? *J. Occup. Environ. Med.* **48**, 1314–20 (2006).
154. Kim, S. H., Park, Y., Matalon, S. & Franses, E. I. Effect of buffer composition and preparation protocol on the dispersion stability and interfacial behavior of aqueous DPPC dispersions. *Colloids Surf. B. Biointerfaces* **67**, 253–60 (2008).
155. Evora, C. *et al.* Relating the phagocytosis of microparticles by alveolar macrophages to surface chemistry: the effect of 1,2-dipalmitoylphosphatidylcholine. *J. Control. Release* **51**, 143–52 (1998).
156. Wang, J.-Y. & Reid, K. B. M. The immunoregulatory roles of lung surfactant collectins SP-A, and SP-D, in allergen-induced airway inflammation. *Immunobiology* **212**, 417–25 (2007).
157. Schulze, C., Schaefer, U. F., Ruge, C. a, Wohlleben, W. & Lehr, C.-M. Interaction of metal oxide nanoparticles with lung surfactant protein A. *Eur. J. Pharm. Biopharm.* **77**, 376–83 (2011).
158. Ghio, A. J. *et al.* Growth of human bronchial epithelial cells at an air-liquid interface alters the response to particle exposure. *Part. Fibre Toxicol.* **10**, 25 (2013).
159. Bitterle, E. *et al.* Dose-controlled exposure of A549 epithelial cells at the air-liquid interface to airborne ultrafine carbonaceous particles. *Chemosphere* **65**, 1784–90 (2006).
160. Aufderheide, M. Novel approaches for studying pulmonary toxicity in vitro. *Toxicol. Lett.* **140-141**, 205–211 (2003).
161. Aufderheide, M. An efficient approach to study the toxicological effects of complex mixtures. *Exp. Toxicol. Pathol.* **60**, 163–80 (2008).

162. Bakand, S., Hayes, A. & Winder, C. An integrated in vitro approach for toxicity testing of airborne contaminants. *J. Toxicol. Environ. Health. A* **70**, 1604–12 (2007).
163. Jones, C. F. & Grainger, D. W. In vitro assessments of nanomaterial toxicity. *Adv. Drug Deliv. Rev.* **61**, 438–56 (2009).
164. Oberdörster, G. *et al.* Principles for characterizing the potential human health effects from exposure to nanomaterials: elements of a screening strategy. *Part. Fibre Toxicol.* **2**, 8 (2005).
165. Kroll, A., Pillukat, M. H., Hahn, D. & Schnekenburger, J. Interference of engineered nanoparticles with in vitro toxicity assays. *Arch. Toxicol.* **86**, 1123–36 (2012).
166. Holder, A. L., Goth-Goldstein, R., Lucas, D. & Koshland, C. P. Particle-induced artifacts in the MTT and LDH viability assays. *Chem. Res. Toxicol.* **25**, 1885–92 (2012).
167. Kroll, A. *et al.* Cytotoxicity screening of 23 engineered nanomaterials using a test matrix of ten cell lines and three different assays. *Part. Fibre Toxicol.* **8**, 9 (2011).
168. Sayes, C. M. *et al.* Correlating nanoscale titania structure with toxicity: a cytotoxicity and inflammatory response study with human dermal fibroblasts and human lung epithelial cells. *Toxicol. Sci.* **92**, 174–85 (2006).
169. Bhattacharya, K. *et al.* Titanium dioxide nanoparticles induce oxidative stress and DNA-adduct formation but not DNA-breakage in human lung cells. *Part. Fibre Toxicol.* **6**, 17 (2009).
170. Giuliano, M. *et al.* Effects of low concentrations of benzene on human lung cells in vitro. *Toxicol. Lett.* **188**, 130–6 (2009).
171. Drakopanagiotakis, F., Xifteri, a, Polychronopoulos, V. & Bouros, D. Apoptosis in lung injury and fibrosis. *Eur. Respir. J. Off. J. Eur. Soc. Clin. Respir. Physiol.* **32**, 1631–8 (2008).
172. Lanone, S. *et al.* Comparative toxicity of 24 manufactured nanoparticles in human alveolar epithelial and macrophage cell lines. *Part. Fibre Toxicol.* **6**, 14 (2009).
173. Sayes, C. M., Reed, K. L. & Warheit, D. B. Assessing toxicity of fine and nanoparticles: comparing in vitro measurements to in vivo pulmonary toxicity profiles. *Toxicol. Sci.* **97**, 163–80 (2007).
174. Mueller-Klieser, W. Three-dimensional cell cultures: from molecular mechanisms to clinical applications. *Am. J. Physiol.* **273**, C1109–23 (1997).

175. Ong, S.-M. *et al.* Engineering a scaffold-free 3D tumor model for in vitro drug penetration studies. *Biomaterials* **31**, 1180–90 (2010).
176. Gutiérrez, L. *et al.* A hanging drop culture method to study terminal erythroid differentiation. *Exp. Hematol.* **33**, 1083–91 (2005).
177. Liu, F. F. *et al.* Hanging drop: an in vitro air toxic exposure model using human lung cells in 2D and 3D structures. *J. Hazard. Mater.* **261**, 701–10 (2013).
178. Carterson, A. J. *et al.* A549 lung epithelial cells grown as three-dimensional aggregates: alternative tissue culture model for *Pseudomonas aeruginosa* pathogenesis. *Infect. Immun.* **73**, 1129–40 (2005).
179. Yan, X., Bergstrom, D. J. & Chen, X. B. Modeling of cell cultures in perfusion bioreactors. *IEEE Trans. Biomed. Eng.* **59**, 2568–75 (2012).
180. Dutta, R. C. & Dutta, A. K. Comprehension of ECM-cell dynamics: a prerequisite for tissue regeneration. *Biotechnol. Adv.* **28**, 764–9 (2010).
181. Sasagawa, T., Shimizu, T., Yamato, M. & Okano, T. Expression profiles of angiogenesis-related proteins in prevascular three-dimensional tissues using cell-sheet engineering. *Biomaterials* **35**, 206–13 (2014).
182. Vaughan, M. B., Ramirez, R. D., Wright, W. E., Minna, J. D. & Shay, J. W. A three-dimensional model of differentiation of immortalized human bronchial epithelial cells. *Differentiation*. **74**, 141–8 (2006).
183. Herold, S., Mayer, K. & Lohmeyer, J. Acute lung injury: how macrophages orchestrate resolution of inflammation and tissue repair. *Front. Immunol.* **2**, 65 (2011).
184. Song, E. *et al.* Influence of alternatively and classically activated macrophages on fibrogenic activities of human fibroblasts. *Cell. Immunol.* **204**, 19–28 (2000).
185. Standiford, T. J. *et al.* Interleukin-8 gene expression by a pulmonary epithelial cell line. A model for cytokine networks in the lung. *J. Clin. Invest.* **86**, 1945–53 (1990).
186. Klein, S. G., Hennen, J., Serchi, T., Blömeke, B. & Gutleb, A. C. Potential of coculture in vitro models to study inflammatory and sensitizing effects of particles on the lung. *Toxicol. In Vitro* **25**, 1516–34 (2011).
187. Wottrich, R., Diabaté, S. & Krug, H. F. Biological effects of ultrafine model particles in human macrophages and epithelial cells in mono- and co-culture. *Int. J. Hyg. Environ. Health* **207**, 353–61 (2004).
188. Rosas Pérez, I. *et al.* Relations between PM10 composition and cell toxicity: a multivariate and graphical approach. *Chemosphere* **67**, 1218–28 (2007).

189. Happonen, M. S. *et al.* Dose and time dependency of inflammatory responses in the mouse lung to urban air coarse, fine, and ultrafine particles from six European cities. *Inhal. Toxicol.* **19**, 227–46 (2007).
190. Midander, K. *et al.* Surface characteristics, copper release, and toxicity of nano- and micrometer-sized copper and copper(II) oxide particles: a cross-disciplinary study. *Small* **5**, 389–99 (2009).
191. Carlson, C. *et al.* Unique cellular interaction of silver nanoparticles: size-dependent generation of reactive oxygen species. *J. Phys. Chem. B* **112**, 13608–19 (2008).
192. Lin, W. *et al.* Toxicity of nano- and micro-sized ZnO particles in human lung epithelial cells. *J. Nanoparticle Res.* **11**, 25–39 (2008).
193. Salonen, R. O., Pennanen, A. & Programme, H. T. *The Impact of Fine Particles on Health. Technology* (2007).
194. Oberdörster, G., Ferin, J. & Lehnert, B. E. Correlation between particle size, in vivo particle persistence, and lung injury. *Environ. Health Perspect.* **102 Suppl**, 173–9 (1994).
195. Prior, S. *et al.* In vitro phagocytosis and monocyte-macrophage activation with poly(lactide) and poly(lactide-co-glycolide) microspheres. *Eur. J. Pharm. Sci.* **15**, 197–207 (2002).
196. Araujo, J. a & Nel, A. E. Particulate matter and atherosclerosis: role of particle size, composition and oxidative stress. *Part. Fibre Toxicol.* **6**, 24 (2009).
197. Karlsson, H. L., Gustafsson, J., Cronholm, P. & Möller, L. Size-dependent toxicity of metal oxide particles--a comparison between nano- and micrometer size. *Toxicol. Lett.* **188**, 112–8 (2009).
198. Halle, A. *et al.* The NALP3 inflammasome is involved in the innate immune response to amyloid-beta. *Nat. Immunol.* **9**, 857–65 (2008).
199. Dalbeth, N. & Lee, Y. C. G. Lymphocytes in pleural disease. *Curr. Opin. Pulm. Med.* **11**, 334–9 (2005).
200. Christensen, B. C. *et al.* Epigenetic profiles distinguish pleural mesothelioma from normal pleura and predict lung asbestos burden and clinical outcome. *Cancer Res.* **69**, 227–34 (2009).
201. Aggarwal, B. B., Shishodia, S., Sandur, S. K., Pandey, M. K. & Sethi, G. Inflammation and cancer: how hot is the link? *Biochem. Pharmacol.* **72**, 1605–21 (2006).
202. Sanchez, V. C., Weston, P., Yan, A., Hurt, R. H. & Kane, A. B. A 3-dimensional in vitro model of epithelioid granulomas induced by high aspect ratio nanomaterials. *Part. Fibre Toxicol.* **8**, 17 (2011).

203. Mercer, R. R. *et al.* Pulmonary fibrotic response to aspiration of multi-walled carbon nanotubes. *Part. Fibre Toxicol.* **8**, 21 (2011).
204. Cho, W. *et al.* Progressive severe lung injury by zinc oxide nanoparticles; the role of Zn<sup>2+</sup> dissolution inside lysosomes. *Part. Fibre Toxicol.* **8**, 27 (2011).
205. Johnston, H. J. *et al.* Identification of the mechanisms that drive the toxicity of TiO<sub>2</sub> particulates: the contribution of physicochemical characteristics. *Part. Fibre Toxicol.* **6**, 33 (2009).
206. Refsnes, M. *et al.* Different particle determinants induce apoptosis and cytokine release in primary alveolar macrophage cultures. *Part. Fibre Toxicol.* **3**, 10 (2006).
207. Schins, R. P. F. *et al.* Surface Modification of Quartz Inhibits Toxicity, Particle Uptake, and Oxidative DNA Damage in Human Lung Epithelial Cells. *Chem. Res. Toxicol.* **15**, 1166–1173 (2002).
208. Erdogdu, G. & Hasirci, V. An overview of the role of mineral solubility in silicosis and asbestosis. *Environ. Res.* **78**, 38–42 (1998).
209. Chang, Y.-N., Zhang, M., Xia, L., Zhang, J. & Xing, G. The Toxic Effects and Mechanisms of CuO and ZnO Nanoparticles. *Materials (Basel)*. **5**, 2850–2871 (2012).
210. Midander, K., Wallinder, I. O. & Leygraf, C. In vitro studies of copper release from powder particles in synthetic biological media. *Environ. Pollut.* **145**, 51–9 (2007).
211. Moos, P. J. *et al.* ZnO particulate matter requires cell contact for toxicity in human colon cancer cells. *Chem. Res. Toxicol.* **23**, 733–9 (2010).
212. Monteiller, C. *et al.* The pro-inflammatory effects of low-toxicity low-solubility particles, nanoparticles and fine particles, on epithelial cells in vitro: the role of surface area. *Occup. Environ. Med.* **64**, 609–15 (2007).
213. Sohaebuddin, S. K., Thevenot, P. T., Baker, D., Eaton, J. W. & Tang, L. Nanomaterial cytotoxicity is composition, size, and cell type dependent. *Part. Fibre Toxicol.* **7**, 22 (2010).
214. Choi, S.-J., Oh, J.-M. & Choy, J.-H. Toxicological effects of inorganic nanoparticles on human lung cancer A549 cells. *J. Inorg. Biochem.* **103**, 463–71 (2009).
215. Karlsson, H. L., Cronholm, P., Gustafsson, J. & Mo, L. Copper Oxide Nanoparticles Are Highly Toxic : A Comparison between Metal Oxide Nanoparticles and Carbon Nanotubes. *In Vitro* 1726–1732 (2008).

216. Karlsson, H. L. *et al.* Cell membrane damage and protein interaction induced by copper containing nanoparticles--importance of the metal release process. *Toxicology* **313**, 59–69 (2013).
217. Wiseman, C. L. S. & Zereini, F. Characterizing metal(loid) solubility in airborne PM10, PM2.5 and PM1 in Frankfurt, Germany using simulated lung fluids. *Atmos. Environ.* **89**, 282–289 (2014).
218. Kang, J. L. *et al.* Comparison of the biological activity between ultrafine and fine titanium dioxide particles in RAW 264.7 cells associated with oxidative stress. *J. Toxicol. Environ. Health. A* **71**, 478–85 (2008).
219. O'Brien, J., Wilson, I., Orton, T. & Pognan, F. Investigation of the Alamar Blue (resazurin) fluorescent dye for the assessment of mammalian cell cytotoxicity. *Eur. J. Biochem.* **267**, 5421–6 (2000).
220. Mosmann, T. Rapid colorimetric assay for cellular growth and survival: application to proliferation and cytotoxicity assays. *J. Immunol. Methods* **65**, 55–63 (1983).
221. Roehm, N. W., Rodgers, G. H., Hatfield, S. M. & Glasebrook, a L. An improved colorimetric assay for cell proliferation and viability utilizing the tetrazolium salt XTT. *J. Immunol. Methods* **142**, 257–65 (1991).
222. Darolles, C., Sage, N., Armengaud, J. & Malard, V. In vitro assessment of cobalt oxide particle toxicity: Identifying and circumventing interference. *Toxicol. In Vitro* **27**, 1699–1710 (2013).
223. Alexis, N. E. *et al.* In vivo particle uptake by airway macrophages in healthy volunteers. *Am. J. Respir. Cell Mol. Biol.* **34**, 305–13 (2006).
224. SEYMOUR, L., SCHACHT, E. & DUNCAN, R. The effect of size of polystyrene particles on their retention within the rat peritoneal compartment, and on their interaction with rat peritoneal macrophages. *Cell Biol. Int. Rep.* **15**, 37–45 (1991).
225. Bernardin, M. P. & Lehnert, B. E. Model of particle-alveolar macrophage relationships during the alveolar clearance of a low lung burden of instilled particles. *J. Aerosol Sci.* **26**, 319–333 (1995).
226. Oberdörster, G., Ferin, J., Gelein, R., Soderholm, S. C. & Finkelstein, J. Role of the alveolar macrophage in lung injury: studies with ultrafine particles. *Environ. Health Perspect.* **97**, 193–199 (1992).
227. Park, S. *et al.* Cellular toxicity of various inhalable metal nanoparticles on human alveolar epithelial cells. *Inhal. Toxicol.* **19 Suppl 1**, 59–65 (2007).
228. Simon-Deckers, A. *et al.* In vitro investigation of oxide nanoparticle and carbon nanotube toxicity and intracellular accumulation in A549 human pneumocytes. *Toxicology* **253**, 137–46 (2008).

229. Stringer, B., Imrich, a & Kobzik, L. Lung epithelial cell (A549) interaction with unopsonized environmental particulates: quantitation of particle-specific binding and IL-8 production. *Exp. Lung Res.* **22**, 495–508 (1996).
230. Lukacs, N. W., Hogaboam, C., Chensue, S. W., Blease, K. & Kunkel, S. L. Type 1/type 2 cytokine paradigm and the progression of pulmonary fibrosis. *Chest* **120**, 5S–8S (2001).
231. Ovrevik, J., Låg, M., Holme, J. A., Schwarze, P. E. & Refsnes, M. Cytokine and chemokine expression patterns in lung epithelial cells exposed to components characteristic of particulate air pollution. *Toxicology* **259**, 46–53 (2009).
232. Li, X. Y., Gilmour, P. S., Donaldson, K. & MacNee, W. Free radical activity and pro-inflammatory effects of particulate air pollution (PM10) in vivo and in vitro. *Thorax* **51**, 1216–1222 (1996).
233. Veranth, J. M., Kaser, E. G., Veranth, M. M., Koch, M. & Yost, G. S. Cytokine responses of human lung cells (BEAS-2B) treated with micron-sized and nanoparticles of metal oxides compared to soil dusts. *Part. Fibre Toxicol.* **4**, 2 (2007).
234. Herseth, J. I., Volden, V., Schwarze, P. E., Låg, M. & Refsnes, M. IL-1beta differently involved in IL-8 and FGF-2 release in crystalline silica-treated lung cell co-cultures. *Part. Fibre Toxicol.* **5**, 16 (2008).
235. Tao, F. & Kobzik, L. Lung macrophage-epithelial cell interactions amplify particle-mediated cytokine release. *Am. J. Respir. Cell Mol. Biol.* **26**, 499–505 (2002).
236. Horowitz, J. C. *et al.* Combinatorial activation of FAK and AKT by transforming growth factor-beta1 confers an anoikis-resistant phenotype to myofibroblasts. *Cell. Signal.* **19**, 761–71 (2007).
237. Chung, K. F. Cytokines in chronic obstructive pulmonary disease. *Eur. Respir. J.* **18**, 50–59 (2001).
238. Zhang, K., Gharaee-Kermani, M., McGarry, B., Remick, D. & Phan, S. H. TNF-alpha-mediated lung cytokine networking and eosinophil recruitment in pulmonary fibrosis. *J. Immunol.* **158**, 954–9 (1997).
239. Wynes, M. W. & Riches, D. W. H. Induction of Macrophage Insulin-Like Growth Factor-I Expression by the Th2 Cytokines IL-4 and IL-13. *J. Immunol.* **171**, 3550–3559 (2003).
240. Lin, C.-C. *et al.* IL-1 beta promotes A549 cell migration via MAPKs/AP-1- and NF-kappaB-dependent matrix metalloproteinase-9 expression. *Cell. Signal.* **21**, 1652–62 (2009).

241. Shahar, I. *et al.* Effect of IL-6 on alveolar fibroblast proliferation in interstitial lung diseases. *Clin. Immunol. Immunopathol.* **79**, 244–51 (1996).
242. Cyktor, J. C. *et al.* IL-10 inhibits mature fibrotic granuloma formation during *Mycobacterium tuberculosis* infection. *J. Immunol.* **190**, 2778–90 (2013).
243. Tsoutsou, P. G. & Gourgoulianis, K. I. Role of interleukin-10 in idiopathic pulmonary fibrosis. *Eur. Respir. J.* **23**, 179–180 (2004).
244. Keane, M. P., Belperio, J. a, Burdick, M. D. & Strieter, R. M. IL-12 attenuates bleomycin-induced pulmonary fibrosis. *Am. J. Physiol. Lung Cell. Mol. Physiol.* **281**, L92–7 (2001).
245. Russo, R. C. *et al.* Role of the chemokine receptor CXCR2 in bleomycin-induced pulmonary inflammation and fibrosis. *Am. J. Respir. Cell Mol. Biol.* **40**, 410–21 (2009).
246. Bantsimba-Malanda, C. *et al.* A role for dendritic cells in bleomycin-induced pulmonary fibrosis in mice? *Am. J. Respir. Crit. Care Med.* **182**, 385–95 (2010).
247. Brar, S. S., Meyer, J. N., Bortner, C. D., Van Houten, B. & Martin, W. J. Mitochondrial DNA-depleted A549 cells are resistant to bleomycin. *Am. J. Physiol. Lung Cell. Mol. Physiol.* **303**, L413–24 (2012).
248. Planus, E. *et al.* Role of collagenase in mediating in vitro alveolar epithelial wound repair. *J. Cell Sci.* **112** ( Pt 2, 243–52 (1999).
249. Khalil, N. Macrophage production of transforming growth factor beta and fibroblast collagen synthesis in chronic pulmonary inflammation. *J. Exp. Med.* **170**, 727–737 (1989).
250. Ley, K. & Zarbock, A. From lung injury to fibrosis. *Nat. Med.* **14**, 20–1 (2008).
251. Duffield, J. S. The inflammatory macrophage: a story of Jekyll and Hyde. *Clin. Sci. (Lond).* **104**, 27–38 (2003).
252. Calcabrini, A. *et al.* Fine environmental particulate engenders alterations in human lung epithelial A549 cells. *Environ. Res.* **95**, 82–91 (2004).
253. Beck-Speier, I. *et al.* Oxidative stress and lipid mediators induced in alveolar macrophages by ultrafine particles. *Free Radic. Biol. Med.* **38**, 1080–92 (2005).
254. Meagher, E. A. & FitzGerald, G. A. Indices of lipid peroxidation in vivo: strengths and limitations. *Free Radic. Biol. Med.* **28**, 1745–50 (2000).
255. Apopa, P. L. *et al.* Iron oxide nanoparticles induce human microvascular endothelial cell permeability through reactive oxygen species production and microtubule remodeling. *Part. Fibre Toxicol.* **6**, 1 (2009).



256. Henle, E. S., Luo, Y. & Linn, S. Fe<sup>2+</sup>, Fe<sup>3+</sup>, and oxygen react with DNA-derived radicals formed during iron-mediated Fenton reactions. *Biochemistry* **35**, 12212–9 (1996).
257. Deguillaume, L. *et al.* Transition metals in atmospheric liquid phases: sources, reactivity, and sensitive parameters. *Chem. Rev.* **105**, 3388–431 (2005).
258. Fenoglio, I., Prandi, L., Tomatis, M. & Fubini, B. Free radical generation in the toxicity of inhaled mineral particles: the role of iron speciation at the surface of asbestos and silica. *Redox Rep.* **6**, 235–41 (2001).
259. Chen, L. C. & Lippmann, M. *Effects of metals within ambient air particulate matter (PM) on human health. Inhalation toxicology* **21**, (2009).
260. Karlsson, M., Kurz, T., Brunk, U. T., Nilsson, S. E. & Frennesson, C. I. What does the commonly used DCF test for oxidative stress really show? *Biochem. J.* **428**, 183–90 (2010).
261. Jin, C., Zhu, B., Wang, X. & Lu, Q. Cytotoxicity of titanium dioxide nanoparticles in mouse fibroblast cells. *Chem. Res. Toxicol.* **21**, 1871–7 (2008).
262. Donaldson, K. *et al.* Oxidative stress and calcium signaling in the adverse effects of environmental particles (PM<sub>10</sub>). *Free Radic. Biol. Med.* **34**, 1369–1382 (2003).
263. Timblin, C. R. *et al.* Ultrafine airborne particles cause increases in protooncogene expression and proliferation in alveolar epithelial cells. *Toxicol. Appl. Pharmacol.* **179**, 98–104 (2002).
264. Bai, N., Khazaei, M., van Eeden, S. F. & Laher, I. The pharmacology of particulate matter air pollution-induced cardiovascular dysfunction. *Pharmacol. Ther.* **113**, 16–29 (2007).
265. Nemmar, A., Holme, J. a, Rosas, I., Schwarze, P. E. & Alfaro-Moreno, E. Recent advances in particulate matter and nanoparticle toxicology: a review of the in vivo and in vitro studies. *Biomed Res. Int.* **2013**, 279371 (2013).
266. Oostingh, G. J. *et al.* Problems and challenges in the development and validation of human cell-based assays to determine nanoparticle-induced immunomodulatory effects. *Part. Fibre Toxicol.* **8**, 8 (2011).
267. Larsson, L. G. *et al.* Phorbol ester-induced terminal differentiation is inhibited in human U-937 monoblastic cells expressing a v-myc oncogene. *Proc. Natl. Acad. Sci. U. S. A.* **85**, 2638–42 (1988).
268. Patel, M. I., Tuckerman, R. & Dong, Q. A Pitfall of the 3-(4,5-dimethylthiazol-2-yl)-5(3-carboxymethoxyphenyl)-2-(4-sulfophenyl)-2H-tetrazolium (MTS) assay due to evaporation in wells on the edge of a 96 well plate. *Biotechnol. Lett.* **27**, 805–8 (2005).

269. Shi, H., Magaye, R., Castranova, V. & Zhao, J. Titanium dioxide nanoparticles: a review of current toxicological data. *Part. Fibre Toxicol.* **10**, 15 (2013).
270. Montiel-Dávalos, A., Alfaro-Moreno, E. & López-Marure, R. PM<sub>2.5</sub> and PM<sub>10</sub> induce the expression of adhesion molecules and the adhesion of monocytic cells to human umbilical vein endothelial cells. *Inhal. Toxicol.* **19 Suppl 1**, 91–8 (2007).
271. Poma, A., Limongi, T., Pisani, C., Granato, V. & Picozzi, P. Genotoxicity induced by fine urban air particulate matter in the macrophages cell line RAW 264.7. *Toxicol. In Vitro* **20**, 1023–9 (2006).
272. Shi, J., Abid, A. D., Kennedy, I. M., Hristova, K. R. & Silk, W. K. To duckweeds (*Landoltia punctata*), nanoparticulate copper oxide is more inhibitory than the soluble copper in the bulk solution. *Environ. Pollut.* **159**, 1277–82 (2011).
273. Das, B., Khatoon, N., Srivastava, R. C., Viswanathan, P. N. & Rahman, Q. Biochemical studies on the toxicity of hematite dust. *Environ. Res.* **32**, 372–81 (1983).
274. Oberdörster, G. Lung particle overload: implications for occupational exposures to particles. *Regul. Toxicol. Pharmacol.* **21**, 123–35 (1995).
275. Kasper, J. *et al.* Inflammatory and cytotoxic responses of an alveolar-capillary coculture model to silica nanoparticles: comparison with conventional monocultures. *Part. Fibre Toxicol.* **8**, 6 (2011).
276. Rao, K. M. K., Porter, D. W., Meighan, T. & Castranova, V. The Sources of Inflammatory Mediators in the Lung after Silica Exposure. *Environ. Health Perspect.* **112**, 1679–1685 (2004).
277. Frampton, M. W. Systemic and cardiovascular effects of airway injury and inflammation: ultrafine particle exposure in humans. *Environ. Health Perspect.* **109 Suppl** , 529–32 (2001).
278. Oberdörster, G. Pulmonary effects of inhaled ultrafine particles. *Int. Arch. Occup. Environ. Health* **74**, 1–8 (2001).
279. Donaldson, K. The biological effects of coarse and fine particulate matter. *Occup. Environ. Med.* **60**, 313–314 (2003).
280. Doherty, M. J., Healy, M., Richardson, S. G. & Fisher, N. C. Total body iron overload in welder's siderosis. *Occup. Environ. Med.* **61**, 82–5 (2004).
281. McCormick, L. M., Goddard, M. & Mahadeva, R. Pulmonary fibrosis secondary to siderosis causing symptomatic respiratory disease: a case report. *J. Med. Case Rep.* **2**, 257 (2008).

282. Pope, C. A. *et al.* Lung cancer and cardiovascular disease mortality associated with ambient air pollution and cigarette smoke: shape of the exposure-response relationships. *Environ. Health Perspect.* **119**, 1616–21 (2011).
283. Fahmy, B. & Cormier, S. a. Copper oxide nanoparticles induce oxidative stress and cytotoxicity in airway epithelial cells. *Toxicol. In Vitro* **23**, 1365–71 (2009).
284. Abbas, I. *et al.* Polycyclic aromatic hydrocarbons within airborne particulate matter (PM(2.5)) produced DNA bulky stable adducts in a human lung cell coculture model. *J. Appl. Toxicol.* **33**, 109–19 (2013).
285. Sun, J. D., Wolff, R. K. & Kanapilly, G. M. Deposition, retention, and biological fate of inhaled benzo(a)pyrene adsorbed onto ultrafine particles and as a pure aerosol. *Toxicol. Appl. Pharmacol.* **65**, 231–44 (1982).
286. Maricq, M. M. Chemical characterization of particulate emissions from diesel engines : A review. *Cycle* **38**, 1079 – 1118 (2007).
287. Verma, A. *et al.* Surface-structure-regulated cell-membrane penetration by monolayer-protected nanoparticles. *Nat. Mater.* **7**, 588–95 (2008).
288. Brandenberger, C., Rothen-Rutishauser, B., Blank, F., Gehr, P. & Mühlfeld, C. Particles induce apical plasma membrane enlargement in epithelial lung cell line depending on particle surface area dose. *Respir. Res.* **10**, 22 (2009).
289. Rimstidt, J. D. Quartz solubility at low temperatures. *Geochim. Cosmochim. Acta* **61**, 2553–2558 (1997).
290. Palmer, D. A. & Bénézech, P. Solubility of Copper Oxides in Water and Steam. in *14th International Conference on the Properties of Water and Steam* (eds. Nakahara, M., Matubayasi, N., Ueno, M., Yasuoka, K. & Watanabe, K.) 491–496 (Maruzen Company, 2003).
291. Brandenberger, C. *et al.* Intracellular imaging of nanoparticles: is it an elemental mistake to believe what you see? *Part. Fibre Toxicol.* **7**, 15 (2010).
292. Szalay, B., Tátrai, E., Nyíró, G., Vezér, T. & Dura, G. Potential toxic effects of iron oxide nanoparticles in in vivo and in vitro experiments. *J. Appl. Toxicol.* **32**, 446–53 (2012).
293. Karlsson, H. L., Nygren, J. & Möller, L. Genotoxicity of airborne particulate matter: the role of cell-particle interaction and of substances with adduct-forming and oxidizing capacity. *Mutat. Res.* **565**, 1–10 (2004).
294. Ingram, J. L., Rice, A. B., Geisenhoffer, K., Madtes, D. K. & Bonner, J. C. IL-13 and IL-1beta promote lung fibroblast growth through coordinated up-regulation of PDGF-AA and PDGF-Ralpha. *FASEB J.* **18**, 1132–4 (2004).
295. Berthier, R. *et al.* Fibroblasts inhibit the production of interleukin-12p70 by murine dendritic cells. *Immunology* **108**, 391–400 (2003).

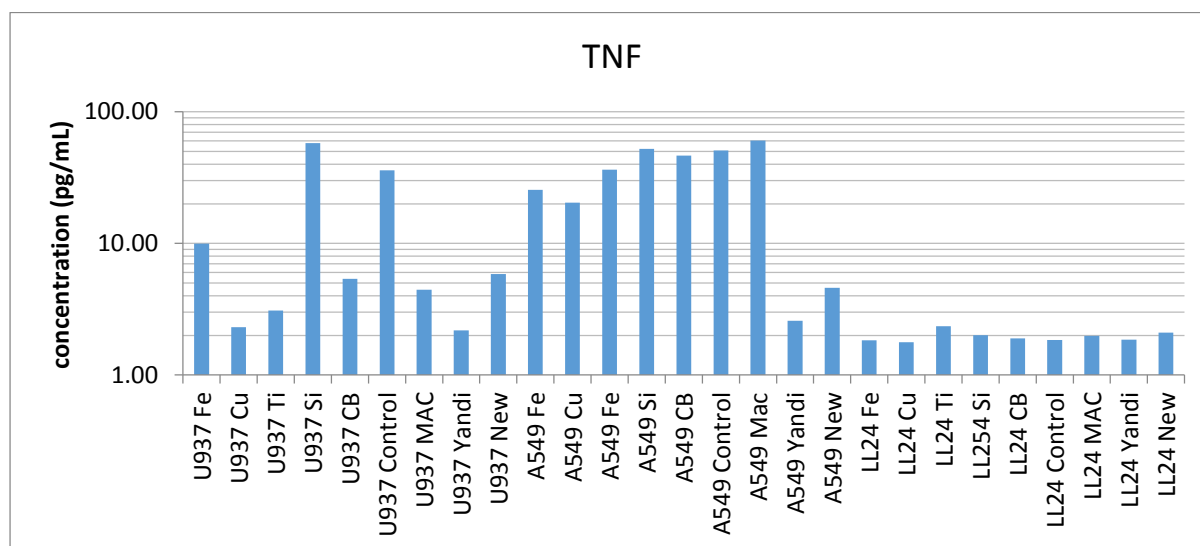
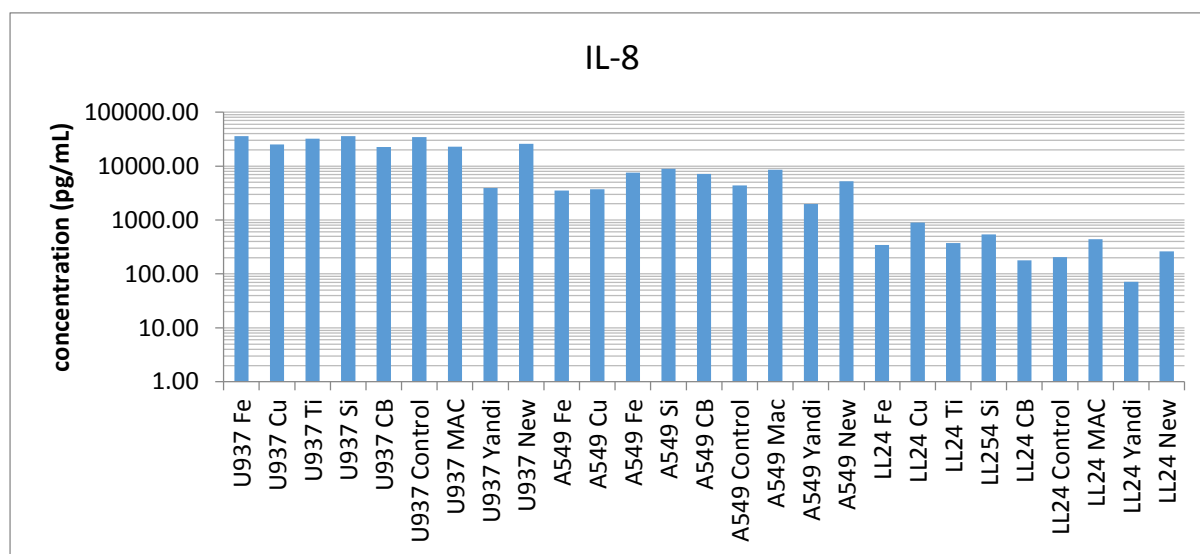
296. Agency for Toxic Substances and Disease Registry (ATSDR). *Toxicological profile for Polycyclic Aromatic Hydrocarbons (PAHs)*. Agency for Toxic Substances and Disease Registry (1995). at <<http://www.atsdr.cdc.gov/toxprofiles/tp.asp?id=122&tid=25>>
297. Hetland, G., Namork, E., Schwarze, P. E. & Aase, A. Mechanism for uptake of silica particles by monocytic U937 cells. *Hum. Exp. Toxicol.* **19**, 412–419 (2000).
298. Rubio, V., Valverde, M. & Rojas, E. Effects of atmospheric pollutants on the Nrf2 survival pathway. *Environ. Sci. Pollut. Res. Int.* **17**, 369–82 (2010).
299. Wang, X. J., Hayes, J. D., Higgins, L. G., Wolf, C. R. & Dinkova-Kostova, A. T. Activation of the NRF2 signaling pathway by copper-mediated redox cycling of para- and ortho-hydroquinones. *Chem. Biol.* **17**, 75–85 (2010).
300. Brewer, G. J. Risks of copper and iron toxicity during aging in humans. *Chem. Res. Toxicol.* **23**, 319–26 (2010).
301. Danielsen, P. H., Loft, S. & Møller, P. DNA damage and cytotoxicity in type II lung epithelial (A549) cell cultures after exposure to diesel exhaust and urban street particles. *Part. Fibre Toxicol.* **5**, 6 (2008).
302. Shukla, R. K. *et al.* ROS-mediated genotoxicity induced by titanium dioxide nanoparticles in human epidermal cells. *Toxicol. In Vitro* **25**, 231–41 (2011).
303. Anard, D., Kirsch-Volders, M., Elhajouji, a, Belpaeme, K. & Lison, D. In vitro genotoxic effects of hard metal particles assessed by alkaline single cell gel and elution assays. *Carcinogenesis* **18**, 177–84 (1997).
304. DONALDSON, K., LI, X. & MACNEE, W. Ultrafine (nanometre) particle mediated lung injury. *J. Aerosol Sci.* **29**, 553–560 (1998).
305. Singh, S. P., Rahman, M. F., Murty, U. S. N., Mahboob, M. & Grover, P. Comparative study of genotoxicity and tissue distribution of nano and micron sized iron oxide in rats after acute oral treatment. *Toxicol. Appl. Pharmacol.* **266**, 56–66 (2013).
306. Bourdon, J. a *et al.* Carbon black nanoparticle instillation induces sustained inflammation and genotoxicity in mouse lung and liver. *Part. Fibre Toxicol.* **9**, 5 (2012).
307. Lakatos, H. F. *et al.* Oropharyngeal aspiration of a silica suspension produces a superior model of silicosis in the mouse when compared to intratracheal instillation. *Exp. Lung Res.* **32**, 181–99 (2006).
308. Dagher, Z. *et al.* Activation of different pathways of apoptosis by air pollution particulate matter (PM2.5) in human epithelial lung cells (L132) in culture. *Toxicology* **225**, 12–24 (2006).

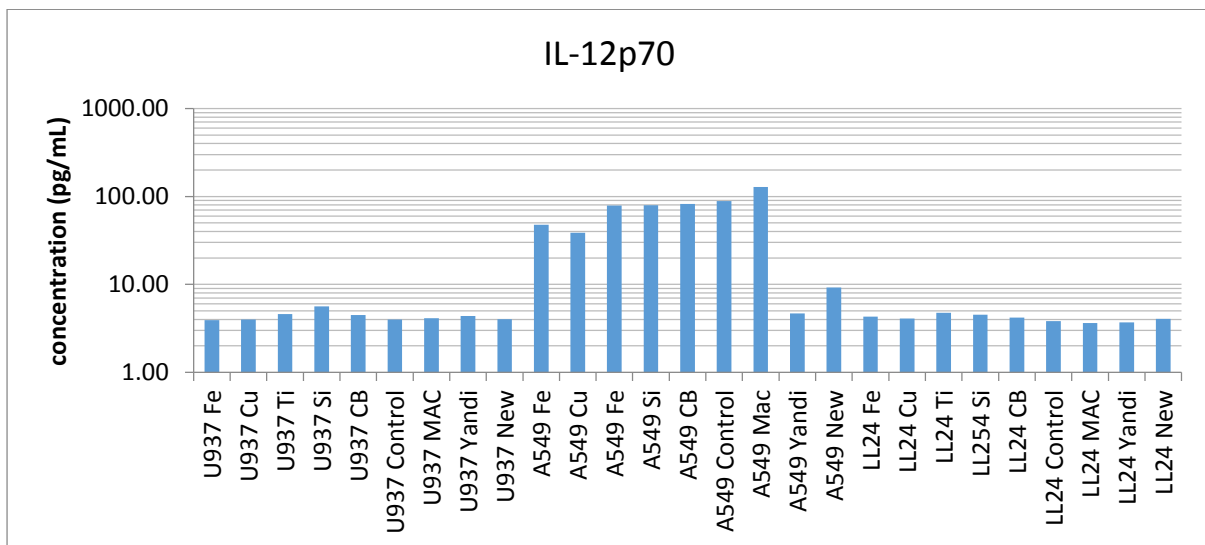
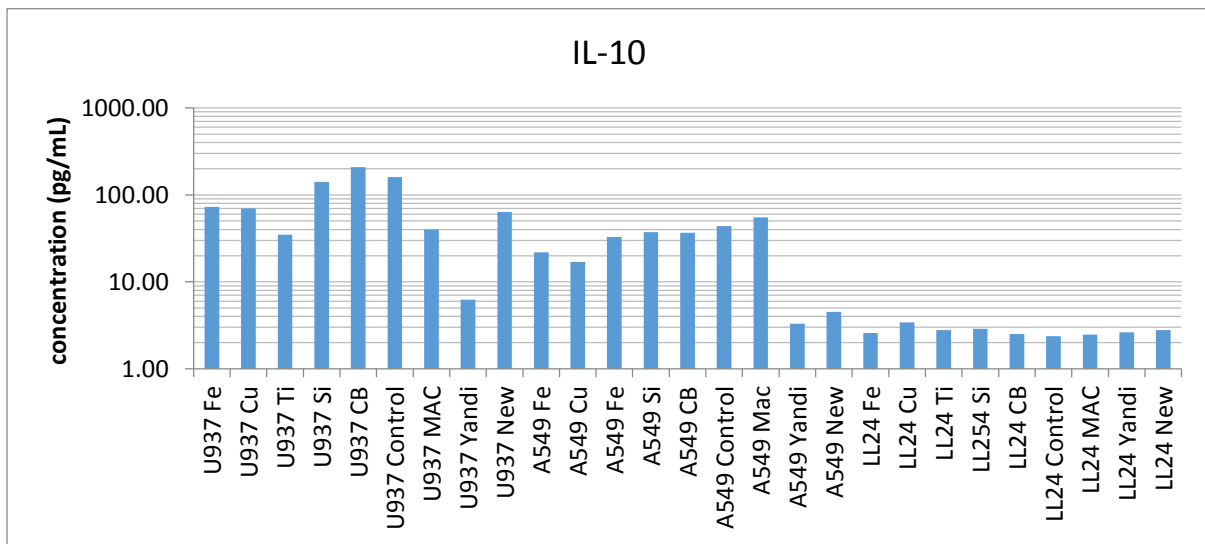
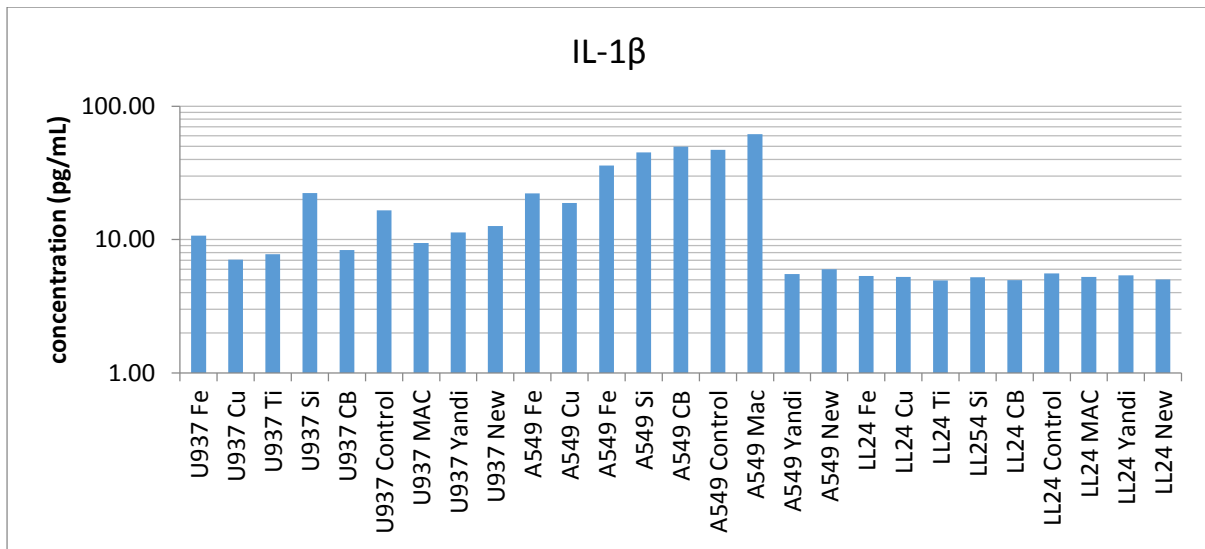
309. Guo, H. *et al.* Characterization of particle number concentrations and PM<sub>2.5</sub> in a school: influence of outdoor air pollution on indoor air. *Environ. Sci. Pollut. Res. Int.* **17**, 1268–78 (2010).

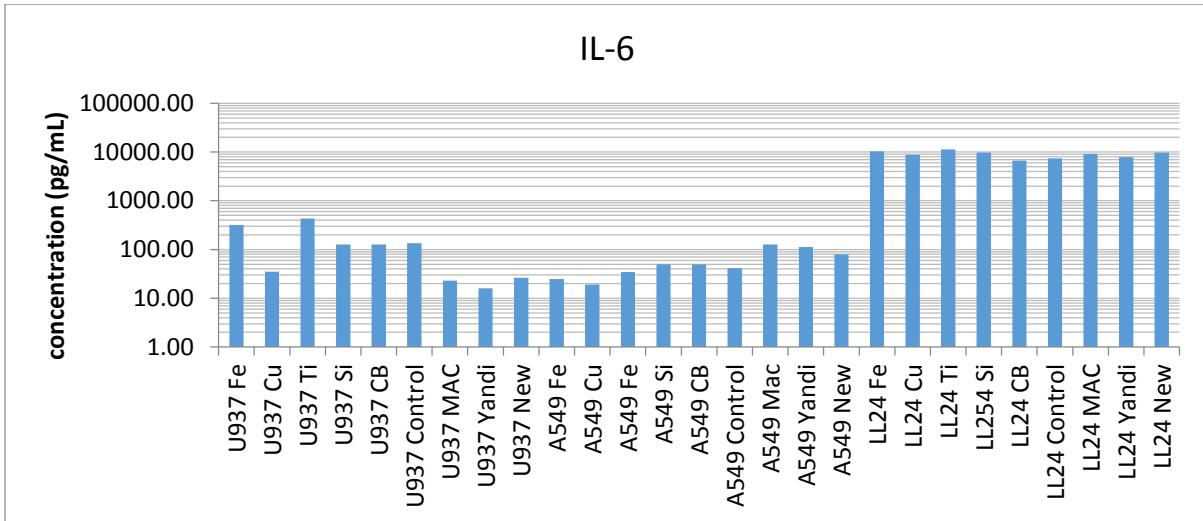
## 10. Appendices

### 10.1 Appendix A: Raw Cytokine Data

#### 10.1.1 Chapter 4 Experiment







10.1.2 Chapter 5 Experiment

